

Atomic scale images of acceptors in III-V semiconductors:
band bending, tunneling paths and wave functions

Dissertation
zur Erlangung des Doktorgrades
der Mathematisch-Naturwissenschaftlichen Fakultäten
der Georg-August-Universität zu Göttingen

vorgelegt von
Sebastian Loth
aus Limburg an der Lahn

Göttingen 2007

D 7

Referent	: Prof. Dr. Rainer G. Ulbrich
Korreferent	: Prof. Dr. Kurt Schönhammer
Tag der mündlichen Prüfung	: 26.10.2007

Introduction

The International Technology Roadmap for Semiconductors (ITRS) predicts that transistors – the primary switching components of every present day computer - will reach dimensions in the 15nm range within the next five years [1]. Then, the feature size will be comparable to the diameter of a single dopant wave function. The typical diameter of an acceptor wave function in bulk silicon is about 4nm and the extension of a donor state is as large as 10nm [2-5]. Within the next ten years both the atomically exact dopant distribution in a device and the electronic structure of single dopant atoms will become increasingly important [6, 7].

Today, the Scanning Tunneling Microscope (STM) and related techniques like Scanning Tunneling Spectroscopy (STS) are unique tools for imaging electronic features on the nanometer length scale. Since their invention in 1981 [8] the electronic contrasts induced by shallow donors and acceptors in semiconductors have been studied vigorously [9-11]. The III-V class of compound semiconductors has emerged as an ideal model system. The synergy effect of two research fields made this possible: (1) Heterostructure growth methods like Molecular Beam Epitaxy (MBE) [12] or Metal-Organic Vapor-Phase Epitaxy (MOVPE) [13] which now allow growth of semiconductor structures with atomic layer precision, and (2) so-called cross-sectional STM (X-STM) studies. In X-STM a semiconductor sample is cleaved along a preferred cleavage plane and an atomically flat cross-section through the sample is laid open, which allows the tip to probe buried dopants and heterostructures [14-16]. Nevertheless X-STM is still far from being a standard analysis method. In the limits of ultra-high vacuum and low temperatures it is still a demanding experimental technique. Despite the abundance of experimental data, the analysis of tunneling spectroscopy information is often a formidable task.

In every spectroscopic method the relation between an external control parameter (e.g. the bias voltage) and the energy scale of the sample must be known. However, for X-STM studies of III-V semiconductors this relation is a priori not clear. The Fermi energy is not pinned at the cleavage surfaces of most III-V semiconductors. This causes the tip's electric field to penetrate into the sample. The sample's energy bands at the surface are shifted with respect to the bulk. A non-trivial relation between single particle energy scales and sample bias is the result [17]. The sample bias dependent energy shift is called tip induced band bending (TIBB). Usually the function TIBB(V) is numerically derived from the self consistent solution of the Poisson equation [18-20]. The microscopic con-

figuration of the tip apex is characterized by parameters like tip work function, radius and tunneling distance. The choice of these parameters has strong impact on the calculation. The location of a certain conductivity peak on GaAs for example, may shift by over 0.5 V in $I(V)$ -spectroscopies when it is measured with different tips [21].

With this background, the adjustment of the TIBB calculation to every individual STM data set is necessary and will be a cornerstone of this thesis. Systematic measurement of the relevant parameters yields an improved description of the bias dependent band bending configuration. $I(V)$ -spectroscopies on different systems become comparable. The first part of this work describes the interplay between the numerical calculations and the parameter analysis taken from the measurements (chapter 2). This method is applied to deep and shallow acceptors in III-V semiconductors. For certain bias voltages, acceptors appear as distinct anisotropic, non-spherical features in the STM images. One expects that the observed contrasts reflect the cubic symmetry of the host crystal's valence bands. However, shallow acceptors show up as triangular contrasts with the dopant atom located in the triangle's tip, breaking the cubic symmetry of the underlying bulk band structure. Deep acceptors have an asymmetric bow-tie like shape reminiscent of the cubic symmetry.

Anisotropic features at shallow acceptors have been known for some time [11, 22], and images of deep acceptors were first reported in 2003 [23]. However, the pronounced asymmetry and the transition between these two contrast types has eluded a convincing theoretical description. The goal of this thesis is to understand the different processes leading to the acceptor contrasts. Buried dopant atoms at the $\{110\}$ cleavage planes of GaAs and InAs are studied with spatially resolved $I(V)$ -spectroscopy. Chapter 4 demonstrates that anisotropic contrasts are related to tunnel channels at the valence band edge. The key finding is that triangular and bow-tie like contrasts are caused by two different imaging processes. A careful analysis of the TIBB allows distinguishing them from each other (chapter 5).

Bow-tie like shapes are visible when the acceptor state itself is imaged. This is the case when the acceptor state is in the energy window between Fermi energy in the bulk sample and applied sample bias. The squared wave function of the acceptor state determines the tunnel current's spatial distribution. Chapter 6 presents detailed studies concerning the acceptor wave function near the InAs surface.

The tunnel process leading to triangular images requires the acceptor to be charged. For certain TIBB configurations the Coulomb potential of the acceptor's negative charge resonantly enhances an otherwise suppressed tunnel channel. Spatially resolved $I(V)$ -spectroscopy reveals a resonant tunnel current within the band gap window of the sample. A model is developed that is in good agreement with the measured $I(V)$ -curves (chapter 7).

The geometry of both tunnel processes is linked to the host lattice structure and have the same symmetry properties. They are symmetric to the $\{110\}$ mirror

planes and have no mirror symmetry over the perpendicular (001) plane. A symmetry reduction effect at the cleavage surface induces this asymmetry. It strongly distorts the resonant tunneling channel and slightly distorts the acceptor wave function. Two possible physical phenomena are discussed in this context: uniaxial strain due to surface relaxation and spin-orbit interaction of the tip induced electric field. Band structure calculations show that both effects induce comparable symmetry reduction.

The standard STM setup does not allow detailed study of these effects. The strain is caused by the surface relaxation and is therefore constant. The tip induced electric field is adjustable but inherently connected to the sample bias. It is not an independent control parameter.

A new experiment overcomes this obstacle: A three-terminal geometry is implemented that introduces an additional, controllable electric field. Acceptor atoms are embedded into a p-i-n diode structure. The cross-section through the heterostructure gives access to buried acceptors inside the diode's active layer (chapter 3). These acceptors are exposed to the strong "built-in" electric field in the plane of the sample. As a result, they are modified depending on the field strength, which is externally adjustable by biasing the diode in forward or reverse configuration. In high-resolution spectroscopic studies, the operating device demonstrates that the in-plane electric field compensates the asymmetry of the acceptor resonances. This experiment allows estimating the strength of the symmetry reducing fields (chapter 8).

The results of this thesis improve the understanding of dopant induced conductivity in STM experiments. Numerical modeling of tip induced band bending in connection with experimental evaluation of the relevant parameters is a valuable asset for the interpretation of $I(V)$ -spectroscopies on semiconductors. The field dependent studies of acceptor resonances demonstrate the ability to study spin-orbit interaction in semiconductors on the atomic scale.

This thesis in ten sentences

This thesis reports measurements of single dopant atoms in III-V semiconductors with low temperature Scanning Tunneling Microscopy (STM) and Scanning Tunneling Spectroscopy (STS). It investigates the anisotropic spatial distribution of acceptor induced tunneling processes at the $\{110\}$ cleavage planes. Two different tunneling processes are identified: conventional imaging of the squared acceptor wave function and resonant tunneling at the charged acceptor. A thorough analysis of the tip induced space charge layers identifies characteristic bias windows for each tunnel process. The symmetry of the host crystal's band structure determines the spatial distribution of the tunneling paths for both processes. Symmetry reducing effects at the surface are responsible for a pronounced asymmetry of the acceptor contrasts along the principal $[001]$ axis. Uniaxial strain fields due to surface relaxation and spin orbit interaction of the tip induced electric field are discussed on the basis of band structure calculations. High-resolution STS studies of acceptor atoms in an operating p-i-n diode confirm that an electric field indeed changes the acceptor contrasts. In conclusion, the anisotropic contrasts of acceptors are created by the host crystal's band structure and concomitant symmetry reduction effects at the surface.

In aller Kürze

Diese Arbeit befasst sich mit der Untersuchung einzelner Dotieratome mittels Rastertunnelmikroskopie (STM¹) und orts aufgelöster I(V)-Spektroskopie (STS²) [8]. Das Verständnis der lokalen elektronischen Struktur von Dotieratomen ist dabei für Grundlagenforschung und Halbleiterindustrie gleichermaßen von Interesse: Innerhalb der nächsten fünf Jahre werden Transistoren, die primären Schaltelemente in jedem gewöhnlichen Computer, auf Strukturgrößen von 15nm geschrumpft sein [1]. Sie sind dann mit der Ausdehnung der quantenmechanischen Wellenfunktion einzelner Dotieratome vergleichbar. Der typische Durchmesser einer Akzeptorwellenfunktion in Silizium liegt bei 4nm und die Ausdehnung einer Donatorwellenfunktion beträgt bis zu 10nm [2-5]. In naher Zukunft wird nicht nur die genaue Verteilung der Dotieratome in einem Bauelement wichtig sein, sondern auch ihre räumliche elektronische Struktur [6, 7].

In diesem Zusammenhang geben Akzeptoren in III-V Verbindungshalbleitern bis heute Rätsel auf. Die Querschnitts-Rastertunnelmikroskopie (X-STM) ermöglicht es, vergrabene Defekte und Heterostrukturen mit dem STM abzubilden [9, 14-16]. Dabei wird eine Halbleiterprobe gezielt entlang einer bevorzugten $\{110\}$ Bruchrichtung gespalten, so dass ein atomar glatter Querschnitt durch die Struktur zugänglich wird. Im STM erscheinen flache Akzeptoren, die knapp unter der Spaltfläche vergraben sind, als dreieckige Bereiche erhöhter Leitfähigkeit [11, 22]. Für tiefe Akzeptoren dagegen wurden bisher flügelförmige Kontraste beobachtet [23]. Obwohl dieses Erscheinungsbild seit einiger Zeit bekannt ist, entziehen sich die beobachteten Akzeptorkontraste bisher einer theoretischen Beschreibung, da sie nicht der Symmetrie der zugrundeliegenden Bandstruktur (c_{2v}) entsprechen.

Das Ziel der vorliegenden Arbeit ist das experimentelle Verständnis der zugrundeliegenden Prozesse. In Kapitel 4 wird gezeigt, dass die anisotropen Kontraste von Tunnelprozessen nahe der Valenzbandkante herrühren. Zwei verschiedene Tunnelprozesse können identifiziert werden, die anisotrope Leitfähigkeitsverteilungen aufweisen.

¹ englisch für „Scanning Tunneling Microscope“

² englisch für „Scanning Tunneling Spectroscopy“

Der erste Prozess ist das konventionelle Abbilden des Moduls der Wellenfunktion des Akzeptorzustands (Kapitel 6). Der zweite Prozess entsteht durch einen resonanten Tunnelprozess durch den geladenen Akzeptor (Kapitel 7). Das Auftreten dieser Prozesse hängt empfindlich von den spitzeninduzierten Raumladungszonen an der Halbleiteroberfläche ab. Die sogenannte spitzeninduzierte Bandverbiegung (TIBB³ [17-19]) ist ein Maß für sie (Kapitel 2). Eine numerische Berechnung der TIBB und die gleichzeitige experimentelle Bestimmung der relevanten Einflussgrößen wie Austrittsarbeit der Tunnelspitze, Spitzenradius oder Tunnelabstand erlauben eine Klassifizierung der verschiedenen Tunnelprozesse (Kapitel 5).

Die laterale Verteilung des Tunnelstroms für beide Prozesse wird durch die Symmetrieeigenschaften der Bandstruktur des Wirtskristalls bestimmt. Die Oberfläche induziert einen Symmetriebruch, der die Abweichung der gemessenen Kontraste von der kubischen Symmetrie erklärt. Die beobachteten Kontraste weisen eine deutliche Anisotropie bezüglich der (001) Spiegelebene auf. Zwei physikalische Effekte, die Einfluss auf die Symmetrie der Bandstruktur haben, werden diskutiert: Ein uniaxiales Spannungsfeld durch die Oberflächenrelaxation und das spitzeninduzierte elektrische Feld. Beide Effekte wirken senkrecht zur Oberfläche und erzeugen den beobachteten, zu ihrer Wirkungsrichtung transversalen Symmetriebruch in der Bandstruktur. Zunächst war es nicht möglich, ihren Einfluss auf den akzeptorinduzierten Tunnelstrom gezielt experimentell zu untersuchen. Das Spannungsfeld wird durch die Relaxation der Oberfläche hervorgerufen und kann nicht weiter beeinflusst werden. Das elektrische Feld der Spitze kann zwar verändert werden, ist aber direkt an die Abbildungsspannung gekoppelt und deshalb ebenfalls kein unabhängiger Kontrollparameter.

Um dennoch ein kontrollierbares elektrisches Feld im Experiment einzubringen, wurde eine Dreipolgeometrie realisiert: Akzeptoren werden gezielt in die aktive Schicht einer p-i-n Diode eingebettet. Der Querschnitt durch die Heterostruktur wird dem STM durch Spalten zugänglich gemacht (Kapitel 3). Auf der freigelegten $\{110\}$ -Fläche lassen sich jetzt einzelne Akzeptoren finden, die dem internen elektrischen Feld der Diode ausgesetzt sind. Die Akzeptorkontraste werden durch das transversale, jetzt in der Oberfläche liegende elektrische Feld beeinflusst. Über die angelegte Diodenspannung ist die Stärke dieses Feldes eine externe Kontrollgröße. In hochaufgelösten STS-Messungen kann die Abhängigkeit des anisotropen Kontrastes von der elektrischen Feldstärke beobachtet werden. Es zeigt sich, dass sich das Erscheinungsbild des resonanten Tunnelkanals an Akzeptoren signifikant verändern lässt. Dadurch werden Rückschlüsse auf die Stärke des symmetriebrechenden Feldes möglich. Bandstrukturrechnungen zeigen, dass das elektrische Feld die Symmetrie der Bandstruktur über Spin-Bahn Kopplung in der beobachteten Weise verändern kann.

³ englisch für „Tip Induced Band Bending“

Die Ergebnisse dieser Arbeit vertiefen das Verständnis der durch Dotieratome induzierten Leitfähigkeit in STM Messungen. Die numerische Berechnung der spitzeninduzierten Bandverbiegung ermöglicht in Kombination mit der experimentellen Bestimmung der notwendigen Parameter eine genaue Analyse der gemessenen $I(V)$ -Kennlinien. Die feldabhängigen Untersuchungen des resonanten Tunnelprozesses deuten darauf hin, dass es mit dem STM möglich ist, die Spin-Bahn Wechselwirkung auf kleinsten Längenskalen zu untersuchen.

Contents

Introduction	i
This thesis in ten sentences	iv
In aller Kürze	v
Contents	ix
1. Experimental setup and theoretical background	1
1.1. STM setup for studies of operating semiconductor devices	3
1.2. Tip preparation	6
1.3. Sample preparation	7
1.4. Sample system: cleavage planes of III-V semiconductors	11
1.4.1. Crystallographic properties	11
1.4.2. Electronic properties of the III-V surfaces	13
1.5. Applicable STM theory	15
1.5.1. I(V)-spectroscopy and normalization	18
2. Tip induced band bending	23
2.1. Three dimensional TIBB(V) calculation	25
2.2. From apparent barrier height to tip work function	30
2.2.1. Rule of thumb estimate	31
2.2.2. Numerical calculation of the tunnel barrier height	34
2.3. Validation of TIBB(V) with I(V)-spectroscopy	38
2.4. Summary	44
3. The p-i-n-diode as source for an adjustable electric field	45
3.1. MBE-grown heterostructure	46
3.2. I(V)-spectroscopy	50
3.3. The built-in potential	52
3.4. External characteristics and internal band-alignment	55
3.5. Summary	59
4. Dopant induced anisotropic conductivity	61
4.1. Topographic properties of the anisotropic contrasts	64
4.2. Origin of the anisotropic shapes	68
4.3. Summary	72
5. Imaging mechanisms at neutral and charged acceptors	73

5.1.	Different charge states at acceptors.....	74
5.2.	I(V)-spectroscopy of Mn in InAs	78
5.3.	Charging signature of the acceptor	82
5.4.	Contrasts of charged and neutral acceptors.....	84
5.5.	Summary.....	86
6.	Wave function imaging of buried acceptors.....	87
6.1.	Depth dependent shape of the acceptor state.....	88
6.2.	Band structure induced asymmetries.....	96
6.2.1.	Strain at the {110} surfaces.....	96
6.2.2.	Electric fields under the STM tip	100
6.3.	Summary.....	102
7.	Resonant tunneling through charged acceptors	105
7.1.	The tunneling process at charged acceptors.....	106
7.1.1.	I(V)-spectroscopy	106
7.1.2.	The resonant tunneling model.....	108
7.1.3.	Sequential tunneling vs. resonant tunneling.....	112
7.2.	Anisotropic shape of the acceptor resonance	113
7.2.1.	Spatially resolved I(V)-spectroscopy.....	114
7.2.2.	Depth independent shape.....	118
7.3.	Complex band structure induced anisotropies.....	120
7.3.1.	Asymmetric decay constants.....	123
7.4.	Summary.....	128
8.	Local manipulation by electric fields.....	131
8.1.	Suppression of the resonant tunneling channel	132
8.2.	Influence of the in-plane electric field on the anisotropy.....	138
8.3.	Summary.....	146
9.	Summary.....	147
10.	Appendix.....	149
10.1.	Band structure calculation.....	149
10.2.	Matlab code for the band structure calculation.....	155
A.	Abbreviations and definitions.....	158
B.	Bibliography	161
	Danksagung	168
	Curriculum vitae.....	169

1. Experimental setup and theoretical background

This chapter presents an introduction to the Scanning Tunneling Microscope and the preparation techniques for in-situ cleavage. The development of a new low temperature STM unit with multiple sample bias contacts is described. Finally, the necessary theoretical framework and basic properties of the sample systems GaAs and InAs are given.

The experiments of this thesis are performed with a Scanning Tunneling Microscope (STM). The STM was the first research tool of a class, which nowadays is referred to as Scanning Probe Microscopy or local probe techniques [24]. A very local interaction of a probe tip and the sample surface is used to gain images down to the atomic scale [25, 26]. The STM reaches unmatched resolution of single atomic structures and resolves the squared wave functions of the sample on this scale. High resolution images and spectroscopic data of single impurities in semiconductors are obtained.

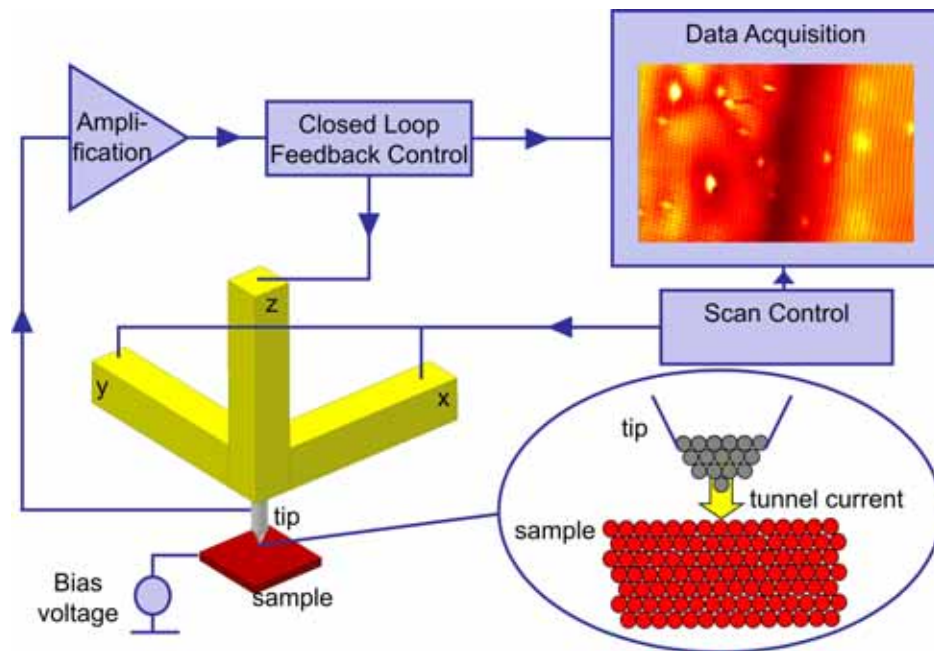


Fig. 1.1 Principle of the scanning tunneling microscope. The description is given in the text.



Fig. 1.2 One of the first STMs designed by Binnig and Rohrer. The sample (center of the image) is placed on a piezo walker and approached to the STM tip which is placed on a piezo tripod (right part). (photograph taken at the ICN+T conference in Basel 2006)

The building blocks of an STM are put together in Fig. 1.1. A conductive sample (red) is biased with respect to the STM tip⁴. The very sharp metallic STM tip is moved laterally and vertically by xyz-piezo actuators. When tip and sample are in close proximity ($\sim 1\text{nm}$ gap) a small electrical current flows through the vacuum gap (see inset of Fig. 1.1). The tunnel current is exponentially dependent on the gap width. An amplification circuit converts the current signal into a voltage signal that is fed into a closed loop feedback control. The z-height of the tip above the sample is actuated by the feedback loop. The standard mode of operation is the so called constant-current mode. The feedback loop is driven such that the tunnel current is kept constant at all times. The height signal is then acquired as topographic height information. A scan control unit actuates the xy-piezoes and scans the tip laterally over the sample. The resulting images are topographic maps of the sample surface. It is worth noting that the recorded height signal does not necessarily represent the morphology of the sample surface. Because an electrical current is used to control the z-height, the height signal represents a surface of constant conductivity rather than the morphological surface. Especially on semiconductors this can be a drawback and an advantage at the same time: the conductivity may change drastically on a nanometer length scale due to doping fluctuations for example. Therefore it is inherently not possible to obtain purely morphological information of the non-ideal semiconductor surface. The big advantage is that it is possible to resolve electronic information of the sample already by topographic measurements (which is the fastest measurement that can be performed with the STM). One of the first STMs conceived by Binnig and Rohrer is shown in Fig. 1.2. The original design is very close to the schematic of Fig. 1.1. The xyz-movement of the tip is accomplished by a tripod of piezo-ceramics. The sample is mounted on a electrostatic walker (“louse”) for coarse approach. The STM setup is built up on a ceramic base plate that is suspended on long springs, which provide an easy way

⁴ This will be the notation in this thesis. All bias voltages are applied to the sample while the tip is kept at ground potential.

of vibration insulation. The presented STM is operated in UHV. Since the original STM setup a lot of experimental improvements have been conceived. The design of the STM used in this thesis will be the focus of the next section.

1.1. STM setup for studies of operating semiconductor devices

The study of semiconductor heterostructures is the focus of this work. The buried heterostructures are accessed by cleaving the sample pieces along one of the preferred cleavage planes of the host crystal. Ideally an atomically flat cross section through the heterostructures is laid open. If the cleavage is done in the UHV, the sample surface is not contaminated and therefore the electronic structure is disturbed only little. The cross-sectional sample preparation is also a good tool to investigate the electronic structure of dopant atoms within the semiconductor host. On homogeneously doped samples, dopants in various depths below the surface are present due to the statistical dopant distribution in the bulk.

All measurements presented in this thesis are carried out in a custom-built STM system that has been developed in Göttingen. This offers a unique advantage: the setup could be modified to accommodate the needs of the experiments. Cross-sectional scanning tunneling microscopy (X-STM) adds some additional requirements to the general STM setups: In order to be able to study the atomic structure of heterostructures it is important to create good cleavage surfaces that stay clean for a few days. Over the past years a preparation method has been developed and improved that routinely produces cleavage surfaces that have low step density and are atomically flat over a few μm^2 . The semiconductor surfaces investigated here (InAs and GaAs) have a high adsorption coefficient for residual gas molecules of the vacuum chamber. Therefore all work on such surfaces requires good vacuum systems. The base pressure of the low temperature STM used here is $<2 \cdot 10^{-11}$ mbar.

Any STM requires a mechanical coarse approach of tip and sample from macroscopic distances (typically 1 mm) into the range of the piezoelectric materials (about 100 nm). In addition to this vertical coarse motion, the tip has to be positioned over the heterostructures in X-STM studies. This requires an additional xy-coarse motion of the tip. In order to be able to find the heterostructures during this coarse lateral positioning, an optical access with a high quality microscope is very desirable. The vacuum system has to be modified such that optical access to the microscope is possible from the outside with a reasonable aperture. It is challenging to achieve this in a low temperature system without getting high thermal instability by room temperature heat radiation. The STM is suspended under a liquid helium bath cryostat and mounted into a copper cup that thermally couples the STM to the helium cryostat. A liquid nitrogen cryostat surrounds the helium system. The STM is shielded from heat radiation by a sec-

ond copper cup that is coupled to the nitrogen cryostat. Optical access is provided by openings in the nitrogen cup that are covered with glass that absorbs or reflects infrared radiation.

The focus on the detailed atomic structure. This results in the requirement of high mechanical and electronic stability of the STM to be able to routinely obtain atomic resolution and at the same time scan relatively large surface areas. The general design of the STM in the X-STM setup used here is based on the ‘beetle’-type STM which was designed by Besocke [27]. Quast and Rosentreter developed a low temperature version in the Göttingen group [28, 29]. The single most important advantage of this type of microscope is the fact that it doesn’t need any mechanical feedthroughs for the coarse vertical approach and the lateral positioning of the tip. The beetle type scanner consists of a base with the xy-stage built of tube piezos and a head with the z-piezo. The head is made of stainless steel and rests on ruby balls at the end of the xy-piezoes. The coarse positioning is done via “slip-stick motion” (inertia motor) [30].

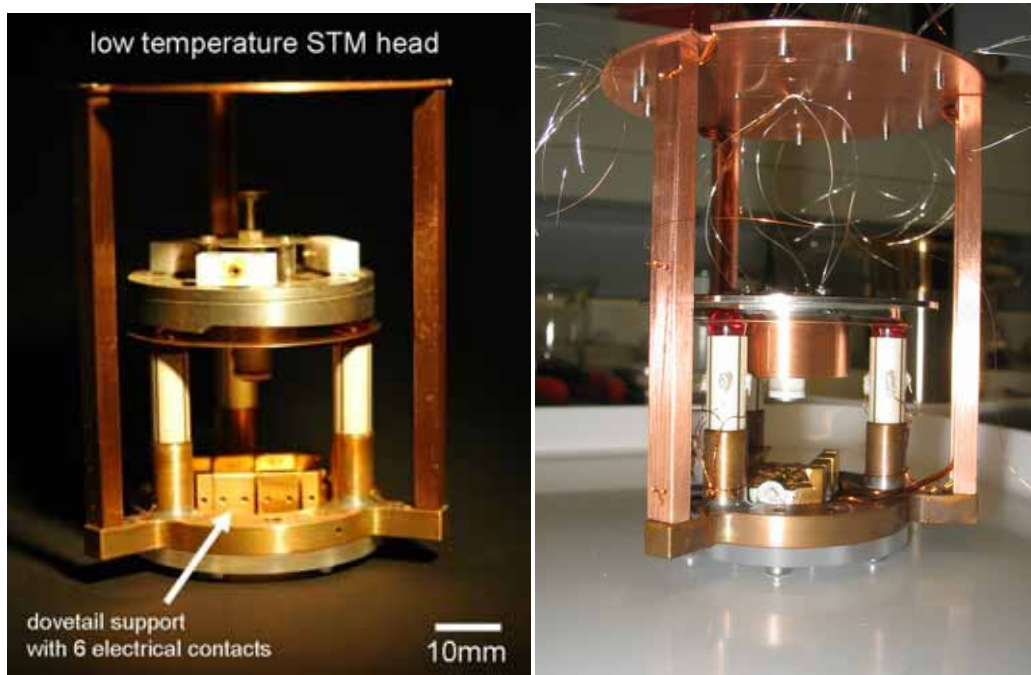


Fig. 1.3 STM scanning unit. The Beetle type STM head allows reproducible coarse positioning in a large area. The sample holders are fixed in a segmented dove tail sample support. The six segments bring multiple electrical contacts to the sample without losing mechanical or thermal stability.

During this thesis a new STM unit has been developed and implemented into the existing cryostat system. It is shown in Fig. 1.3. The fundamental setup of the scanner unit is similar to those already in operation in the Göttingen group. The sample support is upgraded to a dove-tail sample support carrying six separate segments that are electrically isolated. The sample holders (see Fig. 1.8) have a dove-tail body that has the same segmentation (see also [31]). With this setup it is

possible to bring up to six electrical contacts to the sample without losing mechanical stability. Good thermal coupling to the cryostat is of particular interest for the current design (See right image of Fig. 1.3). It is accomplished by mounting the STM unit into a solid copper mounting frame onto a sapphire base plate. The scanner and the sample support are soldered with indium to the base plate. The electrical leads to each segment are thermally coupled to the helium cryostat and the mounting frame at various points. The STM head is thermally coupled via silver filaments to the mounting frame. A ceramic temperature sensor is added to the sample support to be able to monitor heat dissipation when a current is driven through the sample. This setup now routinely operates at 5.6K sample temperature with liquid helium of 4.2K in the cryostat. The compact and rigid design results in quick thermal equilibration of the whole STM after samples are transferred. Within one hour it is possible to begin the STM experiments at low temperature.

Because every piezo ceramic actuator has a slightly different piezo constant, it is necessary to calibrate the new STM head with known structures. The surface states of GaAs (110) serve as grating for the x and y calibration. The lattice constants of GaAs are known with high accuracy. The surface unit cell is 5.65 Å in $[001]$ and 4.00 Å in $\{110\}$. Fig. 1.4 shows a (12x12) nm² area of the GaAs surface. The periodicity of the surface states is observable in $[001]$ and $[\bar{1}10]$ direction. The surface lattice constants are extracted via FFT. The best match with the theoretical values is obtained for the piezo constants

$$c_x = 3.45 \frac{\text{nm}}{\text{V}}$$

$$c_y = 3.53 \frac{\text{nm}}{\text{V}} .$$

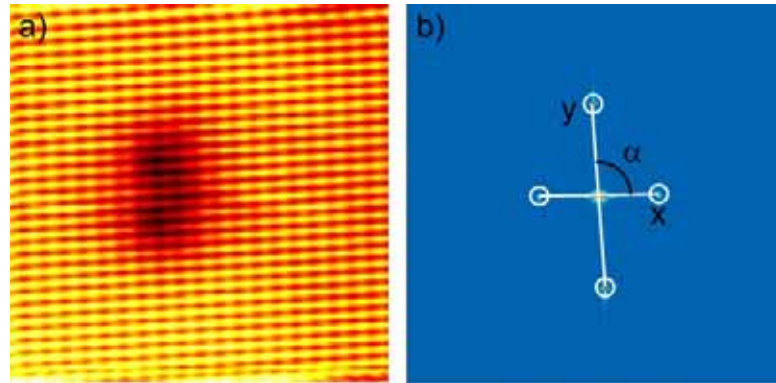


Fig. 1.4 a) (12x12)nm² constant current topography of a GaAs surface. b) Fourier transform of image a) with the four peaks corresponding to the atomic corrugations of the images surface states along $[001]$ and $[\bar{1}10]$. The reciprocal vectors x and y match the GaAs reciprocal lattice constant of for piezo sensitivity in x-direction 3.45 nm/V and in y direction 3.53 nm/V. The images show a slight shearing of the x- and y-direction of 3° off the 90° alignment.

A slight shear remains even though the piezo constants have been adjusted. The angle between x- and y- axis is 93° , so the scanner is 3° non-orthogonal. This shear has to be removed numerically from the measurements where necessary. It is difficult to determine the sensitivity of the z-piezo on GaAs with sufficient accuracy because steps on the $\{110\}$ surfaces are charged [32]. The calibration is done on Cu (100) as shown in Fig. 1.5. The (100) layer to layer distance for Cu is 1.81 \AA . The $(50 \times 50) \text{ nm}^2$ area shows several monoatomic terraces. The histogram gives the height of each step. The linear fit has a slope of $1.81 \text{ \AA/monolayer}$ for the piezo constant

$$c_z = 0.507 \frac{\text{nm}}{\text{V}} .$$

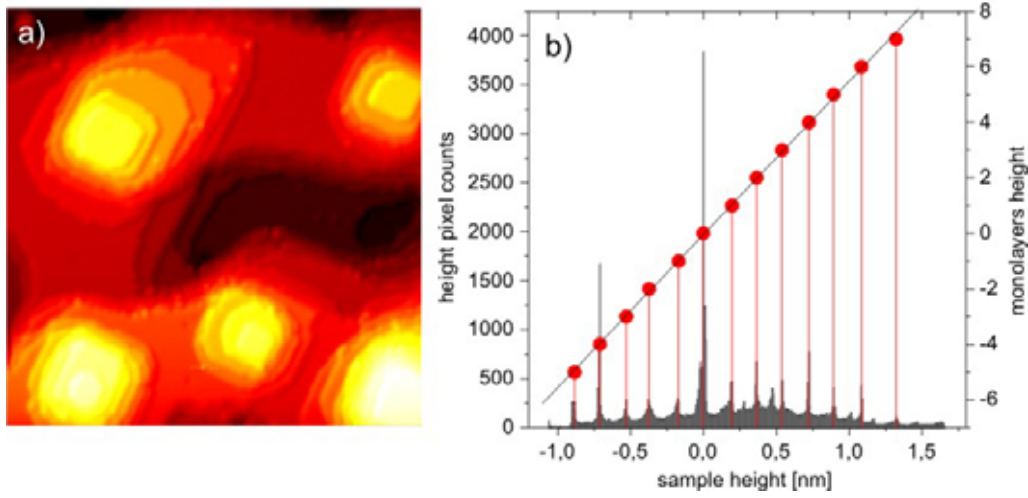


Fig. 1.5 a) $(50 \times 50) \text{ nm}^2$ filtered constant current topography of a Cu (100) surface (measurement by A. Weismann). b) Histogram of the topography in grey (left axis) and analysis of the monoatomic steps from the histogram (right axis). The linear fits gives an average slope of $1.81 \text{ \AA/monolayer}$ (which is $a_0/2$ for Cu (100)) for a piezo sensitivity of 0.507 nm/V .

1.2. Tip preparation

The tip preparation is a critical step in obtaining high quality STM images with atomic resolution. However, the processes used to make “good tips” are sensitively dependent on the exact procedures and some not well controlled parameters. A detailed treatment of the tip preparation technique used in Göttingen are already described extensively in previous works [21, 33]. Only a brief summary of the necessary preparation steps will be given here. Polycrystalline tungsten wire of $250 \mu\text{m}$ diameter is electrochemically etched in KOH solution (chemical process: anodic oxidation) [34]. Nonlinear etching kinetics at the point where the wire pierces the solution surface lead to a constriction directly under the surface. When the constriction becomes too narrow, the remaining wire in

the solution breaks off and pulls out a very sharp apex. Scanning Electron Microscope images (SEM) show typical radii of the end of the apex of such tips of less than 10 nm. The etching renders the W apex covered with a thin oxide layer. The oxide layer is then removed by heating the tip in UHV to about 800°C (red glow). Unfortunately this process also results in blunter tips with a larger tip radius. Consequently, the tips are treated by argon ion sputtering with typical ion-energies of 4 keV. Anisotropic sputtering yields of different crystallographic facets of W result in resharpener of the apex. After the preparation in the shuttle system the tips are transferred into the STM chamber and mounted on the STM head. Fig. 1.6 shows the tip holder and a suspended tip. The W wire is clamped in a small iron dish for all the preparation processes. A magnet mounted at the end of the z-piezo then magnetically attaches the tip. Magnetic attachment has the major advantage over clamping with a spring system that it produces no vibrational noise during scanning.

The microscopic properties of the STM tips and the consequences for the electronic features of the tunnel contact will be discussed in chapter 2.1.

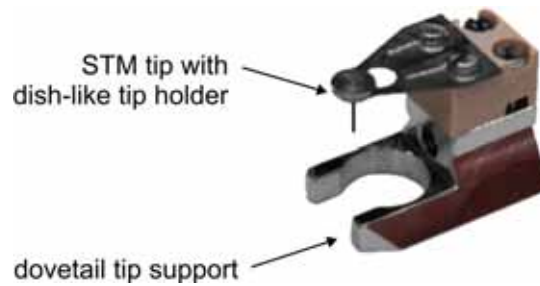


Fig. 1.6 Tip holder with STM tip. The base of the sample holder fits into the dove-tail sample support of the STM, so that tips can be exchanged without breaking the vacuum. The tips are made of tungsten wire and clamped into a tip holder dish. This dish is placed in a key-hole opening in the tip holder and later magnetically attached to the STM.

1.3. Sample preparation

All experiments of this thesis are performed in cross-sectional geometry. In terms of sample preparation the most important requirement is to obtain high quality cleavage surfaces with low step density and large atomically flat terraces. It turns out that this task is not too difficult to accomplish on lightly doped bulk samples without heterostructure. For the case of InAs doped with $1 \cdot 10^{17} \text{ cm}^{-3}$ Mn it is sufficient to cut out sample pieces directly from untreated commercially available wafers with thickness up to 650 μm . But especially for the studies of the p-i-n diodes a careful sample preparation is essential. Three steps are necessary: Cleaving and thinning of the sample pieces, Application of ohmic contacts and preparation of a defined notch as initial cleavage point. Obtaining reproducible cleavage results on heterostructure samples is still challenging [35] and the involved parameters are not completely understood.

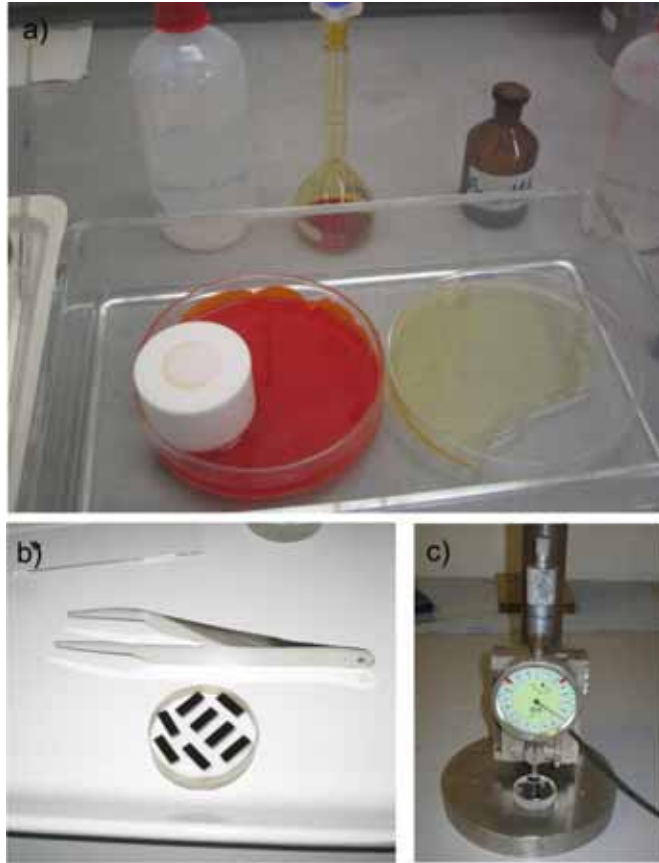


Fig. 1.7 Chemical polishing of MBE-grown GaAs wafer pieces. The substrates have a thickness of 350 – 650 μm . (a) They are thinned down to 80 μm with the bromine methanol etch. (b) The sample pieces are supported on a glass puck. (c) Subsequent measuring of the sample thickness with a precision dial gauge is necessary to hit the intended thickness.

Therefore the preparation of all samples follows one recipe as close as possible. The preparation recipe was optimized during this thesis and is presented here in detail:

Thinning: For all cubic III-V semiconductors the natural cleavage planes are the four $\{110\}$ planes. The starting point therefore are (001) oriented wafers. The p-i-n diodes are grown by molecular beam epitaxy (MBE) on commercial (001) substrates⁵. The wafers have thicknesses of 350 μm to 650 μm , which is too thick for a good cleavage of heterostructures. By prescribing small notches the wafers are cleaved into 6 x 8 mm rectangular sample pieces. The pieces are thinned down to about 80 μm -90 μm . A bromine methanol chemo-mechanical thinning procedure is used [36]. As shown in Fig. 1.7b the sample pieces are glued to a glass puck with the MBE grown structure pointing to the glass. The bottom of a flat Petri dish is covered with filter paper and an amount of bromine methanol is

⁵ The details of the diode growth are given in chapter 3

applied (see Fig. 1.7a). The glass puck is submersed into the etching solution and gently moved over the filter paper. The bromine methanol chemically reacts with the GaAs and dissolves the surface. But simple etching in the bromine methanol solution would result in rough surfaces, because the reaction products would inhibit further etching. Swiping the samples over the filter paper carries away the etching products and results in polished flat surfaces. The glass puck is moved in the Petri dish with the white Teflon hollow cylinder. A Teflon weight provides uniform pressure to ensure constant etching rates. All samples are thinned down to a thickness of $150\mu\text{m}$ with an etchant containing 5% Vol. Br_2 . Then the remaining $60 - 70\mu\text{m}$ are thinned with a etchant containing only 1.67% Vol. Br_2 . Subsequent thickness control with a precision dial gauge allows to reach the intended sample thickness with a precision of $\sim 5\text{-}10\mu\text{m}$ (see Fig. 1.7c). Typical etching rates are $40\mu\text{m}/\text{min}$ for the 5% etchant and $12\mu\text{m}/\text{min}$ for the diluted etchant. With this technique mirror flat surfaces are obtained. In contrast to mechanical thinning procedures (e.g. with diamond paste) this method induces much less surface damage and results in better cleavage properties of the sample. Mechanical abrasion creates microscopic scratches and introduces dislocations, that would interfere with the propagating crack during cleavage.

Ohmic contacts: After reaching the intended sample thickness the GaAs pieces are removed from the glass puck and cleaned in acetone and ethanol. Ohmic contacts are evaporated on front side and back side of the sample pieces [37]. The metallization material is thermally evaporated under high vacuum conditions ($\sim 1 \cdot 10^{-6}\text{mbar}$). The recipes are:

- n-GaAs: 130mg eutectic AuGe alloy + 20mg Ni
- p-GaAs: 150mg AuZn (90:10) mixture

The contacts are alloyed by rapid thermal annealing in a commercial RTA oven under nitrogen atmosphere. The annealing sequence is: (1) ramping to 420°C within 10 sec. (2) annealing at 420°C for 150 sec. (3) cooling down to 150°C within 90 sec. This procedure typically results in ohmic contacts with contact resistances $< 1\Omega$. During annealing, the contact metallization diffuses into the GaAs crystal. With the chosen annealing cycle the approximate diffusion depth is $\sim 100\text{ nm}$ [38]. For investigations of operating devices this has to be taken into account for the heterostructure design. The capping layer must be larger than the contact diffusion length.

Notch preparation: Then the $6 \times 8\text{ mm}$ pieces are cleaved into two $(3 \times 8)\text{ mm}$ pieces to recover one sample side with sharp edges. This is necessary because the sample edges become round during the thinning process. A notch is applied at the sharp edge with a tungsten carbide needle. The notch is about 0.5 mm long and exactly oriented along the intended (110) cleavage plane. The position is chosen such that it is just above the vice when the sample is mounted (see Fig. 1.8 left). The sample is structurally weakened at the notch position. In the vacuum it suffices to apply a small amount of force at the upper end of the sample piece to induce the cleavage at the height of the notch (see Fig. 1.8 right).

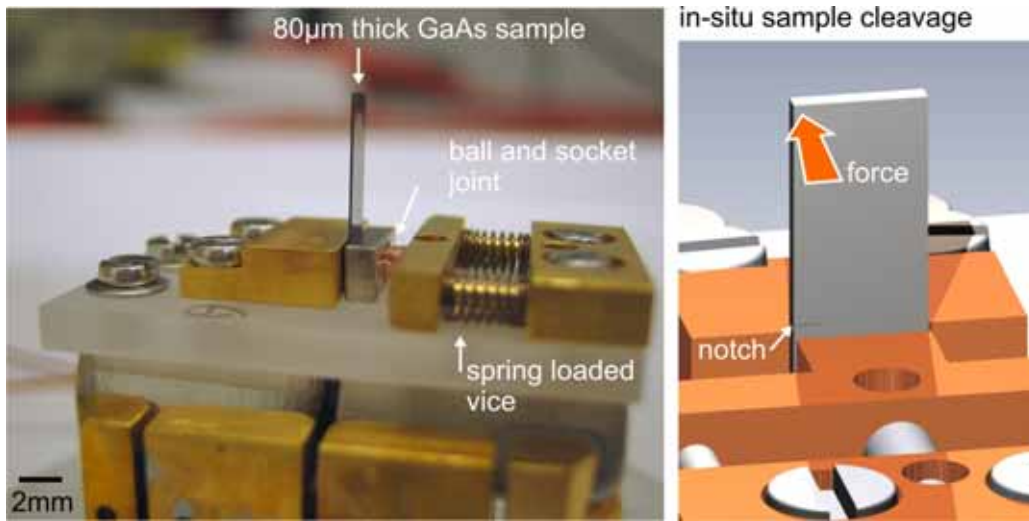


Fig. 1.8 (left) Dove tail sample holder with separate electrical contacts for front side and back side of a semiconductor heterostructure. The spring loaded vice fixates the 80 μm semiconductor sample without any glue like conductive silver or indium. (right) a notch is applied to the sample directly above the vice. The sample is cleaved *in-situ* with a small force acting on the upper side of the sample

Fig. 1.8 shows a sample holder with an uncleaved sample mounted. The sample holder consists of a dove-tail body, a sapphire plate and a spring loaded vice mounted on top of the sapphire plate. The dove-tail body of the presented sample holder has two segments. This allows separate front side and back side contact to the sample. One electrical contact is the left fixed shoe of the vice and the other contact is the moveable shoe on the right side. On both sides of the sample ohmic contacts have been evaporated and alloyed (see next section for details). All copper parts of the sample holder and sample support are gold plated to minimize contact resistances. Besides this it proved to be particularly important to include a ball and socket joint on the moveable vice shoe in order to get electrical contact to the ohmic contact pads on the sample and not only a Schottky contact to one edge of the sample.

The mounted samples are transferred into the UHV with a vacuum shuttle system [39]. They are cleaved *in-situ* just before the measurement. The cleavage is done at room temperature and then the samples are transferred into the pre-cooled STM. The coarse approach to the cleavage surface is monitored with an optical microscope from outside the vacuum chamber. Fig. 1.9 shows two microscope images of the approaching tip. The STM tip is approached from the top. The gold-plated vice and the dark sample piece are visible at the bottom. The distance from tip apex to its mirror image serves as a measure for the relative distance of the tip to the sample (between tip and mirror image a small gap is visible in the right image of Fig. 1.9). When the distance is of the order of 10-20 μm the STM feedback is activated and the tip is carefully approached until tunnel current is detected.

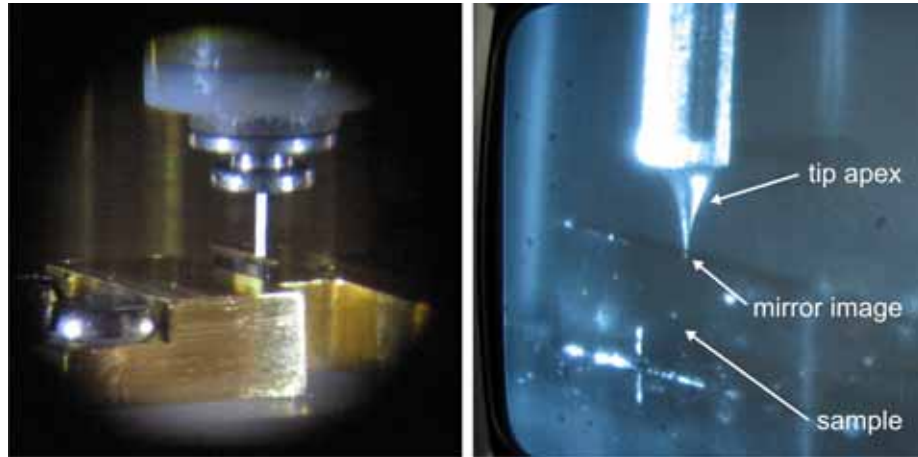


Fig. 1.9 (left) STM in tunneling contact above a GaAs cleavage plane seen through the optical microscope. (right) In the CCD control the position of the tip above the surface is estimated to lie between the tip apex and the mirror image of the apex on the mirror-like sample surface.

1.4. Sample system: cleavage planes of III-V semiconductors

After the preparation, a clean and flat $\{110\}$ cleavage plane is accessed with the STM. The crystallographic and electronic properties of the undisturbed surfaces are well known. Nowadays these surfaces are a standard model system for the study of defects, dopants and heterostructures. In this thesis measurements on GaAs and InAs are presented. In this section only a brief summary of their basic properties that are relevant for the STM measurements is given. Detailed information is found in [9, 40-42].

1.4.1. Crystallographic properties

Both host crystals, GaAs and InAs, are cubic III-V semiconductors. The lattice is of Zincblende symmetry. The Zincblende lattice consists of two overlapping fcc-lattices that are shifted with respect to each other by $1/4$ of the $[111]$ space diagonal. The major difference to the similar Diamond lattice is the lack of a center of inversion. That is due to the fact that one fcc sublattice is entirely occupied by the group III element, i.e., the cation (here Ga or In), and the other sublattice is made up of the group V element, i.e., the anions (here As). Fig. 1.10 sketches the cubic Zincblende unit cell [43].

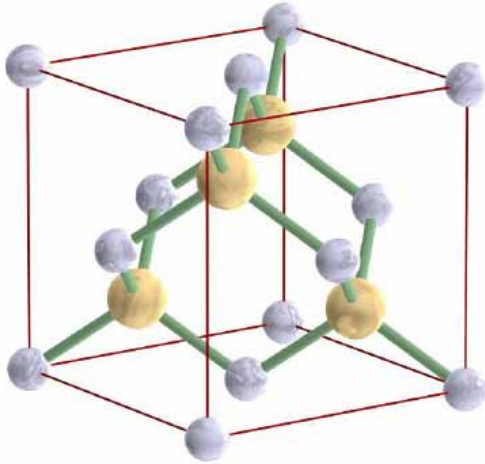


Fig. 1.10 Ball-and-stick model of the Zincblende crystal, the lattice of the cubic III-V semiconductors. The cubic unit cell is indicated by the red boundaries. Image adopted from [43].

The bonds between the group III and group V element is partially ionic [40]. The preferred cleavage planes are the non-polar $\{110\}$ -planes as mentioned above [40]. The cleavage results in two broken ("dangling") bonds in each surface unit mesh that are half filled. The ideal truncated bulk surface is unstable and lowers its energy by relaxation: The anions move outward and the cations move inward. The relaxation does not change the size and orientation of the surface unit cell. All $\{110\}$ surfaces of all III-V semiconductors exhibit the same type of (1×1) reconstruction which is often referred to as buckling [44, 45]. The surface unit cell is 5.65 \AA along $[001]$ and 4.00 \AA along the $\langle 110 \rangle$ axis.

The characteristic structure on the cleavage planes is given by the zig-zag rows of the atoms in the first layer of the surface (see ball-and-stick models in Fig. 1.11). Each zig-zag row runs perpendicular to the $[001]$ direction and consists of alternating cations and anions. Along the $[001]$ direction the topmost zig-zag rows are separated by a trench in which the second layer is visible from the surface. The $\{110\}$ surfaces are divided into two sets of non-equivalent cleavage planes as shown in Fig. 1.11. The (110) and $(\bar{1}\bar{1}0)$ surface are one set and the $(1\bar{1}0)$ and $(\bar{1}10)$ surface form the other. These two sets are orthogonal to each other as seen by the colored cube in the figure. The planes of each set are parallel to each other. The lattice structure of the non-equivalent surfaces differs by a mirror deflection over the (001) plane. The ball-and-stick models in Fig. 1.11 show both surface types. But besides this difference all $\{110\}$ planes have the same lattice properties. This results in equal electronic band structure.

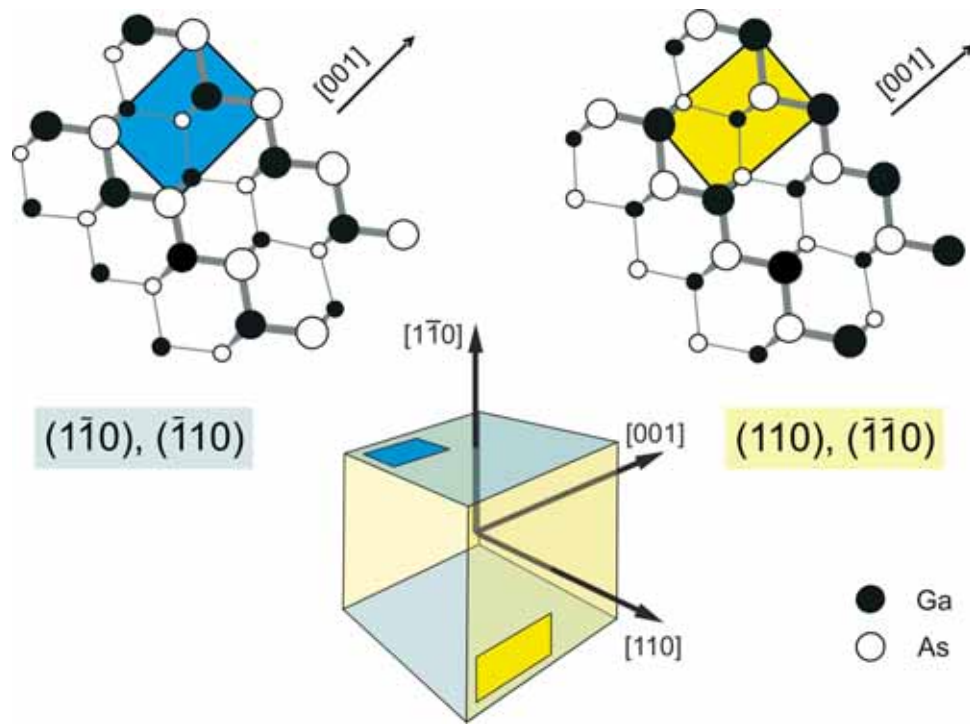


Fig. 1.11 Ball-and-stick models of the non-equivalent cleavage planes of the GaAs crystal (the same picture holds for InAs). The characteristic zig-zag chains of Ga and As atoms in the surface layer are indicated by the larger balls. The surface unit cells are sketched by the blue (yellow) rectangle. Two sets of cleavage planes exist: the (blue) $(1\bar{1}0)$, $(\bar{1}10)$ planes and the (yellow) (110) , $(\bar{1}\bar{1}0)$ planes. The colored cube shows the lattice directions of the four planes.

1.4.2. Electronic properties of the III-V surfaces

The electronic structure of the cleavage surfaces reflects properties of the crystallographic structure. Additionally, the surface relaxation gives rise to the formation of surface states. The major advantage of GaAs and InAs is that these surface states⁶ are energetically located in the bulk bands leaving the fundamental band gap of the bulk sample basically unchanged [46]. Therefore the Fermi energy at the surface is not pinned in the gap for an ideal and clean interface or surface. One consequence is that tunnel current into or out of the bulk states of GaAs is possible for certain bias voltages. The surface resonances do not mask all of the underlying bulk density of states and it is possible to detect deeply buried dopants.

⁶ Strictly speaking, those states are surface resonances.

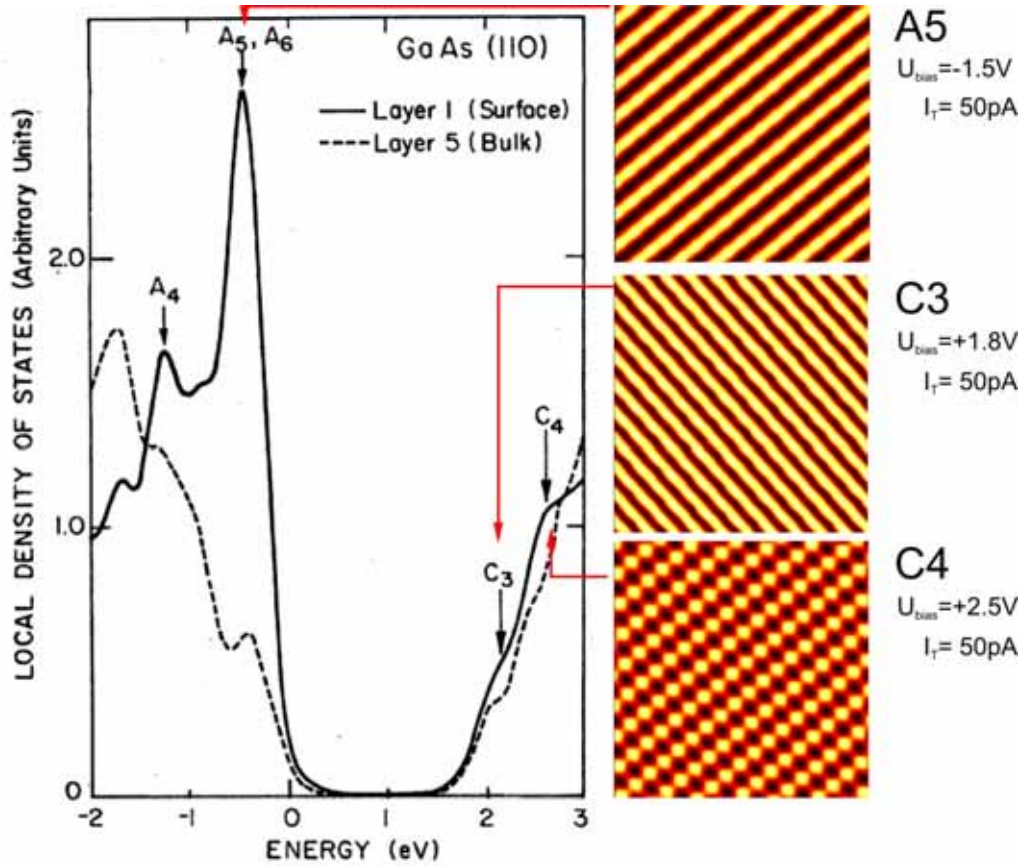


Fig. 1.12 Calculated density of states at the GaAs (110) surface (adopted from [46]). The different surface resonances have distinct appearances in the STM. Their contribution to the DOS is mapped already in a topographic, i.e., integral, measurement. STM images reprinted from [132].

Fig. 1.12 presents the calculated density of states (DOS) of the surface (solid line) and bulk (dashed line) for GaAs together with bias voltage dependent images of the surface. The most important surface resonances for STM images recorded in a bias window between -3 V and +3 V are the A5, A6 and C3, C4 states. The spatial periodicity of these states is equal to the crystallographic surface unit cell. STM images of the different states give markedly different topographies, as illustrated by the constant current topographies in Fig. 1.12. At negative sample bias, i.e., in the filled states image, the topography is dominated by the A5 state. For positive bias voltage chosen such that the tunnel current originates from the bottom of the conduction band, the topography is dominated by the C3 state. For higher bias voltage the corrugation of the image changes due to the C4 surface state that becomes accessible. The A5 and C4 states show up as lines running along the zig-zag rows of the surface while the C3 state exhibits lines that are perpendicular to the zig-zag rows. It is worth noting that due to the unpinning of the Fermi energy it is possible to image valence band and conduction band

related tunnel current at both bias polarities. Sometimes both bands may contribute at the same time. Due to the different appearance of the surface resonance at the valence band maximum (VBM) and that at the conduction band minimum (CBM) it is possible to identify the dominant tunnel channel just by looking at the orientation of the imaged rows (see Fig. 1.12, type A5 and C3 for example).

The electronic properties of the InAs surface are similar to those of GaAs except for the much smaller band gap. GaAs has a band gap of 1.52 eV at the measurement temperature of 5.6K. InAs has a band gap of only 0.42 eV. But the topographic images recorded on InAs close to the VBM or CBM are very similar to those of GaAs.

1.5. Applicable STM theory

The STM is based on the principle of the quantum mechanical tunnel effect. In contrast to classical physics, a quantum mechanical particle can overcome a potential barrier even when its energy is smaller than the barrier height. The probability for this event depends on the height and the spatial extension of the barrier. For an electron wave impinging on a finite barrier there is a reflected and a transmitted part. The portion of the electron flow that tunnels through the barrier is given by the transmission coefficient T . For typical tunneling barriers in the STM experiment (about 4eV height and 1nm width) T is small. In a first one dimensional approximation the transmission coefficient depends on the barrier height V and barrier width d in the following way

$$T \propto e^{-2d \cdot \sqrt{\frac{2m}{\hbar^2}(V-E)}},$$

with m being the electron mass and E its energy [47]. The transmission coefficient depends exponentially on the barrier width. This fundamental property of quantum mechanics enables the extreme spatial resolution of the STM.

A quantitative description of the tunnel junction in the real system of sample, vacuum gap and tip is a challenging problem and still subject to current theoretical efforts (see e.g. [48]). Especially when the interaction between tip and sample cannot be neglected the theoretical framework often provides a qualitative description only. The interaction of the electric field between tip and sample will be discussed in chapter 2. Comprehensive descriptions of the standard model of the tunnel current are given by J. Chen [49], R. Wiesendanger [50] and D. Bonnell [51]. A brief summary of the applicable STM theory will be reviewed here and the relevant definitions and terms will be presented. A few extensions to this model are necessary for the understanding of the spectroscopic measurements of subsurface dopants. They will be given in the respective sections.

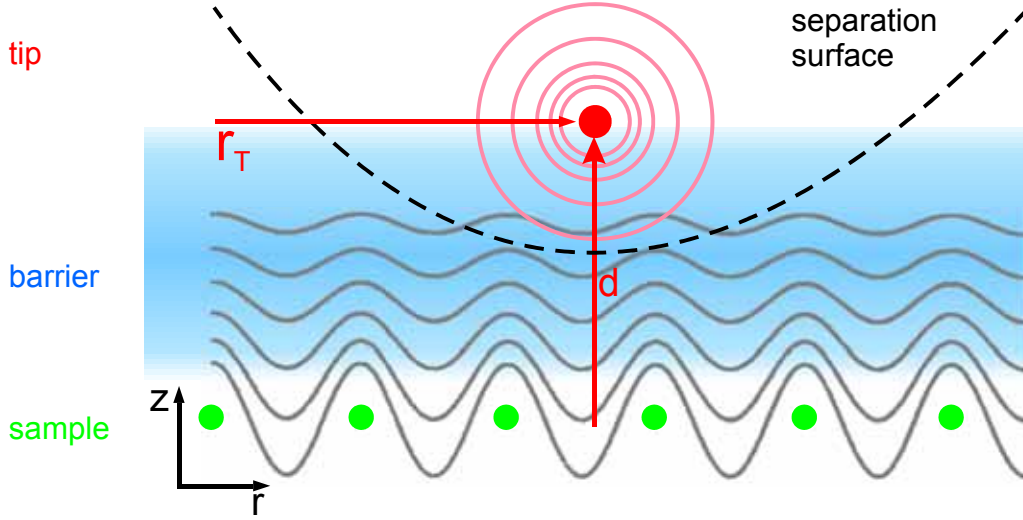


Fig. 1.13 Schematic of the tunnel junction in the Tersoff-Hamann approximation. The tip (red) is approximated by a single s-type wave function with its center at the lateral position r_T in a distance d from the sample surface. The (fictitious) separation surface is shown as a dotted line between sample and tip. The sample and tip wave functions (grey and red waves) decay exponentially in the barrier region (blue) .

The standard theory is based on the Transfer-Hamiltonian approach by Bardeen, which was originally formulated for macroscopic tunneling junctions [52]. According to Bardeen the transition probability from a sample state χ_ν to a tip state ψ_μ is given by the transfer matrix element $M_{\mu\nu}$.

$$M_{\mu\nu} = -\frac{\hbar^2}{2m} \int_S \left(\chi_\nu^* \nabla \psi_\mu - \psi_\mu \nabla \chi_\nu^* \right) d\vec{S} .$$

The integration is over a separation surface between tip and sample. An analytic expression for the tunneling current in STM experiments was first derived by Tersoff and Hamann [53, 54]. Fig. 1.13 shows a schematic of the tunnel junction in the Tersoff-Hamann model. The Bardeen model is simplified by approximating the tip as a single s-type wave function and limiting the energy range to states close to the sample Fermi energy. Then, the tunnel current is given as

$$I_T \propto eV \rho_T(E_F^T) \underbrace{\sum_\mu \left\{ \left| \psi_\mu(\vec{r}_T, d) \right|^2 \delta(E_\mu^s - E_F^s) \right\}}_{=LDOS(\vec{r}_T, d, E_F)} .$$

In this formula ρ_T is the tip density of states and the sum represents the sample density of states at the Fermi energy. Because the applied bias V is small the tip Fermi energy E_F^T and sample Fermi energy E_F^s are approximately equal. It is convenient to define the sample local density of states as

$$LDOS(\vec{r}_T, d, E) = \sum_\mu \left\{ \left| \psi_\mu(\vec{r}_T, d) \right|^2 \delta(E_\mu - E) \right\} .$$

Similar to the overall density of states (DOS) of a given system, the LDOS at a certain energy E reflects the local probability density of all sample states at this energy. But - as the phrase suggests - the LDOS is dependent on the lateral position r_T and the distance d from the surface. In that sense the LDOS is a spatially resolved DOS. Within the Tersoff Hamann approximation the tunnel current is directly proportional to the LDOS at the position of the center of the tip's wave function as sketched in Fig. 1.13

$$I_T \propto \text{LDOS}(\vec{r}_T, d, E_F) .$$

STM is sensitive to the local electronic structure and not to the morphological structure. If the STM is operated in the standard constant current mode this means that the feedback loop is driven such that the tunnel current is kept constant. This implies

$$I_T = \text{LDOS}(\vec{r}_T, d, E_F) = \text{const.} .$$

The recorded “topography” $z(x,y)$ reflects a surface of constant LDOS. The tip sample distance d is not necessarily constant in a topography.

For STM measurements at larger bias voltage the tunnel current is no longer proportional only to the LDOS at the sample Fermi energy. The transfer matrix element changes for states at different energies. A correct treatment of the matrix elements for all states in the energy window from E_F to $E_F + eV$ is quite difficult. Hamers et al. proposed a simplified description [55, 56]. One simplification is that only elastic tunneling is allowed, i.e. the tunneling initial and final states have to be at the same energy. The exact matrix elements are then treated as an energy and bias dependent transmission probability. In the limit of $T=0K$ (The Fermi function is a step function) the tunnel current is given as an integral over the energy window in which tunneling can occur

$$I_T \propto \int_{E_F}^{E_F + eV} \rho_s(E - eV) \text{LDOS}(r_T, d = 0, E) T(E, eV, d) dE .$$

The transmission probability T now combines the usual vacuum decay and the additional energy and bias dependent barrier height. T is approximated within the Wentzel-Kramers-Brillouin approximation [56]

$$T(E, eV, d) \propto \exp\left(-\frac{2d}{\hbar} \sqrt{m(\phi_T + \phi_s + eV - 2E)}\right) .$$

Here ϕ_T and ϕ_s are the tip and sample work functions. The tip density of states $\rho_s(E)$ is often assumed to be constant for further simplification. The following measurements are recorded near the band edges or even within the fundamental band gap. In this energy windows the sample LDOS varies strongly. The tip is made of tungsten and should exhibit a metallic DOS with much less structure than the LDOS of the sample. Therefore this simplification is justified. With this knowledge the previous statement that the topography reflects a surface of constant LDOS is further refined: The topography reflects the integral LDOS over all sample states between E_F and $E_F + eV$.

1.5.1. I(V)-spectroscopy and normalization

Spatially resolved I(V)-spectroscopy is a unique tool to obtain information of the electronic structure of dopants and heterostructures. In local I(V)-spectroscopy single I(V)-characteristics are recorded at certain points of the sample. Spatially resolved I(V)-spectroscopy is done in the following manner: At every point of a topography the feedback loop is switched off for a small time and an I(V)-curve is recorded. The numerical derivative gives the differential conductance and results in a data set that allows analyzing the energetic and spatial evolution of electronic features. If for example standing waves of a surface state are investigated, a dispersion relation $E(k)$ can be derived from the measurement because for every energy position the corresponding wave length is measured, as well [57, 58]. On semiconductors the spatial distribution of dopant states or the lateral variations in the band edge alignment of heterostructures can be resolved.

According to the Hamers approximation the differential conductivity basically reflects the energy resolved sample LDOS masked with the transmission probability.

$$\frac{dI}{dV}(V) \propto LDOS(r_T, 0, eV) T(eV, eV, d) + \int_0^{eV} LDOS(r_T, 0, E') \frac{dT(E, eV, d)}{dV} dE' .$$

The first term is the product of the sample LDOS and $T(E, d)$. The second term contains the dependence of T on the applied bias voltage. Feenstra proposed a normalization of the dI/dV signal with a smoothed overall conductivity (\bar{T}/\bar{V}) [17]. Under the assumption that $T(eV)$ is a smooth function without much structure this normalization would approximately cancel out the second term and the $T(eV, eV, d)$ factor [59]. Then the $dI/dV/(\bar{T}/\bar{V})$ signal would give a more accurate quantity. The comparison of normalized and not normalized dI/dV -maps shows that this normalization accounts for two effects:

- If a large bias window is covered, the bias voltage dependence of T cannot be neglected. The relative weight of the differential conductivity for high positive bias with respect to conductivity at lower bias is corrected.
- The tip sample distance is fixed in a topographic measurement. Thus the dI/dV -maps do not reflect the LDOS on a plane of constant distance (as it is often given by theoretical calculations) but rather on a corrugated surface. The $dI/dV/(\bar{T}/\bar{V})$ signal is approximately normalized [10].

However, for the measurements on buried dopants this normalization is often not suitable. First of all, most analysis of dopant induced conductivity is done within or near the semiconductor band gap. When the overall conductivity nearly

vanishes, (I/V) is no longer a well defined quantity. Additionally, the normalization to a plane of constant height is only approximate. In particular for measurements that contain tunnel channels which are not included in the standard model, the tunnel current does not reflect the LDOS, only. Thus, the normalization to $dI/dV/(I/V)$ makes no physical sense, it may even create artifacts. Therefore all analysis of the measured $I(V)$ -spectroscopies is done on the dI/dV signal only.

Nevertheless a proper normalization is imperative: $I(V)$ -spectroscopies with atomic resolution show that the surface state present in the topography pushes through to the dI/dV signal. The height modulation due to the corrugation of the surface states is of the order of 10pm -20pm. For measurements on heterostructures, especially the p-i-n diodes the electronic height modulation is as large as 2 Å. Fig. 1.14 shows a topography line trace across the p-i-n region. The surface is atomically flat along this line. The same line was recorded with two different bias voltages, one at +2.0 V sample bias the other at -2.0 V. Both curves differ by more than 2 Å. This modulation is of pure electronic origin. It is worth noting that the tunnel current changes approximately by one order of magnitude when the tip sample distance is changed by 1 Å. The recorded dI/dV -maps of this area would not be meaningful without proper normalization to a plane of constant height.

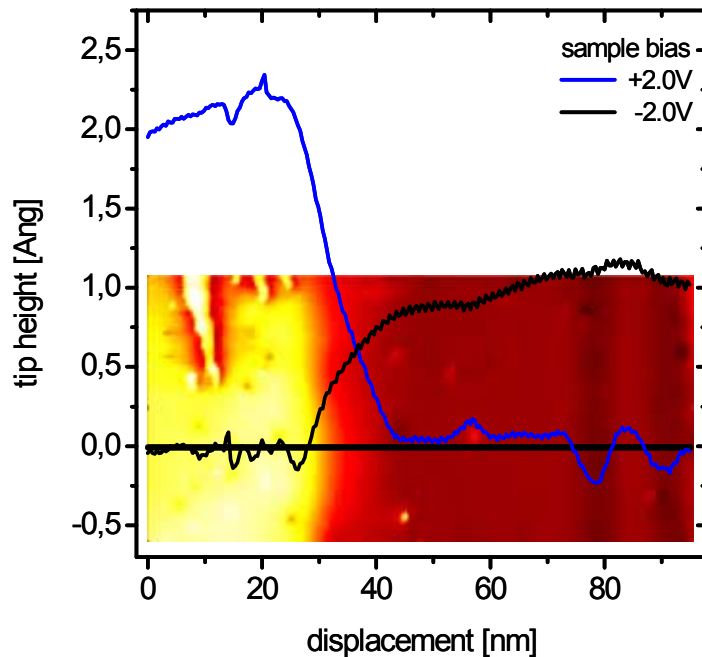


Fig. 1.14 Two topographic traces of the same line of a GaAs surface running across a p-i-n interface. In the background the respective topography is shown. The blue line is recorded at positive sample bias and the black one at negative sample bias. The cleavage surface of this region is atomically flat. The massive height modulation of >2 Å between blue and black line is of pure electronic origin due to the varying doping type. To be able to interpret spectroscopic data taken on such a surface it is crucial to normalize the spectra to a plane of constant height.

During the past years a method has been developed that uses a more realistic normalization technique [39]. The normalization accounts for the vacuum decay of the sample LDOS, rather than normalizing with a total conductance like the $dI/dV/(I/V)$ normalization would. As mentioned in the beginning of this chapter the basic dependence of the tunnel current on tip sample distance goes as

$$I \propto \exp(-2\kappa d), \quad \kappa = \kappa(\vec{r}_T, eV)$$

The tunnel current is exponentially dependent on the tip sample distance d . The exponential factor κ is the decay constant. The basic assumption is that the decay is purely exponential in the vacuum gap. If the decay constant is known, an $I(V)$ -curve measured at a certain distance d_0 can be normalized to any distance d_i .

$$\tilde{I}(V) = I(V) \cdot \exp(-2\kappa(d_i - d_0)) .$$

To accomplish the normalization, the local decay constant is determined experimentally for every $I(V)$ -curve during the measurement. A dI/dz -modulation technique is used. The tip z -position is periodically modulated by Δd around the topographic position d_0 after the feedback loop is switched off. The resulting modulation in the tunnel current ($I_2 - I_1$) is measured. The decay constant is then given by

$$\kappa = \frac{(\ln I_1 - \ln I_2)}{\Delta d} .$$

In general the decay constant varies spatially and depends on the applied bias. A complete spectroscopic measurement therefore always consists of the topography, a decay constant map and the $I(V)$ datasets. This is sketched in Fig. 1.15. The topography is properly plane fitted. Then, the remaining $z(x,y)$ information is directly used as the tip-sample distance map $d(x,y)$. Together with the $\kappa(x,y)$ map the $I(x,y,V)$ datasets are normalized according to the above formula. After this process the dI/dV -maps correspond no longer to a corrugated surface but to a plane of constant height⁷. This procedure is applied to all spectroscopic measurements presented in this thesis.

⁷ This normalizes the $I(V)$ -curve to the fit plane, to be precise. Under the assumption that the fit plane that was subtracted from the topography is parallel to the sample surface, the $I(V)$ -curves are normalized to a plane of constant height.

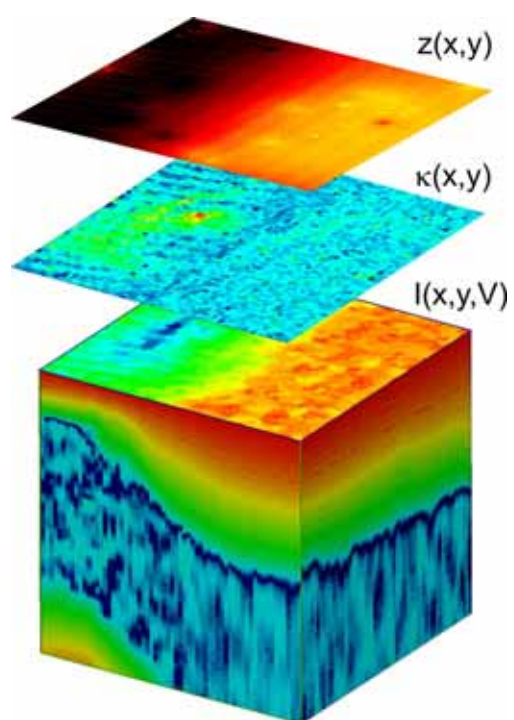


Fig. 1.15 Complete spectrum set as it is recorded with the Goettingen STM controller. For each point of the 2D (x,y) array corresponding to a square area on the sample the following values are measured: topographic height the effective barrier height, via a dI/dz -modulation technique, and $I(V)$ -characteristics.

2. Tip induced band bending

The relation between applied bias voltage and single electron energy scale of the system is determined by the tip induced band bending. This chapter presents the calculation scheme for the TIBB and points out that it has to be adjusted to each STM measurement. The actual tip work function is a crucial parameter. The calculation is further improved by taking into account geometrical shape of the tunneling contact.

STM measurements on semiconductors usually require sample bias voltages on the order of volts. This is a consequence of the semiconductor band structure and in particular the presence of the fundamental band gap at the Fermi energy that is of the same magnitude. These high bias voltages and a tip sample distance of about 1nm lead to extremely high fields. This field has to be screened in the tip and the semiconductor respectively. At the metallic tip the screening length is $<1 \text{ \AA}$ because of a very high density of states at the Fermi energy. Most III-V semiconductors exhibit no surface states within the band gap. Surface resonances are present, that are energetically located in the bands of the bulk crystal. Thus the density of states at the Fermi energy depends on the doping level and is significantly lower than for the metallic tip.

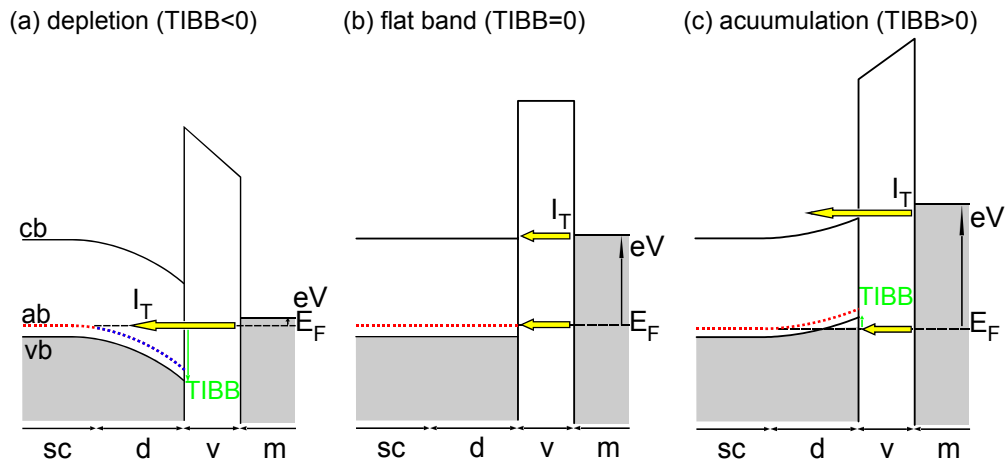


Fig. 2.1 Different types of tip induced space charge layers. Depending on the sign and value of the tip induced band bending (TIBB) on the surface, the sample can have (a) an inversion layer (b) a depletion layer or (c) an accumulation layer at the surface. While the sample is depleted of free carriers for the depletion interval (b), in (a) and (c) free carriers are accumulated directly under the STM tip.

The electric field penetrates into the semiconductor sample. Typical screening lengths are on the order of some tens of nanometers for highly doped semiconductors and can even reach micrometers for lower doping levels [60]. The resulting situation resembles the potential distribution of a Schottky contact except that a fraction of the potential between tip and sample drops over the vacuum gap. These tip induced space charge layers largely affect the measurement and have to be taken into account for **any** analysis of STM data obtained on III-V semiconductors.

The doping level, free carrier densities in the bands and other material parameters determine the space charge layer's properties. The so called tip induced band bending (TIBB) characterizes the bias voltage dependent behavior. The TIBB is defined as the electrostatic potential at a point on the semiconductor surface directly under the tip. Qualitatively different band bending situations are observed depending on the sign and magnitude of the applied sample bias voltage. The following discussion addresses p-doped semiconductors. The majority carriers are holes. On n-doped samples the situations are equivalent. Then, the majority carriers are electrons and the sign of the TIBB and sample bias are reversed. Fig. 2.1 presents the three situations most relevant for the experiments of this thesis: depletion, flat bands and accumulation.

If the TIBB is negative but smaller than the semiconductor band gap energy, the sample is in depletion. The bands are bent downwards and the sample is locally depleted of free carriers. The stationary acceptor cores screen the tip's electric field as depicted by the blue dots in Fig. 2.1a. At a certain bias voltage, the contact potential of tip and sample is compensated by the additional potential drop of the applied bias voltage. The space charge layer vanishes, which is called flat band condition (Fig. 2.1b). The flat band bias for p-doped samples is at positive bias for realistic tip work functions (e.g. 3 V to 5.5 V). Thus, the depletion bias window reaches from negative to positive bias. The TIBB is positive for bias voltages higher than the flat band voltage. The valence band is pushed over the Fermi energy and holes are accumulated under the tip. This situation is called accumulation (Fig. 2.1c), majority carriers are present under the tip.

The tip induced shift of the energy scale in the sample is the reason why spectral features of the sample's density of states appear shifted with respect to their positions in the bulk. The conduction and valence band onsets on lightly doped GaAs for example are shifted against each other and the measured band gap is much larger than the well-known bulk value [61]. In addition the bias dependence of the tip induced band bending TIBB(V) is non-trivial. Therefore the evaluation of the tip induced fields is of great interest since the advent of STM measurements on III-V semiconductors. Unfortunately, it depends on several parameters that are a priori not known. Usually numerical models are employed to derive the TIBB(V) dependence.

2.1. Three dimensional TIBB(V) calculation

The electrostatic potential in the tunneling contact area is solved using a self-consistent solution of the Poisson equation. The TIBB(V) dependence results from the subsequent evaluation of the potential landscape for different tip potentials. In 1987 Feenstra proposed a model to calculate the potential distribution along the tunnel path perpendicular to the surface in one-dimensional geometry [17]. The calculation bases on the approximation of the tip and sample geometry with infinitely extended slices stacked along the line of simulation, i.e., tip and sample form a plate capacitor geometry as depicted in Fig. 2.2a. This model has been widely used up to now, e.g. to explain the voltage dependent onsets of the different surface resonances on GaAs [18]. Recently it has been found that this approximation largely overestimates the tip's effect on the sample [20]. Nowadays, STM tips are typically manufactured by electrochemical etching, resulting in very sharp tips with narrow shanks. The tips used in this work are electrochemically etched from polycrystalline tungsten wire as described previously. The knowledge of typical tip radii and shank opening angles is important for the following calculations. A series of tips is produced with all *ex-situ* and *in-situ* preparation steps, and the tip apexes are investigated with a Scanning Electron Microscope (SEM) (The details of this analysis can be found in the work of H. Schleiermacher [33]).

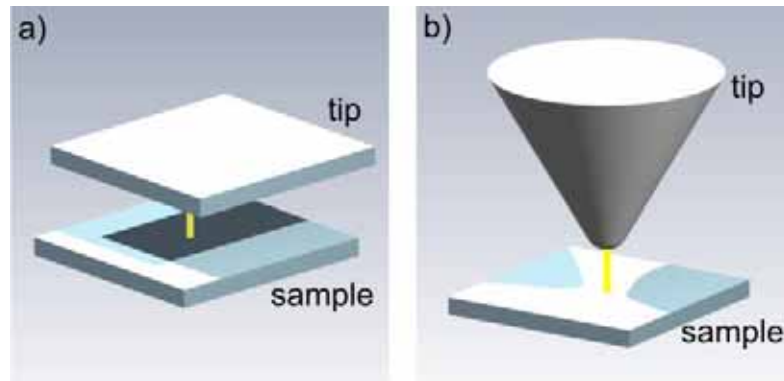


Fig. 2.2 Schematic of the three dimensional capacitor configurations if (a) the tip induced band bending is calculated 1D and (b) if the TIBB is calculated in 3D

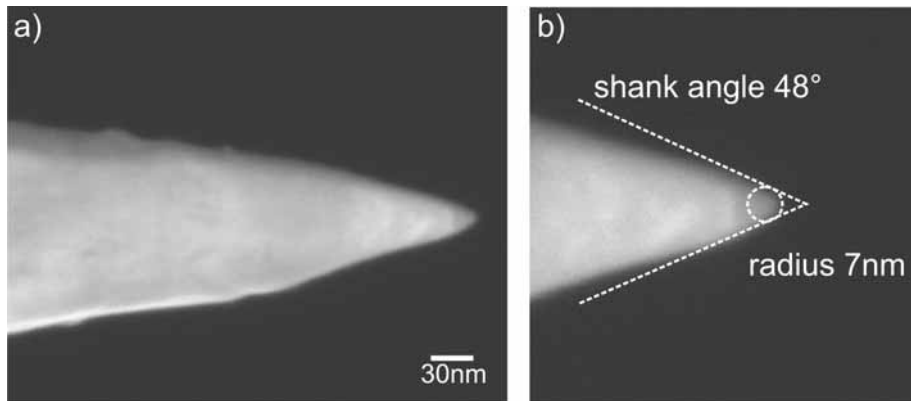


Fig. 2.3 SEM image of a STM tip after all preparation steps. (a) overview. (b) tip apex analysis. The typical tip radius of STM tips prepared in this manner is $\sim 10\text{nm}$ with a shank angle of $\sim 50^\circ$.

Fig. 2.3 shows SEM images of a typical STM tip which is ready for tunneling. The front apex is smaller than 10nm in radius and the shank is very narrow with an opening angle of about 50° . During the STM measurements tips eventually become blunter. Millisecond voltage pulses are applied between tip and sample that “blast away” a fraction of the shank, to recover a sharp apex. After the experiment such tips still exhibit an apex radius of about $20 - 30\text{nm}$ with a shank opening angle of $< 90^\circ$ which was verified by SEM analysis. For such tips the three dimensional nature of the wire-like tip in front of the planar semiconductor surface (Fig. 2.2b) has to be taken into account. Compared to the plate capacitor approximation a larger portion of the potential between tip and bulk sample drops in the vacuum.

However, modeling and self-consistent solving of the realistic three dimensional situation is time consuming, in particular when many different tip potentials need to be evaluated. Recently Feenstra proposed a numerical model based on the prolate spheroidal coordinate system, previously applied for field emission microscopy [62]. The model approximates the tip with a hyperboloid characterized by an apex radius and a shank opening angle (see Fig. 2.4). The tip-sample half-space is described in the prolate spheroidal coordinates. In this coordinate system the electric field distribution resembles the one of the plate capacitor. The sample half-space is described in cylindrical coordinates. The computational effort is reduced drastically. The core algorithm was generously provided by R. M. Feenstra [63] and adopted to the calculations performed in this work.

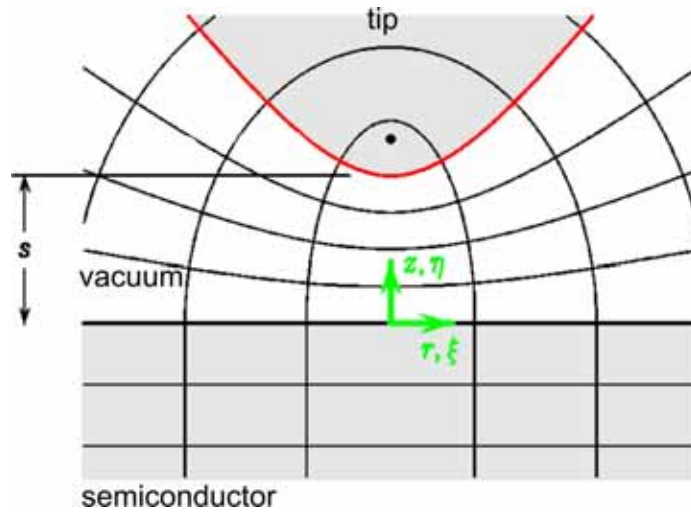


Fig. 2.4 Coordinate system used by Feenstra to reduce the computational effort for the 3D solution of the Poisson's equation for an STM tip in front of a semiconductor. The axis coordinates are sketched in green: z is perpendicular to the sample, r parallel. The semiconductor is modeled in Cartesian coordinates. Prolate spheroidal coordinates describe tip and vacuum gap [20].

The importance of a good three dimensional approximation of the tip is prominently seen when the space charge layer induced by a blunt and a sharp tip are compared. Fig. 2.5 shows the different electrostatic potentials for a tip with 100nm apex radius and 10nm apex radius respectively. A GaAs sample with a n-doping concentration of $3 \cdot 10^{18} \text{cm}^{-3}$ is considered in the calculation. A temperature of 6K is chosen. Typical values of electron affinity and tip work function together with an applied bias voltage of +2.0 V define the overall electric field. The depletion layer induced by the 100nm tip is of calotte shape and extends over $\sim 60\text{nm}$ laterally and penetrates more than 10nm into the crystal. The depletion layer induced by the 10nm tip extends laterally only $\sim 20\text{nm}$ and penetrates about 7nm. Obviously, the induced electrostatic potential is much more confined for the sharper tip. But the most striking difference is the strength of the electric field near the semiconductor surface, which is much more pronounced for the blunt tip. The TIBB values differ by 50% between 10nm and 100nm tip radius.

The difference between a one-dimensional calculation and the realistic three dimensional one is even stronger. Fig. 2.6 shows the TIBB(V)-dependences for the standard one dimensional model (red curve) and the three dimensional model for a 15nm radius tip (blue curve). The sample parameters are adjusted for p-doped GaAs. In the accumulation range (for sample bias larger than $\sim 1.5 \text{ V}$) both curves nearly match. This is due to the efficient screening mechanism by free holes at the semiconductor surface. Due to the high density of states of the GaAs valence bands the tip's electric field cannot penetrate into the sample and the situation stays similar to the planar plate capacitor geometry. But in the depletion range (for sample bias smaller than $\sim 1.5 \text{ V}$) both curves differ largely. The electric field is distributed over a larger area and thereby strongly affected by

the exact geometry. The calculation shows, that the one-dimensional calculation would overestimate the TIBB for a sharp STM tip by almost a factor of three. Therefore, the three dimensional configuration of the STM tip cannot be neglected for the band bending considerations.

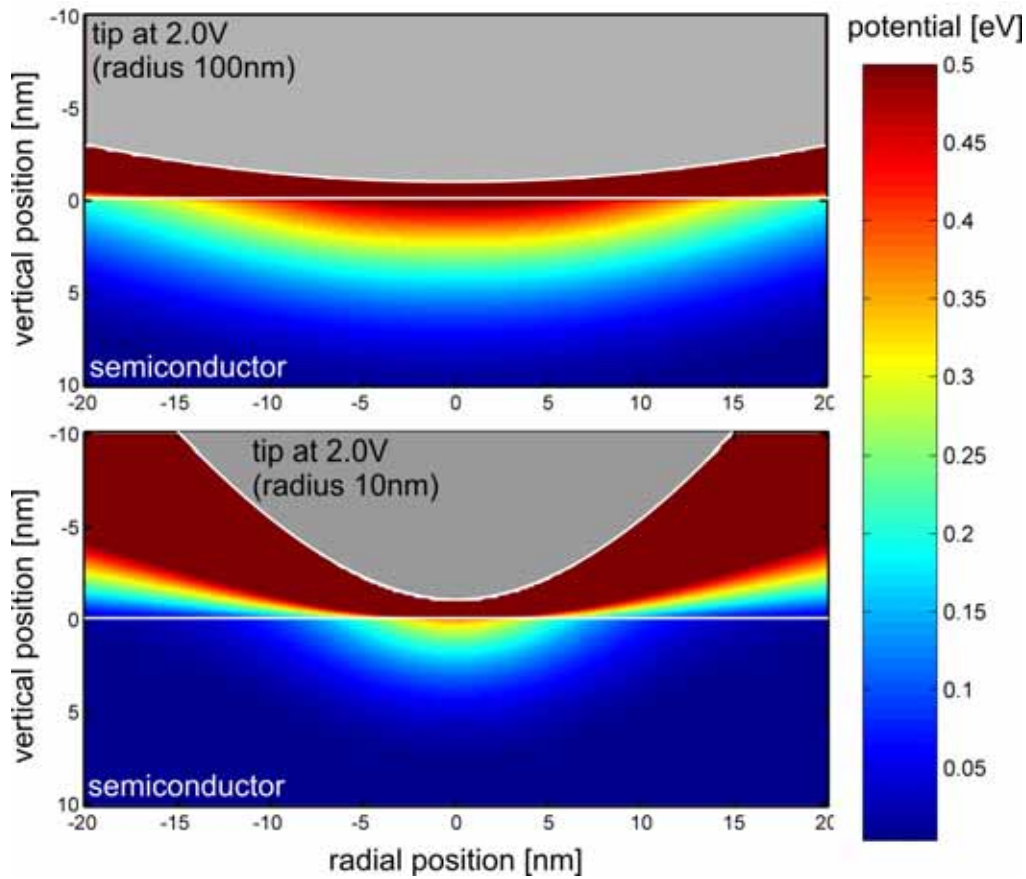


Fig. 2.5 Comparison of the tip induced potential for a blunt tip (upper part) and a sharp one (lower part). The example shows a tip with 100nm or 10nm radius respectively 1nm in front of the (110) surface of GaAs. The GaAs is n-doped with a doping concentration of $3 \cdot 10^{18} \text{cm}^{-3}$. Both calculations are done for a sample bias of +2.0 V and a tip work function of 4.0eV. The comparison of both tip induced potentials clearly demonstrates that not only the lateral extension of the space charge layer in the semiconductor but also the depth and connected to this the energetic height of the space charge layer strongly depend on the apex radius.

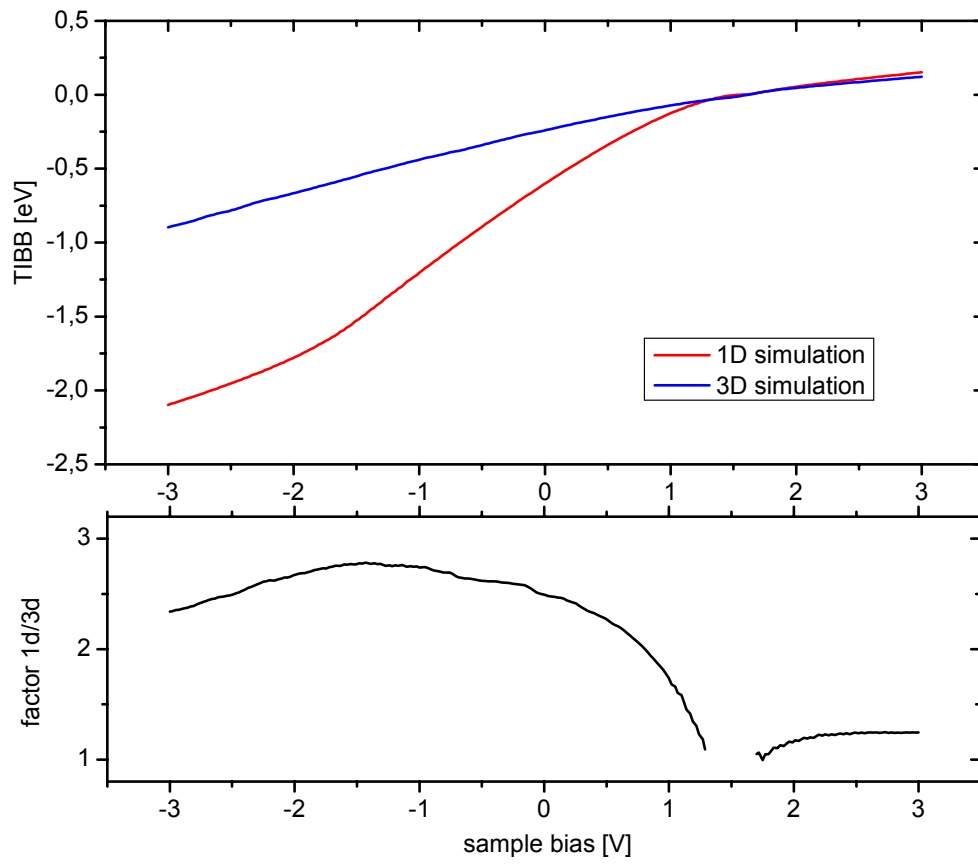


Fig. 2.6 Tip induced band bending at the semiconductor surface at a point directly under the tip. The blue curve is calculated according in 3D geometry according to [20], whereas the red one is calculated in 1D approximation, i.e., plate capacitor geometry, according to [18]. Parameters of the tip are 15 nm radius, 90° shank opening angle, tip sample distance 1 nm. The sample parameters are adjusted for highly p-doped GaAs.

2.2. From apparent barrier height to tip work function

The TIBB(V) function sensitively depends on several parameters characterizing tip and sample. Some experimental methods exist that allow exact determination of sample parameters like doping density, free carrier concentration and electron affinity [64]. It is difficult to obtain the parameters for the tip like its radius, shank geometry and work function. The shape may be estimated in SEM images, but no independent method exists that allows identifying the work function of the front part of the tip apex. However, the tip work function is one of the most important parameters. It enters directly the TIBB(V) dependence. If the work function changes by 100 meV, the TIBB(V) curve is shifted by 100 mV in the sample bias axis. Unfortunately it is not sufficient to identify the work function once, I(V)-spectroscopies show that even small tip modifications lead to different work functions and in turn to a change in the spectroscopies. The major drawback is that while the work functions are well known for clean and low indexed metal surfaces [65], they are a priori not known for small systems with highly curved surfaces [66]. All TIBB calculations reported in literature use constant values for the tip work function. Usually the 4.5eV value of bulk tungsten is used.

Here, a method is demonstrated to systematically determine the tip work function's actual value for every I(V)-spectroscopy in the STM itself. The apparent barrier height of the tunneling gap is acquired simultaneously with the STS measurement. The apparent barrier height is experimentally determined by dI/dz-modulation at the setpoint bias and current of each I(V)-spectroscopy. After the topographic height is adjusted, the feedback loop is halted and the tip is oscillated with an amplitude Δz of typically 0.3 Å around the topographic height and the resulting modulation $\Delta I = I_2 - I_1$ in the tunnel current is recorded. The relation between measured current modulation and distance modulation gives an effective barrier

$$\varphi_B = \frac{\hbar}{2\sqrt{2m_0}} \frac{\ln I_1 - \ln I_2}{\Delta z} .$$

Fig. 2.7 shows two barrier height maps, one acquired at +2.0 V sample bias the other at -2.0 V bias on the same sample area. The tip work function is the same for both maps, but the apparent barrier differs by 2eV. The reason is a change in tunneling conditions due to the changed bias voltage. This points to the fact, that the apparent barrier is not equal to the sample or tip work function. The following sections will present two approaches for the reconstruction of the tip work function from this data.

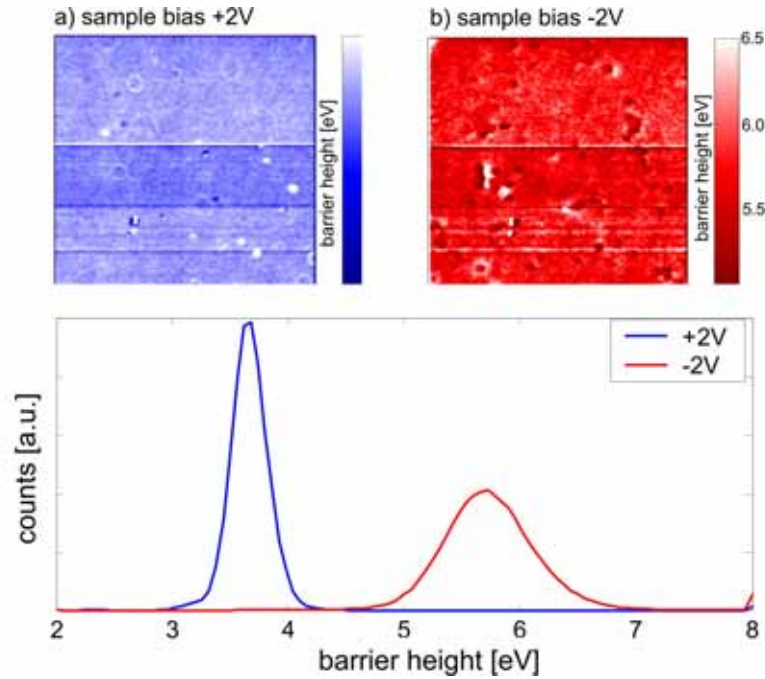


Fig. 2.7 Measurement of the apparent barrier height at positive and negative sample bias on n-GaAs. The apparent barrier height of the same sample area is measured subsequently with different sample bias setpoints (a) +2.V sample bias. (b) -2.0V sample bias. (c) barrier height histogram of both maps. Image reproduced from [69]

2.2.1. Rule of thumb estimate

At first, an approximation to the tunneling condition will be presented, which enables an analytical estimate of the tip work function. This kind of approximation is useful, because it points out the relevant mechanisms that lead to the measured work function value. However, it should be checked, in which sample bias windows it is applicable and in which it is not (see next section 2.2.2).

The following discussion considers p-doped semiconductors, but the derived model is applicable to n-doped systems as well. Fig. 2.8 sketches three different tunneling conditions. The vacuum barrier is approximated with a trapezoidal shape. It originates from its construction in the Schottky barrier model. When tip and sample are not in contact, the barrier between them is rectangular, but the energy from vacuum level to Fermi energy is different for sample and tip respectively. When they are brought closely together, the Fermi levels align via charge exchange. This exchange produces an electric field between tip and sample that shifts one part of the system with respect to the other and generates the linear slope. As a consequence the sample side of the barrier is given by the semiconductor electron affinity χ_s and the tip side is given by the tip work function ϕ_T . This approximation is valid for tip sample distances around 1nm. For very nar-

row tunneling gaps the barrier is lowered by image potentials and the edges of the trapezoidal barrier no longer resemble the vacuum level [67, 68].

Now a drastic assumption is made: the highest tunneling state is assumed to dominate the tunnel current. Then, this state will dominate the dI/dz -signal, as well, and the barrier height is evaluated with respect to the energetic position of this state. Often this assumption is justified, because deeper lying states are exponentially suppressed. The effective barrier felt by the electron tunneling into or out of this state is highlighted with red and blue color in Fig. 2.8. The barrier heights are denoted b_S at the sample side and b_T at the tip side.

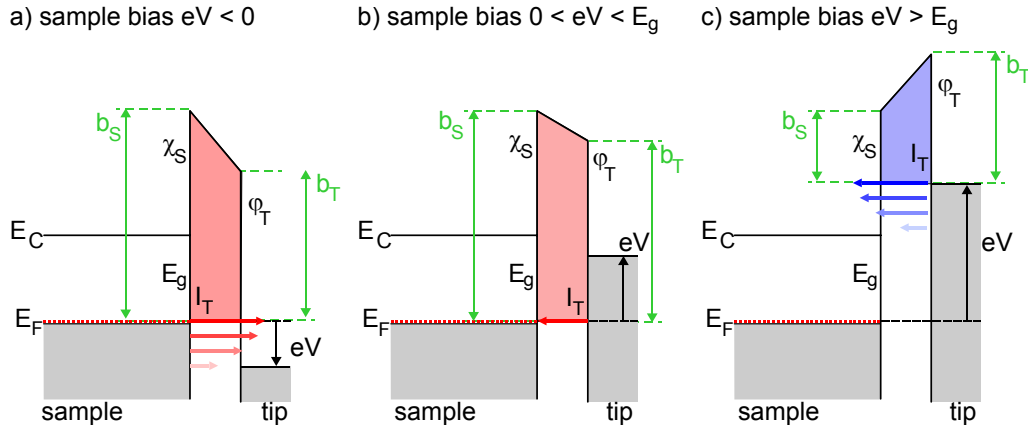


Fig. 2.8 Schematic of the trapezoidal vacuum barrier on p-type material. (a) negative bias ($eV < 0$) electrons tunnel out of the valence band. (b) small positive bias ($0 < eV < E_g$) electrons tunnel into the unoccupied valence band states. (c) high positive bias ($eV > E_g$) electrons tunnel into the conduction band. Note, that (b) and (c) may be active at the same time. The figure omits the TIBB for simplicity.

Fig. 2.8a presents the tunneling condition for negative sample bias. The highest tunneling state is at the valence band edge. Thus, the sample side of the trapezoidal barrier is given by band gap energy E_g and electron affinity χ_S . The tip side of the barrier is lower than the tip work function ϕ_T . The applied bias voltage eV pulls down the tip's energy scale, so the barrier is lowered by the applied bias voltage eV . The barrier is defined as $(\phi_T - eV)$. For small positive sample bias (Fig. 2.8b), when the conduction band is energetically not accessible, tunneling still occurs at the valence band edge. Only the tunneling direction is reversed. Now, the applied bias lifts the tip's energy scale, so the tip side of the barrier is raised by the bias, i.e., it is $(\phi_T + eV)$. The sample side of the barrier does not change.

When the applied bias exceeds the band gap energy, conduction band states become available for tunneling. The highest tunneling state jumps to the conduction band (Fig. 2.8c). The apparent barrier height is significantly lowered. The effective barrier at the sample side is now lowered by the bias voltage. On the tip side the barrier is equal to the tip work function. The tunneling processes in

Fig. 2.8b and Fig. 2.8c may be active at the same time, but within the “highest state” approximation, the valence band related tunneling is negligible⁸. It is worth noting that this model easily explains the change in apparent barrier height presented in Fig. 2.7. At -2.0V bias, the dominant tunnel channel is at the valence band edge. The apparent barrier height corresponds to the condition in Fig. 2.8a. At +2.0V, tunneling occurs well within the conduction band. The situation corresponds to Fig. 2.8c and the apparent barrier height at the sample side is lowered by the band gap and the applied bias voltage.

To relate the trapezoidal barrier model to the measured apparent barrier height value, the barrier shape is further simplified to a rectangular shape with an averaged barrier height (Fig. 2.9). Calculations of the barrier transmissivity within the Wentzel-Kramers-Brillouin approximation (WKB) show that for reasonable tunneling gaps between 5 Å and 10 Å this simplification is justified. The rectangular barrier height ϕ_B given by the arithmetic average of the tip and sample barrier sides

$$\phi_B = \frac{(b_P + b_S)}{2}.$$

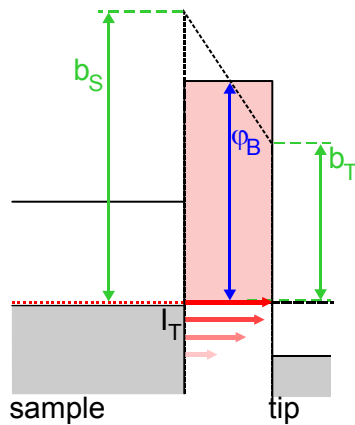


Fig. 2.9 Schematic showing the simplification of the trapezoidal barrier with the left side b_S and right side b_T to a rectangular barrier with height ϕ_B . The tunnel current I_T is indicated by red arrows.

With the TIBB included the sample and tip barrier heights are given by

$$b_S = \begin{cases} \chi_s - eV + (E_C - E_F) + TIBB(V) & eV > E_{gap} \\ \chi_s + (E_C - E_F) + TIBB(V) & eV < 0 \end{cases}$$

$$b_T = \begin{cases} \phi_T & eV > E_{gap} \\ \phi_T - eV & eV < 0 \end{cases}$$

The mean barrier height ϕ_B equals the measured barrier height. A detailed discussion of this simplification is treated in the diploma thesis of K. Teichmann [69]. The above formulas analytically derive the tip work function from the measured apparent barrier height, if the sample electron affinity is known. The III-V semiconductor cleavage surfaces investigated in this work have very well defined

⁸ The next section presents an exception, i.e., p-doped InAs at high positive bias.

cleavage properties. Typically the measurements are performed on atomically flat terraces with a width of several 100 nm and very low adatom densities. Thus, the (110) electron affinities will be used [40, 70]

$$\chi_s(\text{GaAs}) = 4.1\text{eV}$$

$$\chi_s(\text{InAs}) = 4.9\text{eV}$$

2.2.2. Numerical calculation of the tunnel barrier height

In the previous section an analytical way to extract the tip work function was presented. The major prerequisite for the simple model's validity is that the dominant tunnel process is at the highest tunneling state. A more elaborate method to recover the tip work function will be discussed in this section. Fig. 2.10 presents comprehensive dI/dz -measurements of p-doped InAs ($3 \cdot 10^{17}\text{cm}^{-3}$). They are the starting point for the following discussion. The approach employs numerical evaluation of the total tunnel current for the different tunneling conditions of Fig. 2.8. The numerical approach is more accurate and works even if the aforementioned approximation that the highest state dominates the tunnel current is no longer justified.

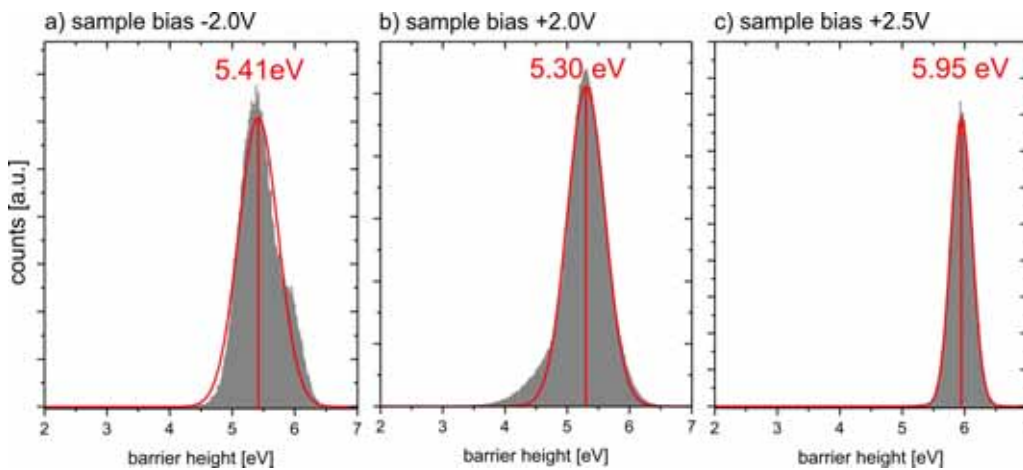


Fig. 2.10 Apparent barrier heights measured on p-doped InAs at (a) -2.0 V, (b) +2.0 V and (c) +2.5 V respectively. The three histograms contain the combined dI/dz -data of 23 STS measurements. The barrier heights for +2.0 V and -2.0 V are approximately equal, whereas the barrier height for +2.5V is significantly larger.

Fig. 2.10 presents three barrier height histograms of spectroscopic measurements on the p-doped InAs. The dI/dz -data of 23 STS measurements are combined to obtain representative histograms. For -2.0 V sample bias, the mean apparent barrier height is 5.41 eV. For positive bias, +2.0 V, the barrier height is 5.30 eV. If the sample bias is further increased to +2.5 V, the barrier height increases to 5.95 eV. The first indication that the simple analytical model does not describe the measurements on lightly doped InAs is that although the applied

bias voltage changes by 4 V, the barrier height lowering is only 100 meV. A more prominent deviation becomes apparent when the positive bias histograms are compared (Fig. 2.10b and Fig. 2.10c). The measured barrier height increases with increasing bias voltage. At bias voltage $>+0.42$ V the conduction band tunneling starts, because the band gap of InAs is only 0.418 eV. For such a tunneling condition (refer to Fig. 2.8c) the analytical model implies decreasing barrier height with increasing sample bias. Obviously, the simple analytical model is no longer capable of describing the situation quantitatively, but still it can be used as a rule-of-thumb to identify the dominant tunneling process: At +2.0 V the sample will be in accumulation. Tunneling into the conduction band and into the valence band is active. The apparent barrier height increases with increasing sample bias, a behavior that is expected only for tunneling at the valence band edge (see Fig. 2.8b). Therefore, the dominant tunneling channel for lightly doped InAs must be valence band related even at positive bias.

For a quantitative analysis of the tip work function, a more elaborate calculation has to be performed. The dI/dz -measurement is numerically emulated by comparing simulated tunnel current densities for the tunneling distance $z_0 + \Delta_z/2$ and $z_0 - \Delta_z/2$. Fig. 2.11 presents the simulation scheme. The modeled band bending situation is depicted by the rigid-band model in the figure.

The band bending in the accumulation layer range, which gives the amount of available valence band states, is assumed to be ~ 100 meV. This is reasonable because TIBB(V) calculations show (see Fig. 2.6) that once the accumulation layer reaches a TIBB of 100 meV, it does not increase much further. Then the total tunnel current density for a given tip sample distance is calculated according to the Hamers integral (see chapter 1.5). The density of states in the conduction band and valence band are evaluated by the effective mass approximation. The transmission coefficient through the vacuum barrier is calculated within the WKB-approximation. The logarithmic difference of the total tunnel current densities for the two distances then results in a simulated apparent barrier height. The only free parameter in this calculation is the tip work function. A normalization curve that relates measured apparent barrier height to tip work function is found by running the simulation for different tip work functions. Fig. 2.11a shows the apparent barrier height acquired at a setpoint bias of +2.0 V. The mean barrier height value is 5.36 eV. Fig. 2.11b presents the numerically obtained dependence of apparent barrier height with tip work function for this bias voltage. The red curve (eff.) shows the simulated apparent barrier heights for tunneling on InAs. All measured apparent barrier height values shown in the histogram are renormalized to tip work function by the red barrier height vs. work function curve as indicated by the arrows. The right histogram presents the resulting tip work function histogram. The resulting tip work function histogram has a mean value of 4.25 eV (Fig. 2.11c).

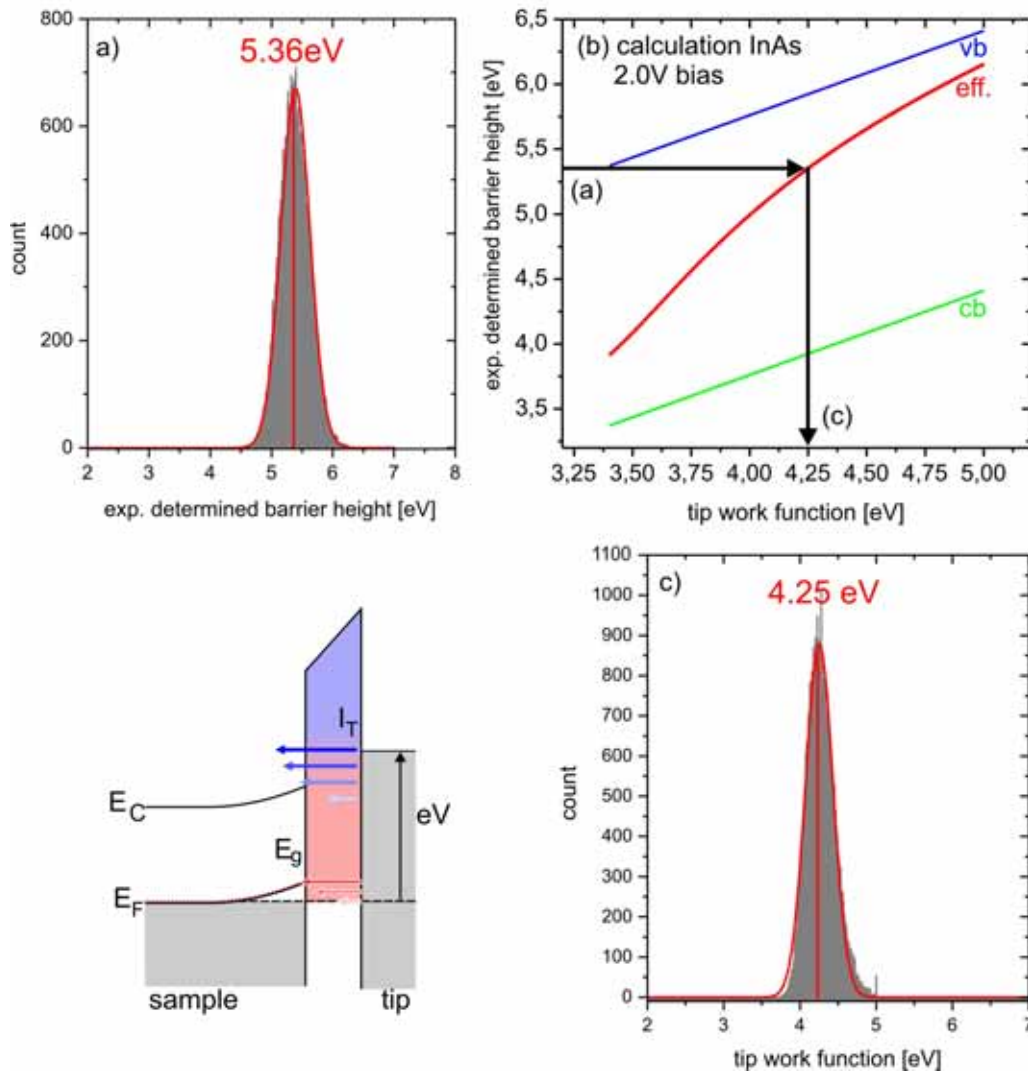


Fig. 2.11 Analysis of the tip work function for p-doped InAs ($3 \cdot 10^{17} \text{ cm}^{-3}$). The dI/dz -measurement is done at +2.0 V setpoint bias. The rigid-band model depicts the situation: the sample is in accumulation (TIBB>0) and holes are accumulated at the valence band. Tunneling is possible into conduction and valence band. (a) The experimentally determined barrier height has a mean value of 5.36 eV. The corresponding $I(V)$ -spectroscopy is shown later in Fig. 5.4. (b) calculation of the tunneling barrier height plotted against tip work function. The approximate valence band barrier is plotted in blue (vb), and the conduction band barrier in green (cb). The calculated apparent barrier is shown in red (eff.). (c) Tip work function obtained by normalization of (a) with (b). Its mean value is 4.25 eV.

The numerical model treats conduction band and valence band tunneling on equal footing. However, it is illustrative to consider each tunnel channel separately. The barrier height for conduction band and valence band tunneling are estimated in the analytical model and plotted as green and blue curves in Fig. 2.11b respectively: The blue curve indicates the apparent barrier height, when only valence band tunneling occurred, while the green one shows the apparent barrier height for conduction band tunneling only. Because the two tunnel channels mix in the experiment, the total apparent barrier height lies in between the blue and green curve. The calculation demonstrates that the effective barrier height is closer to the valence band value for work functions above 4 eV. This is surprising, because the valence band tunneling should be exponentially suppressed. The simulations indicates that about 85% of the total tunnel current originates from the valence band (for 5.36 eV apparent barrier height), although the tunneling barrier is large (>5.5 eV) compared to the conduction band barrier of only ~ 4 eV. The InAs band structure properties explain this behavior. Fig. 2.12 plots the bands of InAs around the fundamental band gap. They are calculated using empirical pseudopotentials (see [71] and the appendix). InAs has an extremely low density of states in the conduction band (effective mass $m^*/m_0=0.02$). The density of states at the valence band edge is much higher (effective mass $m^*/m_0=0.4$ and fourfold degenerate). The higher DOS in the valence band overcompensates the suppression due to the higher tunneling barrier.

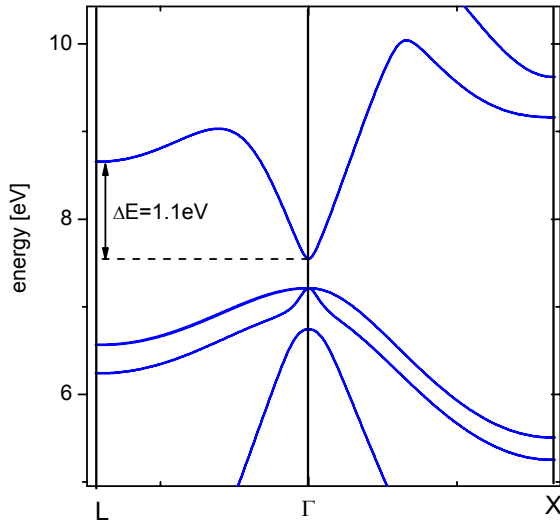


Fig. 2.12 Band structure of InAs in the L [111] and X [100] direction. The band gap is approximately 0.4 eV. In the conduction band the effective mass approximation is valid up to ~ 1 eV above the bottom of the band. The L-Valley is 1.1 eV above the bottom of the conduction band and the X-Valley is even higher in energy. In the valence band the effective mass approximation is valid for ~ 0.5 eV.

The application of this simulation to GaAs shows a different behavior. Fig. 2.13 presents a numerical barrier height calculation for p-doped GaAs ($5 \cdot 10^{18} \text{ cm}^{-3}$). The chosen parameters correspond to the I(V)-spectroscopy that will be presented in the next section 2.3). The calculation is performed for a set-point sample bias of +1.85 V. Up to tip work function of 4.5 eV the numerically derived curve nearly coincides with the estimated conduction band barrier (cb, green curve). The effective apparent barrier height curve (eff., red curve) is close

to that of the conduction band barrier. The dI/dz -measurement at +1.85eV has a mean apparent barrier height of 4.05eV. The resulting tip work function in the numerical model is 4.12 eV and for the simple model of section 2.21 it is 4.14 eV. This indicates that the “rule-of-thumb” model is applicable for GaAs. The higher band gap (1.52 eV) suppresses the valence band tunneling more effectively than for InAs.

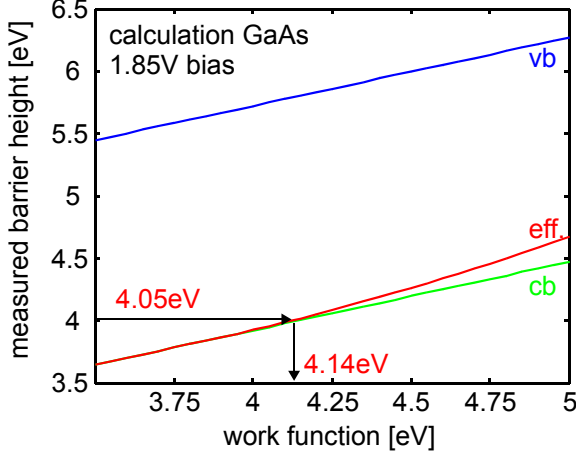


Fig. 2.13 Simulation of the (measured) barrier height plotted against tip work function, similar to Fig. 2.11. Here, the system is p-doped GaAs ($5 \cdot 10^{18} \text{cm}^{-3}$) and a sample bias setpoint of 1.85V. The approx. barrier for valence band tunneling is >5eV (vb, blue) and for conduction band tunneling it is on the order of 4eV (cb, green). The calculated effective barrier (eff., red) is near the conduction band barrier.

2.3. Validation of TIBB(V) with I(V)-spectroscopy⁹

The tip induced band bending has impact on the effective barrier height. The previously described routines for the tip work function evaluation include it by an approximate TIBB(V) dependence. This is a possible source of inaccuracy. However, there is one possibility to circumvent this difficulty. The potential of the tip relative to a point deep in the bulk of the sample is composed of the “contact potential” and the applied bias voltage V . The “contact potential” is the difference between the tip work function and the sample electron affinity with respect to the position of the Fermi energy in the sample. When the bias voltage exactly compensates the “contact potential”, the band bending vanishes. This is the flat band voltage. The following condition is valid

$$eV_{\text{flatband}} + \varphi_{\text{tip}} - \varphi_{\text{sample}} - (E_C - E_F) = 0 .$$

Under the assumption that the sample electron affinity and the position of the Fermi energy in the bulk are known, the flat band bias voltage directly returns the tip work function. No other parameters influence this bias value.

⁹ This part of the thesis was submitted to Physical Review B and is available at arXiv: cond-mat.mes-hal/0708.2937 [112].

Fortunately the flat band condition can often be identified in spatially resolved I(V)-spectroscopy. The flat band condition divides the bias interval of depletion (for $TIBB < 0$) and accumulation (for $TIBB > 0$). This section demonstrates the analysis for the example of zinc doped GaAs. Firstly, the tip work function is evaluated by the dI/dz -measurement. Then, it is fed into the band bending calculation. The result is a $TIBB(V)$ -curve adjusted to the specific spectrum set (see Fig. 2.14). Now, the numerically obtained dependence is validated with characteristic features in the spatially resolved I(V)-spectroscopies. Most prominent is the observation of charge density oscillations.

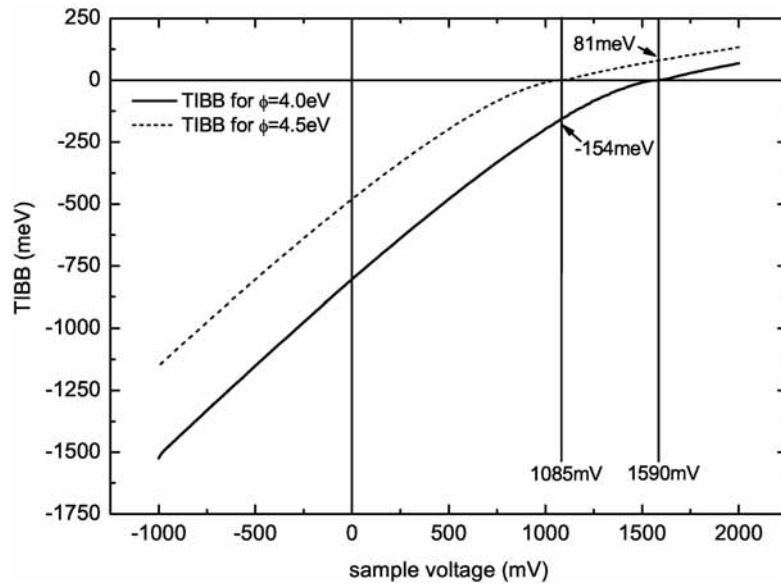


Fig. 2.14 Calculated tip induced band bending curve for p-doped GaAs. Solid line is calculated for 4.0 eV tip work function and the dotted one for 4.5 eV tip work function. Image reprinted from [112].

The analysis of the dI/dz -measurement returns a tip work function of 4.05 eV. The $TIBB(V)$ -curve is calculated for the following parameters: The tip sample separation is approximated to 7 Å. This value is derived from previous works concerning the voltage dependent movement of the tip in $z(V)$ -measurements [72] and the z -movement of the tip, when a jump to contact occurs [73]. As GaAs parameters the low temperature band gap of 1.52 eV and electron affinity 4.1 eV are used [40]. The samples are highly doped with $5 \cdot 10^{18} \text{ cm}^{-3}$, ionization energy for Zn is 31 meV [5]. Fig. 2.14 presents the calculation results. The flat band bias voltage is at +1.59 V. Fig. 2.15 shows dI/dV -maps around this voltage. The maps are arranged according to the different band bending conditions resulting from the $TIBB(V)$ -dependence. Below +1.59 V a depletion layer is present at the surface because the $TIBB$ is negative. Above the flat band bias the $TIBB$ is positive and the bands are bent upwards. The rigid-band diagrams in Fig. 2.15 depict these three configurations for a section per-

pendicular to the surface. The schematics show the alignment of the conduction band minimum (cb), valence band maximum (vb) and the acceptor band (ab) with respect to the Fermi energy (E_F). The bulk of the semiconductor is denoted (sc) and the space charge region (d). The right side of each scheme illustrates the approximate shape of the vacuum barrier (v) and the tip's Fermi energy plus applied sample bias voltage (eV) in the metallic tip (m). Filled states are grey and empty states white. Arrows indicate possible tunnel channels for each of the three cases.

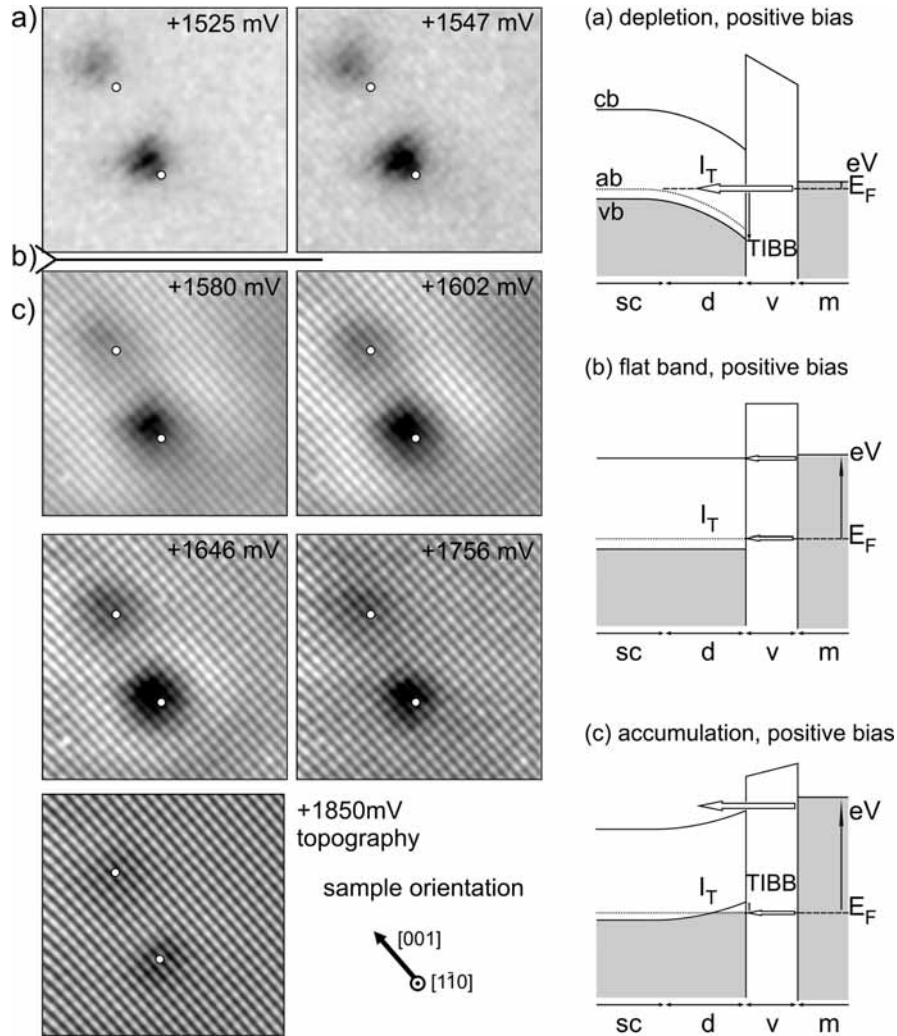


Fig. 2.15 $(10 \times 10) \text{ nm}^2$ dI/dV -maps of a spatially resolved $I(V)$ -spectroscopy on GaAs. The images show two subsurface zinc acceptors under the (110) surface. The dI/dV -maps correspond to different band bending configurations. The situation is depicted by rigid-band models at the right side (description of the abbreviations is given in the text). (a) $\text{TIBB} < 0$: Depletion layer and electrons tunnel from the tip to the sample. (b) $\text{TIBB} = 0$: flat band condition (c) $\text{TIBB} > 0$: accumulation layer. Free states at the valence band are available for tunneling. Image adopted from [112].

For positive sample voltages up to 1590mV the depletion region persists. For sample bias up to +1.52 V the electrons cannot reach the conduction band. The only possible tunnel channel is related to the valence band. The depletion layer suppresses the tunnel current. As a result no current is detected. A dI/dV -signal is detected only at the acceptor atoms. This is due to a special tunneling process that overcomes the depletion layer. This process will be discussed in chapter 7, and is not of importance for this section. When the sample bias overcomes the GaAs band gap of $E_{\text{gap}}=1.52$ eV the conduction band becomes accessible. The slight onset of conduction band related corrugation is visible at the whole surface. It is worth noting, that the onset of certain surface resonances is a good indicator for the energetic configuration under the tip. However, in the presented spectroscopy the distortion of the conduction band onset is vanishingly small (~ 10 mV), because the flat band bias nearly coincides with the conduction band position.

Much more prominent is the onset of long range charge density oscillations (CDO) for higher sample bias. When the flat band bias is crossed at +1.59 V (indicated by the horizontal line (b) in Fig. 2.15), the depletion layer changes over into an accumulation layer. Now, the bands are bent upwards. For sample bias voltages higher than that, the valence band maximum is pulled over the Fermi energy. The corresponding dI/dV -maps are denoted with (c). Electrons tunnel directly into the conduction band and into the valence band. Due to the upwards bending of the valence band, free holes are accumulated under the tip. They are vertically confined by the extension of the accumulation layer. The lateral confinement is determined by the radius of the tip (for our tips 10-20 nm) and is much weaker. A nearly free hole gas is created. Charge density oscillations of this hole gas around charged defects are expected. Those oscillations have been previously reported for electron accumulation layers on n-type semiconductors [74-77]. In literature they are sometimes referred to as Friedel oscillations. First indications of hole charge density oscillations (CDO) on p-GaAs have been reported [78]. In the dI/dV -maps for bias voltages beginning at 1580 mV a bright halo of increased conductivity surrounds the two acceptors. This halo begins with a diameter of about 10nm and decreases in size with increasing sample voltage. This is the signature of a CDO in the hole accumulation layer [79]. With increasing sample bias the TIBB increases, too. The accumulation layer increases in energetic depth and therefore the Friedel oscillation period decreases.

Thus, the onset of the CDO is marked by the onset of delocalized conductivity with a large wave length. The dI/dV -maps allow measuring them, when their wave length is of the order of the image size, here 10 nm. The value of the flat band bias obtained from this observation lies between 1.55 V and 1.58 V. This is in good agreement with the prediction of the TIBB calculation.

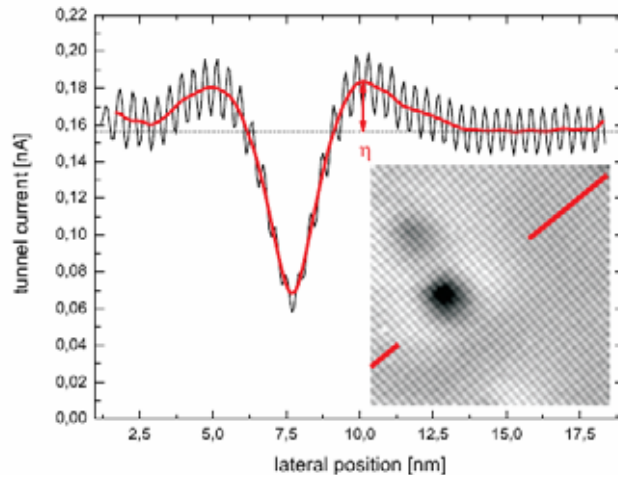


Fig. 2.16 Current map derived from the dI/dV -maps representing the amount of tunnel current originating from the sample bias interval from +1547 mV to +1668 mV. In this interval the hole charge density oscillations are observed. The cross section directly through the center of the oscillatory pattern allows to determine the percentage of tunnel current flowing into the hole accumulation layer compared to the current flowing into the conduction band. About 27 pA flow into the accumulation layer. This demonstrates that the tunnel channel into the hole accumulation layer is not suppressed. Image reprinted from [112].

This interpretation relies on the assumption that the measured CDO onset really corresponds to the onset of hole accumulation. The question whether the accumulation layer could already be present at lower bias voltage should be addressed. It is possible that even when states exist in the sample they are not imaged because tunneling into them is suppressed by low drain rates into the bulk of the sample [80]. Because there is an additional tunnel channel into the conduction band for the voltage interval of interest it is worthwhile to deduce the fraction of the total tunnel current that is attributed to tunneling into the accumulation layer. A current map is derived from the $I(V)$ -spectroscopy by integrating the dI/dV -signal over the bias voltage interval from the onset of the CDO (1547 mV) to the point where they are no longer visible in the dI/dV -map (1668 mV). The inset of Fig. 2.16 presents this $I(V)$ -map. The red line indicates the position of the plotted cross section. The corrugation of the conduction band surface resonance overlays the long-range signal of the CDO. The undisturbed surface (right part of the cross section) gives a signal of 157 pA. The CDO causes an additional current of $\eta=27$ pA in the bias window from 1.55 V to 1.67 V. Thus the CDO has an impact of at least 17% on the tunnel current in the respective voltage interval. This estimation shows that a significant part of the tunnel current can be driven through the accumulation layer, proving that this channel is not suppressed. Once a hole accumulation layer is formed, transport into will be well observable. It is worth noting that the fraction of tunnel current into the accumulation layer becomes negligible for sample bias larger than 1.7 V. Then, the conduction band tunneling completely dominates the dI/dV -maps.

Concluding this section we find that the calculated TIBB(V)-dependence fits to the experiment. The experimentally observed flat band position fits to the numerically derived value of +1.59 V within a few 10 mV. In turn the tip work function value of 4.0 eV determined by the barrier height measurement is corroborated by the dI/dV -measurements. This demonstrates that the local barrier height measurement (dI/dz) is a useful approach to experimentally obtain the tip work function in the STM experiment.

Fig. 2.17 analyzes a total of 25 spatially resolved $I(V)$ -spectroscopies with respect to the tip work function. In most experiments performed here the tip work function is ~ 4.0 eV, which is significantly lower than the value usually used in literature. All TIBB calculations for III-V semiconductors reported in literature so far use a constant value of 4.5 eV, corresponding to a mean bulk value for polycrystalline tungsten surfaces [81]. This apparent discrepancy can be resolved: High work functions, such as 4.5 eV, are only observed for densely packed surfaces, e.g. (100), (110). With higher indexed surfaces the work function is lowered [82]. The work function is further lowered if the density of adatoms and surface steps is increased. LEED investigations show that the lowering of the work function can exceed 500 meV [66, 83]. If the STM tips are considered to be a faceted surface with high step density, a local work function of 4.0 eV or smaller is not surprising.

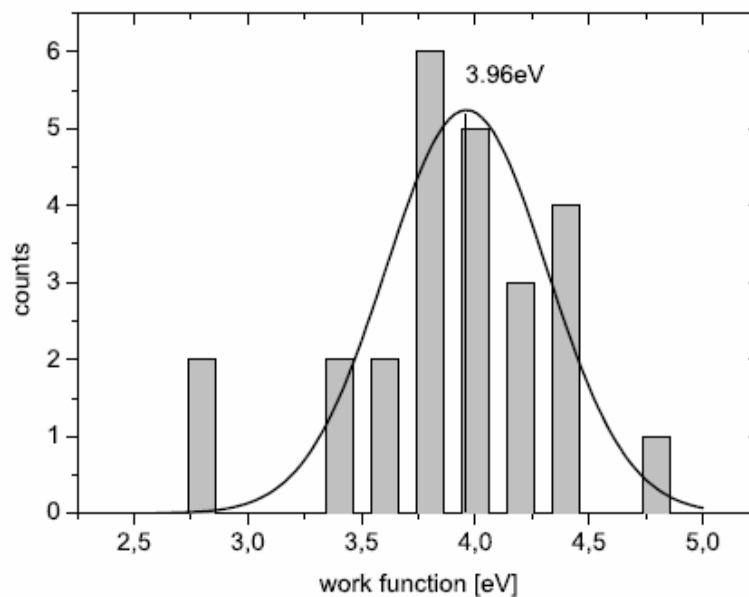


Fig. 2.17 Histogram of all measured work functions on GaAs. The mean value is 3.96 eV. Image reprinted from [112].

2.4. Summary

Now the conceptual framework for the interpretation of topographic and spectroscopic measurements on GaAs and InAs is set. On these systems the total tunnel current has to be considered not only as the sum of all states available for tunneling. Each state is weighted with an energy and sample bias dependent transmission coefficient. This often causes the highest states to dominate the STM-image, as it is true for GaAs, but in some cases lower lying states can strongly contribute, as it is shown for p-doped InAs.

Even more important is the consideration of the tip induced space charge layers, that are characterized by the tip induced band bending (TIBB). The following experiments will show that the TIBB strongly perturbs the sample energetic structure. In most cases the observed spectroscopic features can only be explained under consideration of the TIBB. Thus, the exact knowledge of the TIBB(V)-dependence is of key importance for the understanding of the measurements. This not only necessitates but also justifies employing large efforts to adjust the TIBB simulations to each experiment.

3. The p-i-n-diode as source for an adjustable electric field

This chapter presents a novel experiment for the study of single dopant atoms in a semiconductor. The dopants are incorporated in a p-i-n diode structure. The diode's "built-in" potential can be controlled at the cleavage surface. This results in an adjustable in-plane electric field that acts on the dopant atoms. It has the same magnitude as the tip-induced field.

The previous section demonstrated that the STM tip induces space charge layers in the semiconductor. At the tunnel junction position, i.e., directly under the tip, the corresponding electric field ($E = -\text{grad}(V)$) is perpendicular to the surface as sketched in Fig. 3.1a. The next chapters will focus on the study of single dopant atoms. When they are imaged with the STM they are exposed to the tips electric field and modified by it. This electric field is connected to the applied bias voltage and therefore not independently controllable. Here, the homogenously doped samples are replaced by a heterostructure with a controllable in-plane electric field. A p-i-n diode. A strong electric field is present within the diode's active region (see Fig. 3.1b). The electric field originates from the built-up of space charge layers during the Fermi level equilibration when the n- and p-doped layers are broad into contact (see section 3.3) [84]. This electric field is perpendicular to the interfaces of the diode. The diode structure is grown on a (001) oriented wafer and prepared for cross-sectional STM measurements as described in

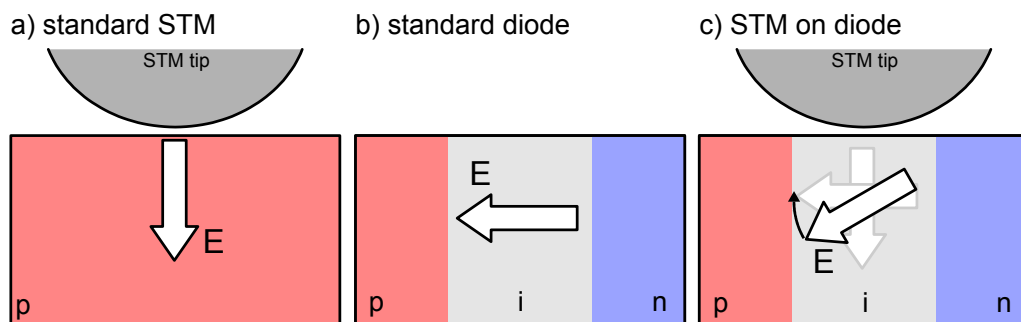


Fig. 3.1 Schematic of the electric fields in a semiconductor sample. (a) the electric field induced by the STM tip is perpendicular to the surface. (b) The electric field of a p-i-n diode is parallel to the surface because it is perpendicular to the heterostructures interfaces. (c) With a STM tip above the diode's active region both fields sum to an effective field that is tilted. The tilt angle is determined by the relative strength of each component.

chapter 1.3. In the STM experiment the diode field lies within the (110) plane, i.e., it acts as an in-plane field. When the STM tip is positioned above the diode's active region, the tip induced electric field and the diode field sum up. They result in an effective electric field that is tilted out of the (110) plane (see Fig. 3.1c). It would be favorable if the diode field is externally controllable, i.e., if the diode is operated during the measurement. Then the angle of the effective field can be externally adjusted.

Diode heterostructures have been studied previously. The study of the atomic structure of semiconductor heterostructures is one of the major applications of X-STM (a few examples are [15, 85-88]). Most studies of diode devices are carried out on p-n superlattices because they are easily addressed with the STM. In these systems the dopant distribution and interface roughness have been studied with high resolution [89-91]. The influence of the STM tip on the diode field in lightly doped diode superlattices has been reported [92]. Unfortunately, p-n superlattices cannot be operated. Their electric circuit analog consists of a series of alternating reverse-biasing and forward-biasing diodes. STM studies of operating diodes are rare. One reason may be the experimental effort. The STM has to be modified to allow at least two electrical contacts and the heterostructure can contain only one diode layer. In 1987 Muralt and coworkers published a pioneering work when they achieved to map the electrostatic potential across an operating double heterojunction laser structure [93]. Recently the carrier dynamics in a GaAs p-n junction were mapped using surface photovoltage measurements [94]. These measurements give information on the internal processes of diodes on length scale of ~ 10 nm. In this work spatial measurements with high resolution are combined with the ability to operate the diode. This will result in the possibility to study electric field-dependent effects on the atomic scale.

3.1. MBE-grown heterostructure

The p-i-n heterostructure for high resolution X-STM measurements is grown by molecular beam epitaxy (MBE) on (001) oriented GaAs substrate. The heterostructure was designed and optimized in cooperation with Dr. Stefan Malzer (Max-Planck-Research Group, University of Erlangen-Nürnberg). The samples are grown in the MBE system in Erlangen. The following preparation is done in Göttingen.

Fig. 3.2 shows the heterostructure design. The sketched layer thicknesses of the heterostructure are true to scale. The p-i-n junction is grown on a p-doped GaAs substrate. All layers are p-doped up to the active interface. Then a small intrinsic region of less than 10nm width is deposited. The p-i-n junction is terminated by n-doped GaAs and a n-doped capping layer. The continuous doping from the back side of the substrate to the active layer and from the active layer to the end of the heterostructure is necessary to be able to contact the diode from the back side and the front side. No processing is required to reach the buried p-

doped layer. The doped layers are terminated with delta doped sheets ($C\delta$ and $Si\delta$) with a dopant concentration of 10^{14}cm^{-2} to provide a very abrupt junction. The p-i-n active region is surrounded by double and triple AlGaAs marker layers that are used as “landing marks” to find the active layer with the STM. A topography is overlaid in Fig. 3.2. The image proves that the measured structure matches the intended layer sequence. The AlGaAs markers are visible as structured stripes running vertically through the image. The p-i-n active layer is visualized as a massive topographic distortion of about 2 \AA .

The measurements are performed in four-terminal geometry as indicated in the figure. One pair of leads is used to apply the diode bias. The current that is needed to maintain a certain bias is monitored. The other pair of leads serves as sense line for the potential drop across the sample itself. In Fig. 3.3 the diode’s macroscopic $I(V)$ characteristic is shown. It shows a p-n diode like characteristic. The diode characteristic improves when the temperature is reduced from 270 K to 5.6 K . The 270 K $I(V)$ -curve shows significant current already for low diode bias. The low temperature characteristic (which was recorded during the STM measurement) has a diode bias window of nearly vanishing current as it is expected of a diode characteristic [84]. But the diode has a poor rectification behavior. In the reverse bias direction the junction breakdown (e.g. Zener breakdown or avalanche breakdown) is reached at -0.25 V (for 5.6 K). It is worth noting that this behavior is expected from such narrow and highly doped p-i-n diodes.

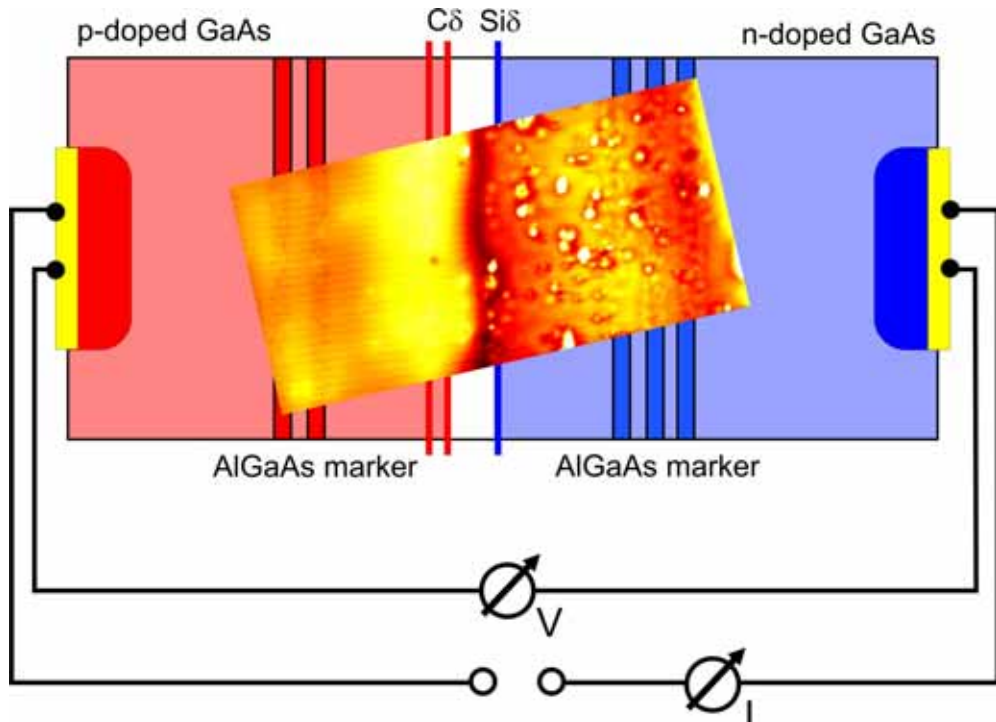


Fig. 3.2 Schematic of the p-i-n diode heterostructure sample. The heterostructure from the left to the right AlGaAs markers is true to scale. The homogeneously doped substrate and capping layer are much thicker. The superimposed image is a constant current topography ($80 \times 150\text{ nm}^2$) recorded at 2.0 V sample bias.

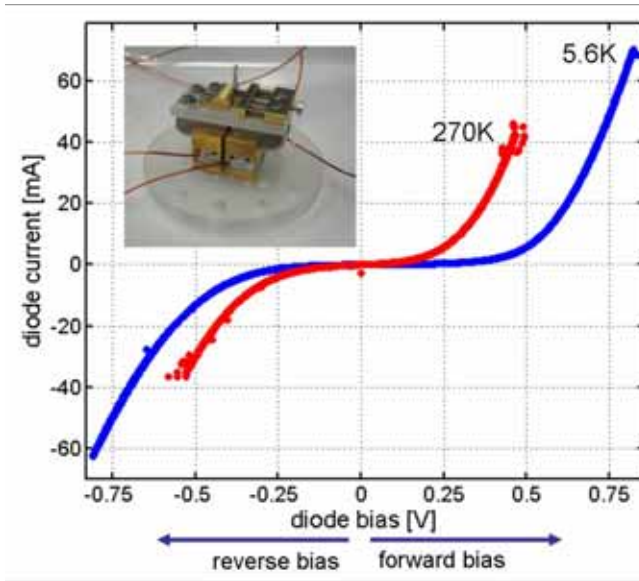


Fig. 3.3 (inset) The spring vice sample holder with a mounted *p-i-n* sample. The plotted $I(V)$ -characteristics are obtained inside the low temperature STM. The blue one was recorded during the STM measurement and the red one after the STM measurements, when the cryostat was warmed up 270K.

The sample structure is optimized for high resolution measurements which require a narrow structure. The *p*- and *n*-layers are degenerately doped and show ohmic behavior even at 4.2 K. This was verified in longitudinal resistance measurements on front side and back side of a sample piece respectively.

The electrical connection scheme of STM and diode is important to understand the observed images. Fig. 3.4 sketches the connection scheme. The bias between tip and sample is referred to as sample bias. The tip is held at ground in analogy to the standard STM measurements. The sample bias is always applied with respect to the *p*-doped contact (red) of the diode. The bias used to operate the diode is referred to as diode bias. It is applied between *p*-doped and *n*-doped contact similar to Fig. 3.2. The polarity is referred to as plus (+) when the diode is operated in forward bias.

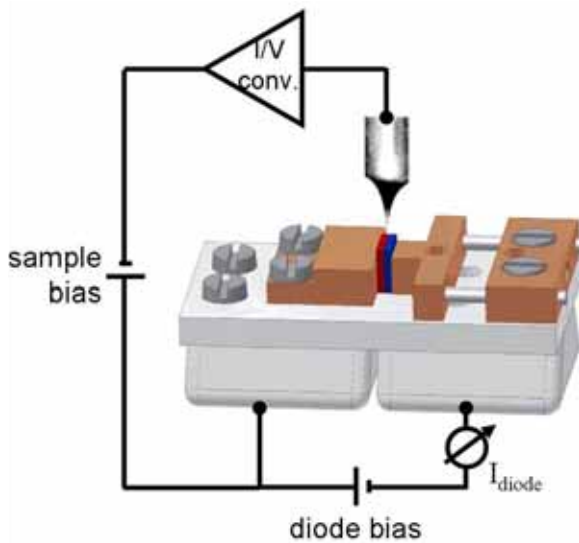


Fig. 3.4 Electrical connection scheme for the STM measurements of the operating diode. The bias between tip and sample is referred to as sample bias. The tip is held at ground potential and the sample bias is always applied at the *p*-doped contact (red). The diode bias is applied between *p*-doped and *n*-doped contact. For forward diode bias the polarity is referred to as plus (+).

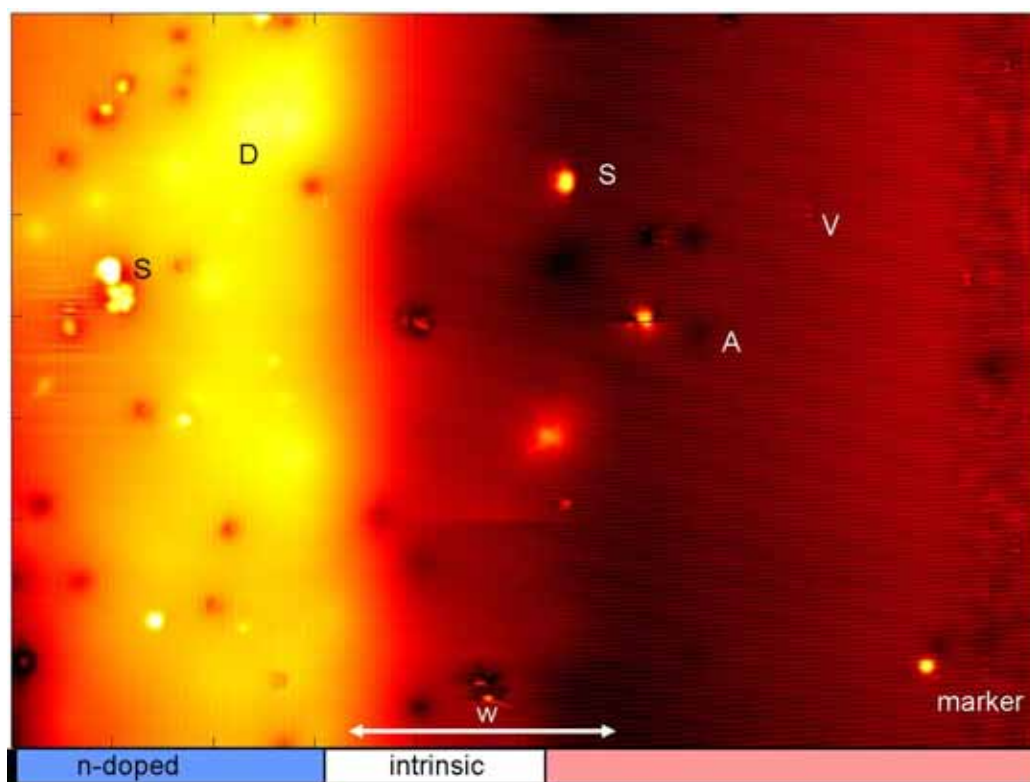


Fig. 3.5 (80 x 58)nm² constant current topography acquired at sample bias +1.8 V. The active layer of the pin-diode is mapped with atomic resolution. Besides a few surface adatoms (S) and some atomic vacancies (V) the surface is cleaved atomically flat throughout the heterojunction. The apparent height difference between n-doped (left) and p-doped (right) region is of pure electronic origin. In this image donors (D) appear as extended circular protrusions and acceptors (A) appear as depressions that are less extended than the donor features. The width of the active region (w) can be estimated in this topography to about 20nm. This allows an estimation of the build-in electric field to about 6×10^5 V/cm

Fig. 3.5 presents the structural properties of the diode's active region imaged with the STM. The (80 x 58)nm² area shows an atomically resolved image of the active region. No diode bias is applied for this measurement. One part of the double AlGaAs is seen at the right side of the image for reference. The most prominent feature is the apparent step between n-doped and p-doped region. This is not due to a surface step. The atomic corrugation shows that the surface is atomically flat, only a few adatoms and vacancies are visible. At positive sample bias, i.e., empty states image, the n-doped side appears higher than the p-doped side because of the different positions of the Fermi energy. The sample bias of +1.8 V allows tunneling into a nearly 1.8 V large bias window on the n-doped region. On the p-doped side the energy window of conduction band tunneling is only 0.3 V because the band gap has to be overcome for positive bias. The conductivity above the n-doped region turns out to be about 100 times higher than on the p-doped side. The tip retracts by 2 Å and the step is imaged. For negative bias, i.e., filled states image, the situation is reversed. Another prominent feature

originates from the same effect. Above the n-doped side the C4 surface state dominates the image. Vertical rows are imaged. On the p-doped side only the C3 surface state is present because tunneling is only possible at the conduction band edge. Horizontal rows are imaged (for comparison see chapter 1.4). The region where both surface states intermix gives first insight to the p-i-n interface roughness and extension of the built-in electric field. This allows estimating the built-in electric potential to about $6 \cdot 10^5$ V/cm.

3.2. I(V)-spectroscopy

Detailed information of the built-in potential is obtained from spatially resolved I(V)-spectroscopy. Fig. 3.6 presents the results of a large scale spectroscopy. The I(V)-curves are recorded at every point of the topography shown in the middle part of the figure. Two single dI/dV-curves are printed. One acquired in the n-doped side and the other in the p-doped side well away from the diode's active region. Both curves resemble those recorded on homogeneously doped samples. For the n-doped region the tunneling into the conduction band starts directly at 0.0 V and increases to the positive bias side. To negative bias the GaAs band gap has to be crossed, before the onset of tunneling into the valence band is measured at about -1.5 V. The situation is exactly reversed for the p-GaAs I(V)-characteristics. Tunneling into the valence band is seen directly at 0.0 V and increases drastically to negative bias. To positive bias the band gap has to be crossed before tunneling into the conduction band is resolved at +1.5 V sample bias. Defect induced conductivity on the order of 1 pA (n-GaAs) and 0.1 pA (p-GaAs) is measured in the band gap bias window.

The first step in the analysis is the normalization of all I(V)-curves to a plane of constant height as mentioned in section 1.5.1 in the theory chapter. The set-point topography of the measurement is at +1.8 V sample bias and 200 pA tunnel. After normalization the maximum tunnel current on the n-doped side is as high as 3-4 nA. The normalization to the plane of constant height applies a factor of 20 to the measured tunnel current. In contrast to this the tunnel current in the p-doped side is suppressed by a factor of 4 by the normalization. This explains why the noise in the band gap region seems to be increased on the n-doped side with respect to the p-doped.

The major advantage of spatially resolved I(V)-spectroscopy compared to taking a few single I(V)-curves becomes apparent in the dI/dV-section evaluated across the diode interface (lower part of Fig. 3.6). The differential conductivity is plotted color coded against lateral position and bias voltage. The conduction band and valence band related conductivity is plotted in yellow and red. The band gap region in between is plotted in blue and green. The dI/dV-section closely resembles the text-book sketches of diode structures (see e.g. [84]). The bands are flat in the p- and n-doped regions. The depletion layers are visible in the vicinity of the intrinsic regions. The bands are bent upwards at the n-doped

interface and downwards at the p-doped border. The shape of the depletion region is approximately quadratic. The potential drop from right to left side equals the GaAs band gap energy of 1.52 eV. Local distortions of the bands due to charged surface steps are also visible. This demonstrates the ability of the STM to resolve the internal band edge alignment in the p-i-n diode structure and the nanometer scale fluctuations of the built-in electrostatic potential.

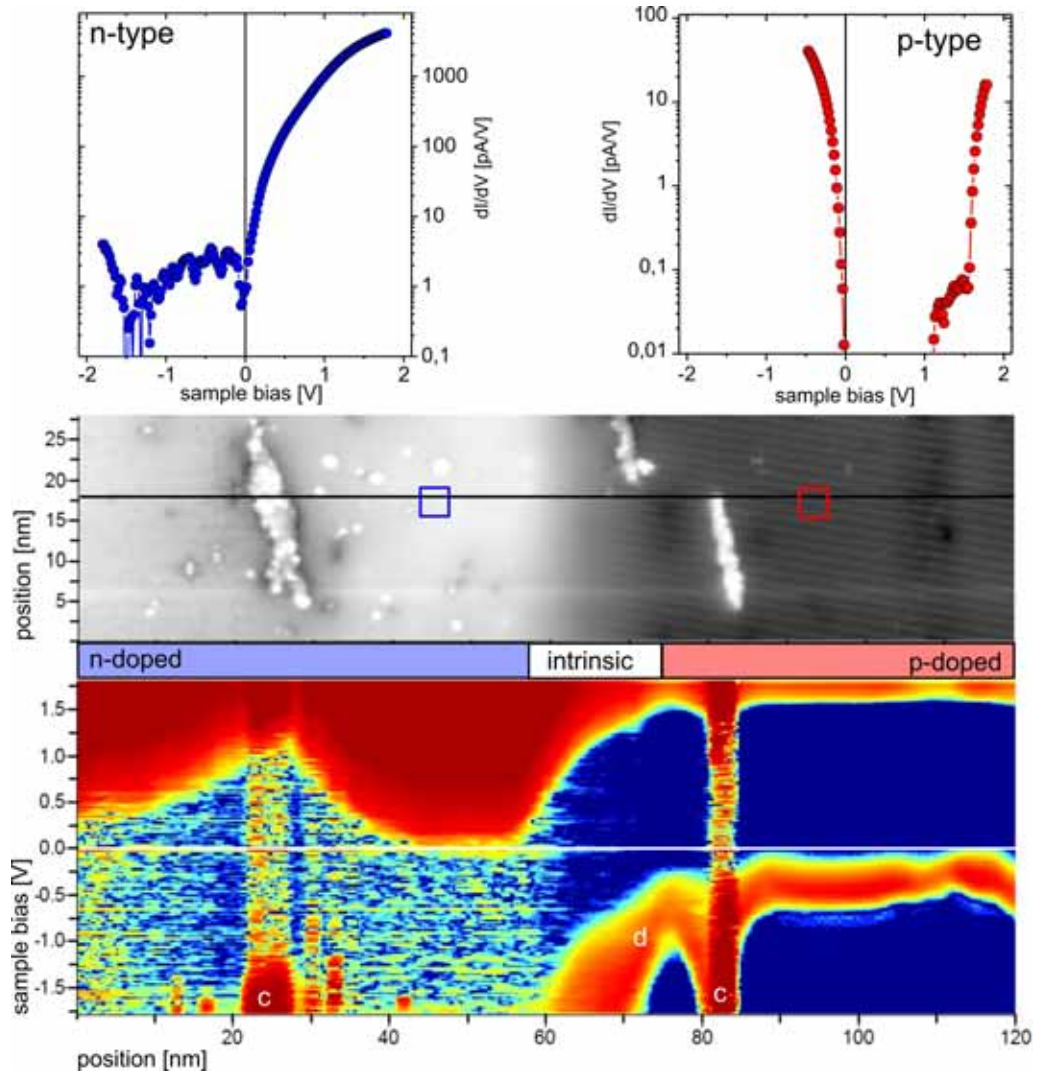


Fig. 3.6 I(V)-spectroscopy of the p-i-n diode active region. (top part) Single dI/dV curves are acquired on the n-doped side and on the p-doped side respectively. (middle part) topography of the spatially resolved I(V)-spectroscopy. The p-i-n layers are indicated with the colored bar. The blue and red square indicate the acquisition positions of the single dI/dV -curves. (bottom) dI/dV section across the diode interface. The section is recorded along the black line in the topography. The differential conductivity is plotted color coded against lateral position and sample bias. Blue and green is low conductivity and yellow and red represent high conductivity. The characteristic shape of the band alignment in the p-i-n diode is resolved. Additional distortion of the bands is visible at charged surface steps (c) and atomic defects (d).

3.3. The built-in potential

The previous section showed that the conduction and valence band edges are visualized in spatially resolved $I(V)$ -spectroscopies. This information is used to extract the built-in potential across the diode's active region. This procedure has been demonstrated previously for the built-in potential of a Schottky diode formed of GaAs and Au [95, 96]. Usually the tip induced band bending is superimposed to the local electrostatic potential in the sample. Numerical models have to be employed to subtract the TIBB. Unfortunately the TIBB calculations are based on a number of parameters that are a priori not known for every measurement, which increases the uncertainty in the calculated potential value.

In this work a different approach is pursued. As mentioned in chapter 2.1 the tip can be conditioned during the STM measurement by millisecond voltage pulses. The voltage pulses cause a modification of the tip apex. The tip work function after each voltage pulse is determined with the previously described technique (see chapter 2). This procedure is repeated until a tip configuration is found that exhibits a work function of $4.1 \text{ eV} \pm 0.1 \text{ eV}$. For this value the tip work function is equal to the electron affinity of GaAs. As a consequence the TIBB vanishes (flat band condition) when the sample bias is such that the tip Fermi energy is aligned with the conduction band minimum. This means that irrespective of the local electrostatic potential the TIBB becomes negligible, when tunneling into the conduction band becomes possible. The measured conduction band onset is not disturbed by TIBB. Then, the bias voltage for this onset equals the electrostatic potential in the sample. Fig. 3.7 shows the results of the potential evaluation with this technique for a line scan across the *p-i-n* interface. The red curve represents the electrostatic potential in the sample plotted against the position with respect to the *p-i-n* interface. The colored bar shows the lateral extension of the doped layers and the exact position of the delta doped sheets. These positions are determined in the topography (upper part of Fig. 3.7). The electrostatic potential is evaluated from the simultaneously recorded $I(V)$ -spectroscopy and is exactly registered to the topography. The conduction band onset is determined as the bias voltage where the tunnel current overcomes the threshold of 5 pA (red curve). Choosing higher threshold currents just shifts the potential curve rigidly but does not change its shape (green curve). For lower thresholds the measurement reaches the noise level of the spectroscopy and the evaluated potential becomes noisy (see blue curve, 1pA). The accuracy of the potential determination is limited by the current noise and the accuracy of the preparation of the tip work function to about 0.1 eV.

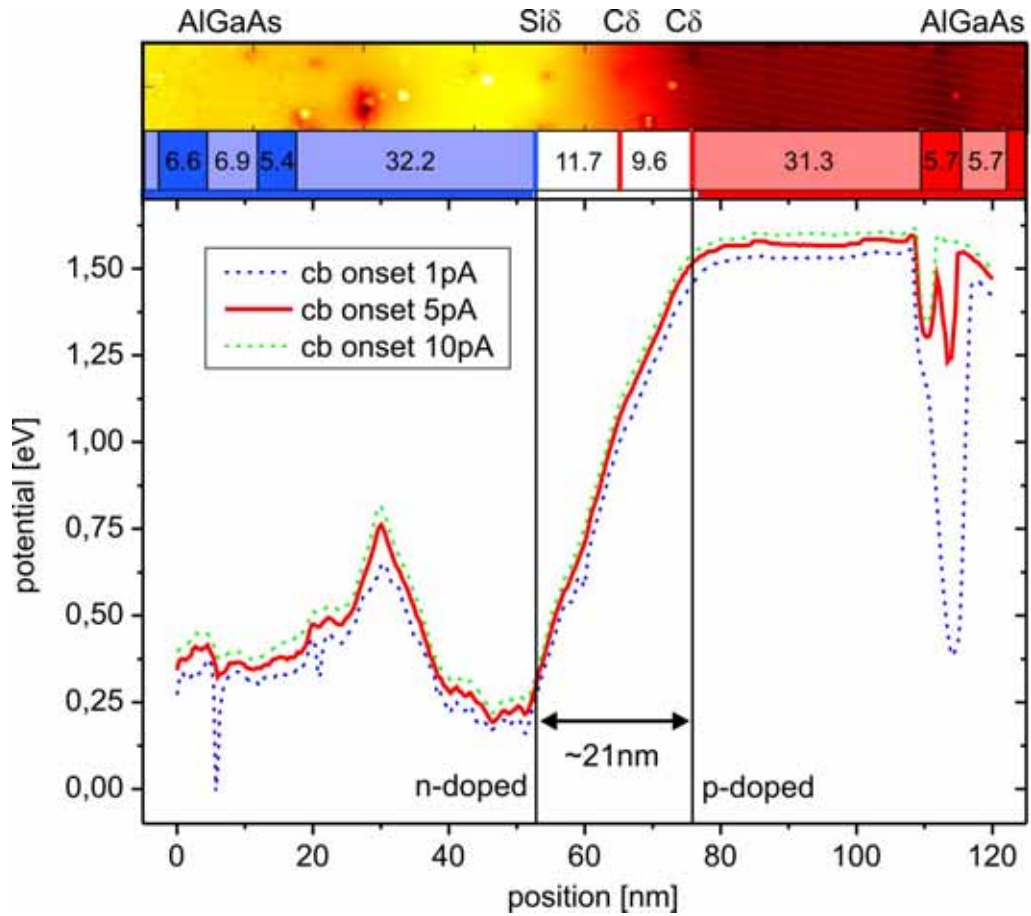


Fig. 3.7 Profile of the local potential evaluated along a line across the p-i-n heterostructure. Upper part topographic section showing the exact lateral position on the surface with respect to the marker layers. The local positions of the delta layers is indicated, too. The Potential distribution at this topographic section is evaluated from an STS measurement. The potential drop of ~ 1.5 V across the p-i-n active region is clearly resolved.

In the presented section a potential drop of 1.5 V is resolved. In the intrinsic region the potential drops linearly. On the p-doped side the quadratic shape of the depletion layer is clearly seen. The diode potential penetrates through the delta doped sheet into the homogeneously doped region. The potential drop ends abruptly at the position of the Si delta layer on the n-interface. The local donor concentration is sufficient to screen the diode potential on the length scale of a few nanometers. In the n-doped region the additional Coulomb potential of a charged defect is also resolved.

Of course the electrostatic potential can not only be evaluated along a line but on a whole spectrum set as shown in Fig. 3.8. The image shows the three dimensional visualization of the electrostatic potential at the diode's active region. The underlying topography is registered to the potential landscape. The spectroscopic measurement was done with atomic resolution. The effective resolution of the potential determination is ~ 1 nm. Two kinds of distortions are resolved by the

potential determination: Faint short range fluctuations with a length scale of ~ 5 nm and stronger long range fluctuations with a length scale of ~ 15 nm. The short range fluctuations are due to single dopant atoms or surface impurities and introduce only faint distortions of the uniform potential drop. The long range fluctuations are visible by the slight bending of the contour lines and might originate from dopant clustering effects as previously observed in p-n superlattices [97]. Besides these slight distortions the built-in potential drops very uniformly across the p-i-n interface. The average built-in electric field is given by the average slope in the middle of the intrinsic region. The field is in the (110) plane and oriented along $[001]$. Its strength is:

$$E_{diode} = 59 \frac{\text{meV}}{\text{nm}} = 590 \frac{\text{keV}}{\text{cm}}$$

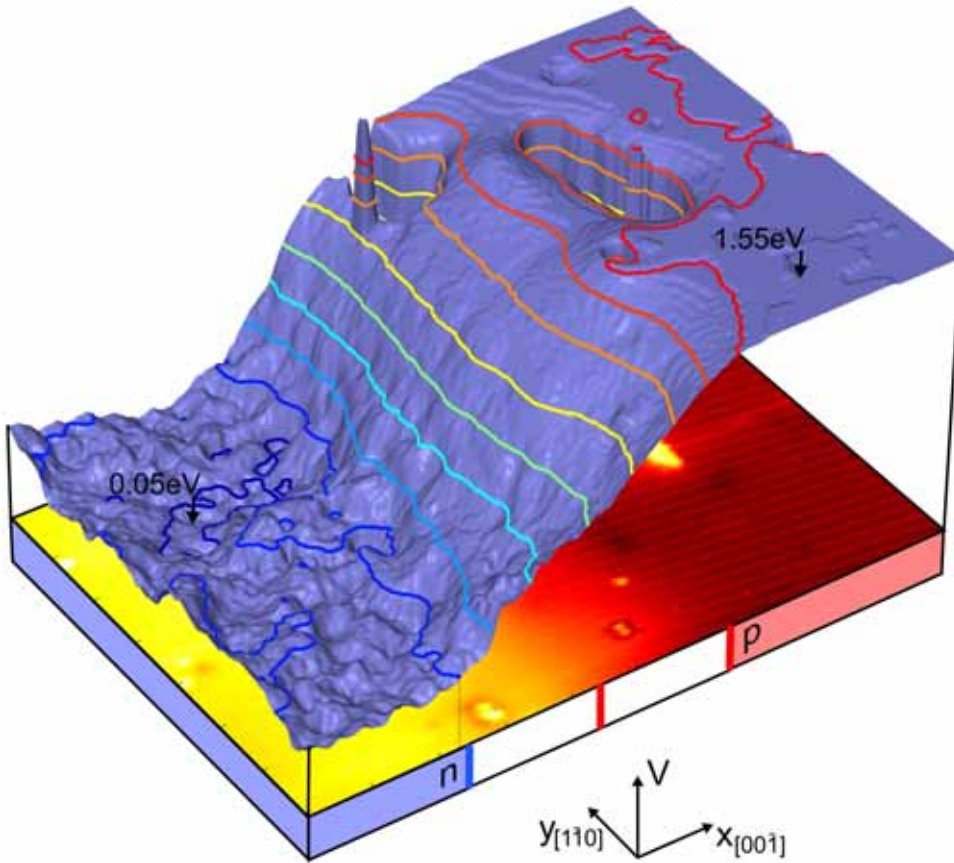


Fig. 3.8 $(42 \times 59) \text{ nm}^2$ three dimensional plot of the potential distribution throughout the p-i-n heterostructure (blue). Above the n-doped region the potential is as low as 50 meV and rises across the junction up to about 1.55 eV in the p-doped region. The setpoint topography of the measurement is plotted below the potential for reference. The sharp depression on the p-doped side is caused by the charge of a surface step. The step is visible in the underlying topography.

3.4. External characteristics and internal band-alignment

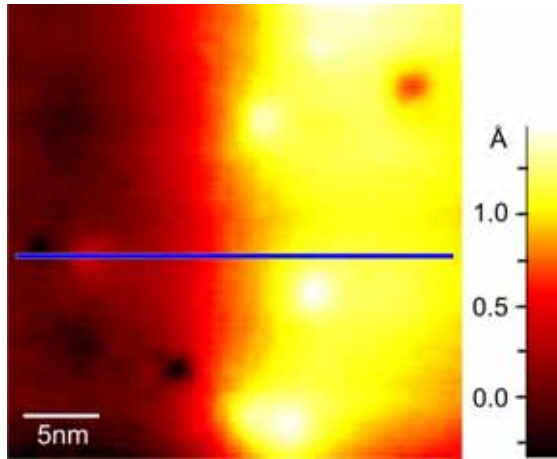


Fig. 3.9 (30 x 30)nm² setpoint topography at +2.0 V sample bias and 1.0nA tunnel current. The log I(V)-sections in Fig. 3.10 are evaluated along the blue line in this sample area.

The previous measurements presented first spectroscopic studies that resolve the band edge alignment in an unbiased diode. The next step is to perform the same spectroscopic studies on the operating diode. Fig. 3.9 presents the sample area chosen for this analysis. Again, an atomically flat region of the interface is chosen for the measurement to avoid artifacts. Fig. 3.10 presents the evolution of the band edge alignment under different diode bias conditions. The sections are evaluated along a line across the p-i-n interface.

The presented diode bias series in Fig. 3.10 shows four characteristic diode bias regions from reverse bias over zero bias to forward bias and finally high forward bias. The conduction band and valence band related tunnel current is colored yellow and red. The band gap region is visible in black and blue (similar to Fig. 3.6). The sample bias is applied with respect to the p-doped interface at the left side, hence the band edge positions on the left side do not change throughout the diode bias series. The externally applied diode bias modifies the internal potential. The macroscopic diode I(V)-characteristic is measured simultaneously to the STM spectroscopy. The log I(V)-sections demonstrate that changes in the built-in potential are resolved with the STM. With changing potential the band edges in the n-doped region (right side) are shifted with respect to the p-doped side (left side). The conduction band edge is indicated by a white line for reference. The shift with respect to its position at zero diode bias is drawn, too.

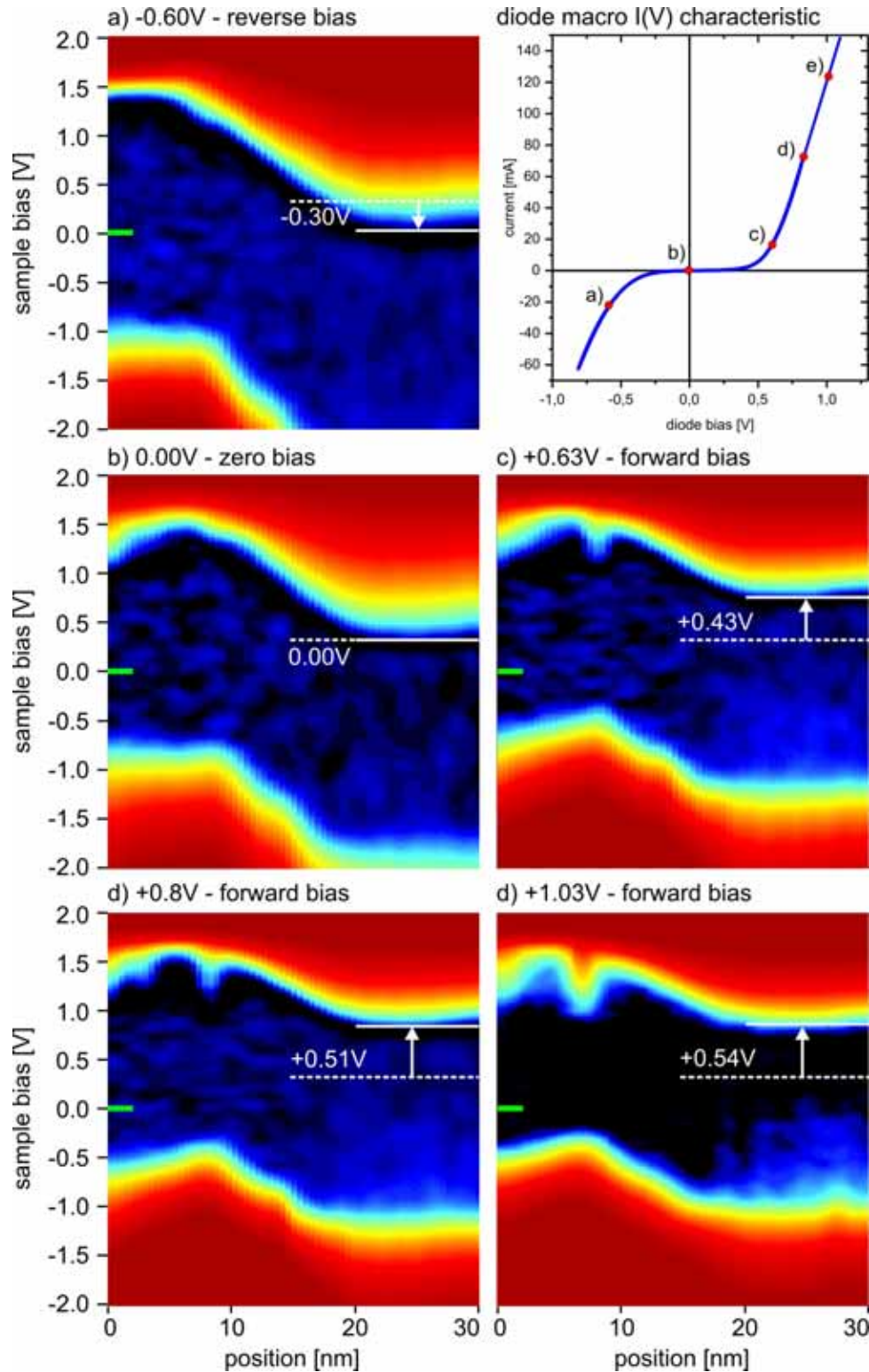


Fig. 3.10 (a) - (e) log I(V)-sections of the same 30nm wide section across the pin-junction. Different diode bias voltages are applied. The macroscopic I(V)-characteristic is plotted, as well. With changing external diode bias the internal fields are modified which is measured with the STM. The diode bias is applied such that the sample bias is defined with respect to the p-side contact (left edge of the images). The applied diode bias is thus imaged as a shift in the conduction band onset on the n-side (right edge of the images). The log I(V)-plot resolves the apparent band onsets.

At reverse diode bias the slope of the CBM is as high as 92 meV/nm. At zero diode bias the in-plane field has decreased to 84 meV/nm. The potential drop across the interface is smaller. When going to forward bias the built-in potential decreases further and the conduction band alignment becomes flatter. At an externally applied diode bias of +0.63 V the conduction band edge is lifted up by +0.43 V (Fig. 3.10c). This proves that nearly all of the applied diode bias reaches the p-i-n interface and decreases the built-in potential. With further increase of the external bias, the diode potential is further decreased and the conduction band edge moves up to +0.51 V for 0.80 V external diode bias. For even higher diode bias of +1.03 V, when the current driven through the diode exceeds 100mA, the internal potential is not decreased further. The built-in potential does not become smaller than ~ 1 V. The internal field is now decreased to 55 meV/nm.

It should be mentioned that the subsequent measurement of five spatially resolved $I(V)$ -spectroscopies requires a lot of time. The maximum time for a series is given by the lifetime of the liquid helium cryostat of 20 h. The energetic resolution of the measurements presented here is reduced so that the whole series is recorded within one cycle on the same position on the sample (Still the acquisition required 14 h). Unfortunately the band tunneling is not completely resolved due to the reduction in energetic resolution.

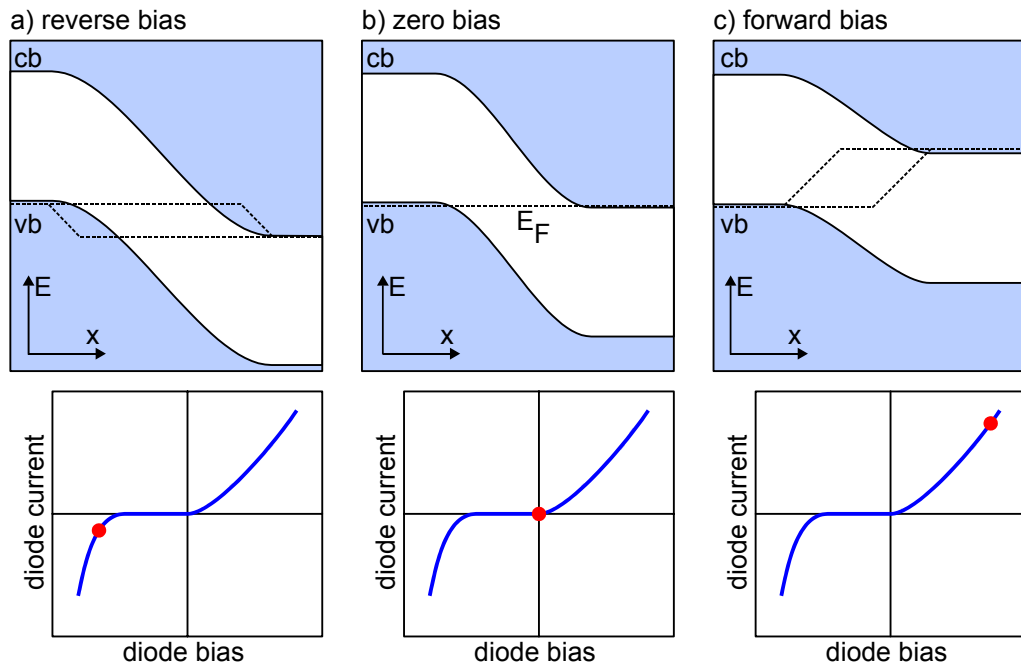


Fig. 3.11 Band diagrams of a p-i-n diode junction (upper part) and the corresponding $I(V)$ -curve (lower part). The conduction band (cb) and valence band (vb) are depicted in blue. Three situations are plotted: (a) reverse diode bias in the breakdown voltage range, (b) zero diode bias, and (c) forward diode bias. The Fermi energy is plotted as dotted line in (b) and the quasi Fermi energies for the biased device are plotted in (a) and (c).

The valence band tunneling reaches the noise level of this STS measurement before the band onset is resolved. Therefore the band gap region appears somewhat wider than 1.52 eV. But nevertheless the band edge alignment across the diode structure is clearly resolved by the conduction band onset.

The measured band alignment is in good agreement with the theoretically derived rigid band models found in semiconductor text books. Fig. 3.11 sketches the three situations: reverse bias, zero bias and forward bias. This is the first demonstration of the capability to experimentally resolve the band alignment of an operating device with $\sim 1\text{nm}$ resolution. Now the different diode current intervals are directly imaged with their characteristic band alignment configurations. The analysis of the macroscopic diode $I(V)$ -characteristic in a log $I(V)$ -plot (see Fig. 3.12) allows comparing the macroscopic information with the microscopic band alignment. The slopes in the log $I(V)$ indicate that the diode reaches the series resistance or high-injection condition for a forward bias of $\sim 0.6\text{ V}$ (analysis according to [84]). This is in good agreement with the local measurements. The band alignment sections show that starting at $+0.8\text{ V}$ diode bias the built-in potential does not decrease further. The additional voltage drops in the homogeneously doped layers due to the ohmic resistance. The same holds for reverse diode bias. The measured band edge alignment at a reverse diode bias of -0.6 V shows an additional potential drop of only -0.3 V at the *p-i-n* junction. This illustrates that the breakdown voltage is smaller than -0.6 V diode bias. It can be estimated to about -0.3 V because the built-in potential is enlarged by this amount. Then, the diode becomes highly conductive and any additional diode bias drops in the homogeneously doped regions due to series resistance. The macroscopic $I(V)$ -curve indicates that the diode breakdown is reached between 0 V to -0.2 V .

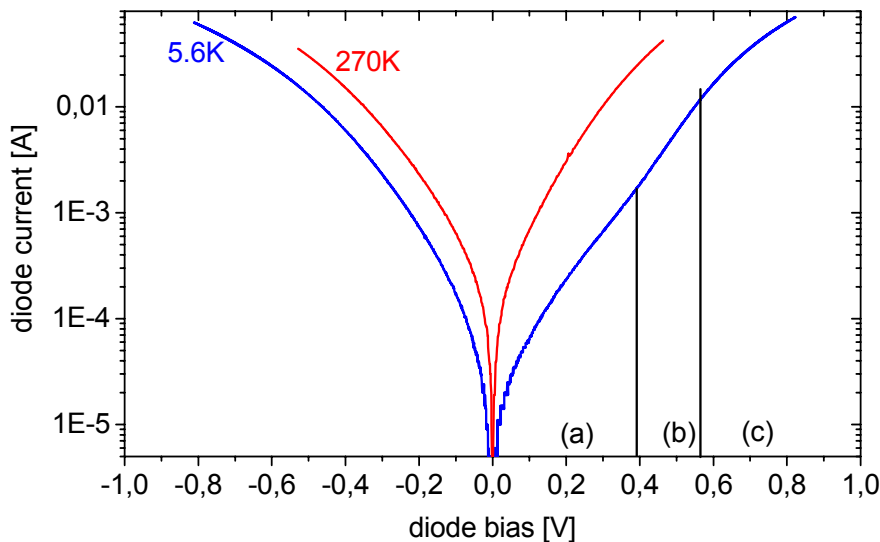


Fig. 3.12 $\log(I)/V$ plot of the above $I(V)$ -characteristic the 270K curve is featureless, but in the low temperature curve (blue) the three current contributions in forward bias are visible: (a) Generation – recombination current (b) Diffusion current (c) high-injection or series-resistance region

Table 1 shows the total range in which the diode's electric field is adjustable by the external diode bias. A comparison of the diode's electric field with the tip induced field is given. According to the calculations in chapter 2.1 the TIBB for a highly doped GaAs sample (p-doping on the order of 10^{18}cm^{-3}) varies from about -1V at large negative sample bias and +0.1V at high positive bias voltages. The resulting tip induced electric field is perpendicular to the sample surface. The field strength at a point at the sample's surface directly under the tip reaches strengths between -55 meV/nm and +17 meV/nm along [110]. The diode's electric field is of equal magnitude. Depending on the applied diode bias it ranges from -92meV/nm and -55 meV/nm along [001]. This comparison demonstrates that the in-plane electric field of the diode may significantly rotate the effective electric field vector. It is worth noting that the tip induced field decreases approximately linear with increasing depth from the surface. This is due to the quadratic shape of the tip induced space charge layers. The given values are the maximum field strengths at the surface. Deeper in the sample the tip induced field is smaller. The diode's field on the other side is uniform throughout the sample.

electric field range	from	to
diode induced in [001] direction	$-92 \frac{\text{meV}}{\text{nm}}$	$-55 \frac{\text{meV}}{\text{nm}}$
tip induced in [110] direction	$-55 \frac{\text{meV}}{\text{nm}}$	$+17 \frac{\text{meV}}{\text{nm}}$

Tab. 1 Comparison of the diode's electric field and the tip induced electric field at the sample surface. The diode induced electric fields are extracted from the above mentioned I(V)-spectroscopies. A p-doping of 10^{18}cm^{-3} and a TIBB between -1V and +0.1V is assumed for the evaluation of the tip induced electric field at the surface.

3.5. Summary

The combination of a well defined MBE grown p-i-n diode structure with the multiple contact low temperature STM gives the possibility to map local electronic properties of the operating device with nanometer resolution. Different diode current situations are well resolved in the local measurement. In spatially resolved I(V)-spectroscopy the band edge alignment across the diode's active region is visualized. The log I(V)-sections or log dI/dV-sections closely resemble the theoretically derived rigid band models of the p-i-n junction. The potential drops uniformly across the p-i-n interface. Slight lateral variations are resolved

that are on length scales of 10nm. The diode's built-in potential results in an in-plane electric field that is still present directly at the surface. The electric field vector is along $[001]$ and the field strength is externally controllable by the diode bias. With a strength between 55 meV/nm to 92 meV/nm it is comparable to the tip induced electric field. The initial goal to superimpose an in-plane electric field to the tip induced electric field is achieved with this structure (refer to Fig. 3.1). It will be used in the following chapters to study the field dependent properties of single dopant atoms.

4. Dopant induced anisotropic conductivity

A variety of dopants near the $\{110\}$ cleavage planes of III-V semiconductors has been investigated. All known acceptors exhibit anisotropic contrasts, some are of bow-tie like shape and some exhibit triangular contrasts. A comparative study demonstrates that the anisotropic contrasts originate from tunnel processes at the valence band edge.

In the past decade the electronic contrasts induced by shallow donors and acceptors in STM images of III-V semiconductors have received extraordinary attention. The $\{110\}$ cleavage surfaces represent an ideal model system for studies of dopant properties in semiconductors for two reasons: 1) The $\{110\}$ surfaces are the natural cleavage planes of III-Vs. Atomically flat terraces of hundreds of nanometers width are easily achieved [35]. 2) Usually the STM is only sensitive to the surface density of states. But because there is no reconstruction

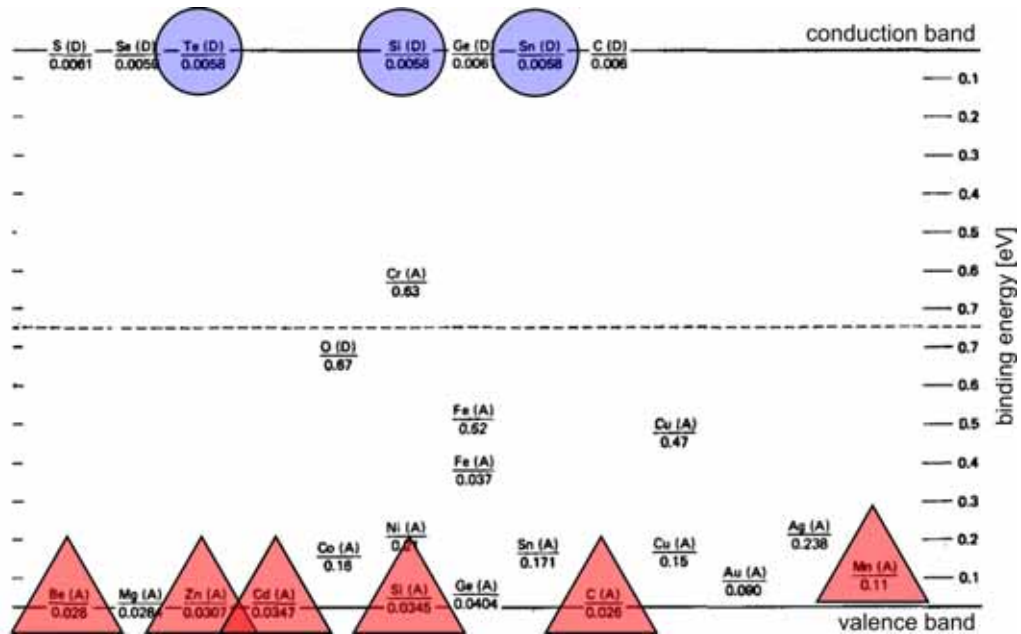


Fig. 4.1 Schematic of all known dopant elements in GaAs. Each element is drawn with its correct energetic position relative to the band edges. Acceptors are denoted with (A) and donors with (D). The blue circles indicate dopants that exhibit circular symmetric features in STM experiments. The red triangles indicate dopant atoms that exhibit highly anisotropic features in STM measurements [98].

of the cleavage surfaces the fundamental band gap is free of surface states. Thus bulk properties become accessible with the STM. This opens the door to do dopant profiling of heterostructures with atomic precision [91]. Studies performed during this thesis show that the STM catches up features originating from acceptors that are buried deeper than 14 monolayers under the surface.

A large variety of dopant elements has been studied in different III-V hosts, so far. Fig. 4.1 presents the list of studied dopants for the example of GaAs [98]. The diagram shows all possible dopant elements. The acceptors and donors that were analyzed with the STM are marked. They are classified with respect to their binding energy and appearance. Of all possible donor species, the elements tellurium (Te) [74], silicon (Si) [10, 21, 69, 99, 100] and tin (Sn) [101] have been reported so far. In the STM image they appear as circular protrusions centered on the dopant atom. In the schematic this is indicated by blue circles. The circular features of the shallow donors comply with what is expected of an impurity hybridized with states of the nearly isotropic and parabolic conduction band [10]. Nine doping elements are known to form an acceptor state with 100meV binding energy or lower in GaAs. Six of them have been investigated with the STM: Zn [11, 22, 72, 78, 102], Cd [78], Be [102], Mn [23, 103, 104], C [105, 106] and Si (see chapter 4.2). For most bias voltages the acceptors exhibit circular symmetric features in the STM images. But in contrast to donors, all known acceptors exhibit highly anisotropic features for certain bias voltages. This is indicated by the red triangles in the diagram. Additionally these features are also observed in different III-V semiconductors, i.e. GaAs, InP, InAs and GaP.

Fig. 4.2 illustrates the different voltage dependent contrasts of shallow and deep acceptors. For certain positive bias voltages shallow acceptors show up as distinct triangular protrusions. In voltage dependent topographies the position of the dopant atom underneath the surface is deduced [107]. The projected position of the acceptor atom is located in the triangle's tip. The zinc acceptor in GaAs is an example for this group and is presented in the upper row of the figure. The triangular contrasts extend over several nanometers along the $[001]$ direction of the crystal (Fig. 4.2b). Deep acceptors show a more bow-tie feature. Manganese in InAs is shown in the figure's lower row (Fig. 4.2e). The anisotropic contrast is also oriented along $[001]$ and the feature extends to both sides of the dopant atom. However, the bow-tie like contrasts are still asymmetric over $[001]$ and therefore exhibit the same anisotropy as the triangular ones. In topographic measurements these anisotropic contrasts are only visible in a narrow bias window. For higher or lower bias voltages, the acceptors appear as circular protrusions or depressions. The circular features are explainable in analogy to the donor contrasts. The stationary negative charge electrostatically shifts the surrounding density of states of the host crystal to higher energy. Depending on the tunneling condition (valence band or conduction band tunneling) this results in increased or decreased number of states available for tunneling. Then the STM images circular contrasts because the Coulomb interaction has spherical symmetry.

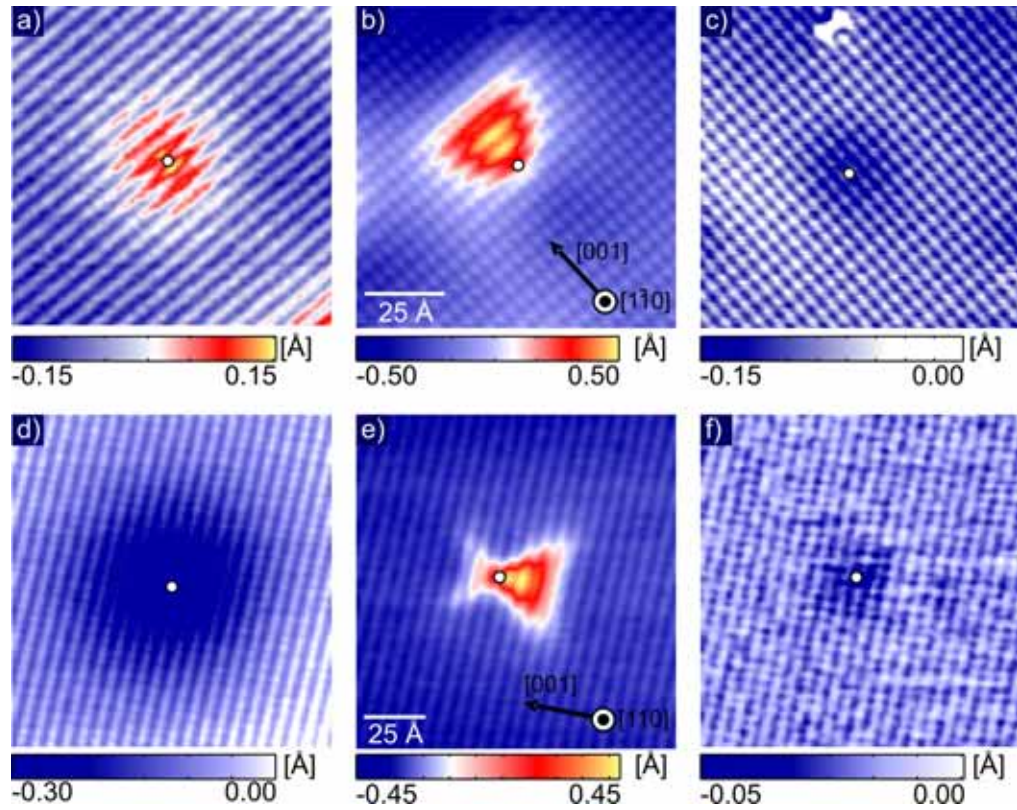


Fig. 4.2 Topographic contrasts of acceptors in III-V semiconductors. The voltage dependent features of a shallow Zn acceptor in GaAs are shown in the upper row ($10 \times 10 \text{ nm}^2$): (a) -0.7 V . (b) $+1.6 \text{ V}$. (c) $+2.0 \text{ V}$. The lower row shows the voltage dependent features of a deep Mn acceptor in InAs ($13 \times 13 \text{ nm}^2$): (d) $+0.7 \text{ V}$. (e) $+1.0 \text{ V}$. (f) $+2.0 \text{ V}$. The projected positions of the dopant atoms under the surface are indicated by white circles.

The anisotropic contrasts at acceptors have attracted attention of fundamental research, because they seem to contradict the theoretical predictions. Usually it is assumed that the STM images either the electrostatic influence of the dopant's stationary charge or the additional local density of states of the dopant's state, i.e., the acceptor wave function. The electrostatic interaction produces a circular symmetric contrasts and explains the images (a), (c), (d) and (f) in Fig. 4.2. The anisotropic contrasts of images (b) and (e) are not explained by electrostatic interaction only. They could be attributed to imaging of the acceptor wave function. Fig. 4.3 shows the calculated shape of an acceptor wave function [108]. The presented calculation is based on an effective mass approach and a Luttinger-Hamiltonian. A nearly rectangular contrast is expected on the $\{110\}$ surfaces, if the bulk acceptor wave function was imaged. The contrast is aligned with the host crystal lattice and symmetric along $[001]$. The comparison of the anisotropic contrasts in Fig. 4.2 with the expected shape of the wave function (Fig. 4.3) clearly demonstrates that the measured triangular or bow-tie like shapes are not easily explained.

The following chapters will focus on experimental studies revealing the origin of these features and development of a model that accounts for their asymmetric shape.

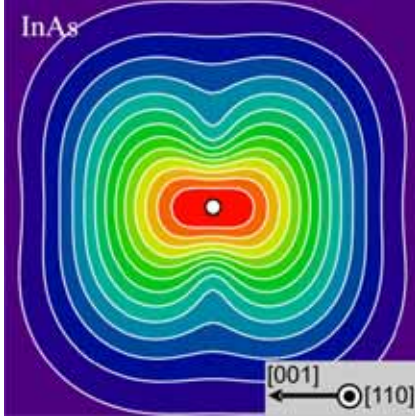


Fig. 4.3 $(8 \times 8) \text{ nm}^2$ image of the acceptor state's squared wave function. A deep acceptor in InAs is calculated here. The wave function was obtained in effective mass approximation with a Luttinger-Hamiltonian. The image shows a (110) section in a distance of 6 monolayers from the acceptor core. The projected position of the dopant atom is indicated by white circles. The bow-tie like contrast is symmetric over $[001]$. Image reproduced from [108].

4.1. Topographic properties of the anisotropic contrasts

The origin of the acceptor's anisotropic contrast has been subject to several reports during the past years. Most acceptor contrasts have been characterized by means of constant current topographies and first results of $I(V)$ -spectroscopies have been reported. But there is no comparative study of the spectroscopic properties of this variety of doping species. The comparison of results obtained on different systems will be the core of the following sections. Fig. 4.4 shows all acceptor species investigated during this thesis. In Fig. 4.5 supplementary studies of additional acceptor elements reported by other groups are put together. Constant current topographies are presented in the figures. They are recorded with a small positive setpoint bias so that tunneling into the conduction band is minimal. All acceptor contrasts in Fig. 4.4 show that all contrasts possess the same basic symmetry properties. The same holds for the acceptors investigated by other groups (Fig. 4.5). The symmetry properties of the contrasts are sketched in Fig. 4.6. The shallow acceptors appear as triangular protrusions. The triangle is shifted nearly completely to one side of the dopant atom along the $[001]$ axis. The deep acceptors have a bow-tie like shape, where one side of the bow-tie is larger and more pronounced. Comparative studies show that on the same sample the bow-tie's pronounced side points into the same direction as the triangle of the shallow acceptors.

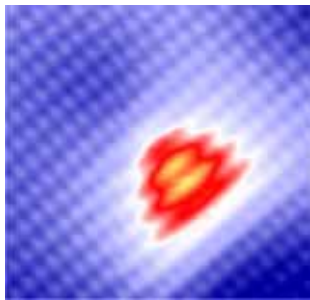
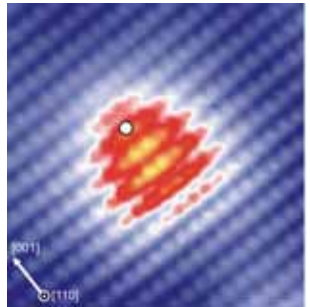
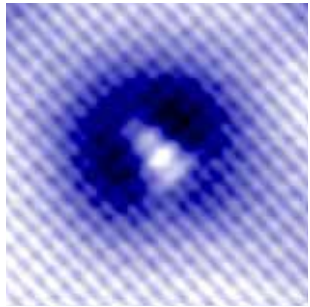
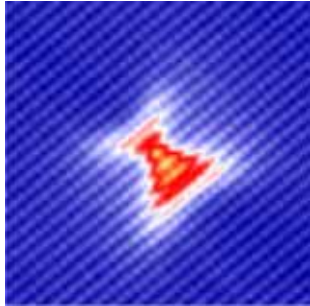
dopant element	investigated host	binding site	binding energy	type
Zinc	GaAs	cation	31 meV	
Carbon	GaAs	anion	26 meV	
Silicon	GaAs	anion	35 meV	
Manganese	InAs	cation	23 meV	

Fig. 4.4 List of dopants that have been investigated during this thesis. Shallow acceptors appear as triangular features for certain tunneling conditions. Deep acceptors also exhibit highly anisotropic shapes that are related to the triangular shape of shallow acceptors but the shape is more cross-like.

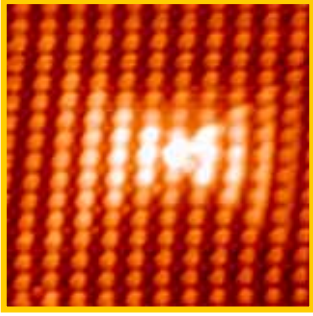
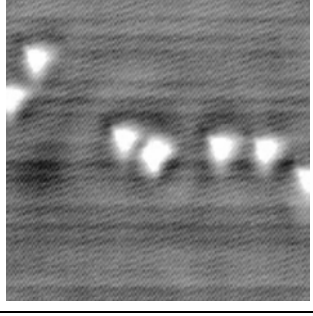
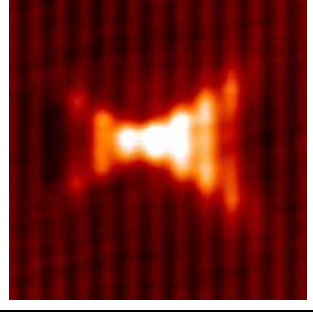
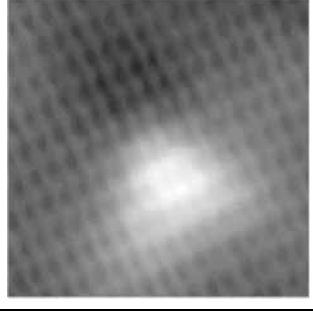
dopant element	investigated host	binding site	binding energy	type
Manganese [109]	GaAs	cation	115 meV	
Cadmium [78]	InP	cation	35 meV	
Cadmium [110]	GaP	cation	100 meV	
Beryllium [102]	GaAs	cation	28 meV	

Fig. 4.5 Additional dopants that have been investigated by other groups show similar behavior.

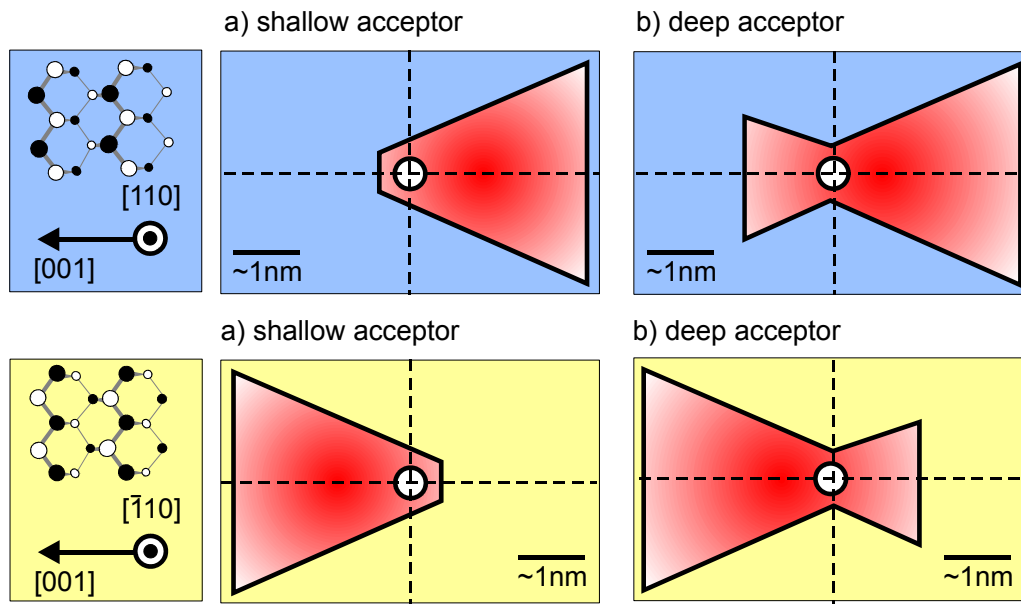


Fig. 4.6 Schematic showing the symmetry properties of shallow and deep acceptors in III-V semiconductors. The position of the acceptor atom underneath the surface is indicated by a white circle. The schematic is drawn for the contrasts observed at positive bias. The upper row (blue) represents the contrasts on the $[110]$ and $[\bar{1}\bar{1}0]$ surfaces. The lower row (yellow) represents the contrasts on the $[110]$ and $[\bar{1}\bar{1}0]$ surfaces. (a) Shallow acceptors appear as triangular shaped contrasts shifted nearly completely to one side of the dopant core. (b) Deep acceptors exhibit a bow-tie like shape. One side of the bow-tie is more pronounced than the other.

All contrasts have a symmetry perpendicular to $[001]$ which means that there is a $\{110\}$ mirror plane along this axis. However, there is no mirror symmetry along $[001]$ for the shallow and deep acceptors.

The III-V semiconductors possess two sets of non-equivalent cleavage planes: One is made up of the even signed surfaces $[110]$ and $[\bar{1}\bar{1}0]$ and the other of the odd signed surfaces $[1\bar{1}0]$ and $[\bar{1}10]$. The crystal lattice of the one set is exactly mirrored on the other one with respect to the (001) mirror plane. The lattice reversal is most prominently seen by the reversal of the top zig-zag rows (see ball-and-stick model in Fig. 4.6). On the even signed group (blue) the Ga atoms point towards $[001]$ and on the odd signed group (yellow) the As atoms. The same contrast reversal is observed for the acceptor induced contrasts. The pronounced side of the contrast is shifted to $[00\bar{1}]$ on the even signed surfaces. On the odd signed surfaces the triangular contrast is reversed and the pronounced side is shifted to $[001]$. The contrast reversal has been published in Jap. Journ. Appl. Phys. [72] and was also reported by another group [102].

Different models have been proposed for the formation of anisotropic contrasts in the past. Unfortunately all the proposed models lack the coherent description of all acceptor species. It was suggested, that d-electrons could cause such an anisotropic shape [11]. Zn ($[\text{Ar}].3d^{10}.4s^2$) and Cd ($[\text{Kr}].4d^{10}.5s^2$) for ex-

ample have d-orbitals, but acceptors like C ($1s^2.2s^2.2p^2$) and Be ($1s^2.2s^2$) do not possess occupied orbitals higher than p. Nevertheless they show the same triangular contrast. Another work argued whether the deformation of a circular contrast due to strain could explain the acceptor shape [78, 111]. The dopant atoms have different covalent and ionic radii than the host atom they replace. They locally introduce strain of tetragonal symmetry in the host lattice which could lead to a triangular contrast near the acceptor. This model could be discarded by the comparison of the acceptors Be and Zn which are substituted on the same site but induce different strains [102]. A third model inferred that the triangle reflects the first excited state of the wave function of a hole bound to the acceptor core. At low negative sample bias the ladder from ground state through a few excited states should be observed [102]. Unfortunately high resolution measurements could not find this “ladder” and the observation of the triangles at small positive bias could not be explained as excited states, as well [112].

4.2. Origin of the anisotropic shapes

Dopant induced anisotropic contrasts have been observed solely on acceptors. For donors only circular symmetric features have been reported [10, 21, 69, 100, 107]. However, all studies have been carried out on homogeneously doped sample areas. On p-doped material all dopants exhibit anisotropic contrasts, but there are only acceptors. On n-doped material the situation is reversed. No anisotropic contrasts are visible, but at the same time, there are no acceptors present. A comparative study, whether the anisotropic shapes are due to the electronic environment or if they are an intrinsic property of the acceptor atom, is not possible.

Here, spectroscopic measurements of autocompensated GaAs are presented. The doping consists of donors and acceptors that are mixed within the same area of the crystal. This system is provided by doping the GaAs crystal with high concentrations of silicon. Silicon is an amphoteric dopant in GaAs. It can be substituted either on the Ga site, where it becomes a shallow donor, or on the As site, where it is a shallow acceptor. Although Si is predominantly incorporated as donor, the significant formation of Si_{As} acceptors happens automatically for doping levels exceeding $2 \cdot 10^{18} \text{cm}^{-3}$ [113]. The following studies are carried out on a sample doped with $6.5 \cdot 10^{18} \text{cm}^{-3}$ Si. The n-type doping is $\sim 5 \cdot 10^{18} \text{cm}^{-3}$ and the acceptor concentration is about $\sim 1 \cdot 10^{18} \text{cm}^{-3}$, so the Fermi energy is still well within the conduction band. In order to obtain reproducible spectroscopic information, the good mixing of donors and acceptors is important. Fig. 4.7 presents a constant-current topography acquired on the (110) cleavage plane. All buried donors and acceptors are marked. The dopant distribution is nearly homogenous and the different dopant species are intermixed. The samples were provided by Dr. U. Kretzer (Freiberger Compound Materials GmbH, Germany).

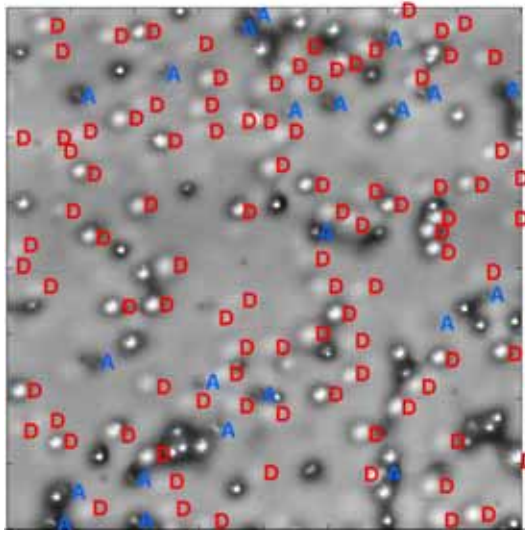


Fig. 4.7 (100x100) nm² constant current topography on the autocompensated GaAs sample. Sample bias -1.7 V, tunnel current 50pA. Donors are marked with red (D)s and acceptors with blue (A)s. The donors and acceptors are identified by their charge signature.

Fig. 4.8 shows a silicon acceptor and a silicon donor. Both topographies are recorded at -1.8 V. The donor appears as a circular protrusion with an extension of about 4 nm. The voltage dependent behavior is the same as for donors in homogeneously doped samples [10, 21]. In contrast to that, the acceptor shows up as a circular depression superimposed with a triangular protrusion. The triangle's extension is about 2nm. The circular depression above the acceptor exists for the whole voltage range, but the anisotropic contrast only appears in a narrow energy interval around -1.6 V to -1.9 V. This may be the reason why the triangular contrast above the Si_{As} acceptor is not reported in literature up to now, while the circular depression is [99, 113]. This demonstrates that the same doping element can exhibit either only circular or anisotropic contrasts. In a spatially resolved I(V)-spectroscopy the whole bias interval from -2 V to +2 V is covered.

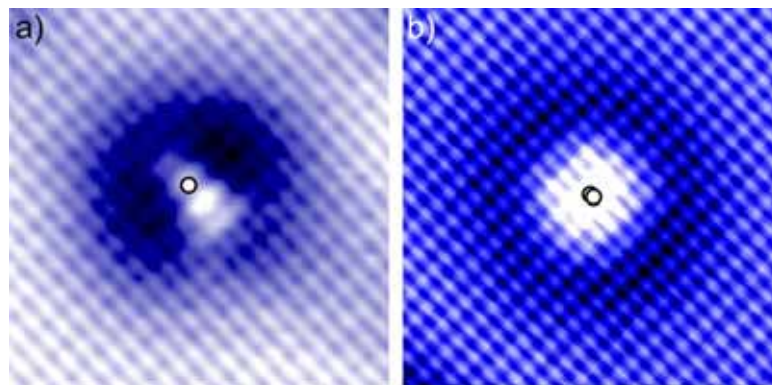


Fig. 4.8 Two constant current topographies of Si dopants in GaAs both recorded at -1.8 V bias. (a) (7.8 x 7.8) nm² Si on an As site is a shallow acceptor and exhibits a triangular contrast (b) (9.2 x 9.2) nm² Si on a Ga site is a shallow donor and exhibits only circular symmetric contrasts.

Fig. 4.9 presents the characteristic dI/dV -maps of this spectroscopy. The $I(V)$ data set is normalized to a plane of constant height prior to the analysis. Two Si_{As} acceptors and one Si_{Ga} donor are visible in the imaged area. The dopant atom positions under the surface are indicated by white circles. The comprehensive spectroscopic data set demonstrates that the Si_{Ga} donor possesses circular symmetric contrasts only. Additionally, the energetic origin of the triangular shaped conductivity is resolved. For positive sample bias only a circular depression is imaged for the acceptor and a ring-like charging signature is observed for the donor [69]. The charging signature is not the focus of this chapter. A similar effect will be discussed for Mn acceptors in chapter 5.3. The characteristic differences between donors and acceptors are measured at negative sample bias.

Four different configurations are found. The four respective dI/dV -maps are shown in Fig. 4.9. The band bending configuration along the tunnel path perpendicular to the surface is depicted in rigid-band models. The left side sketches the situation for the acceptors and the right side shows the configuration for the donor atom. The major difference is the local charge as indicated by the Coulomb potential like distortion of the conduction band (cb) and the valence band (vb) edge. The position of the Fermi energy (E_F) at the conduction band is indicated by the dotted green line, and the sample bias is indicated by a solid green line. The filled states are drawn in grey, and empty states are white. The tip induced band bending (TIBB) produces the quadratic slope of the band edges. The band alignment is sketched according to the calculated TIBB(V) dependence for this sample. The tip work function is larger than 4.1 eV, so at 0 V sample bias the bands are bent upwards.

For small negative bias voltage <100 mV (Fig. 4.9a), conductivity is detected only above the donor atom. The circular shaped conductivity directly reflects the donor state wave function. Delocalized conductivity on the whole sample is observed for larger negative bias (Fig. 4.9b -763 mV). For such voltages the sample is in depletion. The conduction band is pulled under the Fermi energy by the TIBB and free electrons are accumulated. The electrons are confined laterally by the extension of the tip and vertically by the depletion layer depth as seen in the rigid band model. A so-called tip induced quantum dot is formed and charge density oscillations of the confined states are imaged in the dI/dV -signal [75-77]. The donor locally deepens the accumulation layer. The electrons of the tip induced quantum dot are scattered at the attractive potential and the conductivity is locally enhanced. In contrast to that the negative charge at the acceptor atom locally repels the electrons. The delocalized conductivity seen as orange color on the undisturbed surface does not reach the acceptor atom. A depression of about 4 nm width around the acceptors is visible. This conductivity produces the circular depression in the topography (see Fig. 4.8).

When the applied bias overcomes the band gap of 1.52 eV (Fig. 4.9c) an additional tunnel channel becomes possible. Electrons can tunnel out of the valence band edge in the bulk of the semiconductor.

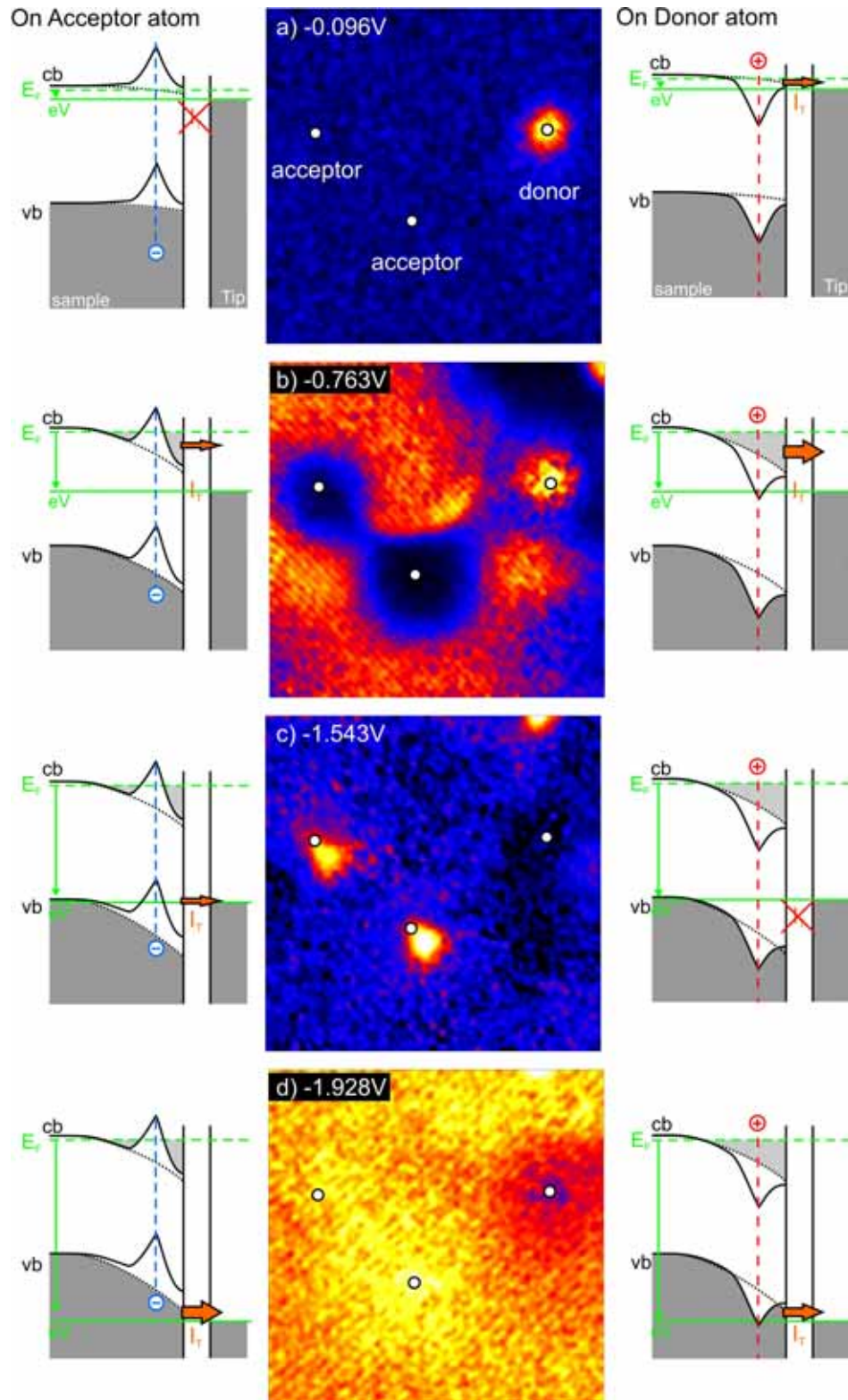


Fig. 4.9 (20 x 20)nm² dI/dV-maps of two acceptors and one donor in autocompensated GaAs. The dI/dV-maps represent characteristic conductivity windows of the sample. The band bending configurations for the acceptor are depicted on the left side and for the donor on the right side (description of the symbols is given in the text). (a) Small negative TIBB: The donor state is imaged. (b) Electron accumulation at negative TIBB: Charge density oscillations are imaged. (c) Negative TIBB: anisotropic conductivity at the acceptors. (d) Valence band tunneling.

However the TIBB is negative and the valence band is pulled downwards as depicted in the corresponding rigid-band model. No valence band states are accessible directly at the surface for the dI/dV -map acquired at -1.55 V. The conductivity on the undisturbed surface is low (black and blue color). In the bias window from -1.55 V to -1.75 V enhanced conductivity is only visible at the acceptors. Here, triangular shaped conductivity is measured. The donor atom on the other side has no feature. The triangular shaped protrusion in the topography originates from this tunnel channel at the valence band edge.

When high negative bias is applied (Fig. 4.9d), the sample bias overcomes the band gap plus the TIBB and tunneling out of the valence band dominates the tunnel current. The conductivity is spread over the whole sample area. The conductivity shows lines running diagonally through the image. This is the atomic corrugation of the first surface resonance of the valence band (A5). The dopants induce only a slight contrast due to their charge. The acceptors are negatively charged and imaged as enhanced conductivity and the donor's positive charge slightly decreases the conductivity.

The dI/dV -maps allow decomposing the topographic contrast observed for the Si_{As} acceptors at -1.8 V. The circular depression reflects the influence of the acceptor's negative charge on charge density oscillations in the conduction band. The triangular protrusion is traced back to a tunnel process at the valence band edge. As soon as electrons from the valence band in the bulk crystal can elastically tunnel into the tip, the triangular shaped conductivity is measured. Although the possible tunnel channels for the donor are the same, no anisotropic shapes are observed. When tunneling occurs deeper in the valence band or in the conduction band, no anisotropic features are visible, at all.

4.3. Summary

A variety of different acceptor species in several III-V semiconductors has been investigated by means of X-STM. Besides circular symmetric features that are also known for donors, all investigated acceptors exhibit distinct anisotropic features for certain tunneling conditions. Either triangular shaped or bow-tie like contrasts are imaged. These contrasts are linked to the host lattice symmetry. They are mirror-symmetric over the $\{110\}$ mirror planes and have an asymmetry with reference to (001) .

The comparative $I(V)$ -spectroscopy of Si_{As} acceptors and Si_{Ga} donors illustrates that the two basic prerequisites for the formation of anisotropic conductivity are the presence of an acceptor atom and a tunneling channel at the valence band edge. For no other configuration anisotropic conductivity is detected. The following chapters will focus on the possible tunneling processes that can lead to such conductivity near acceptor atoms.

5. Imaging mechanisms at neutral and charged acceptors

This chapter derives energy scaling diagrams that show the bias dependent energy shift of the acceptor state at the sample surface. These diagrams identify two different energetic configurations for the observation of bow-tie like or triangular contrasts.

The previous chapter demonstrates that the anisotropic features are related to a tunneling process at the valence band edge which is induced by an acceptor. Two qualitatively different tunnel processes are possible in these STM measurements:

- The first tunnel channel involves tunneling directly into or out of the acceptor wave function. At positive bias the electron tunnels from the tip into the unoccupied acceptor state and is drained into the bulk sample afterwards. For negative bias the acceptor state has to be occupied. The electron tunnels into an unoccupied state in the tip and the emptied acceptor state is refilled from the bulk sample. Whether this process is observable or not depends on the alignment of the acceptor state with the Fermi energy in the sample and in the tip.
- The second tunneling process is a one-step process. It is not required that the acceptor state itself contributes to the tunnel current. The acceptor perturbs its surroundings due to its stationary negative charge. The corresponding Coulomb potential electrostatically influences the alignment of the semiconductor bands on a 10nm length scale. Together with the tip induced potential at the surface it may induce additional tunneling paths that are not present in the bulk system. This tunnel process is most likely observed when the acceptor is charged and the negative core charge is not screened.

The band bending has to be considered to distinguish the possible configurations. At first, a model will be derived that allows identifying bias windows for both tunnel processes. Experimental results that directly show the transition from one process to the other will be discussed on the basis of I(V)-spectroscopies.

5.1. Different charge states at acceptors

The tip induced band bending (TIBB) determines what processes are possible and for which bias intervals tunneling can occur. If the positions of the bands and states in the semiconductor are described within a rigid-band model (see Fig. 2.1) the TIBB at a certain bias voltage equals the shift of the states with respect to their bulk position. The TIBB(V) dependence can be calculated for a specific sample configuration (doping, band gap, electron affinity) and a specific tip configuration (work function, shape). At the flat band bias the tip induces no field. Then, the bands on the GaAs and InAs {110} surfaces are flat, and the energetic positions of the semiconductor states at the surface equal their positions in the bulk of the sample [20]. For every other bias between tip and sample, the states are shifted by the TIBB. Their energetic positions with reference to the sample Fermi energy are directly given by the TIBB(V) function. The energetic position of a state at the surface with reference to the bulk sample Fermi energy is given by

$$E(V)\big|_{\text{surface}} = \text{TIBB}(V) + (E - E_F)\big|_{\text{bulk}}$$

with $(E - E_F)$ being the energy of the respective state with reference to the Fermi energy E_F . Curves are derived, that show the energetic position of the acceptor state and the valence band maximum plotted against the sample bias. Fig. 5.1 presents the resulting energy scale diagrams for three different systems. The regions where tunneling into or out of the states can occur are determined by two conditions: The state of interest has to be unoccupied for positive sample bias and occupied for negative sample bias. Thus, it has to lie above the sample Fermi energy for positive bias and below for negative bias (this is indicated by the horizontal border of the green areas). In addition, it needs to be in the voltage interval where elastic tunneling can occur, i.e., between $E_{F,\text{sample}}$ and $(E_{F,\text{tip}} + eV)$. The areas fulfilling these conditions are marked by green color in the figure.

The three systems in Fig. 5.1 are: (a) GaAs doped with shallow acceptors. The parameters chosen for the band bending calculation are matched to the I(V)-spectroscopy presented in chapter 7. The Fermi energy is assumed to be at the valence band edge. The sample is doped with $5 \cdot 10^{18} \text{ cm}^{-3}$ zinc acceptors (binding energy 31 meV). If all acceptors were ionized, the Fermi energy would be in the valence band. Due to the low temperature of 8 K this will not be true, so E_F will be in between the valence band maximum and the acceptor band. Therefore the chosen position is a good approximation for the calculation. The second system is GaAs doped with deep acceptors (Fig. 5.1b). This system is not investigated here, and plotted to demonstrate the strong impact of the acceptor binding energy. The parameters of the first model are used, but the binding energy of the acceptor is increased to 110 meV. The last system, Fig. 5.1c, is InAs doped with $3 \cdot 10^{17} \text{ cm}^{-3}$ Mn acceptors (binding energy 23 meV). Section 5.3 shows that this system allows validating the energy scale diagrams derived here.

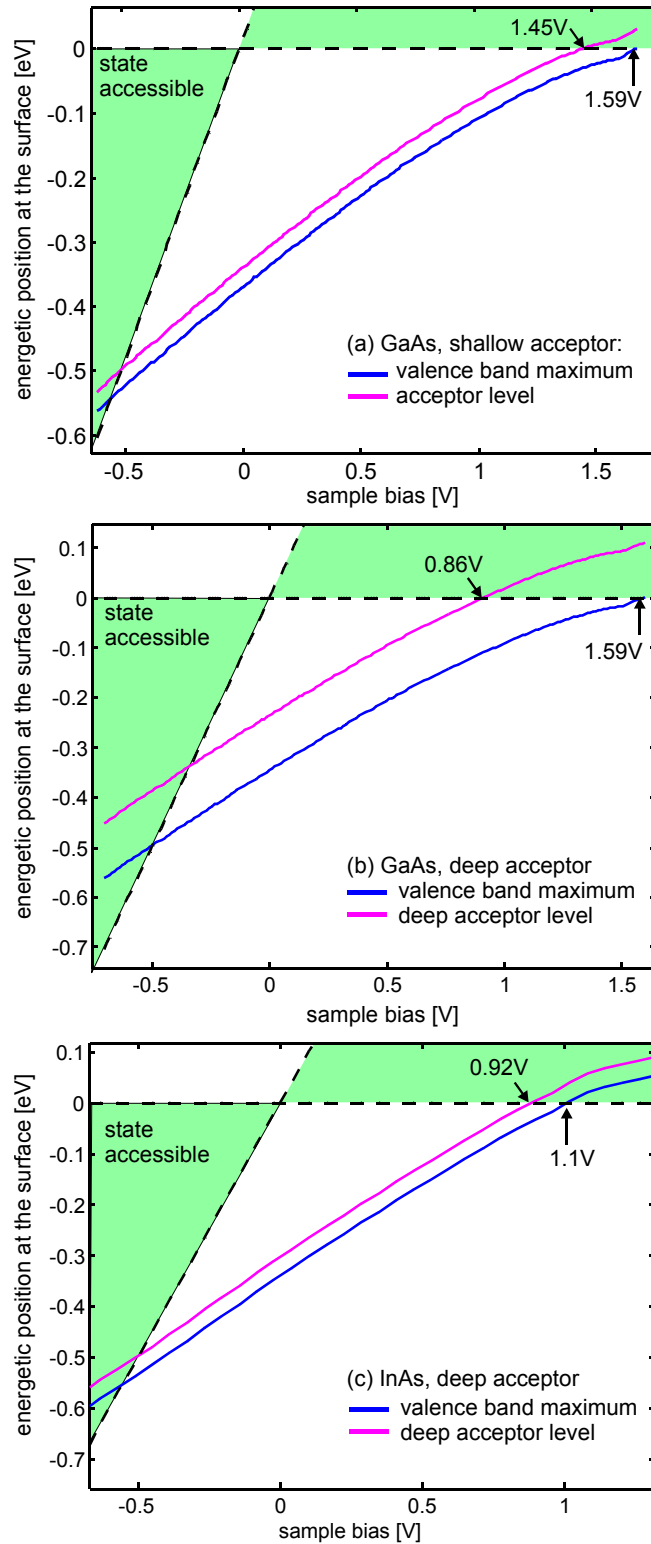


Fig. 5.1 Energy scale diagrams. The diagrams show the energetic shift of the valence band maximum and the acceptor state with reference to their energy in the bulk. These quantities are plotted against the applied sample bias. When the plotted energy lines are in a green region, the corresponding state is directly accessible at the surface. The numerical method is described in the text. The diagrams show the systems (a) GaAs and a shallow acceptor (30 meV binding energy). (b) GaAs and a deep acceptor (110 meV binding energy). (c) InAs and a deep acceptor (23 meV binding energy).

The two possible processes leading to anisotropic conductivity are now examined with reference to the tunneling condition. The first tunnel process involves direct tunneling into or out of the acceptor state. This process can only contribute to the formation of anisotropic contrasts for bias windows in which the acceptor state is shifted into the green areas of the energy scale diagram. For p-doped GaAs and shallow acceptors (Fig. 5.1a) this happens above +1.45 eV for positive bias and below -0.5 V for negative bias. In the whole interval from -0.5 V to +1.46 V tunneling through this state is not possible. If a deep acceptor in GaAs is considered, the acceptor state would be accessible for other voltage intervals. The deep acceptor with 110 meV binding energy considered in Fig. 5.1b becomes available for tunneling from +0.9 V on for positive bias and below -0.3 V for the negative bias side. The comparison of the shallow and deep acceptor gives an astonishing result: The interval boundaries shift by about 500 mV although the binding energy shifted by only 80 meV. The TIBB acts like a lever arm that strongly distorts the sample energy scale.

The third system, InAs doped with Mn (Fig. 5.1c), shows an energy scale diagram similar to GaAs doped with shallow acceptors, although Mn in InAs is usually considered a deep acceptor [114]. This is due to the fact that the absolute binding energy of Mn in InAs is similar to that of zinc or carbon in GaAs. It is less than 30 meV. According to the diagram the Mn acceptor state becomes accessible for tunneling at +0.9 V for positive bias and from -0.5 V for negative bias. Between -0.5 V and +0.9 V the acceptor state cannot participate in the tunnel process directly. However, the acceptor state is below the Fermi energy, so the acceptor is charged. The hole (which is the free carrier of the valence band) is stripped away and the acceptor core exhibits its localized negative charge. Then, the bands of the semiconductor host are influenced by the corresponding Coulomb potential. This gives rise to the second tunneling process (see introduction of this chapter). The condition (acceptor charged) is fulfilled for any bias voltage lower than the voltage where the acceptor state crosses the horizontal border of the green areas. Again, the binding energy of the acceptor is important: shallow acceptors in GaAs stay charged up to +1.45 V, while deep acceptors in GaAs are discharged already at +0.9 V.

In this manner the energy scale diagrams allow to determine the bias intervals for the qualitatively different configurations at the acceptors. A summary of the possible intervals and conditions is presented in Fig. 5.2. The three diagrams of Fig. 5.1 are the basis of this summary. The first bar (blue) indicates the interval in which the acceptor exhibits a Coulomb potential. The second bar (yellow) shows the regions in which tunneling at the valence band edge is the predominant tunnel channel. The third bar (green) indicates the bias intervals where the acceptor state can be accessed directly. The first system (GaAs: shallow acceptor) and the second system (InAs: deep acceptor) are investigated in this thesis. The red bar indicates bias windows for which anisotropic contrasts are observed in I(V)-spectroscopy. For the white regions in this bar measurements show that no anisotropic contrast is visible.

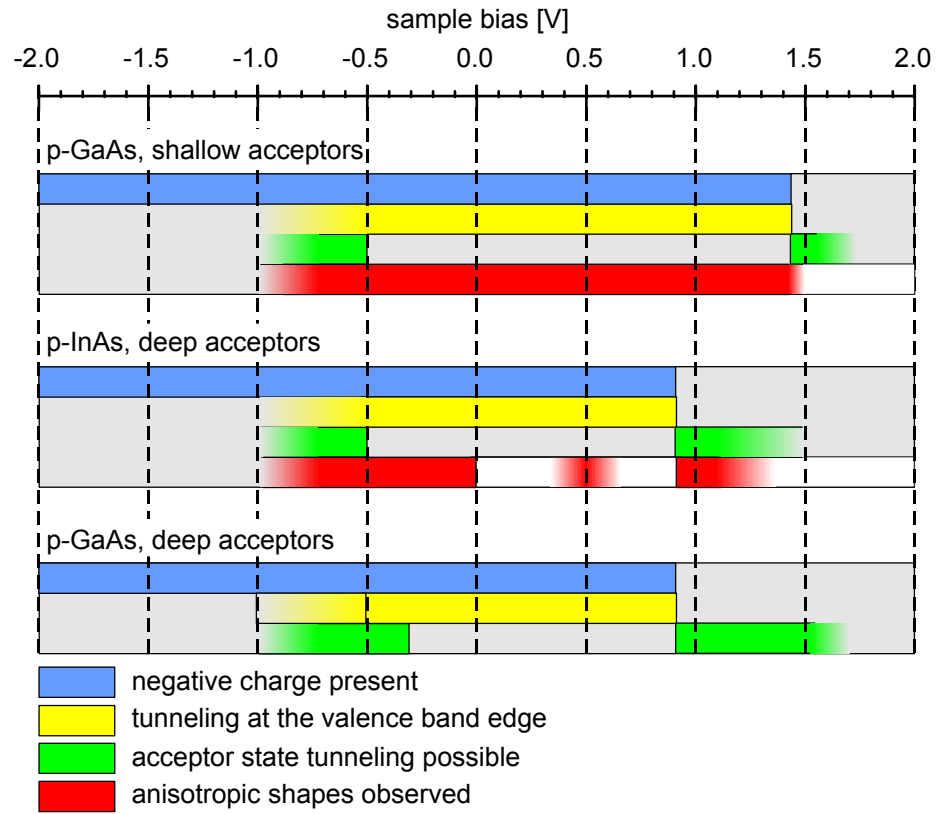


Fig. 5.2 Schematic of the different configuration intervals found for acceptors in the sample systems of interest. The horizontal axis represents applied bias voltage. Blue bar: bias interval for which the acceptor exhibits an unscreened Coulomb potential. Yellow bar: bias interval where tunneling occurs at the top of the valence band edge. Green bar: bias interval where the acceptor state is available for direct tunneling. Red bar: bias intervals for which anisotropic contrasts are observed in the $I(V)$ -spectroscopies. The white parts in this bar indicate bias windows for which the measurements show no anisotropic shapes.

Fig. 5.2 clearly shows that anisotropic contrasts are imaged for both energetic configurations in InAs.

- The acceptor is within the green regions of Fig. 5.1 and directly carries tunnel current.
- The acceptor is charged and tunneling is restricted to the valence band edge. The acceptor can induce additional conductivity without the acceptor state participating directly.

On the negative bias side both processes can overlap, so observed anisotropic conductivity cannot be attributed to one specific channel without additional information. For positive bias voltages both tunnel processes are clearly divided by the bias voltage where the acceptor is discharged. The following discussions concentrate on this bias side. It is worth noting that the bias thresholds dividing the different intervals have an uncertainty that depends on the accuracy of the

TIBB(V)-calculation. Another factor is the exact binding energy of the acceptor state near the surface. Even though the TIBB can be cross-checked with the I(V)-spectroscopies the exact slope of the TIBB(V) curve is often not validated. Therefore measurements performed well within each bias window are reasonable, but analysis of measurements at the border from one interval to another should be considered with care.

The best sample for a comparison of both tunnel processes is InAs. The schematic shows that anisotropic shapes are observable in relatively large bias windows for the two different bias windows. This will be the focus of the next section. Additionally, chapter 5.3 demonstrates that the transition between both tunnel processes is directly detectable in InAs.

5.2. I(V)-spectroscopy of Mn in InAs

In Fig. 5.3 the setpoint topography of a spatially resolved I(V)-spectroscopy is presented. The setpoint bias and current are chosen such that the acceptors have nearly no impact on the topography. Artifacts in the I(V)-signal that could arise from strong height modulations of the STM tip are minimal. Nevertheless, the STM measures a surface state of the InAs (110) surface which causes periodic height modulations of the tip. The tip was shifted towards the sample for small bias to increase the signal to noise ratio (z-shift of 1.3 Å/V). The I(V)-curves are numerically normalized to constant tip height throughout the measurement in the manner described in section 1.4. The normalized data is used to calculate the dI/dV -curves and dI/dV -maps presented in Fig. 5.4 and Fig. 5.5.

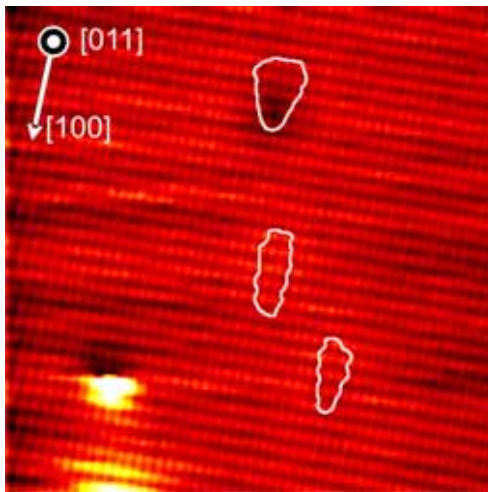


Fig. 5.3 (16 x 16) nm² setpoint topography of the spatially resolved I(V)-spectroscopy. The topographic setpoint is at 1.9 V bias and 0.3 nA tunnel current. The acceptors are indicated by current contour lines extracted from the I(V)-signal at -1.0 V. The upper acceptor exhibits a faint circular depression, but the other two have no measurable impact on the topography.

Two representative differential conductivity curves (dI/dV -curves) are plotted in Fig. 5.4. One is recorded above the undisturbed surface a few nanometers away from the acceptors (blue curve). The other one is recorded above the lower

acceptor of Fig. 5.3 (red curve). Both curves are plotted in logarithmic scale against sample bias. The undisturbed surface shows the onset of tunneling into the filled states (negative sample bias) at -208 mV. The onset of tunneling into empty states is observed at +385 mV. Due to the sample's low doping concentration ($2 \cdot 10^{17} \text{ cm}^{-3}$) the band bending induces very large space charge layers. Therefore the onset of tunneling out of the filled states in the valence band does not start directly at 0 V as it would be expected of a p-doped sample. The sample bias has to be decreased by about 200 mV until the tunnel current becomes large enough ($\sim 200 \text{ fA}$). At this bias tunneling out of the valence band and out of the conduction band is possible. The TIBB becomes larger than the band gap energy at -0.21 V sample bias.

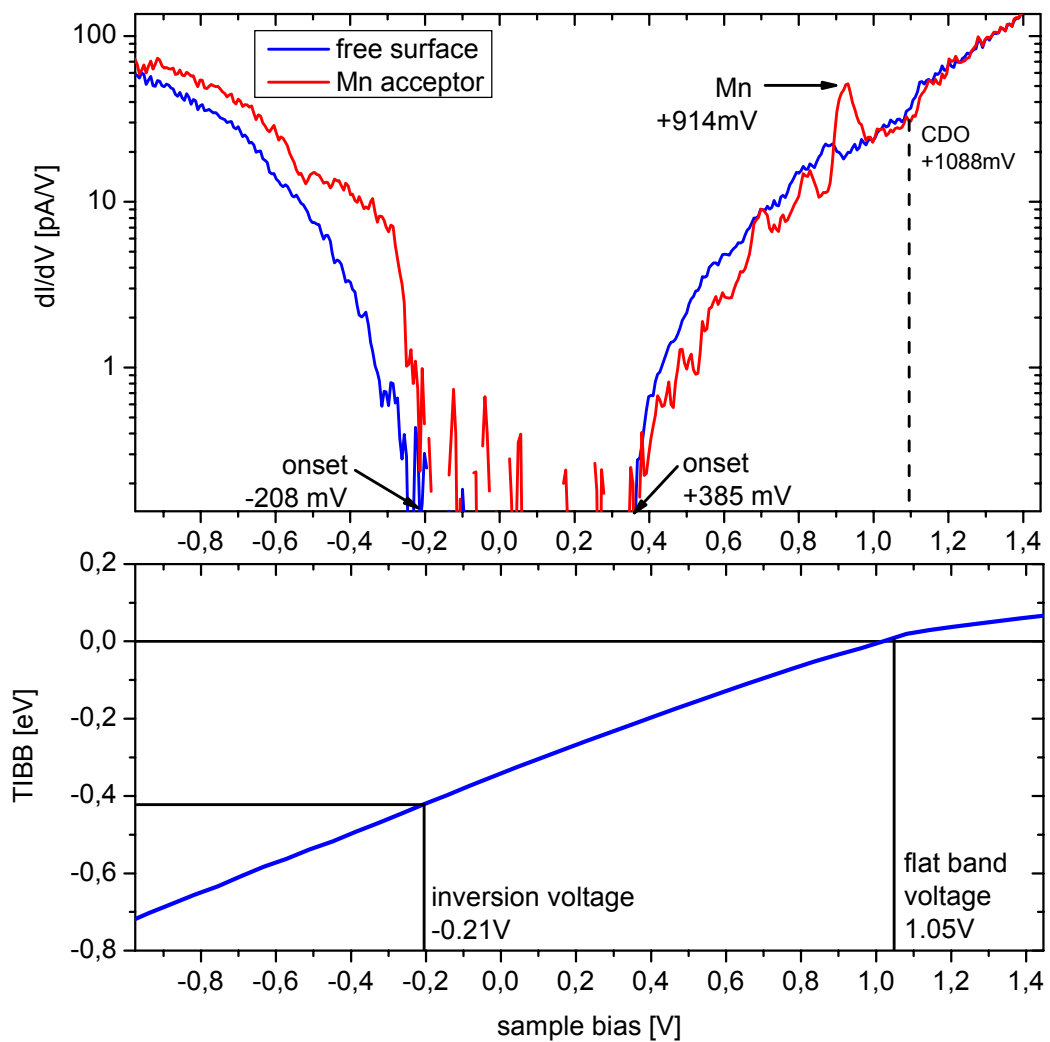


Fig. 5.4 (top) dI/dV curves on Mn doped InAs. The blue curve corresponds to the undisturbed surface and the red one was recorded directly above the lower acceptor (see Fig. 5.3). (bottom) TIBB(V) curve for the $I(V)$ -spectroscopy. The TIBB is calculated using the experimentally obtained tip work function value (4.25 eV). A tip with 15 nm apex radius, 90° shank slope and a vacuum gap of 8 Å. The characteristic bias voltages, inversion limit and flat band bias are marked.

The conduction band is pulled under the Fermi energy and an inversion layer may contribute to the total tunnel current. However, the inversion layer related tunnel current seems to be negligible. In the corresponding dI/dV -maps only valence band related surface states are observed (see Fig. 5.5a and b). This is reasonable, because the inversion layer is separated from the bulk sample by a depletion layer of more than 50nm width. The rate at which electrons are transferred from the bulk sample into the inversion layer will be low. Furthermore, the DOS in the valence band is much higher than in the conduction band. The total tunnel current is dominated by valence band tunneling. For positive bias the band gap has to be overcome to enable tunneling. The free surface shows nearly no structure in the dI/dV -curve, only a smooth slope is imaged except for one step at +1088 mV. The same step is present in the dI/dV -curve of the acceptor atom. The spatial distribution of the additional conductivity is clearly seen in Fig. 5.5g and Fig. 5.5h. Starting at 1088 mV a delocalized conductivity is observed across the whole surface that evolves into broad waves that travel from the lower left to the upper right corner. In Fig. 5.5g at 1111 mV the wavelength is larger than the image size. At 1124 mV in Fig. 5.5h the wave maximum traveled a few nanometers to the upper right corner and the wave length is approximately 20nm. The additional conductivity is attributed to the onset of charge density oscillations in the accumulation layer at the valence band. From the onset at 1088 mV on the accumulation becomes larger with increasing bias voltage. Thus, the wavelength of the CDOs becomes smaller. The work function derived from the apparent barrier height measurement of this spectroscopy is 4.25 eV. According to this value flat band condition is reached at ~ 1050 mV. The onset of CDOs at about 1100 mV confirms this result. The CDOs fade below the noise level for bias voltages exceeding 1580 mV (Fig. 5.5i).

The dI/dV -curve of the acceptor strongly deviates from the one of the free surface until the onset of the CDOs. For tunneling of filled states the conductivity above the acceptor is larger than on the free surface (negative bias). For positive bias the conductivity above the acceptor is smaller than on the free surface. This holds for bias smaller than +914 mV. A strong peak is observed in the dI/dV -map centered at +914 mV. The dI/dV -curves of the free surface and the acceptor match for bias voltage above this peak. This is the first indication that the acceptor charge state changes when this peak is crossed. According to the energy scale diagram (refer to Fig. 5.2) the acceptor state crosses the Fermi energy at about 0.9 V. For lower bias the acceptor exhibits a negative charge that electrostatically influences the LDOS of the sample. The band edges are shifted upwards. For negative bias this causes enhanced conductivity with respect to the free surface because the upwards bending of the acceptor counteracts the downwards bending of the TIBB. The depletion layer is smaller and tunneling is more probable. A dI/dV -map recorded at large negative bias (e.g. -838 mV) shows the nearly circular symmetric influence of the acceptor (Fig. 5.5a). For tunneling into the empty states the situation is just the other way around. Tunneling occurs into the conduction band. Above the acceptor the conduction band is shifted upwards which decreases the amount of available states. For bias above 0.9 V the

acceptor is neutral and the shift disappears. The conduction band tunneling starts at +385 mV, so well below the bias threshold where the acceptor crosses the Fermi energy it can be used as a probe for the charge state of the acceptor (refer to chapter 5.3).

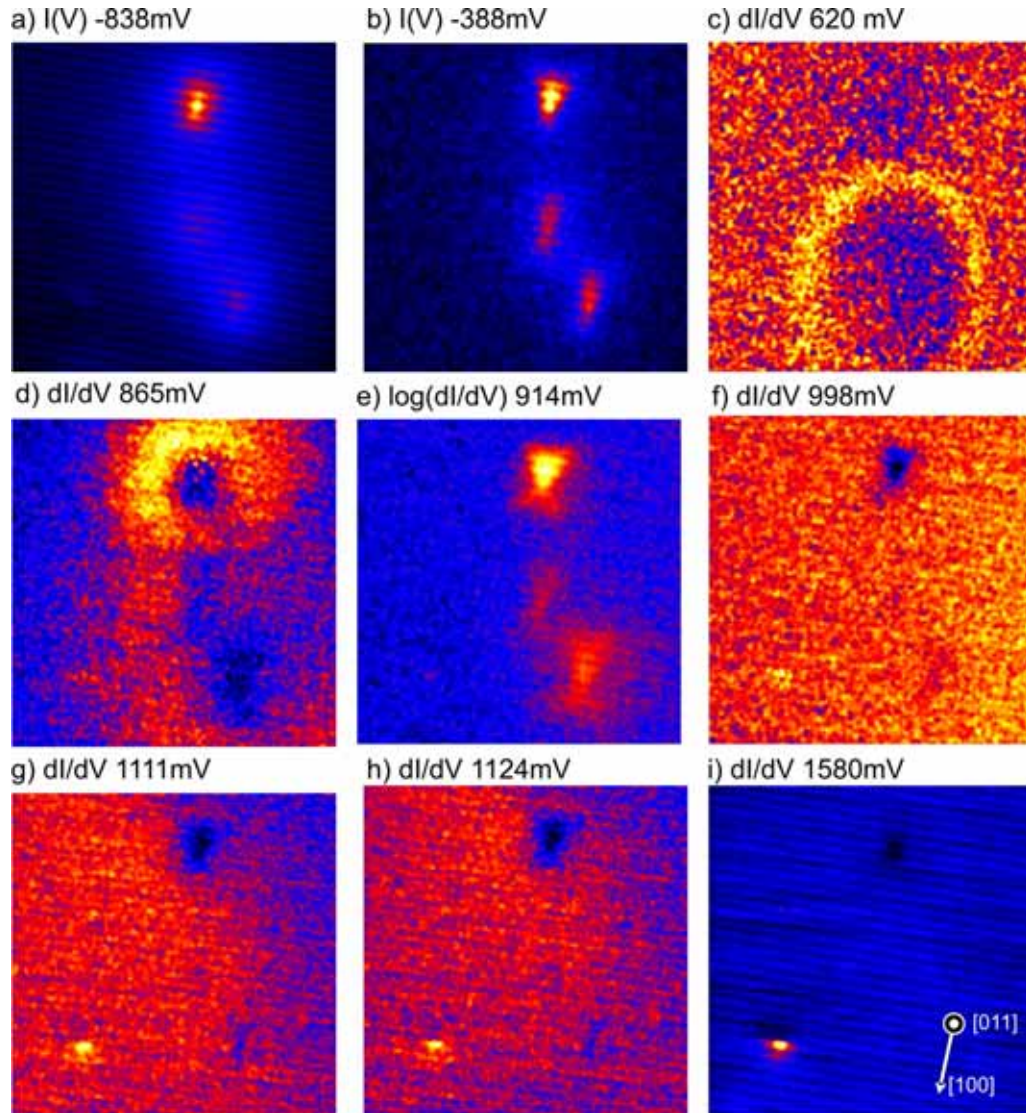


Fig. 5.5 dI/dV maps (15×15) nm² of the same spectroscopy as in Fig. 5.4. (a) nearly circular contrasts for large negative bias. (b) anisotropic resonance at moderate negative bias. (c) ring-like features for moderate positive bias. This is the charging signature of a deeply buried Mn. (d) ring-like feature around the three Mn acceptors closest to the surface – these are the charging signatures of the three Mn acceptors. (e) anisotropic features at 900mV directly after the charging signature is observed. (f) reduced conductivity at ~1 V. (g) onset of CDO on the whole surface. The charge density wave is coming in from the lower left corner and has a wavelength of approximately the whole image. The CDO evolves in (h) and becomes shorter in wavelength (i) only uncharacteristic current into the bands.

The dI/dV -map evaluated at the peak position (+914 mV) shows three anisotropic contrasts one above each acceptor (see Fig. 5.5e). The next two sections will show that for this bias voltage the acceptor state is imaged. For negative bias near the onset bias of (-208 mV) anisotropic contrasts are observed, as well.

5.3. Charging signature of the acceptor

The TIBB which is responsible for the bias dependent charging has to be treated three dimensional as mentioned in chapter 2. Therefore the value of the tip induced band bending at the position of the acceptor depends not only on the applied bias voltage but also on the lateral distance to the tip. On p-InAs the bias dependent charging is directly visible in the dI/dV -maps as a ring of enhanced conductivity closing around the acceptor's position (see Fig. 5.6).

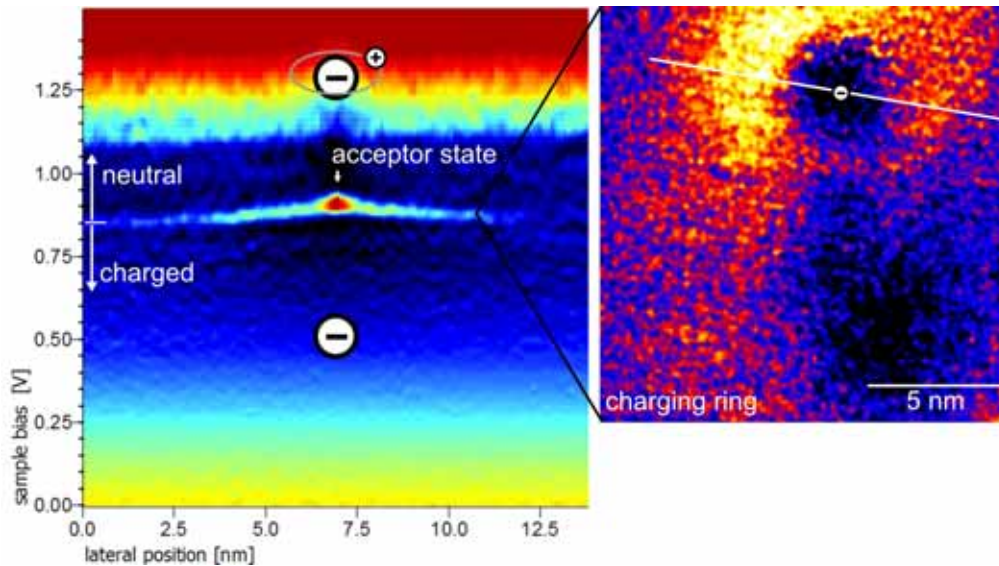


Fig. 5.6 (left) dI/dV -section through a Mn acceptor in InAs. The acceptor state is visible as a red dot at 0.9 V sample bias. Coming from lower bias voltage a charging ring closes around the acceptor position. (right) $(15 \times 15) \text{ nm}^2$ dI/dV -map evaluated at 854 mV shows the bright ring closing around the indicated acceptor position. A section through the dI/dV -map results in the flat parabola which is visible in the left dI/dV -section. It is opened to the negative voltage side and visible at 0.8 V to 0.9 V sample bias. When the bias crosses this parabola the acceptor state is pulled over the Fermi energy by the TIBB.

According to the energy scale diagram (see Fig. 5.2) the acceptor state becomes charged at +0.9 V. InAs has a band gap of only 418 meV at low temperature. Before the acceptor state becomes visible, tunneling into the conduction band is possible. The phenomenon that leads to the observation of a “charging ring” in the dI/dV signal is sketched in Fig. 5.7. The $I(V)$ -spectroscopy presented in Fig. 5.6 has the flat band condition at 1.05 V (see section 5.2). At 0 V sample bias the TIBB starts with a negative value, i.e. downwards bending of the bands. The amount of band bending becomes smaller with increasing volt-

age. When the tip induced space charge layer is large, it pulls the acceptor state under the Fermi energy even if the tip is positioned a few nanometers away from the dopant atom (see Fig. 5.7a). Then; the acceptor exhibits a Coulomb potential that is still present at the tip's position. For a distance of a few nanometers from the dopant core ΔV is still 10-20 meV. The local potential under the tip is the sum of all potentials. The shift induced by the acceptor directly influences the bias window available for tunneling. From 0.42 V sample bias on a small amount of tunnel current flows into the conduction band and acts as a probe for this shift. In the $I(V)$ -spectroscopy the tip is kept at the same position and the bias voltage is ramped up. At a certain bias the tip induced field becomes too small at the acceptor's position to keep the dopant charged (Fig. 5.7b). The acceptor state crosses the Fermi energy and becomes neutral. The dopant core's Coulomb potential is screened by the bound hole and no longer influences the LDOS at the tip position. The electrostatic shift ΔV jumps to 0 and the bias window available for tunneling changes. A jump is observed for the tunnel current into the conduction band.

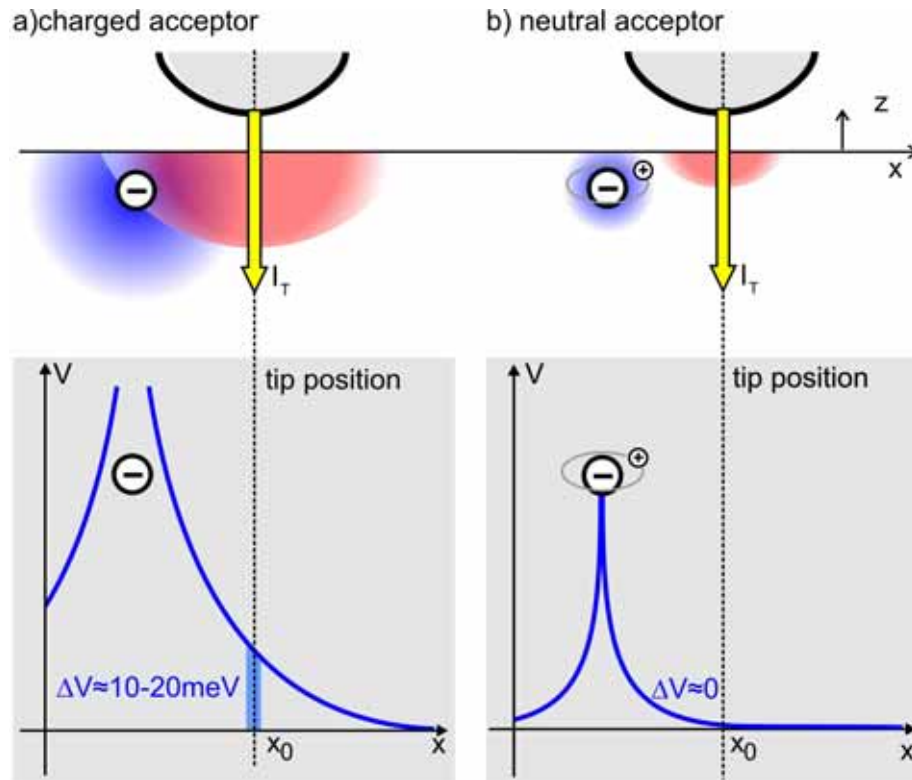


Fig. 5.7 Schematic for the creation of a charging ring, at an acceptor. (a) When the tip induced space charge layer (red) is large, the acceptor state is under the Fermi energy even if the tip is positioned a few nanometers away from the dopant atom (upper part). The acceptor is charged and exhibits a Coulomb potential (blue curve) that is still present at the tip's position. The additional electrostatic potential under the tip is ΔV . (b) When the tip induced field is small at the acceptor's position, the acceptor state becomes neutral. Then the dopant core's Coulomb potential is screened (blue curve) and the additional potential at the tip ΔV is zero.

The same situation holds for donors in n-doped GaAs. The donor becomes positively charged for a certain positive bias voltage when tunneling into the conduction band is already active. For the case of donors these charging rings are much more prominent and a detailed analysis is possible. The charging phenomena on n-doped samples are discussed in detail by K. Teichmann [69].

In the dI/dV -section of Fig. 5.6 the jump is clearly seen as a very flat parabola that is opened to the negative bias side. The jump is seen as a ring in the dI/dV -map. The ring is caused by the fact that the jump occurs for a specific TIBB value at the position of the dopant. The local TIBB is dependent on the distance from the tip and the applied bias voltage. For every distance there is one specific bias to reach the threshold. The parabola indicates the transition from the charged to the neutral acceptor.

5.4. Contrasts of charged and neutral acceptors

The previous chapter demonstrated that it is possible to identify the charge state of a Mn acceptor in InAs. Fig. 5.8 shows a sequence of dI/dV -maps. One is acquired at lower bias than the threshold of 0.9 V, one at the threshold and one above the threshold. Three subsurface acceptors are imaged in the dI/dV -maps. At 715 mV all three are charged and exhibit an unscreened Coulomb potential. Above the center acceptor a faint conductivity peak is observed. This conductivity is of distinct triangular shape. At 865 mV the charging rings around all three acceptors are imaged. These rings close around the three acceptors with further increasing bias. At 914 mV all rings are closed, the acceptors are neutral. The bow-tie like contrasts are observed in this dI/dV -map. The anisotropic contrasts observed for the charged and neutral acceptor do not match. The enhanced conductivity above the center acceptor is more extended to the bottom of the image than the triangular contrast at 715 mV is. The triangular contrast is shifted to one side of the dopant atom for the charged acceptor. The contrast imaged at the neutral acceptor is more symmetric along $[001]$. For the other two acceptors only the anisotropic contrasts at the neutral acceptor are observed. No conductivity is detected for the charged state.

At +914 mV the neutral acceptor is imaged. The tunnel current is injected into the acceptor state and drained into the bulk of the crystal as depicted in Fig. 5.9b. When the acceptor is directly at the Fermi energy the drain process is most efficient. With increasing bias the acceptor state is pulled up above the Fermi energy. The drain process becomes less probable. This might lead to the observation of decreased differential conductivity in the dI/dV -map at 998 mV (see Fig. 5.5f). Within this model the anisotropic distribution of the differential conductivity for this state reflects the spatial anisotropy of the Mn acceptor's wave function. A study on highly doped InAs also observed these anisotropic contrasts, but no triangular contrasts were resolved [103].

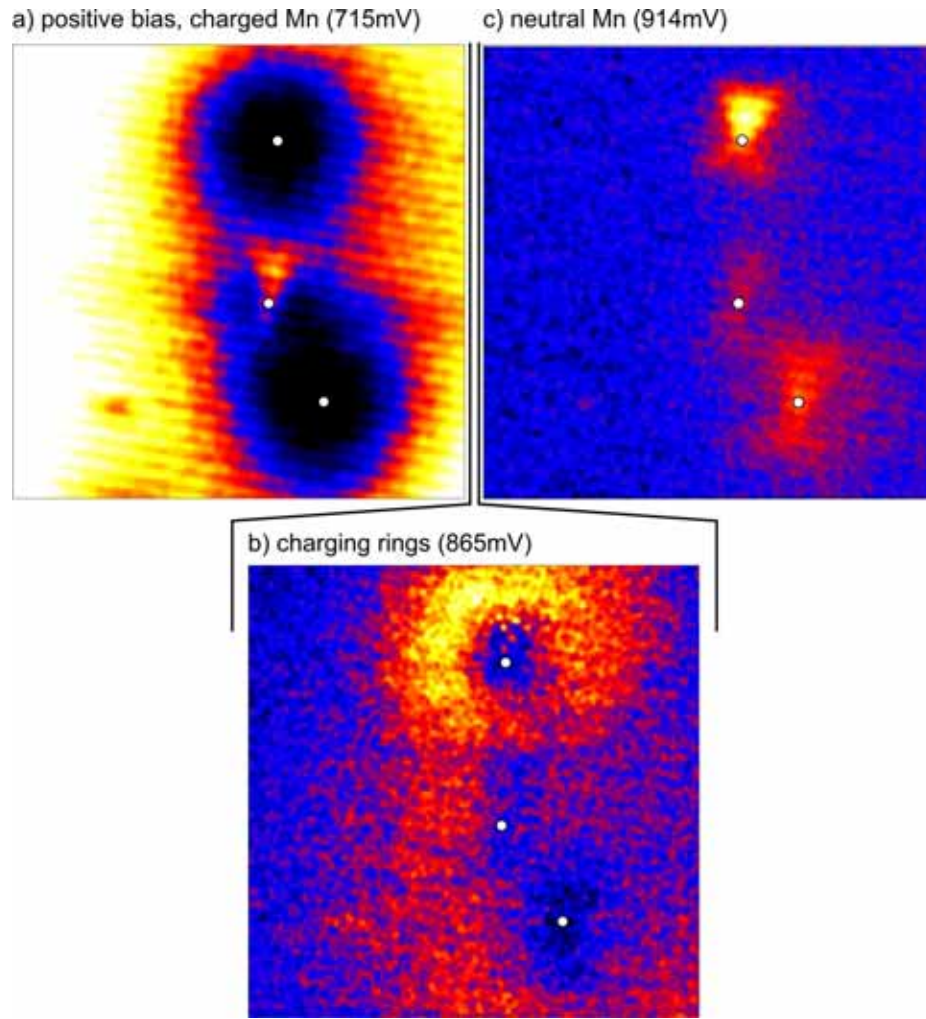


Fig. 5.8 (15 x 15) nm² spatially resolved I(V)-spectroscopy above three subsurface Mn acceptors. The Mn atoms are indicated by white circles in the conductivity maps. (a) at 715mV bias the acceptors are charged. Above the middle acceptor a triangular contrast is visible. (b) at 865mV bias three charging rings close around the three acceptors. Inside the respective circle the acceptor is charged and outside it is neutral. (c) Directly when the charging rings close, the cross-like anisotropic contrasts appear above all three acceptors. This image corresponds to the neutral state of the acceptors.

For a similar configuration the Mn acceptor state has been investigated in GaAs. A similar anisotropic bow-tie like feature was found in the dI/dV-signal [104]. The triangular contrast imaged at 715 mV (see Fig. 5.8a) cannot be due to tunneling into the acceptor state. The bias is well below the point, where the charging of the respective acceptor is observed. The band alignment for this situation is depicted in Fig. 5.9a. The acceptor state is below the Fermi energy. Therefore the state is occupied and the electron in this state cannot be drained into the bulk. Another tunneling process must be involved, that gives additional conductivity at this configuration. The Mn acceptor related contrast at +715 mV is similar to the triangular shaped contrasts seen at shallow acceptors in GaAs (compare with Fig. 4.4).

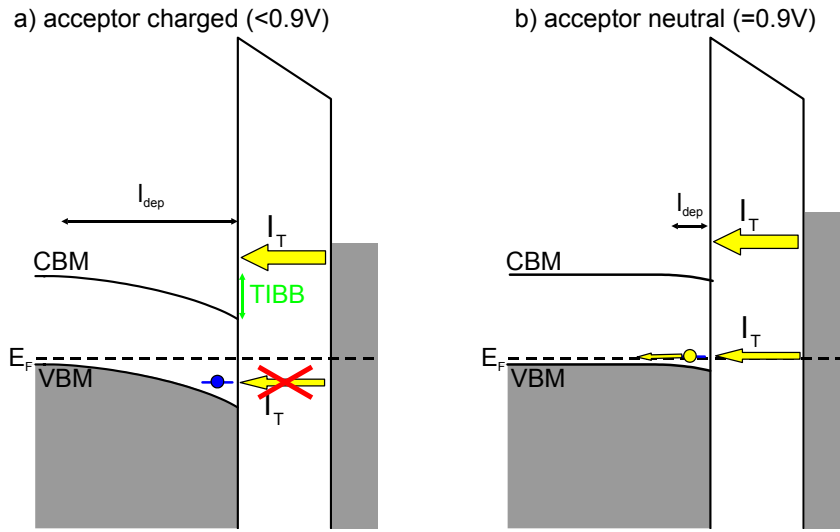


Fig. 5.9 Rigid band model of the band alignment for the dI/dV -maps presented in Fig. 5.8. Tunnel channels I_T are indicated by yellow arrows. (a) At bias smaller than 0.9 V the acceptor is charged and below the Fermi energy. No tunneling can occur directly into the acceptor state. (b) At ≥ 0.9 V bias the acceptor state is above the Fermi energy. The state is empty. Tunnel current into the acceptor state is possible. Note that the injected electrons have to be drained into the bulk semiconductor.

5.5. Summary

The bias dependent configuration of the acceptor state at the surface is deduced on the basis of TIBB calculations that are adjusted to individual $I(V)$ -spectroscopies. The resulting energy scale diagrams determine the bias windows in which the acceptor state is directly accessible for tunneling and those intervals in which it does not contribute to the tunnel current directly. P-doped InAs allows studying both acceptor configurations. The bow-tie like contrasts are an image of the spatial distribution of the acceptor state. A faint triangular feature is visible in the bias interval when the acceptor is charged and the acceptor state is not accessible. The observation of triangular and bow-tie contrast on the same acceptor demonstrates that the difference between both contrast types is caused by different imaging mechanisms.

6. Wave function imaging of buried acceptors

This chapter makes theoretical predictions for the acceptor state and analyses measurements of acceptors located in different depths under the surface. Images of deeply buried Mn acceptors closely resemble theoretical predictions for bulk geometry. Uniaxial strain and an electric field at the surface are capable of producing the observed symmetry reduction for acceptors close to the surface.

One result of the previous chapter is that at 0.9 V sample bias the acceptor state of Mn in InAs is accessible for tunneling. Within the Tersoff-Hamann approach (see chapter 1.5), the tunnel current is proportional to a sum of probability densities of all sample states available for tunneling (This discussion considers only the empty sample states, because the acceptor related state is imaged at positive sample bias.). Thus, constant current topographies recorded at 0.9V will contain information that reflects the spatial distribution of states, but it will be superimposed by additional tunnel current into all other available states. The possible states for InAs are the bulk conduction band states and the empty states' surface resonances which energetically overlap with the conduction band. These states show modulation based on the periodicity of the surface lattice. At the acceptor an additional state is present. The acceptor introduces a negative charge and a positively charged hole into the semiconductor. A hydrogen atom like state forms which is a hybrid of the valence band states. The Bohr radius of the acceptor ground state is about 3nm [5]. According to the above discussion it is this state which is imaged at 0.9 V bias in the I(V)-spectroscopy.

Tight binding calculations have been used to describe the acceptor state in the bulk crystal [104, 115]. Usually the semiconductor surface is not included into the calculation because the necessary slab would exceed today's computing capabilities. The probability density of a subsurface acceptor that is accessed by the STM is extracted from the bulk calculation by simply cutting the calculated 3D probability density at a certain distance from the acceptor atom. The vacuum decay is then artificially added to the resulting 3D section. It is worth noting that the acceptor state will be affected by the surface. An acceptor in the vicinity of the surface will differ in its electronic properties like binding energy and spatial extension of the wave function. These effects are not accounted for, if a bulk acceptor is calculated.

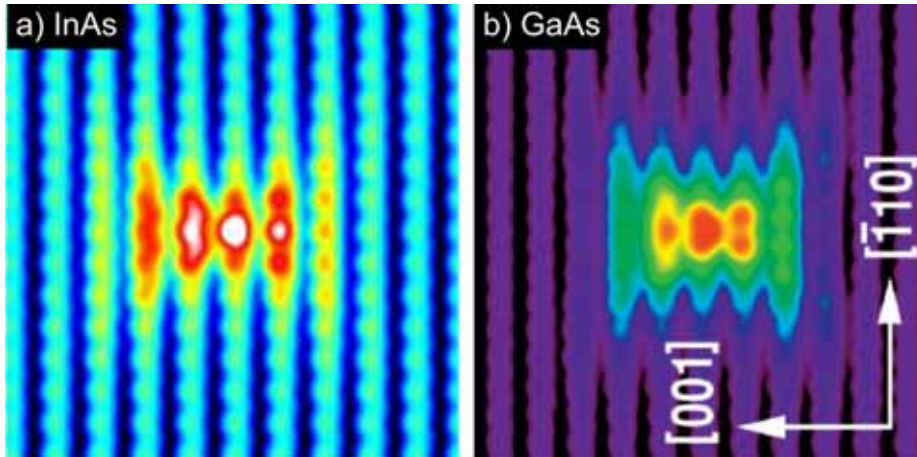


Fig. 6.1 Tight binding calculation of a Mn acceptor in (a) bulk InAs and (b) bulk GaAs. The images show the LDOS on the (110) section in a distance from the dopant atom corresponding to a depth of (a) six layers / (b) four layers. Image (a) is reproduced from [116], and image (b) is taken from [115].

Fig. 6.1 shows the 2D sections of Mn acceptor states in InAs [116] and GaAs [115]. The sections are parallel to (110) . For InAs it is cut at a distance of about 13 Å from the acceptor atom. This is the simulated contrast of an acceptor in the sixth subsurface layer. The contrast has a bow-tie like shape and is mirror symmetric to the $[\bar{1}10]$ direction and nearly mirror symmetric over the $[001]$ direction, which is the consequence of the cubic band structure symmetry (c_{2v}). The acceptor is not perfectly symmetric along $[001]$, but the asymmetry is very low. It has been theoretically predicted that the asymmetry is slightly dependent on the orientation of the Mn spin relative to the host crystal [115]. The Mn acceptor state in GaAs has a similar appearance, because the underlying band structure is of the same symmetry as InAs. Fig. 6.1b shows the tight-binding image of a Mn acceptor in the fourth subsurface layer of GaAs [104, 115, 117].

6.1. Depth dependent shape of the acceptor state

The acceptor state may be investigated by means of spatially resolved $I(V)$ -spectroscopy as presented previously. Another approach is the use of Multibias topographies. Here, a certain region of the sample is scanned in constant current mode quasi-simultaneously with different bias voltages. The different topographies are recorded in an interlaced mode. Each line is scanned repeatedly with different voltages before the STM moves to the next line. Piezo drift and hysteresis effects act equally on all topographies, so that positions in the images become quantitatively comparable. A multibias series of the Mn doped InAs is presented in Fig. 6.2. The (207×207) nm² area is scanned with atomic resolution.

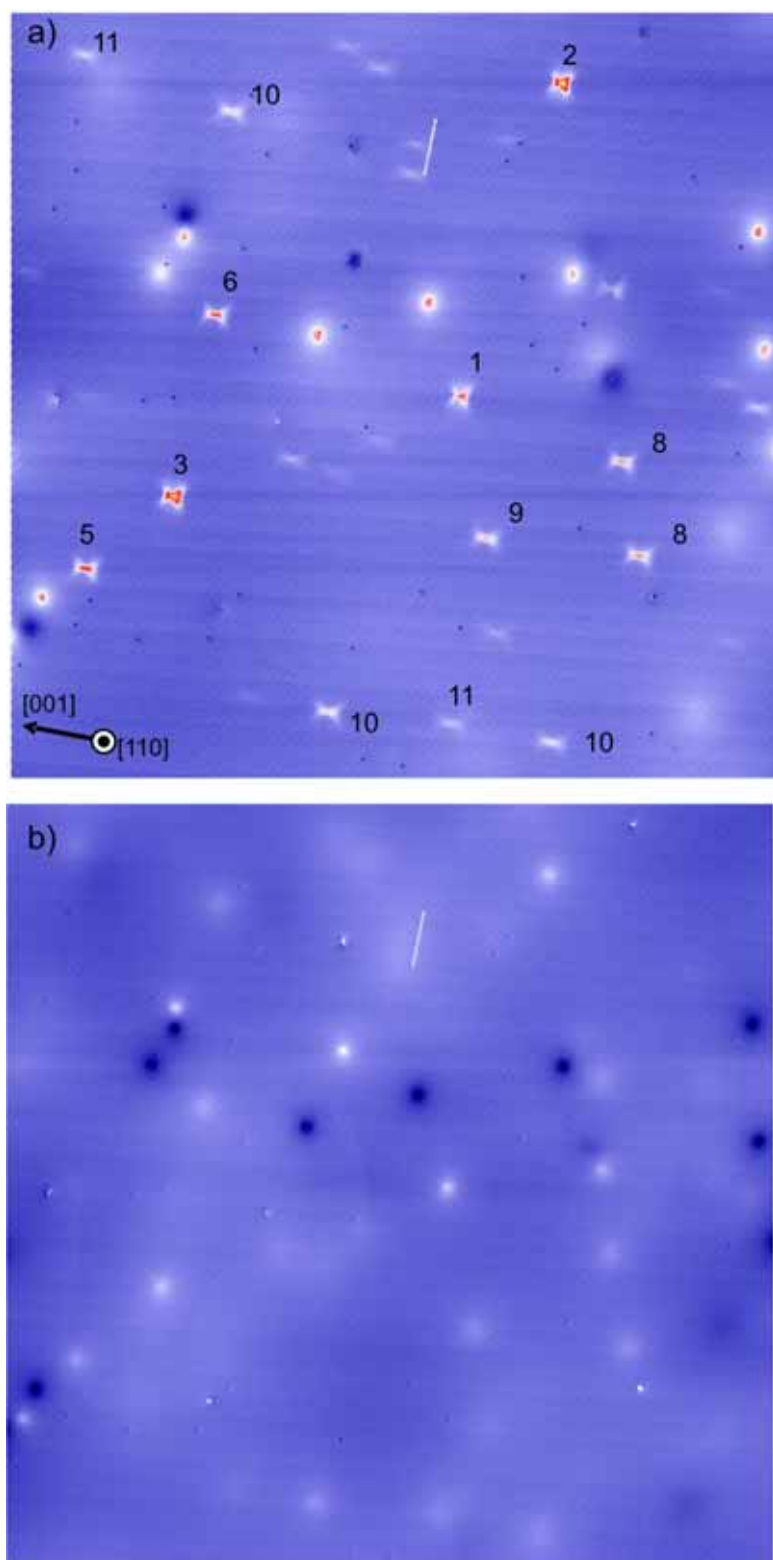


Fig. 6.2 (207 x 207)nm² multibias topography of InAs doped with Mn $2 \cdot 10^{17}$ cm⁻³. The image is recorded with atomic resolution. Zooms to separate acceptors are presented in Fig. 6.3. (a) In a very narrow bias interval around 1.0 V sample bias, the anisotropic contrasts of the Mn acceptors are visible in constant current topographies. The Mn acceptors appear as bow-tie like highly anisotropic protrusions. The contrasts of Mn acceptors down to at least 14 monolayers depth are imaged. The depths of dopant atoms down to the 11th subsurface layer is indicated with numbers in the image. (b) in the filled states image, at -1.0 V, the acceptors appear as extended circular protrusions.

The biases are chosen such that the acceptor state is imaged in one topography while the acceptor core position is determined in the other. The first topography is recorded at -1.0 V, in which the acceptors appear as circular symmetric protrusions. The filled states image recorded at -1.0 V is dominated by the valence band states. The circular protrusion reflects the electrostatic influence of the negative acceptor charge on the bands. In an about 10nm wide region around the dopant core, the valence band is bent upwards by the acceptor Coulomb potential. Due to this additional bending more valence band states become available, the tunnel current increases and a protrusion is imaged [11]. The center of mass of this contrast indicates the position of the acceptor core under the surface, because the electrostatic interaction is circular symmetric. The absolute positions of both topographies match to an accuracy better than the surface lattice constant. Thus, the acceptor positions determined in the filled states image are transferred to the empty states image (+1.0 V). The empty states topography is recorded at +1.0 V, slightly above the acceptor state. The acceptor state has its conductivity peak at +914 mV. The image shows the anisotropic contrasts of 29 subsurface Mn acceptors. Some other types of defects are visible in the images. For example vacancies appear as a small dip only 1-2 Å in diameter [118]. Positively charged defects appear as broad protrusions in the empty states image and as depressions in the filled states image.

The depth of each acceptor is determined as follows: all visible acceptors are ordered to increasing depth under the assumption that the circular protrusion in the filled states image is strongest for the acceptor nearest to the surface and becomes fainter for deeper acceptors. Of course it is a priori not certain that there are acceptors in every monolayer within the scanned area. An additional check is that the center of the acceptor contrasts has to follow a certain ordering with respect to the host lattice [21, 107]. Mn is a substitutional acceptor on the Ga site. At +1.0 V the dominant surface state is C3. It has its corrugation maxima on the Ga sites of the topmost zig-zag row. Therefore an acceptor atom in the first monolayer is positioned directly on the corrugation maximum. If the acceptor is positioned in the second monolayer, the acceptor atom is located between the C3 corrugation maxima. For the third layer it is again on the corrugation maximum, etc.. The acceptor core positions can be determined for acceptors down to the 10th monolayer under the surface. There are even deeper lying acceptors visible, but their exact position cannot be determined any more because of the vanishing feature height. At least 4-5 additional depths are visible. This demonstrates that the STM resolves acceptors lying up to 3nm under the surface!

Fig. 6.3 puts together the images of the different subsurface acceptors. Each image has the same size and the acceptor atom is directly in the middle of each image. All images are cut out of the large multibias topography of Fig. 6.2. No tip modification occurred during the acquisition of the whole image. The relative heights of all acceptor contrasts are quantitatively comparable. The positions of the white circles indicate the acceptor core position under the surface.

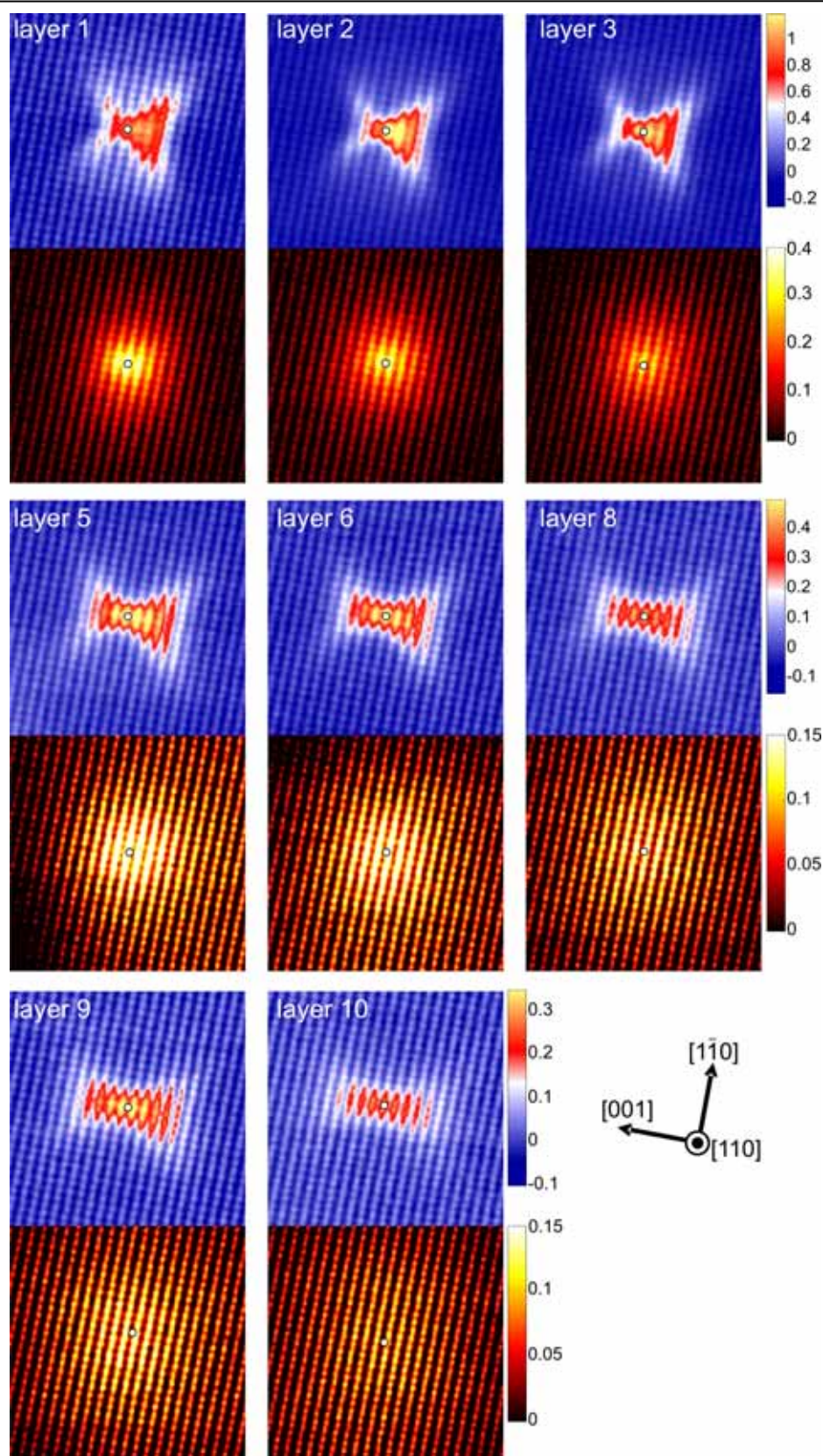


Fig. 6.3 (13 x 13)nm² zooms into the multibias topographies of Fig. 6.2. The white circles indicate the location of the dopant core under the surface. The blue – red colored image is recorded at +1.0V and the black – yellow images are acquired at -1.0V. The images of one row have the same color scaling. The height is indicated by the color bar in Å.

The round contrast for each acceptor is the -1.0 V topography. With increasing depth the circular symmetric contrasts become fainter. The anisotropic contrasts have the same behavior. Only the one in the surface layer (1st layer) does not follow this trend.

In addition, the contrast shape changes drastically. The acceptors in the first and second layer have a nearly triangular shape. The main part of the contrast is shifted to the $[00\bar{T}]$ side of the acceptor atom, whereas the acceptors in large depths appear nearly symmetric with respect to $[001]$. For the acceptor in the third layer, the $[001]$ side develops more weight in the image. Unfortunately, no acceptor in the 4th layer was measured. For the 5th layer acceptor the anisotropy is still visible, but the rectangular shape of the contrast is already noticeable. This behavior carries on until the acceptor shape is nearly perfectly symmetric along $[001]$ for the acceptors in the 10th layer. They have equal weight on both sides of the dopant atom.

A gradual shift from nearly triangular to nearly rectangular shape is observed for the image sequence. The degree of asymmetry with respect to the $[001]$ direction is evaluated in Fig. 6.4. The topography of each acceptor is divided into a symmetric and an asymmetric part. The symmetric part $z_s(x,y)$ is evaluated with respect to a (001) mirror plane that cuts through the acceptor atom. The symmetric part is subtracted from the topography, which results in an image of the asymmetric part $z_a(x,y)$. The atomic corrugation of the surface states is suppressed in the images by FFT filtering to minimize the background signal. The degree of asymmetry of each acceptor contrast is described by the relative weight of the derived symmetric and asymmetric part. The quotient η is a quotient of the integrals of symmetric and asymmetric images and serves as this weight.

$$\eta = \frac{\int z_a(x, y) ds}{\int z_a(x, y) ds + \int z_s(x, y) ds}$$

This analysis is applied to all acceptors from the 1st to 10th subsurface layer. It prominently shows that a significant asymmetry exists for the acceptor near the surface. The 2nd layer acceptor is presented in the left column of Fig. 6.4. The image of the symmetric part has a cross-like shape and the lateral extension of the symmetric part is smaller than the contrast extension in the topography. The asymmetric part exhibits a trapezoidal or triangular shape that is completely shifted to the $[00\bar{T}]$ side of the acceptor atom. The asymmetric part extends further away from the acceptor core than the symmetric part. No asymmetric image components exist on the $[001]$ side of the acceptor. This demonstrates that the Mn contrast is more pronounced on one side *and* extends further into the $[00\bar{T}]$ direction than it does into the other.

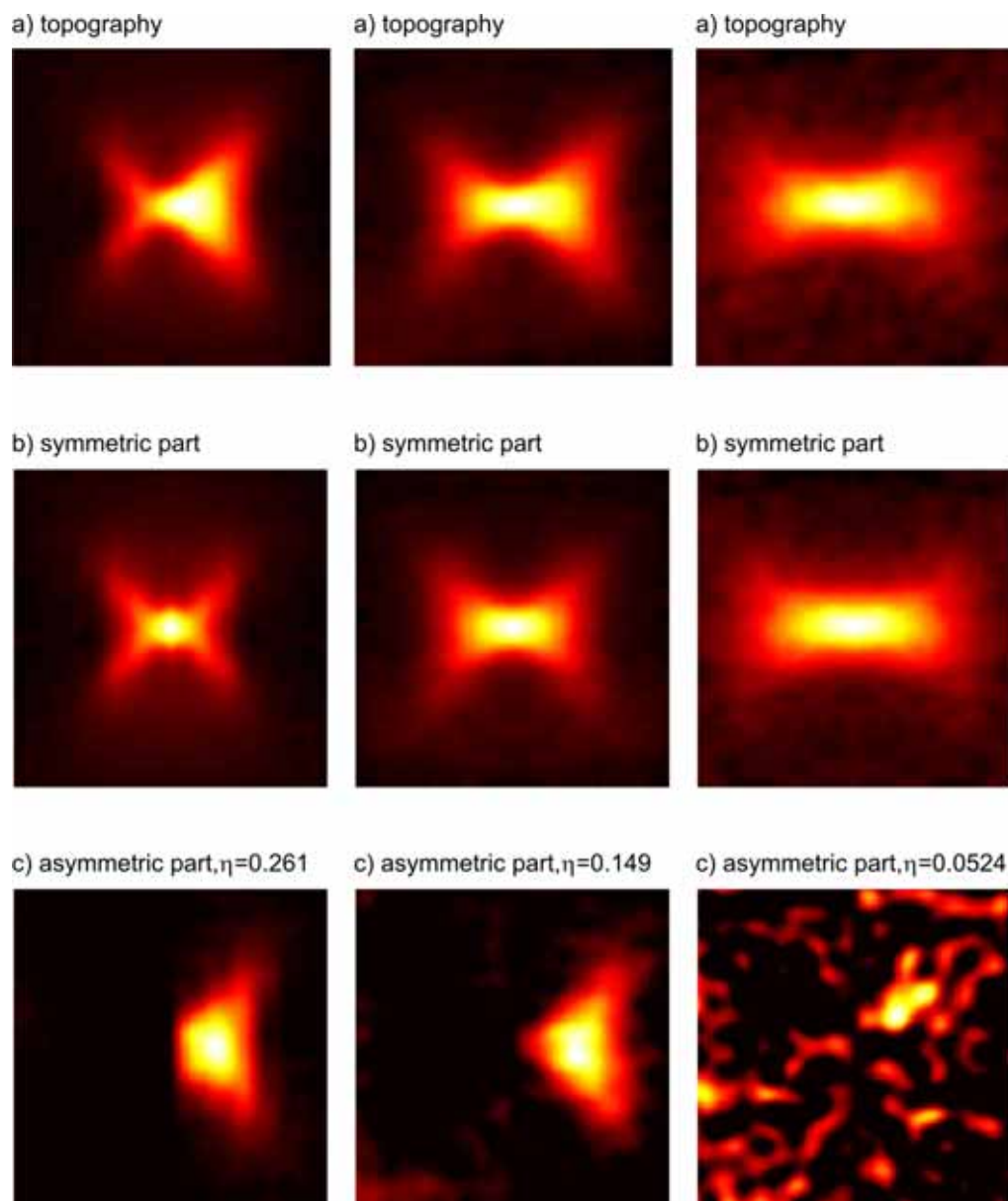
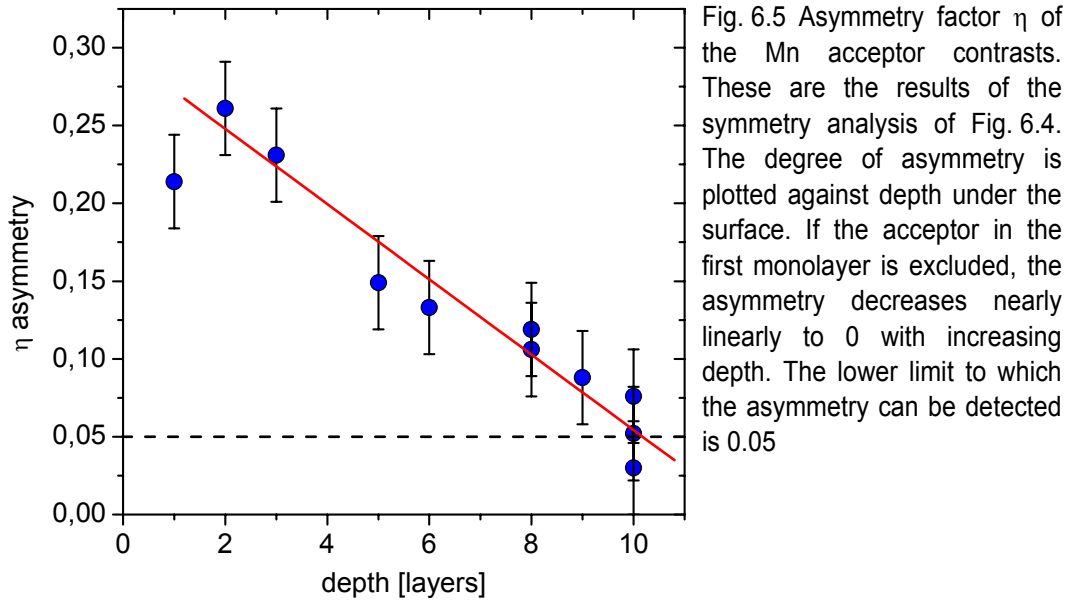


Fig. 6.4 Symmetry analysis of three Mn acceptors in InAs. a) topography. The atomic corrugation is suppressed by FFT filtering. (b) symmetric part of the image. The mirror axis (100) is centered directly at the acceptor atom position. (c) The asymmetric part of the image. The sum of (b) and (c) gives (a). The left column is the analysis for the 2nd layer acceptor, the middle column for the 5th layer acceptor, and the right column is evaluated for a 10th layer acceptor.



For an acceptor far below the surface the contrast is nearly symmetric (a 10th layer acceptor is shown in the right column of Fig. 6.4). The image of the symmetric part and the topography look nearly identical. The image of the asymmetric part is a noisy image without pronounced structure. The determined asymmetry value is 0.05. Within the accuracy of the analysis this contrast is fully symmetric along the principal $[001]$ axis. Acceptors in intermediate depths show a behavior similar to that of the surface acceptor (a 5th layer acceptor is shown in the middle column of Fig. 6.4). The extension of the symmetric part is smaller than the topography. The triangular asymmetric part extends further away from the acceptor core and is broadened. But the degree of asymmetry is smaller than that of the surface acceptor. The relative weights of symmetric and asymmetric components differ. The ratio η gives the portion of the topography that is asymmetric. Fig. 6.5 plots the values for all acceptors of Fig. 6.2 against the acceptor depth.

The degree of asymmetry is as high as 27% for the acceptor in the 2nd layer. With increasing depth the asymmetry decreases nearly linearly. The slope of the linear fit gives a decrease of 0.024 per monolayer depth. Acceptors in the 10th subsurface layer under the surface are fully symmetric within the accuracy of the analysis mentioned above. The detection limit is indicated by the dashed line in the diagram. It was estimated by performing the same analysis with the mirror plane $(1\bar{1}0)$. The Mn acceptor is mirror symmetric with that plane, but because of residual noise the value η varies between 0 and 0.05 for this direction. The uncertainty of the symmetry analysis is lower than the measurement noise. It is $\Delta\eta = 0.03$. This is the variation of the value η caused by a variation in the exact position of the mirror plane with respect to the determined position of the acceptor core. If the linear fit is extrapolated to deeper acceptors, the 12th layer acceptor would be completely symmetric.

As a result acceptors buried below the 10th to 12th layer under the surface appear as rectangular contrasts that are mirror symmetric with respect to the $(1\bar{1}0)$ plane and the (001) plane. Acceptors located within the first 10 layers under the surface have an asymmetry over the (001) plane. The $[00\bar{1}]$ side of the acceptor contrast is more pronounced than the $[001]$ side.

It is worth noting that similar measurements of buried Mn acceptors in InAs have been performed in parallel and independently in the group of R. Wiesendanger [116]. They report of similar depth dependent behavior for samples with higher doping level. The asymmetric bow-tie shape is also observed for different doping systems, like Cd in GaP [110, 119]. As far as it is reported in literature they exhibit the same behavior as discussed above for Mn in InAs. In all these studies, the dopant represents a deep acceptor. As discussed with the energy scale diagrams in chapter 5 it is possible to observe the acceptor state for positive bias, i.e., in the empty states image. But the observation of the acceptor state is not restricted to deep acceptors. According to the energy scale diagram for shallow acceptors in GaAs (see chapter 5.1) the acceptor state participates in the tunnel process for negative bias of about -0.5 V. Then, the filled states are imaged to observe tunneling of electrons out of the occupied acceptor state. Fig. 6.6 shows a multibias topography of a carbon acceptor in the fifth subsurface layer. The dopant atom position is determined by the center of mass of the circular protrusion at large negative bias (Fig. 6.6.b) and the faint depression at high positive bias. At -0.5 V the anisotropic contrast is visible. The anisotropic contrast is of trapezoidal shape. Like the Mn acceptor state the C acceptor state is symmetric over the (110) mirror plane and asymmetric over (001) . This time, the contrast is shifted to $[001]$ because the $(1\bar{1}0)$ cleavage surface is investigated (refer to Fig. 4.6). The anisotropic shape of the acceptor is less prominent than in the empty states image. At negative bias additional tunnel channels out of the valence band contribute that have different symmetry and cover the anisotropic shape.

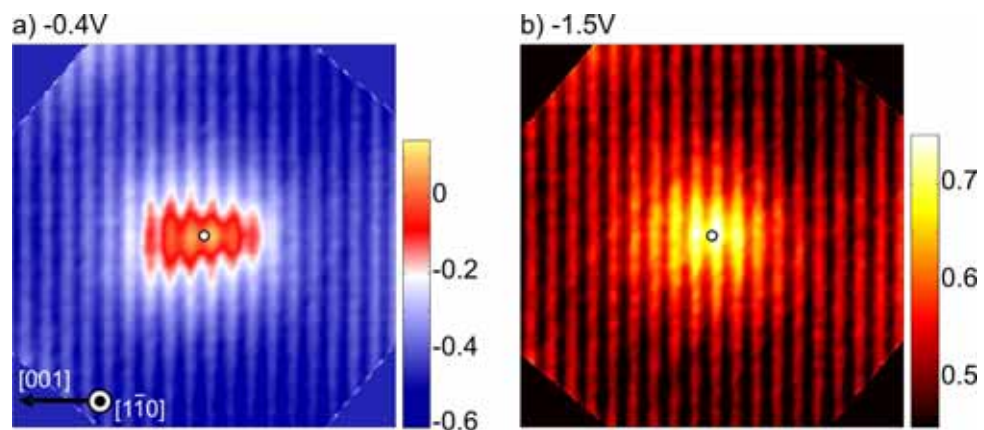


Fig. 6.6 (10 x 10) nm² multibias topographies of a carbon acceptor located in the fifth subsurface layer. (a) the anisotropic contrast at -0.5 V. (b) a circular protrusion at -1.5 V. The numbers at the color scale are in Å.

6.2. Band structure induced asymmetries

The previous section demonstrated that the wave function of deeply buried acceptors has a nearly rectangular shape. This fits well with the theoretical expectation for a bulk acceptor: The acceptor state is a hybrid of the highest valence band states. The energy window of the valence band needed to form the localized state approximately equals the binding energy of this state [120]. The Mn acceptor in InAs is 23 meV above the valence band maximum [114], so less than 10% of the Brillouin zone participates in the hybridization. The symmetry of the wave function is determined by the host crystal's band structure. If the band structure is symmetric along a certain direction, the wave function will be symmetric, as well. Anisotropies in the wave function can only develop when the band structure exhibits this asymmetry. Therefore this section focuses on the symmetry properties of the InAs bands. An explicit calculation of the wave function will not be given.

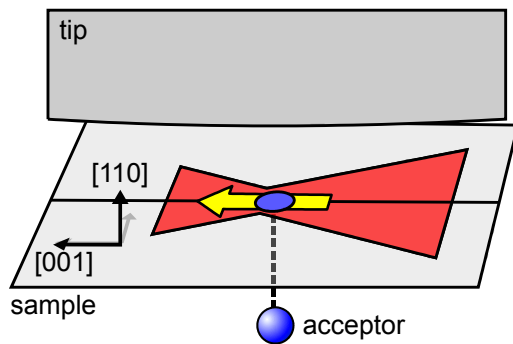


Fig. 6.7 Schematic of the anisotropic contrast of the acceptor wave function. The bow-tie like shape has more weight on one side

The bulk bands are to good approximation cubic in this range. In particular they are symmetric with respect to the $[001]$ direction. Effects that break this symmetry are known but usually considered to be small in the bulk semiconductor. The so-called k -linear terms cause a splitting of less than 1 meV at the valence band edge [121]. However, acceptors close to the surface exhibit a strong asymmetry along $[001]$ as depicted in Fig. 6.7. This asymmetry cannot be described with the bulk band structure. The surface induces a symmetry breaking that lifts the cubic symmetry along $[001]$ but preserves it perpendicular to $[001]$. There are two possible effects that can induce strong changes of the band structure: Local strain fields and strong electric fields. Both are present under the STM tip at the relaxed surface.

6.2.1. Strain at the $\{110\}$ surfaces

Strain has strong influence on the properties of the band structure and will certainly occur at the surface. Due to the cleavage, In (Ga) and As atoms at the surface are no longer in a symmetric configuration. The surface atoms have one

half filled dangling bond and only three back bonds to the crystal. On most $\{110\}$ surfaces of the III-V semiconductors, no reconstructions are known, but these surface layers do indeed relax. This is often referred to as buckling (See chapter 1.4 Sample system: cleavage planes of III-V semiconductors). For InAs and GaAs this is reported by several theory groups [44, 46, 122] and verified experimentally by low energy electron diffraction (LEED) [123, 124].

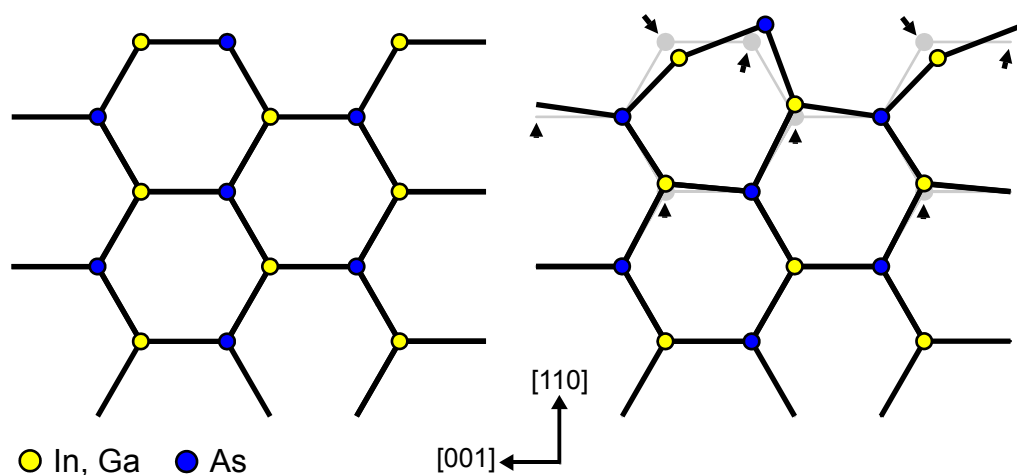


Fig. 6.8 Ball and stick model of a section of the first five InAs (GaAs) surface layers. The unrelaxed lattice (left) exhibits the perfect hexagonal alignment of the bulk crystal. The surface relaxation (right) causes the 2-3 highest atomic layers to rearrange. The unrelaxed lattice is seen in grey behind the relaxed blue and yellow lattice. The surface relaxation is sketched according to [125, 44].

The relaxation of InAs is shown in Fig. 6.8. The same considerations are also valid for GaAs. The ball and stick models show the (110) surface viewed along the $[\bar{1}\bar{1}0]$ direction. The left model shows the unrelaxed surface and the distinct hexagonal openings in the lattice. The total energy of the surface is minimized by the relaxation mechanism shown in the right model. The half filled dangling bonds of the surface atoms give rise to the surface resonance. They are discussed in chapter 1.4. Here, the structural rearrangement of the layers near the surface will be considered. The As atom of the surface layer rotates out of the highest surface layer. In (Ga) atoms are pulled to the side and inwards as indicated by the arrows. The bond lengths remain nearly unchanged, but the bonds are tilted (bond rotation). For reference the unchanged lattice is repeated in grey. LEED investigations show that also the In (Ga) atoms of the second layer move outwards while the positions of the As atoms in the second layer remain nearly unchanged. The lattice distortions are significant. According to the atoms in the surface layer move out approximately 0.3 \AA in InAs (0.69 \AA in GaAs). The second layer In atoms move by 0.14 \AA (in GaAs 0.12 \AA) which is still 7% of the interlayer distance [122, 125]. Most calculations assume that the atoms of the third layer are not affected by the relaxation. Considering that the movement of

the first layer is about 15% of the monolayer distance and the movement of the second layer is about 7% it seems plausible that at least small relaxation is expected for the deeper layers.

A recent experiment demonstrated that strain has a strong influence on the wave function shape of a dopant. Mn acceptors near InAs quantum dots in GaAs are investigated with X-STM [126]. The acceptor is exposed to a strong uniaxial strain field along the $\langle 111 \rangle$ directions, for certain configurations of Mn acceptor and InAs quantum dot. The bow-tie like acceptor wave function is elongated along the strain axis and compressed perpendicular to it. Thus the symmetry of the cubic band structure is lowered and the acceptor wave function becomes ‘S’ shaped. This is achieved by an in-plane uniaxial strain.

A similar strain field is present at the surface itself. The atoms of the first few layers relax outwards. In terms of strain this outward relaxation decomposes into a hydrostatic component and uniaxial component. The uniaxial strain is along $[110]$ for the relaxation shown in Fig. 6.8. Neither the hydrostatic nor the uniaxial components induce symmetry breaking with respect to $[001]$. However, the Zincblende crystal has the additional property that uniaxial strain along the $\langle 110 \rangle$ directions results in shear components in the strain tensor [127].

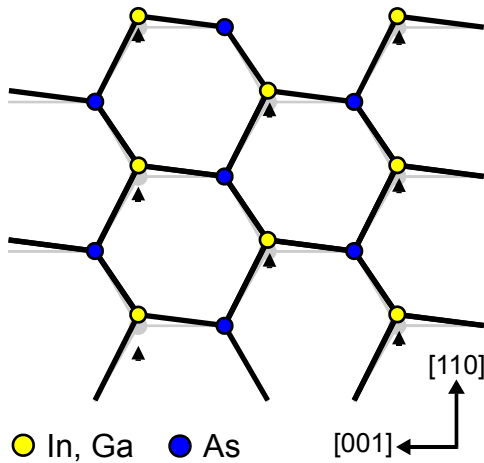


Fig. 6.9 Ball and stick model of a GaAs lattice under shear stress. Here the Ga sublattice is shifted slightly with respect to the As lattice. The unstrained crystal is seen in grey behind the strained blue and yellow lattice.

The shear components correspond to the off-diagonal components ϵ_{ij} of the strain tensor, and the uniaxial strain is part of the diagonal components ϵ_{ii} . In recent experiments it was shown that even small $[110]$ uniaxial strain (that can be applied by an external vice) leads to large anisotropies in the electron propagation properties in GaAs [128]. This gives rise to the idea that the shear components induced by the $[110]$ uniaxial strain induce the observed symmetry reduction along $[001]$. To elucidate this possibility band structure calculations are performed. The induced shear is modeled by a slight shift of the In (Ga) sublattice in the $[110]$ direction as shown in Fig. 6.9. This is a first approximation of the surface relaxation. The comparison of the right model in Fig. 6.8 shows that this approximation is justified at least for the subsurface layers (2nd layer and below).

The band structure is calculated by empirical pseudo-potentials. The spin-orbit interaction is explicitly included in the calculation. A basis set of 65 plane

waves was chosen and the pseudo-potentials of [71] are used. The calculation scheme is discussed in detail in the appendix. The band structure is calculated for the example of GaAs. The InAs valence bands are similar to GaAs, so the calculation results are representative for both materials InAs and GaAs. Fig. 6.10 shows energy contour plots of the highest valence band of GaAs. The band structure is evaluated on a plane defined by the $[001]$ and $[110]$ directions.

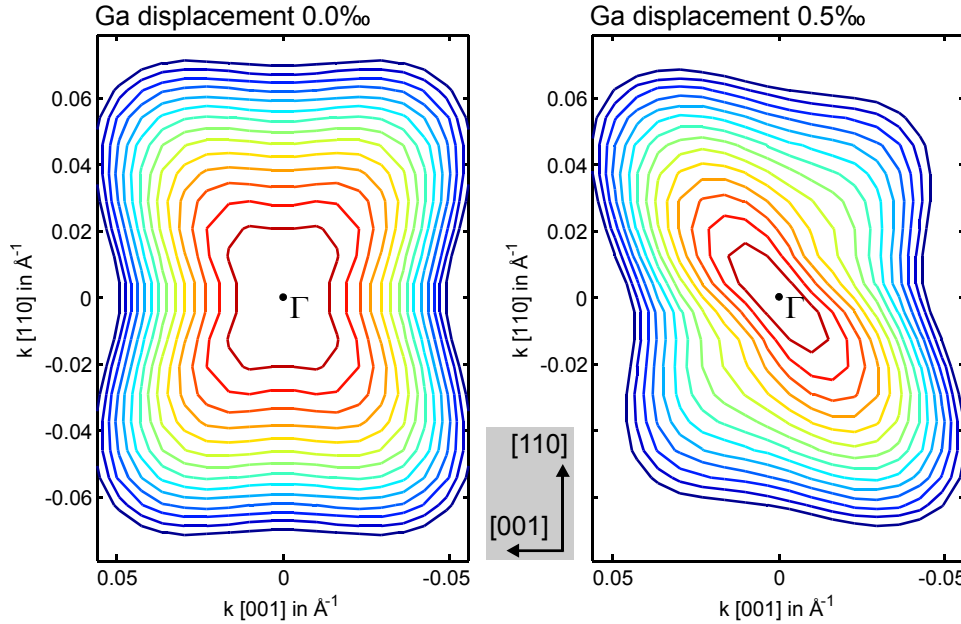


Fig. 6.10 Band structure of GaAs in a plane containing $[001]$ and $[110]$. The colored lines are iso-energy lines of the upmost valence band. Both plots show about 10% of the Brillouin zone. (left) no strain applied, i.e., bare GaAs band structure. (right) a shear strain is applied according to the ball-and-stick model of Fig. 6.9. The Ga atom is displaced by 0.5‰ of the (110) layer distance.

The plotted section has an extension of about 10% of the Brillouin zone. The vertical axis is perpendicular to the sample surface and the horizontal axis is the $[001]$ direction. The results show a prominent symmetry reduction with respect to $[001]$. In the absence of strain, the valence band is mirror symmetric to the (001) plane (Fig. 6.10 left). The acceptor wave function would have the same symmetry, too. Displacement of the In (or Ga) sublattice by only 0.05% of the interlayer distance induces a prominent distortion of the valence band (Fig. 6.10 right). The band elongates along $[111]$ and contracts in the perpendicular direction. An acceptor state hybridized of such a valence band inherits the anisotropic elongation. The resulting wave function is contracted along $[111]$ and elongated in the perpendicular direction $[11\bar{1}]$ due to the reciprocity between real and reciprocal space. If this state is imaged with the STM, a (110) section through this shape is observed. The $[00\bar{1}]$ side of the contrast has a higher density of states and extends further than the other side $[001]$. This matches with the measured contrast (refer to Fig. 6.7).

The band structure calculations show that already very small shear in $[110]$

leads to a symmetry lowering that is compatible with the observed contrasts. Because the strain field is localized within a few monolayers of the surface, it is plausible that only acceptors near the surface are influenced by this effect. With increasing acceptor depth the part of the wave function that reaches into the strained region decreases. Larger parts of the wave function are formed by the unstrained crystal, and the anisotropy decreases. It vanishes when the acceptor is no longer affected by the surface strain, which seems to be the case for acceptors deeper than 10 monolayers under the surface.

6.2.2. Electric fields under the STM tip

The second effect that is capable of producing the $[001]$ anisotropy is the tip induced electric field. The tip has an electric field penetrating into the semiconductor as described in chapter 2. Typical tip induced electric fields are on the order of 10^5 V/cm. Such field strengths are capable of influencing not only the acceptor's Coulomb potential but also the semiconductor band structure. This section discusses the symmetry reducing effect of this electric field in the semiconductors band structure. Fig. 6.11 illustrates the situation of the STM tip over the acceptor contrast. The true-to-scale sketch of a 30nm tip and the contrast of a dopant near the surface is shown in part (a) of the figure. The acceptor wave function is small compared to the tip's extension. In addition, the long-range nature of the Coulomb interaction causes the field to extend even further than the tip apex itself. In the area of the dopant atom the electric field is nearly uniform and perpendicular to the sample surface as depicted in Fig. 6.11b.

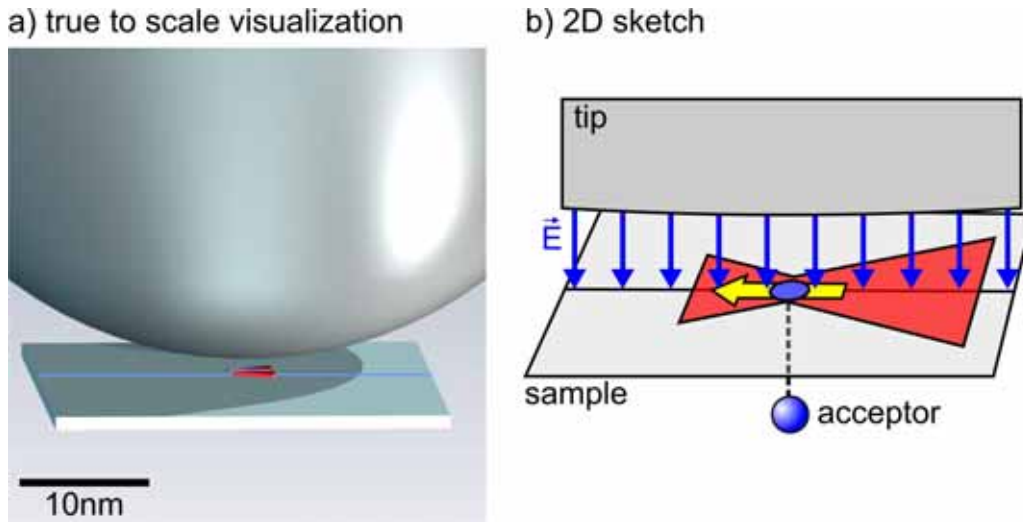


Fig. 6.11 (a) True to scale schematic of an STM tip with 30nm radius above the GaAs surface. The anisotropic contrast of an acceptor is depicted in red on the surface. The contrast extends only about 3nm on the surface. (b) The electric field at the acceptor contrast is approximately uniform.

The STM images of the acceptor wave function show that the relative weight of the acceptor wave function shifts perpendicular to the electric field. An electrostatic distortion of the wave function due to the electric field would only produce changes that are symmetric with reference to the (001) mirror plane. An elongation or compression of the wave function along $[110]$ would not explain the observed asymmetry. An effect is needed, that acts differently for the $[001]$ and $[00\bar{1}]$ wave vector components. The spin-orbit interaction (SOI) is capable of introducing this kind of symmetry reduction in the band structure [129]. The SOI has strong influence in InAs and GaAs. The energetic splitting of the split-off valence band and its pronounced cubic shape are caused by the spin-orbit interaction of the Bloch states with the crystal potential of the semiconductor. Additionally the otherwise spin degenerate bands are split. The amount of spin splitting depends on the wave vector direction. This effect is called bulk inversion asymmetry (BIA). It is a result of the lack of a center of inversion in Zincblende type semiconductors. The above band structure calculation is extended to implement a homogenous electric field in the $[110]$ direction. It is introduced to the Hamiltonian via the SOI term in the form of the Rashba Hamiltonian

$$\hat{H}_{so} = \frac{\hbar}{4m^2c^2} (\vec{E} \times \hat{\sigma} \cdot \hat{p})$$

with the Pauli spin operator $\hat{\sigma}$ and the momentum operator \hat{p} [130, 131]. As illustrated by Fig. 6.11b the electric field represents another inversion asymmetry to the system which is called structure inversion asymmetry (SIA).

Fig. 6.12 shows the results of the band structure calculation for an electric field of 1 nm/V in the same way as for the strain calculations. Again energy contour lines of the highest valence band are shown. Without an electric field, the known cubic symmetry is reproduced. No asymmetry over $[001]$ would be expected for the acceptor state. When the electric field is turned on, a prominent symmetry reduction is induced in the band structure. The valence band is elongated approximately along the $[111]$ direction and compressed along the perpendicular direction $[11\bar{1}]$. The valence band has a pronounced asymmetry over $[001]$. The resulting acceptor state has the same symmetry properties. Its probability density at a (110) section is shifted to the $[00\bar{1}]$ side of the dopant atom.

The calculated deformation of the valence band is caused by the combination of BIA and SIA. As mentioned above the BIA enhances the cubic shape of the valence bands, i.e. their elongation in all $\langle 111 \rangle$ directions and compression in the $\langle 100 \rangle$ directions. The spin splitting of the bands due to SIA is largest perpendicular to the electric field. Therefore the deformation of the valence bands is largest in the (110) plane. Solely external electric field or solely crystal field would not produce the calculated asymmetry over $[001]$. However, the sum of both effects induces the symmetry reduction over $[001]$.

The sign of the spin splitting due to SIA and BIA in the $[111]$ direction is the same. Both effects add up. In the perpendicular $[11\bar{1}]$ direction SIA and BIA have opposite sign and decrease each other.

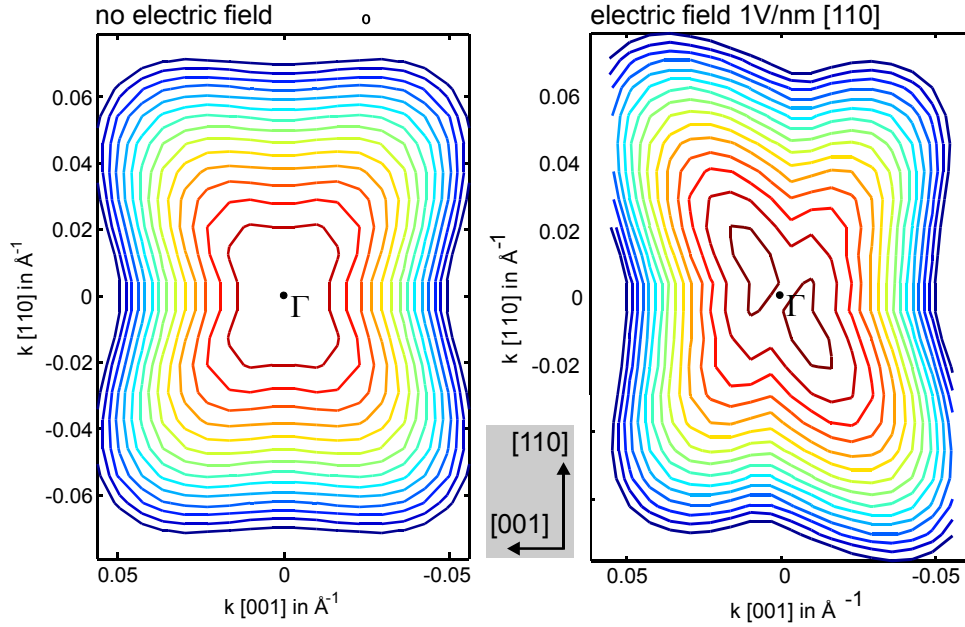


Fig. 6.12 Band structure of GaAs in a plane containing $[001]$ and $[110]$. The colored lines are iso-energy lines of the upmost valence band. Both plots show about 10% of the Brillouin zone. (left) no electric field applied, i.e., bare GaAs band structure. (right) an electric field is applied along the $[110]$ direction with a strength of 1 V/nm.

6.3. Summary

The charging signature of the Mn acceptor in InAs showed that for 0.92 V - 1.0 V, the STM visualizes the acceptor state. Therefore the anisotropic contrasts observed above the Mn acceptor cores can be considered an image of the probability density of the acceptor hole state. In other words, the STM visualizes the wave function of this state. The shapes of the acceptor states for different depths under the surface are analyzed. The measured contrasts for acceptors buried below the 10th subsurface layer closely match the theoretically derived shape of the bulk acceptor wave function. However, acceptors located within the first ten subsurface layers of the semiconductor show an anisotropy that is not explained by the bulk calculations. The spatial distribution of the acceptor state is changed by the presence of the surface. The nearer the acceptors are to the surface, the stronger the anisotropy with respect to the (001) mirror plane grows.

The symmetry reducing effects of strain and electric fields at the surface are discussed. Small shear strain resulting from the surface relaxation is capable of producing the observed $[001]$ anisotropy. A strong electric field in $[110]$ direction has the same effect and is capable of producing the anisotropy as well. Both effects are present in the measurement and both effects act similarly on the wave function. The calculated valence bands look alike, so it is not possible to distinguish between strain and electric field in the experiment. Comparison of Fig. 6.10 and Fig. 6.12 yields estimated relative strength of both effects: The valence bands of both images have nearly the same anisotropy. A relatively strong electric field of 1 V/nm is needed. However, only a relatively small shear strain of 0.05% of the interlayer distance is needed to produce the same anisotropy.

The next chapter demonstrates that this symmetry reduction has a strong effect on the imaging mechanism at charged acceptors. Chapter 8 will discuss the change in contrast symmetry due to an in-plane electric field.

7. Resonant tunneling through charged acceptors

The long-range Coulomb potential of a charged acceptor core distorts the tip induced space charge layer and produces a double barrier structure which resonantly enhances the otherwise vanishing tunnel current. This leads to the observation of triangular shaped acceptor resonances that retain their asymmetry even for deeply buried dopants.

The STM visualizes the spatial properties of the acceptor wave function only when the acceptor state is accessible for tunneling. Within this framework no acceptor related conductivity would be expected, if the acceptor state itself does not contribute to the tunnel current. This is the case for sample bias between 0 V and the threshold bias for the acceptor charging. However, a triangular shaped contrast at a Mn acceptor was measured in this bias window, when the acceptor is still negatively charged (see Fig. 5.8). The previous chapters 4 and 5 argued that the anisotropic conductivity is related to a tunneling process at the valence band edge. Unfortunately, the anisotropic tunneling process is masked on InAs by tunneling into the conduction band.

Another sample system allows studying the valence band tunneling process separately: GaAs doped with shallow acceptors. Due to its higher band gap of 1.52 eV the tunnel channels into the valence band and into the conduction band can be well distinguished and the acceptor's low binding energy results in a transition from charged to neutral at higher positive bias. This simplifies the analysis of the participating tunneling channels. The origin of the triangular shaped con-

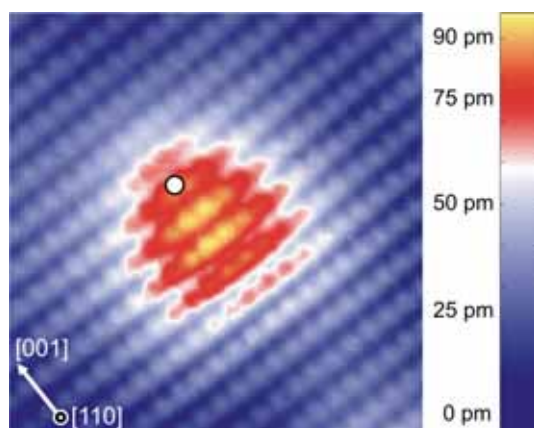


Fig. 7.1 (7.1 x 7.1) nm² STM image of a single carbon acceptor near the (110) surface of GaAs. The image was acquired simultaneously with a STS measurement at sample voltage +1.5 V and current set-point 600 pA. The white circle indicates the position of the dopant atom beneath the surface. Image reprinted from [106].

ductivity will be discussed on the basis of $I(V)$ -spectroscopies of carbon and zinc doped GaAs. The GaAs samples doped with $5 \cdot 10^{18} \text{cm}^{-3}$ carbon or zinc respectively show the triangular features in a large bias window ranging from -0.3 to about +1.5 V bias. The topographic image of a carbon acceptor is seen in Fig. 7.1.

7.1. The tunneling process at charged acceptors¹⁰

This section focuses on the understanding why enhanced conductivity builds up at the charged acceptor. The first step is local $I(V)$ -spectroscopy. The STM tip is positioned above a certain point of the surface and a single $I(V)$ -characteristic is recorded. The comparison of an $I(V)$ -curve acquired above the triangular contrast with one recorded on the undisturbed surface gives information of the energetic distribution of the tunnel current and leads to the development of a model that explains this conductivity built-up.

7.1.1. $I(V)$ -spectroscopy

Fig. 7.2 presents the results of an STS-measurement performed on a carbon doped sample region. One of the $I(V)$ -characteristics is taken above the triangular contrast (red), the other several nanometers away on a region where no acceptor related contrast is visible (blue). Both $I(V)$ -curves yield semiconductor characteristics that are typical for highly p-doped samples. The Fermi energy is at the valence band edge. An immediate onset of valence band tunneling is seen for negative sample bias. Conduction band related tunneling is measured at sample bias higher than +1.5 V. Both band tunneling regions are separated by a band gap region of about 1.5 V, which roughly resembles the GaAs fundamental band gap. But above the triangular shaped contrast a large amount of tunnel current is measured in the band gap window from 0 V to 1.5 V. In contrast to this the tunnel current does not exceed 0.3 pA at the undisturbed surface (the $I(V)$ -curve is magnified by a factor of 30 for better visibility). This behavior is particularly surprising if the band bending situation is considered. The apparent barrier height has been measured simultaneously with the $I(V)$ -spectroscopy. The resulting mean work function for both $I(V)$ -curves is 4.05 eV. According to the TBB dependence derived in chapter 2, the flat band bias for these samples is 1.59 V. This implies that the sample is in depletion for all bias voltages smaller than this value. Usually the depletion layer efficiently suppresses the tunnel current in this bias window. Above the topographic carbon contrast two groups of peaks are visible with a spectral weight of more than 10% of the setpoint current (150 pA).

¹⁰ This part of the thesis was published in Physical Review Letters Phys. Rev. Lett. **96**, 066403 (2006) [106].

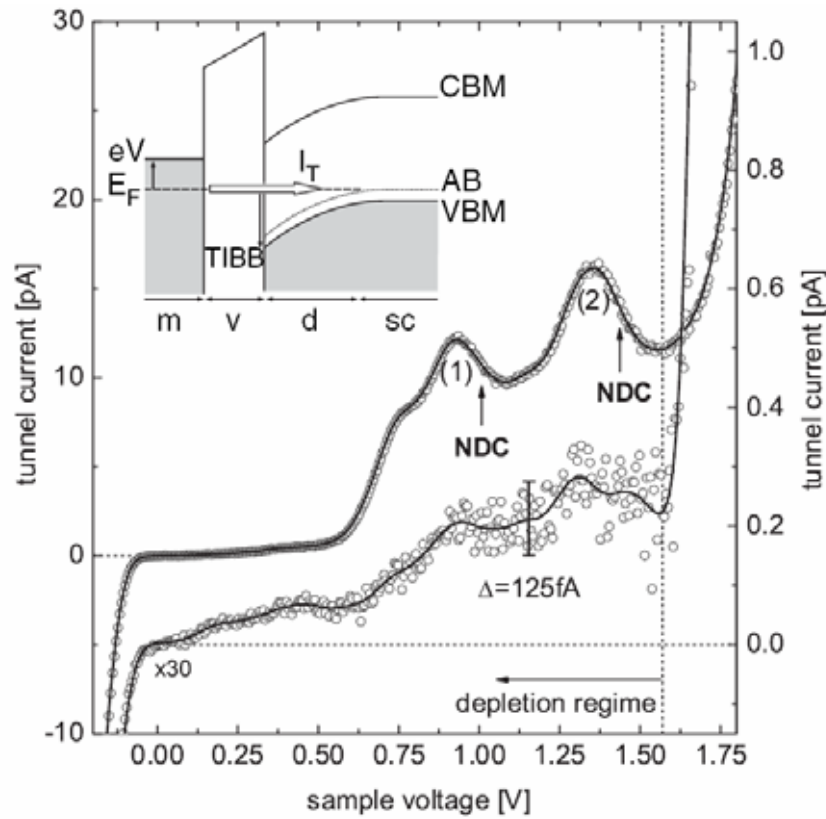


Fig. 7.2 $I(V)$ -characteristics of a buried carbon acceptor (upper curve) and the undisturbed surface (lower curve) obtained by local $I(V)$ -spectroscopy (STS). The raw data are plotted as points. The lines represent a Gauss weighted average. The $I(V)$ -curve acquired on the undisturbed surface is scaled by a factor of 30 with respect to the one taken on the C acceptor. Note that the spectroscopic features indexed with (1) and (2) are followed by negative differential conductivity (NDC). Noise level for both curves is smaller than 125 fA. The inset sketches the energetic conditions of the depletion layer bias window in the voltage interval from 0V to 1.57V in a rigid-band model: (m) metallic tip, (v) vacuum barrier, (d) depletion layer, (sc) bulk semiconductor, (TIBB) depletion barrier height, (VBM) valence band maximum, (CBM) conduction band minimum, (AB) acceptor band, and (I_T) tunneling channel. Image reprinted from [106].

The tunnel process at the charged acceptors largely enhances the otherwise vanishing conductivity. Fig. 7.3 derives dI/dV -curves from the $I(V)$ -characteristics and clearly shows that the conductivity above the carbon acceptor is spread out over the whole band gap region. A significant deviation of the differential conductivity from the free surface is detected down to 0.1 V. The group of conductivity peaks denoted with (1) in Fig. 7.2 relates to peaks in the differential conductivity (Fig. 7.3) lying at 682 mV and 870 mV, and the second group marked with (2) relates to a peak at 1250 mV. Although the tunnel current above the undisturbed surface never exceeds 0.3 pA, the dI/dV -curve exhibits the same characteristic shape as the one recorded above the acceptor (Fig. 7.3). The magnified $I(V)$ -curve in Fig. 7.2 shows that it is well above the noise level of the raw data points of about 125 fA.

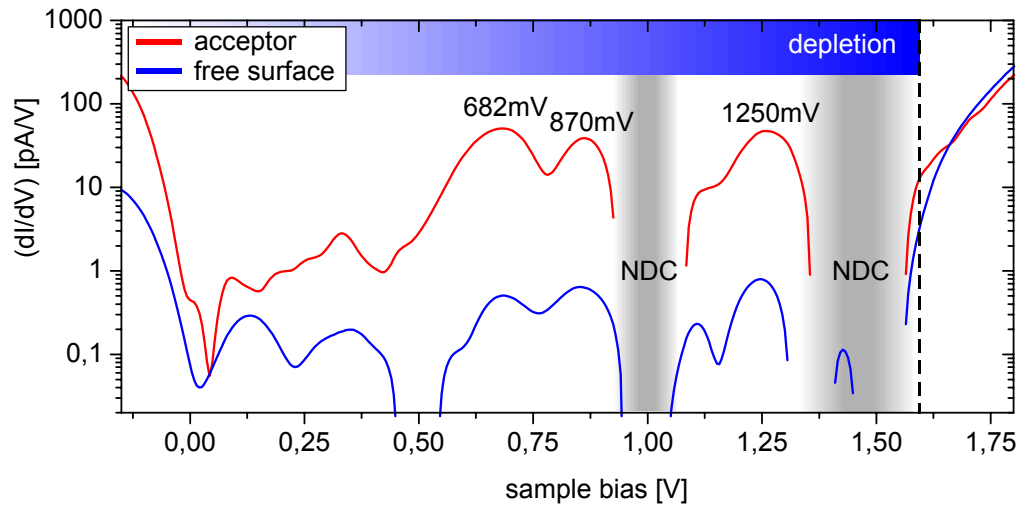


Fig. 7.3 dI/dV curves of the two $I(V)$ -characteristics presented in Fig. 7.2. The conductivity is plotted in logarithmic scale against sample bias. The bias windows of negative differential conductivity are marked in grey.

One important observation leads to the development of a model for this conductivity enhancement: The peaks in the differential conductivity are accompanied by negative differential conductivity (NDC) causing a negative slope of the $I(V)$ -curve in the voltage intervals from 932 mV to 1080 mV and from 1357 mV to 1559 mV as seen in Fig. 7.2. The observation of NDC in tunneling structures is a strong indicator for resonant processes. It is important to note that the observation of NDC cannot be described with the commonly employed tunneling theory. According to the standard STM theory (see chapter 1.5) the differential conductivity represents the sample local density of states (LDOS). This interpretation would lead to negative sample LDOS, which is unphysical. A more detailed model for the tunnel current will be developed in the next section.

7.1.2. The resonant tunneling model

The measurements show that the anisotropic conductivity is restricted to the bias window of depletion for shallow acceptors. Unlike the measurements of InAs only valence band related tunneling is possible. Here, the conduction band minimum (CBM) is higher than the applied bias voltage. It cannot participate in tunneling because the tunneling electrons have not enough energy to reach it. Thus, all of the conductivity detected in the band gap interval originates from a tunnel channel at the valence band (see inset of Fig. 7.2).

For the bias window of interest from 0 V to 1.5 V one tunnel channel is in principle possible even in the absence of an acceptor (see inset of Fig. 7.2): Due to the depletion layer (d) present at the surface, no valence band states are directly accessible. But the doping concentration of $5 \cdot 10^{18} \text{ cm}^{-3}$ causes an impurity band of $\sim 10 \text{ meV}$ spectral width [5] centered 30 meV above the valence band

edge. Injected carriers are drained through the acceptor band (AB, see inset of Fig. 7.2) and the samples are conducting even at 4.2K. At low temperatures the band is partially filled. Unoccupied states in the acceptor band are present in the bulk. For bias voltage between 0 V and 1.5 V these states are available for electrons tunneling from the tip through the vacuum gap **and** the depletion layer. The depletion layer has a depth on the order of 10nm (doping $>10^{18}\text{cm}^{-3}$). The exponential decay over such large distances is usually thought to efficiently suppress the tunneling process [17]. The $I(V)$ -curves recorded on the undisturbed GaAs surface (Fig. 7.2) show this behavior. In the depletion bias window the overall tunnel current does not exceed 300fA. But this situation is completely different above the acceptors. The conductivity already reaches levels of 50pA/V for bias voltage well below 0.75 V (Fig. 7.3). The acceptor is negatively charged and introduces a strong distortion to the band edge alignment under the tip as depicted in Fig. 7.4.

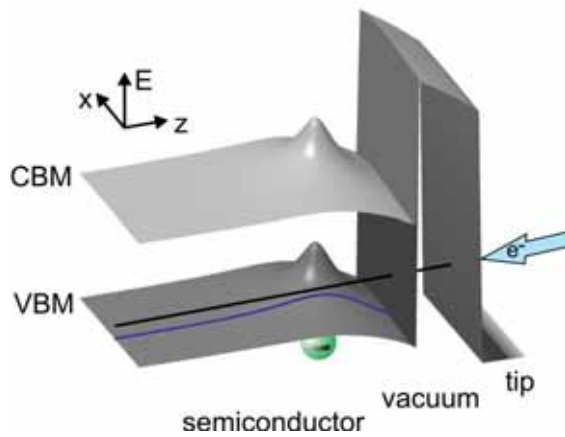


Fig. 7.4 Schematic of the band alignment in the vicinity of an acceptor core. From right to left: metallic tip, vacuum barrier and semiconductor. Under the tip, the sample is in depletion, i.e., the conduction band (CBM) and the valence band (VBM) are bent downwards. The subsurface acceptor atom (in green) locally bends the bands upwards because of its negative charge.

Starting from the empirical knowledge of the potential configuration a more precise model for the "band gap conductivity" can be developed now. The aim is a numerical evaluation of the tunnel current in the bias window from 0 V to 1.5 V. The quantum mechanical transmission probability from the tip into the bulk of the sample has to be evaluated. For these bias voltages the tunnel current is linear proportional to the transmission probability because the tunnel path is energetically pinned to the acceptor band. No integral over a large bias range has to be employed. At first, the three dimensional potential configuration consisting of the tip induced depletion layer, vacuum barrier and acceptor Coulomb potential is projected to a one-dimensional potential distribution along a tunnel path perpendicular to the surface. In Fig. 7.4 the overall potential is sketched in two dimensions. The resulting one-dimensional potential is depicted in Fig. 7.5a. The depletion layer potential is extracted from the three-dimensional TIBB calculations (see chapter 2). The acceptor Coulomb potential is parameterized by the surface dielectric constant and the distance from acceptor core to the tunnel path. Both potentials are summed up with the trapezoidal vacuum barrier potential. It is important to account for the band structure and especially to include the

fact that tunneling occurs at the valence band edge. Thus, holes have to be considered in the semiconductor instead of electrons. In these terms one tunneling event is treated as an electron tunneling from the tip to the surface and a hole tunneling from the sample's bulk to the surface.¹¹

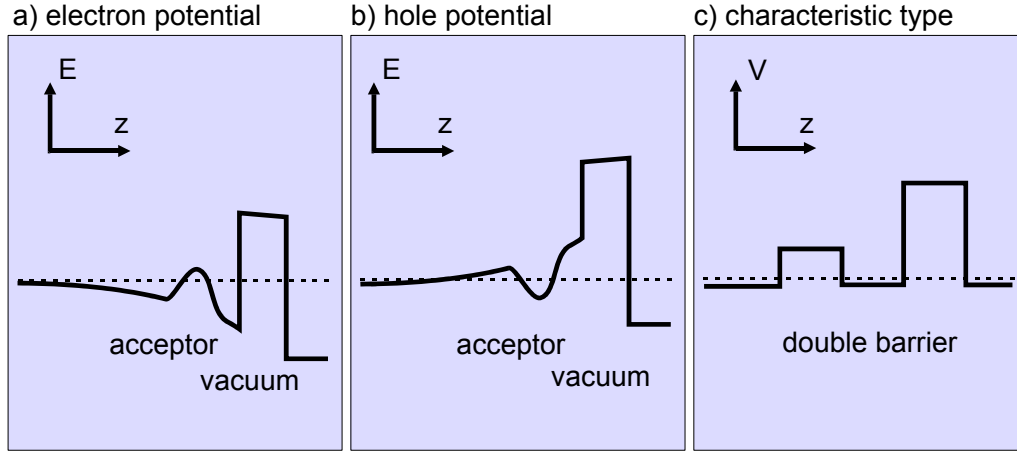


Fig. 7.5 Construction of the effective potential along a tunnel path perpendicular to the surface. (a) The acceptor Coulomb potential is superimposed to the depletion layer potential. (b) Because tunneling occurs near the valence band edge not electrons but holes have to be treated. The energy scale in the semiconductor reverses for a hole. (c) The distortion by the acceptor leads to the formation of a double barrier potential for holes.

A more accurate description of the tunneling process employs the framework of the complex band structure. An electron that is injected into the semiconductor is treated as a complex plane wave with real and imaginary components in the wave vector. For single particle energies in the bands, the wave vector is real and the electron is a propagating plane wave. For energies in the band gap, the wave vector is imaginary and the electron is exponentially decaying. This behavior is translated into an effective potential landscape, i.e., at every point along the tunnel path the potential is chosen such that it reflects the propagation properties of the considered electron at this point [106, 132]. For energies close to the valence band edge this implies that the effective potential is negative if the energy of the considered tunnel path is within the band. For energies in the band gap, the effective potential is positive. The important advantage of this method is that the quantum mechanical transmission through this system is described as the coherent transmission through one effective one-dimensional potential $V_{\text{eff}}(z)$. The 1-d transfer matrix technique is used and the potential $V(z)$ is modeled by stepwise constant potentials [71]. The transition across the metal vacuum semiconductor interfaces is accounted for by the BenDaniel Duke boundary conditions [133].

¹¹ The negative differential conductivity was first observed in the author's diploma thesis [132]. A first numerical simulation on the basis of a one dimensional transfer matrix technique revealed that the NDC may be attributed to a resonant tunnel channel. These results are the starting point of the model developed here.

The tunnel current is calculated as a function of the height of the depletion layer potential and rescaled to the sample voltage using the TIBB(V) relation. The result is a numerically calculated $I(V)$ -characteristic, plotted in Fig. 7.6. The employed model already gives qualitative trends: for large distances, i.e. in the absence of an acceptor, the $I(V)$ -curve is monotonous and shows negligible current up to 1 V (dashed line). However, in the vicinity of the acceptor, i.e., averaged over distances smaller than 1 nm, the tunnel current shows two regions of enhanced conductivity, one lying below 1.0 V and one above 1.0 V sample voltage (solid line). Such transmission enhancements are attributed to a build-up of resonances in the acceptor potential. Both current peaks are accompanied by negative differential conductivity. Within the applied model the NDC observed in the measurement is related to resonant tunneling channels. The band bending causes the potential $V_{\text{eff}}(z)$ to change with changing bias voltage. For certain potential configurations, i.e., for certain bias voltage, a resonance condition is met and a peak in the $I(V)$ -signal is measured.

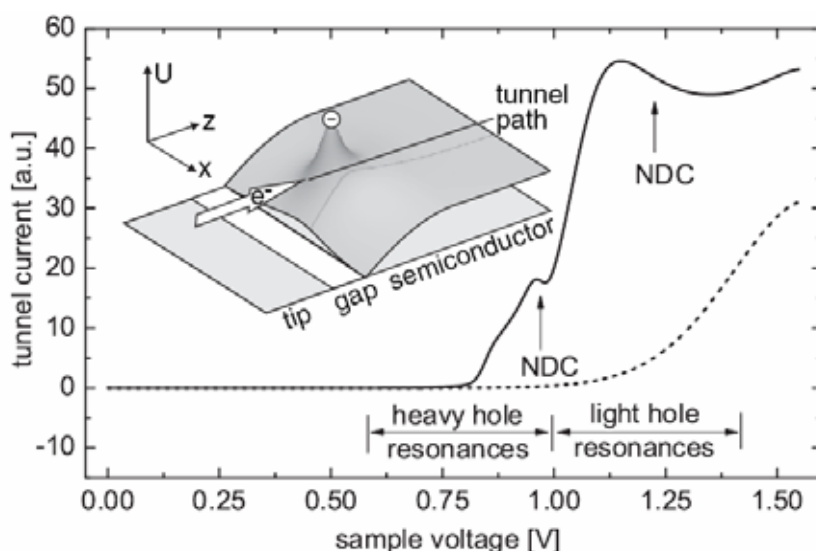


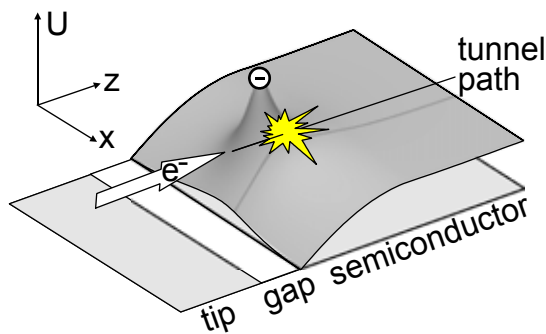
Fig. 7.6 Numerical simulation of the tunnel current for an acceptor buried five monolayers beneath the surface (solid line) and the undisturbed surface (dashed line). The light hole and heavy hole contribution to the transmission is indicated, as are the two intervals of negative differential conductivity (NDC). Reprinted from [106].

The comparison of simulated (Fig. 7.6) and measured $I(V)$ -characteristic (Fig. 7.2) gives good qualitative agreement for positions close to the acceptor. Both curves show two regions of enhanced tunnel current followed by negative differential conductivity. The simulation includes the light hole and heavy hole valence bands by constant effective masses. Although this procedure is very approximate, it points to an interesting effect: within the crude approximation peaks (1) and (2) in Fig. 7.2 can be identified as heavy hole and light hole resonances separated up to 560 meV from each other, suggesting the capability to map energetic properties of the participating sample states with the STM.

The dI/dV -curves presented in Fig. 7.3 clearly show that the characteristic features found above the acceptor contrast are also present on the undisturbed surface. At the undisturbed surface a little amount of tunnel current in the order of 300 fA is detected. The simulated $I(V)$ -curve for the bare surface shows no structure. This apparent contradiction is easily resolved: The samples are homogeneously doped with a doping density of $5 \cdot 10^{18} \text{ cm}^{-3}$. The average extension of the triangular contrasts is about 10 nm for the deepest buried acceptor that can be detected with the STM (8th monolayer under the surface). The average thickness of the depletion layer is between 5-10 nm. Therefore, just by geometric consideration, there is no point on the surface on which a tunnel path perpendicular to the surface is not influenced by at least one acceptor. The conductivity measured above the undisturbed surface is attributed to acceptors that are buried below the detection limit of topographic STM techniques but well within the resolution of STS measurements.

7.1.3. Sequential tunneling vs. resonant tunneling

For STM studies on semiconductors it is imperative to check whether different effects could lead to NDC. It should be checked if the NDC could be produced by a non-resonant process. The first possibility is the influence of the TIBB on the transparency of the vacuum gap. Because the tunnel current is pinned at the valence band edge, increasing the applied bias results in an increase of the vacuum barrier for this tunnel channel. In the transfer matrix calculation this dependence is easily checked. The above calculations (see Fig. 7.6) are repeated with a rectangular vacuum barrier that does not change with the applied bias and with a trapezoidal barrier that changes according to the TIBB(V) calculation. However the calculated $I(V)$ -characteristic does not change. Without an acceptor no NDC is detected. The increasing vacuum barrier is overcompensated by the decreasing depletion layer. Higher sample bias results in higher conductivity.



Another possibility to observe NDC is sequential tunneling into an acceptor related state and limited tunneling rate from this state into the bulk of the sample [80]. Sequential tunneling can be accounted for in the simulation by a loss of phase coherence of the wave function at the position of the acceptor atom. This is

indicated in schematic **Fehler! Verweisquelle konnte nicht gefunden werden..** A random phase shift is added to the wave function at the projected position of the acceptor atom. Then, the transmission coefficient is calculated as an ensemble average. The transmission probabilities for many randomly distributed phase shifts are averaged. The result is shown in Fig. 7.7. The tunnel current is plotted against the TIBB value. For fully coherent tunneling the strong resonance is visible in the red curve. From the upper curve to the lower curve the phase decoherence is increased. Already for random phase shift of π the resonance peak is strongly suppressed and can no longer be identified as a resonance. For a fully incoherent process, i.e. a maximum phase difference of 2π , the tunnel current resembles the curve of the undisturbed surface.

This simulation demonstrates that only the coherent tunneling process reproduces the observed peaks and NDC in the $I(V)$ -characteristics. A resonant tunneling process is accountable for the enhanced conductivity in the depletion bias window.

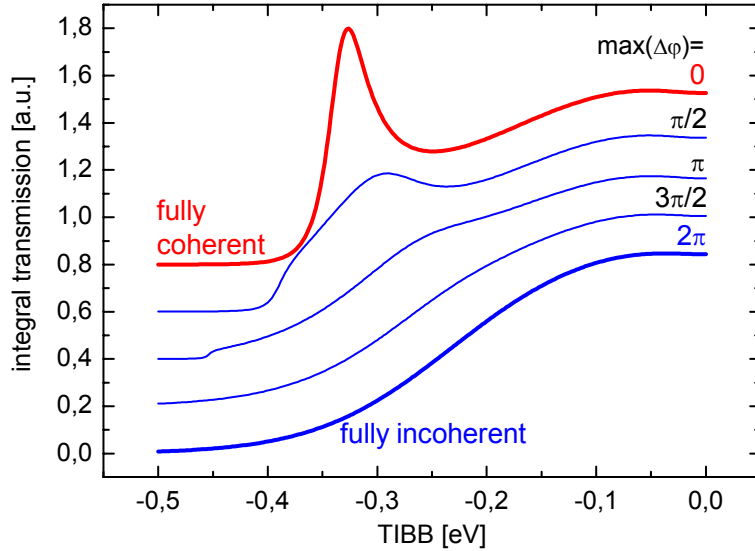


Fig. 7.7 Comparison of calculated transmission probability curves. (red) Coherent transport over the whole structure. This case describes resonant tunneling. (blue) With a random phase-shift added to the wave function directly at the acceptor atom an incoherent, i.e., sequential tunneling process, is simulated. The maximum phase shift is increased from the upper to the lower curve. For a maximum phase shift of 2π , i.e., sequential tunneling the resonance is no longer observed.

7.2. Anisotropic shape of the acceptor resonance

The previous section demonstrates that tunneling at charged acceptors is connected to a resonant tunneling process through the combined potential of depletion layer and acceptor Coulomb potential. In this section spatially resolved

I(V)-spectroscopy is employed to study the energetic evolution and spatial distribution of the acceptor related contrasts. The connection of the triangular shaped acceptor contrasts to the resonant tunneling channel is the focus of the next section.

7.2.1. Spatially resolved I(V)-spectroscopy

The results of a spatially resolved I(V)-spectroscopy of two shallow acceptors in GaAs are shown in Fig. 7.8. The dopants here are zinc atoms. Zinc has a different electronic configuration than C (C: [He] $2s^2 2p^2$, Zn: [Ar] $3d^{10} 4s^2$) but is also a shallow acceptor in GaAs with a binding energy of 31 meV [5]. It exhibits the same behavior in the STM measurements.

The detailed analysis of the potential configuration and the connection to the anisotropic conductivity was submitted to Physical Review B and is available at arXiv: cond-mat/0708.2937 [112].

Fig. 7.8 plots different dI/dV -maps from -135 mV up to 1800 mV sample bias. The maps are arranged with respect to ascending bias from bottom left to top right. They are grouped according to the TIBB(V) dependence calculated for this measurement. The calculated flat band voltage is at +1.60 V. The consequence are three qualitatively different bias windows that are sketched with rigid-band diagrams in the figure:

- Negative bias (-0.15 V to 0 V): The sample is in depletion and tunneling out of the valence band is possible. All electrons contributing to the tunnel current have to tunnel through the depletion layer.
- Small positive bias (0 V to +1.6 V): The sample is in depletion and tunneling into the sample is possible. The conduction band is energetically not accessible, so the only possible tunnel channel involves electrons tunneling through the depletion layer into the partially unoccupied acceptor band.
- High positive bias (+1.6 V to +1.8 V): The sample is in accumulation. Holes are accumulated at the valence band and are accessible for tunneling. At the same time tunneling into the conduction band is possible.

The overall evolution of the measured conductivity can be divided into two intervals: The dI/dV -maps show triangular shaped features for both depletion bias windows Fig. 7.8a and Fig. 7.8b. The anisotropic shapes are present from -135 mV to +1547 mV. The features are positioned to the $[001]$ side of the dopant atoms with the triangle's tip pointing to the $[00\bar{1}]$ direction. In the accumulation bias window Fig. 7.8d circular symmetric features are observed. The accumulation and depletion layer intervals are separated by the flat band condition Fig. 7.8c.

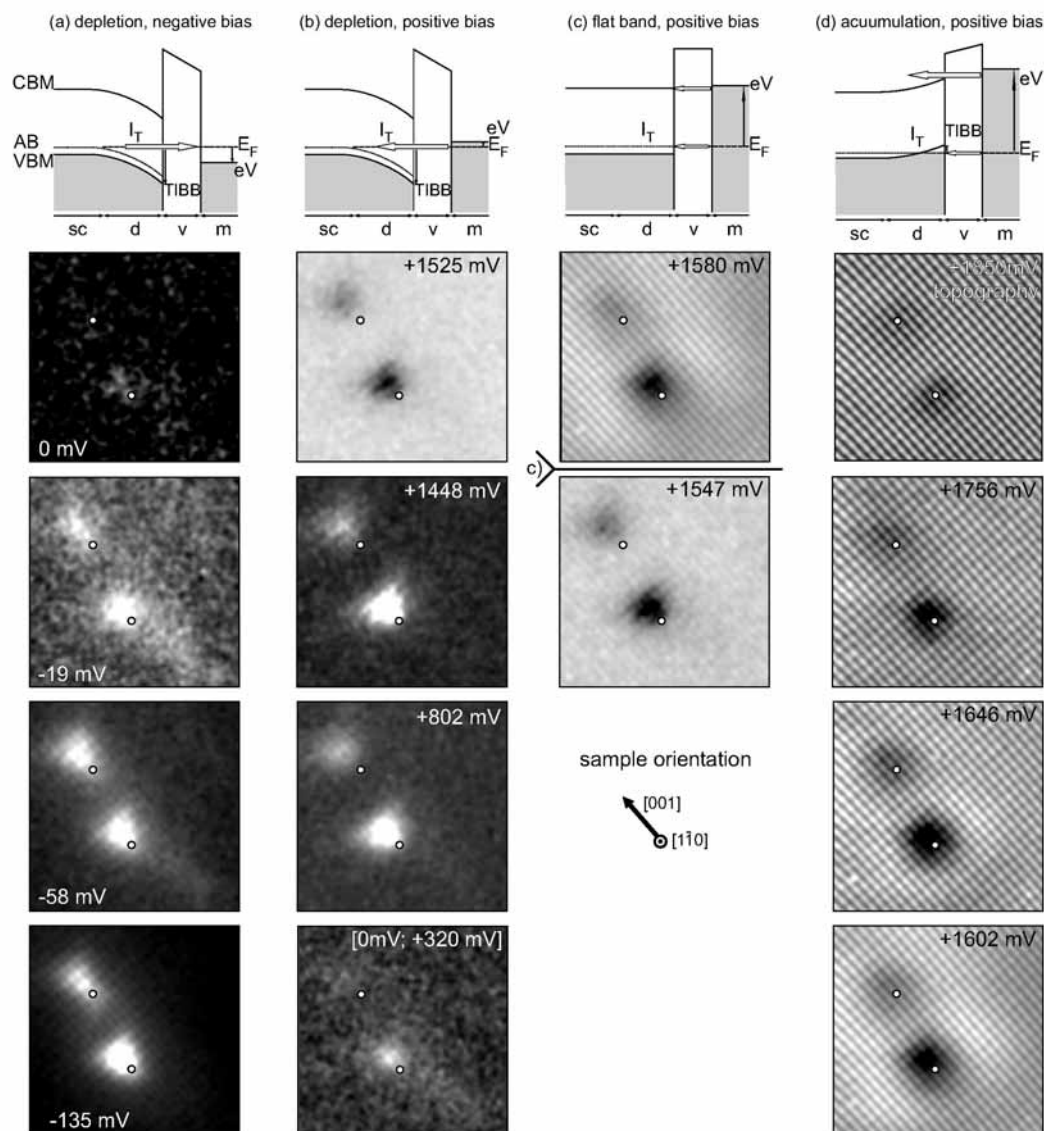


Fig. 7.8 Some representative dI/dV -maps extracted from the STS-measurement on Zn acceptors. The differential conductivity is shown in grey scale. Black is reduced and white enhanced conductivity with respect to the mean conductivity in each map. The black triangles in the maps for +1525mV to 1547mV are negative differential conductivity. The STS-measurement covers different tunneling situations. Each column of this figure has the same underlying potential configuration. They are sketched with rigid-band diagrams: (a) depletion layer under the surface and electrons tunneling from the bulk of the sample through the depletion layer and the vacuum gap to the tip, (b) depletion layer and electrons tunneling from the tip through vacuum and depletion layer into the bulk sample, (c) flat band condition and electrons tunneling into the acceptor band and the conduction band, (d) accumulation of free holes under the surface and tunneling into the conduction band and the accumulation layer. Image reprinted from [112].

Circular features:

For high sample bias a circular feature appears at about +1580 mV. This is nearly at the computed flat band voltage position (c). In addition, the onset of strong surface corrugation is observed. For further increasing sample bias the circular feature becomes more prominent and shrinks towards the acceptor atoms' positions until it is no longer visible at +1756 mV. The onset of the circular feature is related to an accumulation layer under the tip. The valence band edge is pulled over the Fermi energy shortly after the flat band condition is passed as already mentioned in chapter 2.3. Free holes are accumulated under the tip. They are vertically confined by the extension of the accumulation layer. The lateral confinement is determined by the dimension of the tip (for our tips 10-20nm) and much weaker. Charge density oscillations of the nearly free hole gas around charged defects are expected. Those oscillations have been previously reported for electron accumulation layers on n-type semiconductors [74-77] and first indications of hole charge density oscillations (CDO) on p-GaAs have been observed [78]. In the dI/dV-maps a bright halo of increased conductivity surrounds the two acceptors for bias voltages beginning at 1580 mV. This halo begins with a diameter of about 10nm and decreases in size with increasing sample voltage. This is the signature of a CDO in the hole accumulation layer [79]. With increasing sample bias the TIBB increases, too. The accumulation layer increases in energetic depth and therefore the Friedel oscillation period associated with the filled states within the potential well decreases. The flat band voltage is immediately before the onset of the CDO. Thus the CDO allow pinpointing the flat band voltage to +1.56 V. This is in good agreement with the flat band position derived from the TIBB calculations.

Triangular features:

The triangular shaped features are only observable well below the flat band voltage. The sample is in depletion for this bias window. In the whole bias range from +1.547 mV down to the end of the measurement at -0.15 V only triangular shaped conductivity is imaged at the acceptors. When the voltage approaches 0 V from either positive or negative bias the triangles fade slowly into the background noise but do not change qualitatively. At voltages next to 0 V (-19 mV or up to +320 mV) enhanced conductivity seems to branch away from the lower acceptor atom. This is an artifact due to another acceptor buried below the two prominent acceptors.

The spatially resolved I(V)-spectroscopy demonstrates that the triangular shaped enhanced conductivity is connected to the resonant tunneling channel at acceptors: Over the whole depletion bias interval the only possible tunnel channel involves tunneling through the depletion layer. As described in section 7.1.2 the acceptor resonantly enhances the conductivity for this configuration. The enhanced conductivity possesses the triangular shape.

A dI/dV -section through an acceptor gives information of the energy dependent evolution of the acceptor resonances. Fig. 7.9 shows a dI/dV -section through the upper left acceptor of Fig. 7.8. The acceptor atom position is indicated by a white line. The band related tunnel current is shown in red color (high conductivity). The band gap bias window has blue color due to the vanishing conductivity. The acceptor resonances show up as greatly enhanced conductivity in the band gap window subsequently followed by negative differential conductivity (dark blue in the section and seen as black depressions in the dI/dV -map at +1525 mV in Fig. 7.8, as well). The enhanced conductivity is shifted nearly completely to one side of the dopant atom.

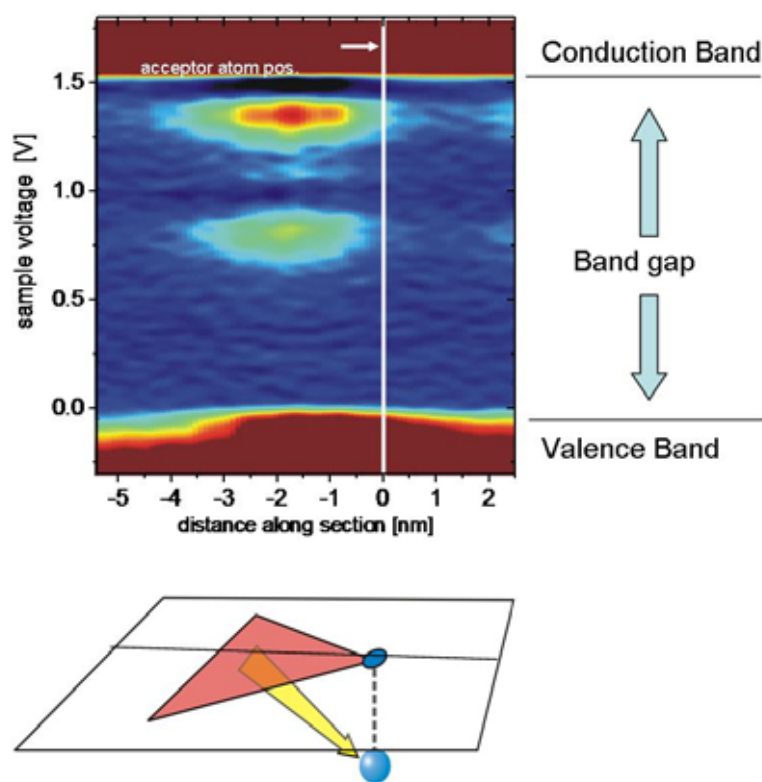


Fig. 7.9 dI/dV section through the triangular contrast of an acceptor as indicated in the schematic (lower part). The position of the acceptor atom (blue point in the schematic) is shown as a white line in the section. The acceptor induced conductivity in the band gap is clearly shifted to one side of the atom's position.

7.2.2. Depth independent shape¹²

The spatially resolved $I(V)$ -spectroscopy showed that the acceptor resonances have a strong asymmetry with respect to $[001]$. Earlier it was shown that the acceptor wave function exhibits a depth dependent anisotropy along this direction (see chapter 6.1). It is the focus of this section to study the depth dependence of the triangular acceptor resonances.

Depending on the tip work function the bias window for the observation of the triangular resonances may extend up to 1.6 V sample bias. At 1.50 V sample bias it is possible to drive a small tunnel current into the conduction band. Topographic measurements of the triangular shaped acceptor resonance at +1.6 V sample bias are possible. Besides time consuming spectroscopic measurements Multibias topographies give information of the resonances' spatial distribution. For tip work functions of ≤ 4.0 V the enhanced conductivity is still present at +1.6 V and the small tunnel current into the conduction band prevents the STM tip from crashing in areas without acceptor contrasts. At the same time the topographic measurement at +1.6 V is very sensitive to the acceptor resonances. The previously presented spectroscopy (see Fig. 7.8) has its setpoint at +1.85 V. In topographic measurements at +1.60 V the STM tip is up to 1.7 Å closer to the surface. The sensitivity is increased by nearly a factor of 100. Acceptors buried up to eight monolayers under the surface are detected. The circular shaped contrasts at high positive or large negative bias are only visible for acceptors down to the sixth subsurface layer. Fig. 7.10 presents a series of C acceptors. The acceptor contrasts are arranged with increasing depth of the acceptor core. The images are aligned with respect to the acceptor cores' positions to demonstrate the depth dependence of the triangular contrasts. The analysis is based on a Multibias series above a homogeneously C doped region of the GaAs sample. Topographies at -1.5 V, +1.6 V and +2.5 V are recorded quasi-simultaneously. The projected positions of the dopant atoms under the sample surface are determined as the center of mass of the circular protrusion at -1.5 V. The determined position is cross-checked with the topography recorded at +2.5 V. At this voltage the acceptors appear as circular depressions. Both circular contrasts are caused by the electrostatic interaction of the negative acceptor core charge with the valence and conduction band of the sample. The dopant atom position is in the center of both circular contrasts and turns out to be in the tip of the triangular contrast. The dopant atom positions are marked by yellow crosses. The dopant depth is determined with the same technique that was employed for the Mn acceptors.

All contrasts are of triangular shape. The triangles point into the $[00\bar{1}]$ direction, because the investigated sample surface is $(1\bar{1}0)$. The triangular contrasts are mirror symmetric with respect to the (110) mirror plane. Nearly all enhanced

¹² This work has been published in the Japanese Journal of Applied Physics Jap. Journ. Appl. Physics **45** 2193 (2006) [72].

conductivity is shifted along $[001]$ to one side of the acceptor core. The acceptor resonances show a strong asymmetry with respect to the (001) mirror plane for all observed depths. This agrees with the previously described spectroscopic measurements. Only the acceptor in the first layer has significant amount of tunnel current on the $[00\bar{1}]$ side of the dopant atom.

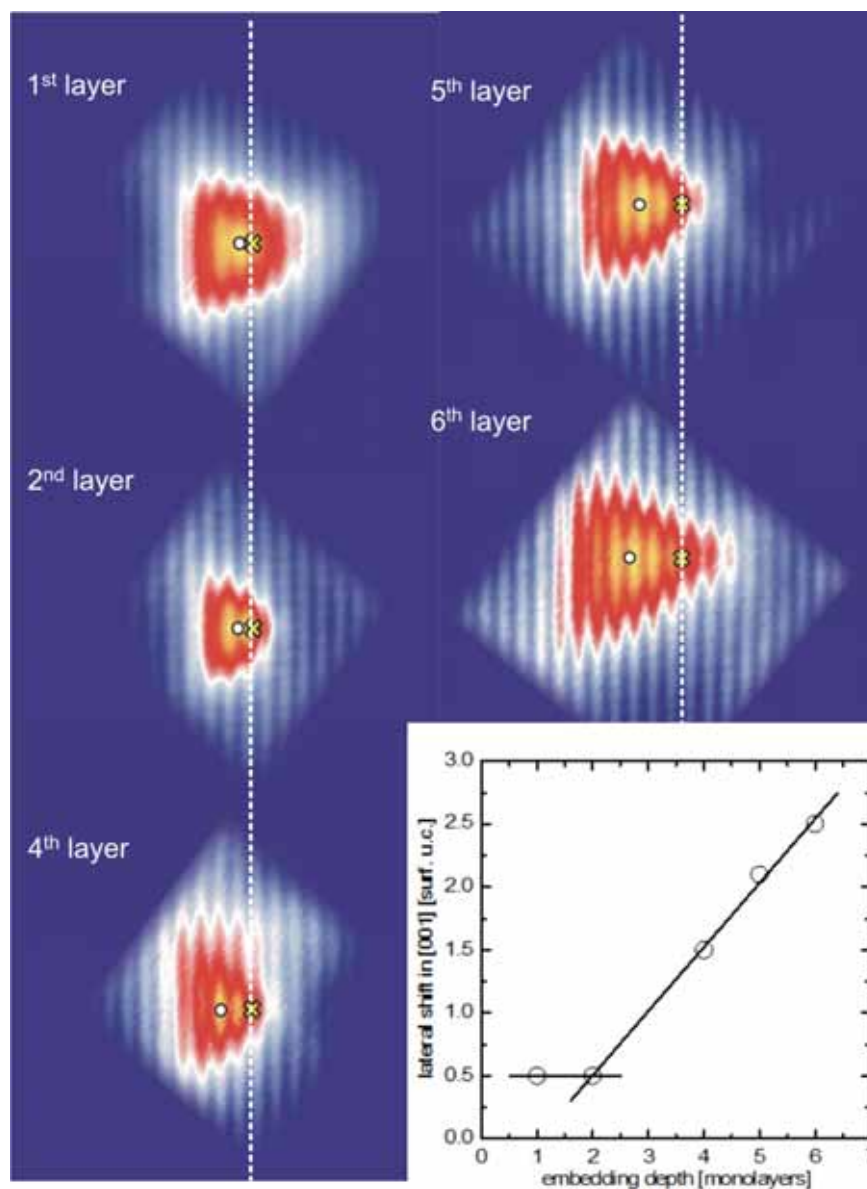


Fig. 7.10 Multibias topographies of C acceptors in different subsurface layers recorded at +1.6 V sample bias and 100pA tunnel current. The topographies are aligned with respect to the acceptor core positions indicated by the yellow crosses and the white lines. The contrast maxima are indicated by white circles. The diagram shows the $[001]$ shift of the contrast maximum plotted against the depth of the dopant.

With increasing depth the triangular shapes seem to become even more pronounced than for acceptors near the surface. The maximum of the enhanced conductivity is determined in a low pass filtered image of each acceptor. The maxima are marked by white circles. It shifts away from the acceptor core's position (white dashed line). The diagram in Fig. 7.10 is a plot of the amount of shift against the depth of the respective dopant atom. The shift increases linearly with the embedding depth. This behavior illustrates the observed trend. Deeper acceptors exhibit more pronounced triangles than shallow ones. Therefore the anisotropy of the acceptor contrasts with respect to the (001) mirror plane even increases with increasing depth.

This is in contrast to the depth dependence of the wave function images at Mn acceptors. The wave functions observed for Mn acceptors start as nearly triangular shapes for the Mn atoms in the first and second layer. Then with increasing depth the wave functions quickly evolve into symmetric bow-tie like shapes. The anisotropy along $[001]$ vanishes for acceptors in the 10th subsurface layer (see Fig. 6.3). The acceptor resonances observed for the shallow acceptors (as shown in Fig. 7.10) retain their highly anisotropic triangular shape.

7.3. Complex band structure induced anisotropies

The previous sections derived a model that explains the observation of enhanced conductivity above the charged acceptors. The measured resonance curves in the $I(V)$ signal correspond to a resonant tunneling channel. A one-dimensional model was developed that qualitatively reproduces the observed $I(V)$ -characteristics. But it is not possible to describe the triangular shape of the acceptor resonance in a one-dimensional model. Measurements show that the triangular shape is connected to the host lattice [72, 102]. And the symmetry properties of the triangular shaped acceptor resonance are similar to those of the acceptor state (compare with 6). This gives rise to the idea that the same band structure properties are accountable for the anisotropic distribution of the acceptor resonance.

Indeed the semiconductor band structure has impact on the resonant tunnel process. As described previously electrons resonantly tunnel from the tip through the vacuum gap and the depletion layer in the sample. The rigid band model in Fig. 7.11 sketches the situation. The electrons are in the band gap when they tunnel through the depletion layer. Neither valence band nor conduction band states participate in the tunnel process. It was recently demonstrated that the crystalline environment strongly influences the tunneling process [134]. The decay constant for a certain energy in the barrier becomes dependent on the direction of tunneling in the crystal. The exponentially decaying wave of a tunneling electron is described by the complex band structure.

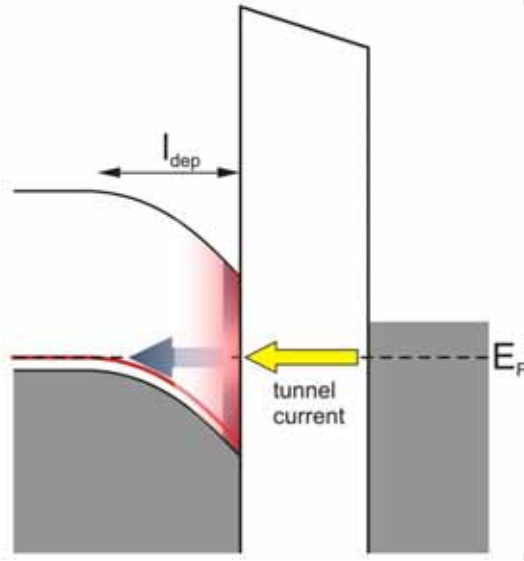


Fig. 7.11 Schematic of the band alignment for the resonant tunneling channel. The tunnel current is mediated by states within the semiconductor band gap (light red) until unoccupied states are reached in the bulk of the crystal. The band gap states are the decaying wave solutions of the semiconductor. They are part of the complex band structure.

The complex band structure arises from a straight-forward generalization of description of plane waves: In the vacuum propagating waves are usually described as

$$\psi(\vec{r}) = \exp(i\vec{k} \cdot \vec{r}), \quad \vec{k} = \hat{e}_k \sqrt{\frac{2m}{\hbar^2}(E - V)}. \quad (1)$$

The wave vector k is dependent only on the electron's kinetic energy $(E - V)$. In a region in which the electron has an energy that is smaller than the local potential, it is tunneling. The electron is described as an exponentially decaying wave [47].

$$\psi(\vec{r}) = \exp(-\vec{\kappa} \cdot \vec{r}), \quad \vec{\kappa} = \hat{e}_r \sqrt{\frac{2m}{\hbar^2}(V - E)}. \quad (2)$$

The decay constant κ does only depend on the difference between electron energy and height of the potential. The differentiation which formula is used for the wave function is only whether $(E - V)$ is positive (propagating wave) or negative (decaying wave). In this description κ and k are real values. If the wave vector is allowed to become a complex value, formula (1) describes propagating as well as decaying waves¹³.

The simple relation between wave vector k and energy E as given in (1) is only valid in the vacuum. For electrons propagating in a crystalline environment it is well known that this relation is given by the dispersion relation $E(k)$, i.e., the band structure. If k is treated in the generalized framework as a complex value, $E(k)$ is called the complex band structure. Decaying waves in a crystal are affected by the band structure in the same way propagating waves are. It was shown by Heine [135], that real eigenvalues $E(k)$ of the crystal electron Hamiltonian can be found not only for real wave vectors k , but also for waves associated

¹³ For $E < V$ the square root becomes imaginary. The resulting expression equals (2).

with complex wave vectors z . Fig. 7.12 sketches the qualitative behavior of the complex band structure. Real wave vectors ($k=a+i\,0$) give the conduction and valence bands. Imaginary wave vectors ($k=0+i\,b$) describe how an electron will propagate (resp. tunnel) through a finite region of the crystal when its energy E lies in a band gap. The conduction band and valence band are connected by a loop in the imaginary plane.

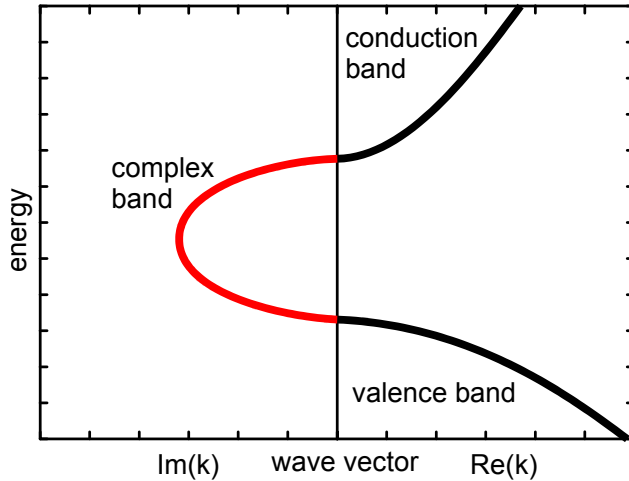


Fig. 7.12 Qualitative diagram of the complex band structure. The conduction band and valence band are found for real k values. The complex band is found for imaginary k . It is a loop connecting the valence band and conduction band in the imaginary plane.

Standard numerical methods that are usually used to calculate the real band structure are easily extended to treat complex k values [136]. In this work the empirical pseudo-potential method is used, that was already presented in chapter 6.2 [71] (see also appendix 1). Fig. 7.13 shows the real and imaginary bands for the $[001]$ direction in GaAs [136]. The energy scale is set to 0 eV at the valence band edge. The complex bands inherit the symmetry properties of the real bands. Therefore the loops connect only bands with the same symmetry. The conduction band (the band starting at 1.5 eV at the Γ -point) is connected with the light hole band, while the heavy hole band closes a loop with the next higher lying conduction band (at 4.3 eV).

It is important to note that the complex band structure is not just of theoretical interest: The concept of complex band structure is particularly important when electronic properties of solid interfaces or surfaces are considered [137, 138]. In the past decade the evanescent states have come to the attention of several fields of research, e.g. when transport through semiconductor heterostructures or superlattices [139, 140], magnetic tunnel junctions [134, 141], or molecular electronic systems [142, 143] is considered.

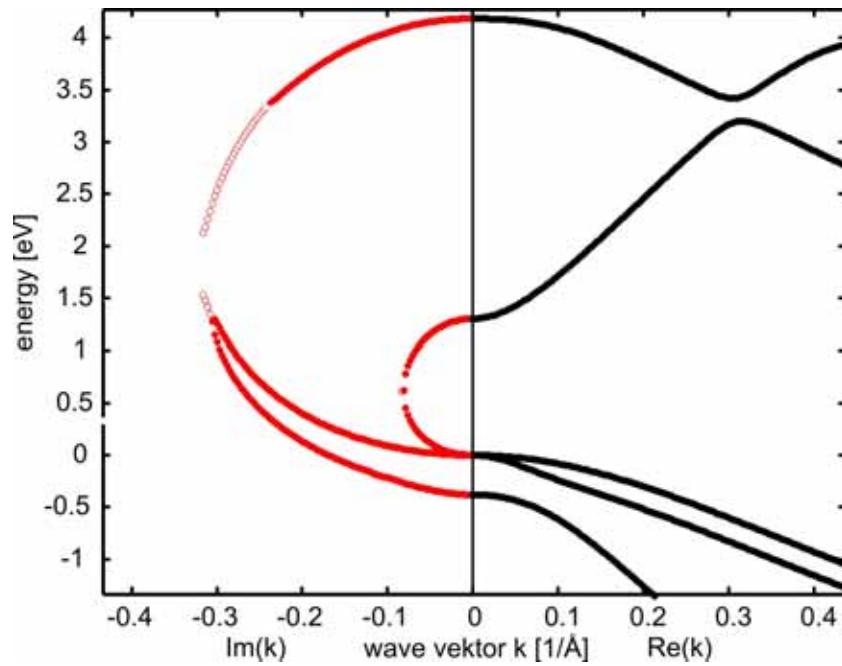


Fig. 7.13 Complex and real band structure of GaAs in the $[001]$ direction. The shown band structure is calculated with empirical pseudo-potentials. (in red) complex bands and (in black) real bands (refer to [136]).

7.3.1. Asymmetric decay constants

Chapter 7.2 shows that the acceptor resonances have a triangular distribution. The most prominent feature is that the resonance is shifted nearly completely to one side of the dopant atom. The decay constants in the semiconductor directly enter the resonant tunneling calculation. In chapter 7.1 they are accounted for by the simple equation (2). They depend only on the energy in the barrier. In a more accurate description - the complex band structure - the decay constants also depend on the direction of tunneling. Whether a resonance can build up or not now depends on the direction of incidence of the tunneling electron. One approach to extend the resonant tunneling model to the three-dimensional problem is to account for different tunneling paths. Similar to path integrals the tunneling is still treated one-dimensional, but the tunneling path is curved by the local variations in the potential. This approach was demonstrated previously by Feenstra to calculate interband tunnel current from a tip induced quantum dot to the bulk sample [144].

The acceptor locally perturbs the depletion layer potential. It lowers the tunneling barrier through the depletion layer. Therefore it is more favorable for an electron to tunnel through the Coulomb potential of the acceptor than through the bare depletion layer. The resulting tunneling paths are bent towards the acceptor core when the tip is nearby. This situation is sketched in Fig. 7.14. The

electrons tunnel along different tunneling paths as the tip scans over the surface. The tunneling direction is no longer strictly perpendicular to the surface. The tunnel paths have in-plane components.

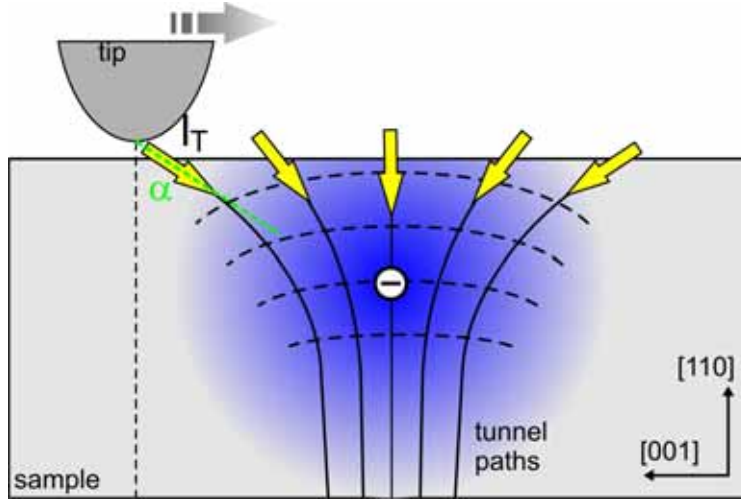


Fig. 7.14 Schematic of the tunnel paths near an acceptor atom in an eikonal approximation. The Coulomb potential of the acceptor core perturbs the depletion layer that is present at the surface. Without an acceptor the tunnel path is a straight line perpendicular to the surface (dotted line). With an acceptor the tunnel paths are bent (solid lines) because it is more favorable for an electron to tunnel near the acceptor Coulomb potential. At the surface the tunnel path has an in-plane component α .

The position of the tip with respect to the dopant atom translates into a certain direction and angle of the incident electron. The tip's lateral position is projected to a certain wave vector.

Of course the approximation of the direction dependent tunneling in terms of curved tunneling paths is quite crude. But equally crude is the approximation that the electron is tunneling strictly perpendicular to the surface. The electron probability density during tunneling is spatially broadened [145]. For example the calculated tunnel current distribution from a point-like tip has a Gaussian distribution [146]. Although the STM favors states with wave vector perpendicular to the sample, it is sensitive to tunnel current with in-plane wave vector components. Usually the states without in-plane component dominate the tunnel current because the tunnel matrix element is largest for those states. But if the vertical tunneling is suppressed, states with high in-plane component are visible [147]. On Si (111) (2x1) it was shown that even states from the edge of the surface Brillouin zone may contribute [39]. In the bias window of the acceptor resonances, conventional tunneling through the depletion layer is suppressed. Near an acceptor the tunnel paths without in-plane wave vector are negligible. The tunnel paths through the acceptor resonance are enhanced and tunneling with in-plane wave vector is observable.

In an isotropic medium there is no difference for the tunnel paths to the left or right side of the acceptor in Fig. 7.14. But in the semiconductor the decay constants for both paths may be different because the left one has a $[00\bar{1}]$ component and the right one a $[001]$ component. As mentioned above the decay constant is dependent on the electron energy **and** the direction of tunneling (wave vector) in the semiconductor. The angular distribution of the complex band structure therefore determines the spatial symmetry properties of the acceptor resonance.

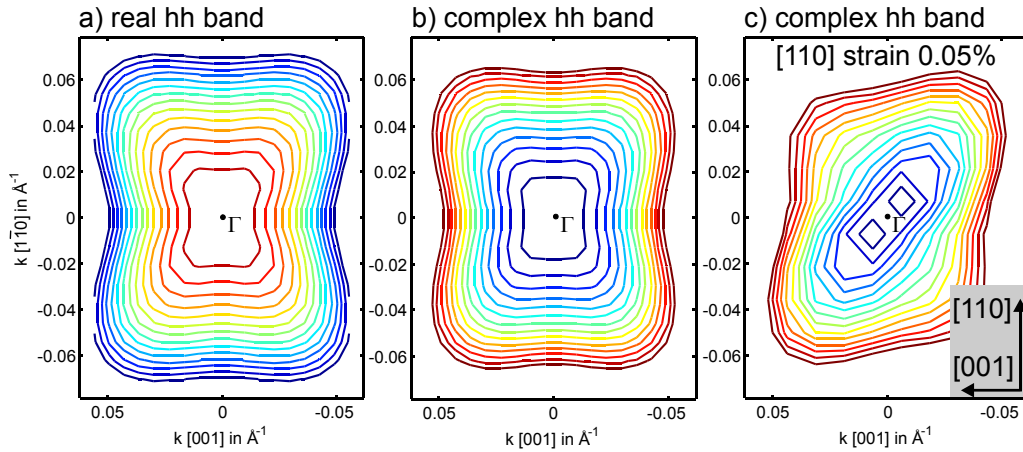


Fig. 7.15 Band structure of GaAs in a plane spanned by $[001]$ and $[110]$. All three plots show energy contour lines of the heavy hole (hh) band. About 10% of the Brillouin zone are plotted. (a) the real band structure, (b) the corresponding complex band structure, and (c) the complex heavy hole band under shear strain. The strain is chosen: $[110]$ shear strain by 0.05% of the $[110]$ monolayer distance.

The same band structure calculations used to calculate the surface induced anisotropy of the acceptor wave function are now employed to calculate the angular distribution of the complex band structure. Fig. 7.15 presents 2D sections of the band structure, similar to those presented in chapter 6.2. The real heavy hole band (Fig. 7.15a) is reproduced from Fig. 6.10 and exhibits the well-known rectangular shape of the bulk GaAs crystal. The corresponding complex band (same lattice directions, but imaginary wave vector) has the same characteristic shape (Fig. 7.15b). In the complex valence bands the zone center is a minimum, because the decay constant is smallest close to the valence band edge and increases with increasing energy in the bands. The rectangular shape points to one important finding. The bulk complex band structure has the same symmetry as the bulk real band structure. In particular it has no asymmetry with respect to the $[001]$ direction. But the measured acceptor resonances have a strong $[001]$ asymmetry. The bulk band structure alone is not capable to explain this effect. This is similar to the acceptor wave function.

The previously discussed surface induced asymmetries have to be included. In Fig. 7.15c a shear strain in $[110]$ direction is applied. The complex bands become asymmetric along this direction. The band elongates along the $[11\bar{1}]$ direction

and is compressed along the $[111]$ direction. The plane spanned by $[110]$ and $[001]$ gives a first hint to the angular asymmetry of the decay constants. A better understanding is reached, if the decay constant is evaluated with respect to the sample surface. The angular distribution of the decay constants for a certain energy in the band gap is evaluated for a section of the reciprocal space. The hemisphere spanned by the $[001]$, $[\bar{1}10]$ and $[110]$ direction is chosen. All tunneling directions that may occur on the $[110]$ surface for positive bias are represented in this hemisphere. The results are shown in Fig. 7.16 and Fig. 7.17 respectively. For the calculation of the former a shear strain is included in the band structure calculation. The latter includes an electric field along $[110]$.

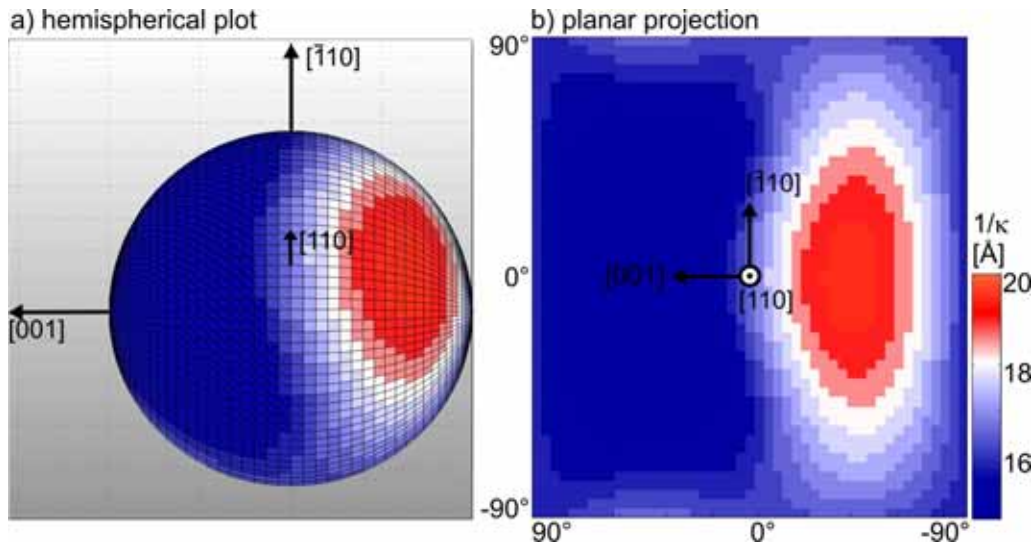


Fig. 7.16 Angular distribution of the inverse decay constant $1/\kappa$ in the units of Å. A shear strain of 0.25% of the $[110]$ monolayer distance is applied. The color scale for both images is the same. (a) 3D visualization of the angular distribution on a sphere. The lattice directions are indicated by black arrows. (b) projection of the angular distribution to the (110) plane. The lattice directions are indicated in the middle. The transverse angles in units of degrees are the image axis

Detailed information on the origin of these surface induced fields has been discussed in chapter 6.2 and will not be repeated here. Instead of the decay constant κ the inverse decay constant $1/\kappa$ is shown in the figures. The inverse decay constant is the characteristic length on which the tunnel current drops to $1/e$. Large inverse decay constant means that the electrons reach far into the barrier (shown in red color) and small $1/\kappa$ corresponds to a rapidly decaying wave (shown in blue color). Each figure shows a 3D visualization of the simulated hemisphere and a projection of the decay constant distribution to the (110) plane. The band with the largest inverse decay constant is chosen for the images. The calculated decay constant distributions match the triangular symmetry of the acceptor resonances. The triangular resonances are shifted to the $[00\bar{1}]$ side of the acceptor atom on the (110) surface. Both decay constant distributions are asym-

metric with respect to the (001) plane. The inverse decay constant is largest on the $[00\bar{1}]$ side of the hemisphere. A tunnel path along this direction reaches further into the semiconductor than one along the opposite direction. The surface induced asymmetries that act along the $[110]$ direction cause a distinct asymmetry along the perpendicular $[001]$ direction. No asymmetry is induced with reference to the $[\bar{1}10]$ direction. This is supported by the measurement. The triangular resonances are mirror symmetric with respect to $[\bar{1}10]$. Even the triangular shape is approximately reproduced by the inverse decay constants. This is best seen in the 3D visualizations.

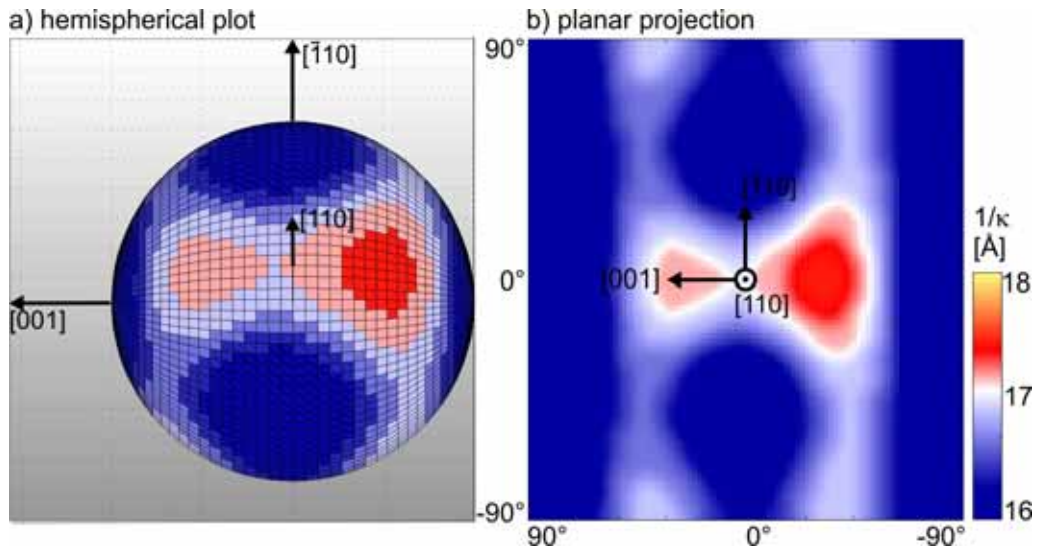


Fig. 7.17 Angular distribution of the inverse decay constant $1/\kappa$ in the units of \AA . An electric field of 1.5eV/nm in $[110]$ direction is applied. The color scale for both images is the same. (a) 3D visualization of the angular distribution on a sphere. The lattice directions are indicated by black arrows. (b) projection of the angular distribution to the (110) plane. The lattice directions are indicated in the middle. The transverse angles in units of degrees are the image axis

The reduced decay constants are concentrated in a cone tilted out of the $[110]$ direction to the $[00\bar{1}]$ side. The projection of this cone to the (110) surface results in a triangular shaped region. Within the tunnel path approximation the triangular shaped resonance is explained by the anisotropic distribution of the decay constant in the semiconductor. The resonant tunnel process enhances the asymmetric decay and gives rise to highly anisotropic shapes. The anisotropy is not present in the bulk band structure. Additional symmetry reduction at the surface due to the surface strain field or the electric field of the tip causes the anisotropic shape of the resonances. Both effects produce the same symmetry reduction, but the comparison of the decay constant distributions suggests that the asymmetry with respect to $[001]$ is stronger for the strain field.

7.4. Summary

In summary a model has been derived that explains the enhanced conductivity at acceptors if the acceptor state is occupied. The acceptor exhibits an unscreened Coulomb potential. For the bias window of depletion no valence band states are directly accessible at the surface. Nonetheless a tunnel channel from the tip through vacuum gap and depletion layer into the acceptor band in the sample is possible. The acceptor's Coulomb potential in the depletion layer forms resonant tunneling paths, that enhances this tunnel channel for certain bias voltages. Fig. 7.18 sketches the two prerequisites for the resonant tunneling process. The acceptor in the depletion layer acts as an amplifier (1). The otherwise vanishing band gap conductivity becomes detectable. The acceptor band pins the tunnel channel to a narrow energy window in the bulk semiconductor (2). In these terms it acts as an energy filter. Both parts together (amplifier and energy filter) result in the observed non-monotonous $I(V)$ -characteristics. Within a one-dimensional model the $I(V)$ -characteristics are reproduced.

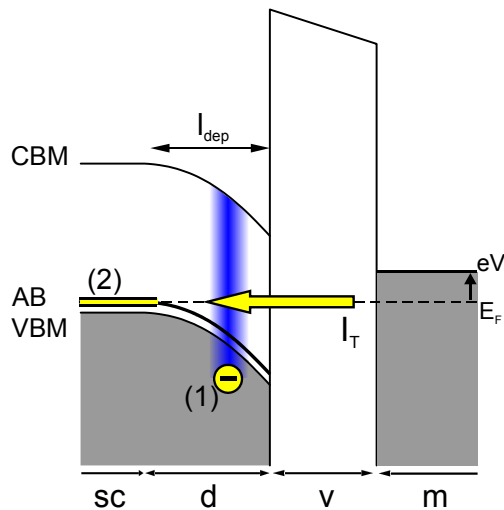


Fig. 7.18 Schematic of the band alignment for the depletion bias window (similar to the inset of Fig. 7.2). A peak in the $I(V)$ -curve, and in particular the NDC, need two prerequisites: (1) the acceptor Coulomb potential, which acts as an “amplifier” and the acceptor band in the bulk, which acts as an “energy filter”.

The acceptor resonances exhibit a highly anisotropic shape. The enhanced conductivity is shifted nearly completely to one side of the dopant atom along the $[001]$ direction. This is qualitatively explained by the angular anisotropy of the decay constant in the semiconductor depletion layer. The surface induces a symmetry reduction that accounts for the anisotropy with respect to the (001) mirror plane. Measurements of acceptors in different depths under the surface show that the anisotropy becomes stronger for increasing dopant depth. This implies that the acceptor resonance is dominated by the decay constant anisotropy in the surface region. The exact depth of the dopant is not relevant for the overall symmetry of the resonance. They lead to a spatially broadened resonance that produces a better image of the anisotropic shape.

These findings lay weight on an important issue: On III-V semiconductors a large amount of the measured tunnel current may not be interpreted only as the local density of states of the undisturbed surface or defect. The tip induces band bending is a strong perturbation! Additional tunneling channels near dopant atoms are created and may be associated with states / resonances localized at the dopant atom but they differ largely from the “bulk-like” dopant-state, or even do not exist in the bulk sample.

8. Local manipulation by electric fields

This chapter studies the influence of electric fields on anisotropic acceptor contrasts of dopant atoms in a p-i-n junction. The spatial distribution of the acceptor resonance is strongly affected by fields on the order of 0.1 eV/nm. In addition, the resonance can be suppressed by depleting the host crystal of unoccupied states directly behind an acceptor atom.

The previous chapters demonstrated that uniaxial strain or electric fields perpendicular to the sample surface have a strong influence on the acceptor induced tunnel processes. Unfortunately it is not possible to disentangle both effects. The strain is always present at the surface. And the electric field is induced by the tip itself and therefore connected to the sample bias. It is not possible to do a spectroscopic measurement with separately controlled symmetry reducing effect. At this point the p-i-n diode structure provides the unique possibility to gain an additional control parameter. The diode structure consists of sandwiched layers of p-doped intrinsic and n-doped GaAs. It possesses a strong electric field that lies in the plane of the surface. It is perpendicular to tip induced electric field and the

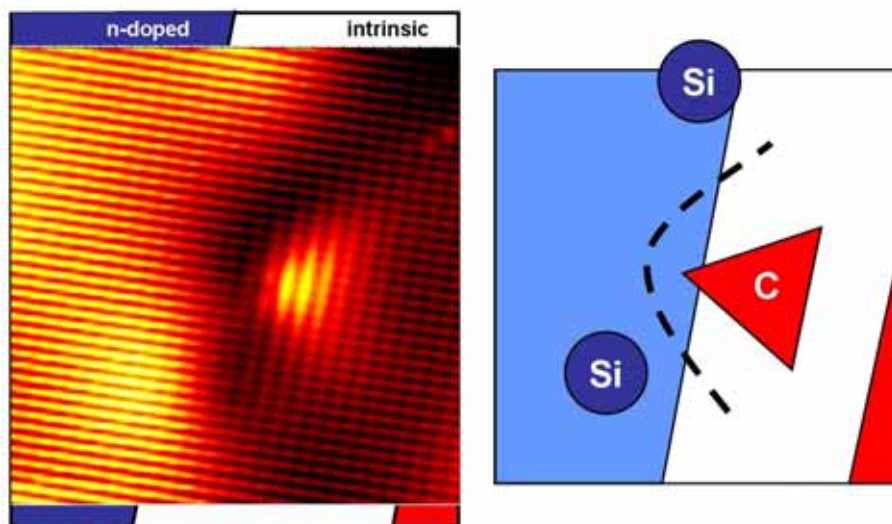


Fig. 8.1 (left) (14 X 14) nm² constant current topography of a single carbon acceptor in front of the n-interface. The electrostatic situation can be estimated from the sketch of the dopant distribution (right). The acceptor is directly exposed to the electric field of two nearby silicon acceptor. The influence of this field is visible in the topography by the topographic height change from left to right.

surface strain field. The strength of the in-plane field is an externally adjustable parameter by means of the diode bias. The heterostructure presented in chapter 3 is modified for the following measurements. A low concentration of carbon dopants is incorporated in the intrinsic region. Fig. 8.1 shows one carbon acceptor that is directly in front of the n-doped interface. The acceptor is identified by its prominent triangular shape. The distortion of the electric field around the acceptor atom is prominently seen by the change in color of the surface. At the right side of the dopant the surface is dark red and on the n-side it is yellow and orange.

The acceptor atoms within the intrinsic region are exposed to the in-plane field. The impact of this field on the acceptor resonances is studied with spatially resolved $I(V)$ -spectroscopy. The p-i-n diode internal field has impact on acceptors in two ways:

- The p-i-n built in potential is added to the tip induced field. The diode locally shifts the energetic positions of the bands and acceptor states with respect to their configuration in a homogeneously doped sample. This effect will be exploited in the next section. It is used to detune the resonance condition of a subsurface acceptor
- The diode built-in potential has a strong in-plane electric field. The acceptors are exposed to the electric field and their anisotropic shape is affected by it. This will be discussed in section 8.2.

Which effect is predominantly observed at a specific acceptor depends on the surrounding dopant distribution.

8.1. **Suppression of the resonant tunneling channel**

The detuning of the acceptor resonance is studied at the acceptors shown in Fig. 8.2. Here, two carbon acceptors stick out of the p-doped region (the upper and lower acceptor in the image). A third acceptor lies about 2 nm to the right side and thus further into the field free p-doped region. Without a diode bias applied all three acceptors exhibit the triangular contrast (Fig. 8.2a). The triangular protrusion on the two foremost acceptors is faint but still visible. Then the diode is operated in reverse bias at -0.78 V. Fig. 8.2b shows the topography of the same region under this condition. The triangular contrast of the middle acceptor is still present, but the triangular contrast of the two foremost acceptors disappeared. Only circular depressions are imaged. The diode's built-in potential must have an impact on the acceptor resonance. By applying a reverse bias, the built-in potential is increased. In spatially resolved $I(V)$ -spectroscopy the situation is analyzed in detail.

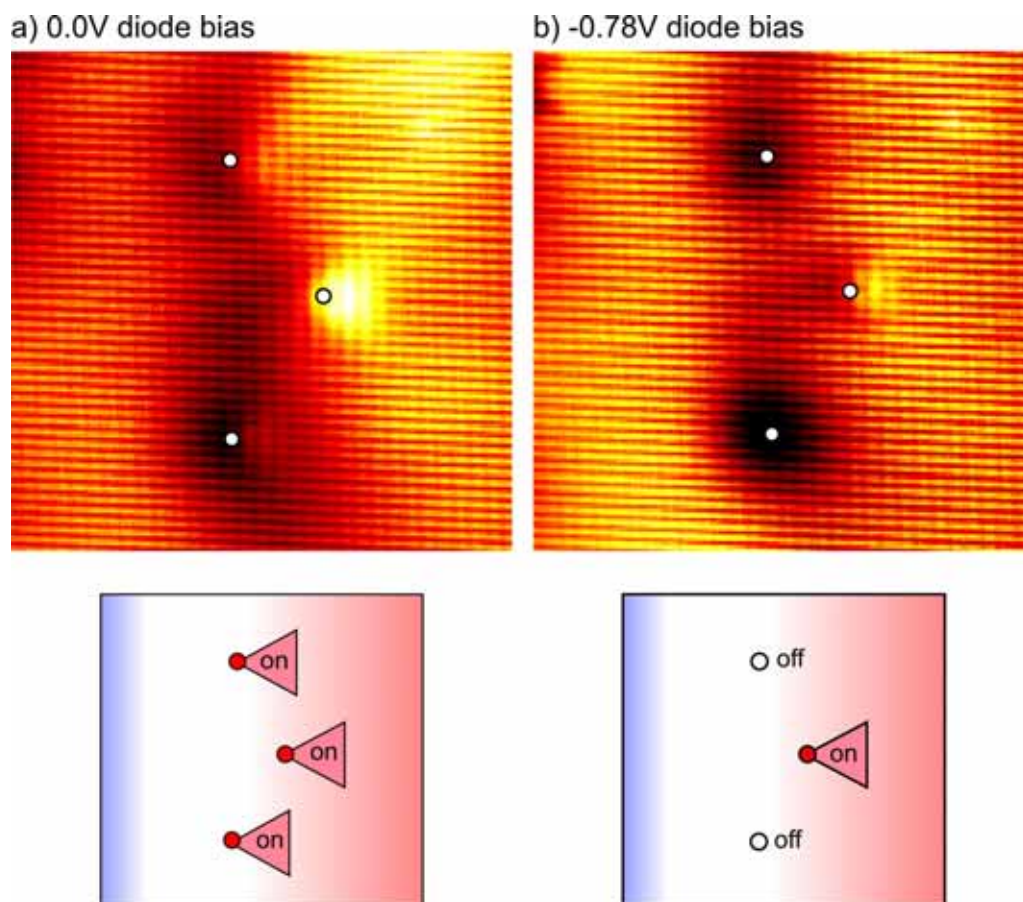


Fig. 8.2 Two constant current topographies of the same (18×18) nm^2 area at the p-side interface of the p-i-n-junction far away from any surface defect, recorded at +1.6 V sample bias with 100pA tunnel current. The left part of the image is the intrinsic region and the right half is the end of the p-doped region. a) Without a diode bias applied, the triangular contrasts of three buried acceptors are visible. They terminate the p-doped region. b) with reverse bias of -0.78 V applied, the triangular contrasts of the two foremost acceptors at the interface disappear. Only the circular depression caused by the acceptor charge remains. The acceptor that is positioned $\sim 2\text{nm}$ further away from the pin-interface is still visible.

Fig. 8.3 presents two dI/dV -sections through one of the acceptors of Fig. 8.2. The conductivity is plotted with logarithmic scale against sample bias and lateral position. The section in Fig. 8.3a is recorded without diode bias applied. The built-in potential of the diode is resolved. The upper red region of the section represents the conduction band tunneling. The lower red region represents the valence band tunneling. The conduction band and valence band tunneling is separated by the band gap region (black in the dI/dV section). The band edges are bent downwards into the direction of the intrinsic region by the diode built-in potential. This has been described earlier for the bare diode structure (refer to chapter 3.4). The slope of the band edges in this region is a measure for the field strength. The acceptor core position is extracted from the setpoint topography and indicated by the white arrow. In Fig. 8.3a the diode field is already screened

in the vicinity of the acceptor. The band edges are flat above the acceptor core. The distortion of the valence band tunneling due to the acceptor's negative charge is visible. The valence band tunneling region (negative sample bias) is bent upwards above the acceptor's position. In the band gap region from 1.0 V to 1.5 V the acceptor induced resonances are resolved and highlighted by the white circle. The dI/dV -section across the acceptor matches those recorded above acceptors in homogenously doped samples.

This situation changes, when the reverse diode bias is applied. The acceptor resonance in the band gap region disappears. However, the impact of the acceptor charge is still present in the valence band. The detection limit of the presented dI/dV -measurement is a tunnel current of 50 fA. Within this resolution it can be assumed that the resonance is not just shifted to a different energy, but it is completely suppressed. The built-in potential is increased as seen by the higher slope of the band edges in the intrinsic region. Additionally the diode field penetrates further into the doped regions. The changed potential configuration perturbs the acceptor induced conductivity in the band gap region. The acceptor resonance is switched off! The changed potential configuration at the acceptor seems to suppress the resonances.

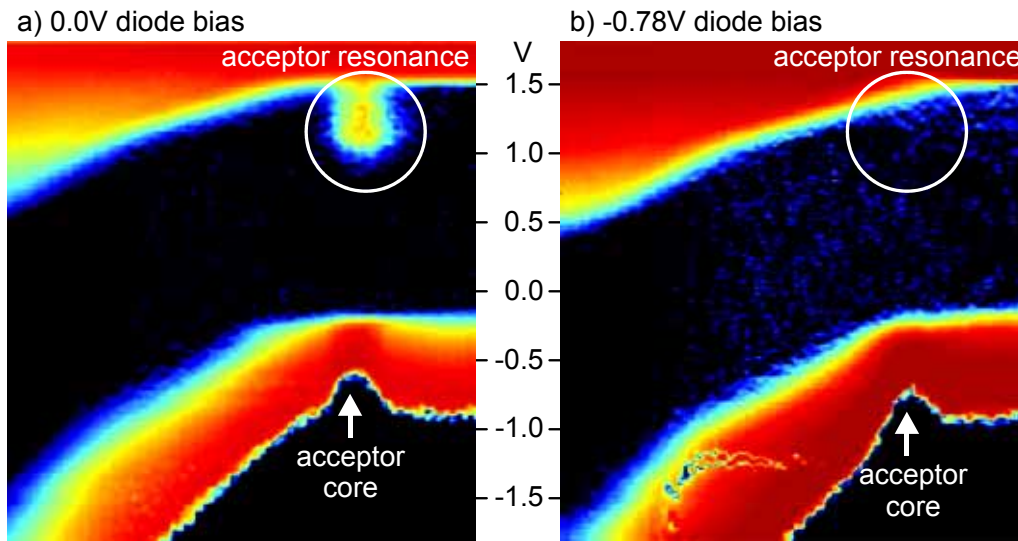


Fig. 8.3 $\log(dI/dV)$ sections of spatially resolved $I(V)$ -spectroscopies recorded on the acceptors presented in Fig. 8.2. The vertical axis resembles the sample bias (interval from -1.8 V to +1.8 V) and the horizontal axis is the lateral displacement on a line perpendicular to the p-i-n interface directly through the acceptor atom. The logarithm of differential conductivity is plotted color coded. The detection limit of the tunnel current in the dI/dV -sections is ~ 50 fA a) without a diode bias applied, the acceptor resonance is clearly visible above the acceptor core at a sample bias from 0.7V to 1.5 V. b) With the reverse diode bias voltage of 0.78 V applied, the acceptor resonance vanishes. The electrostatic effect of the acceptor core on the band tunneling regions is visible irrespective of the applied diode bias.

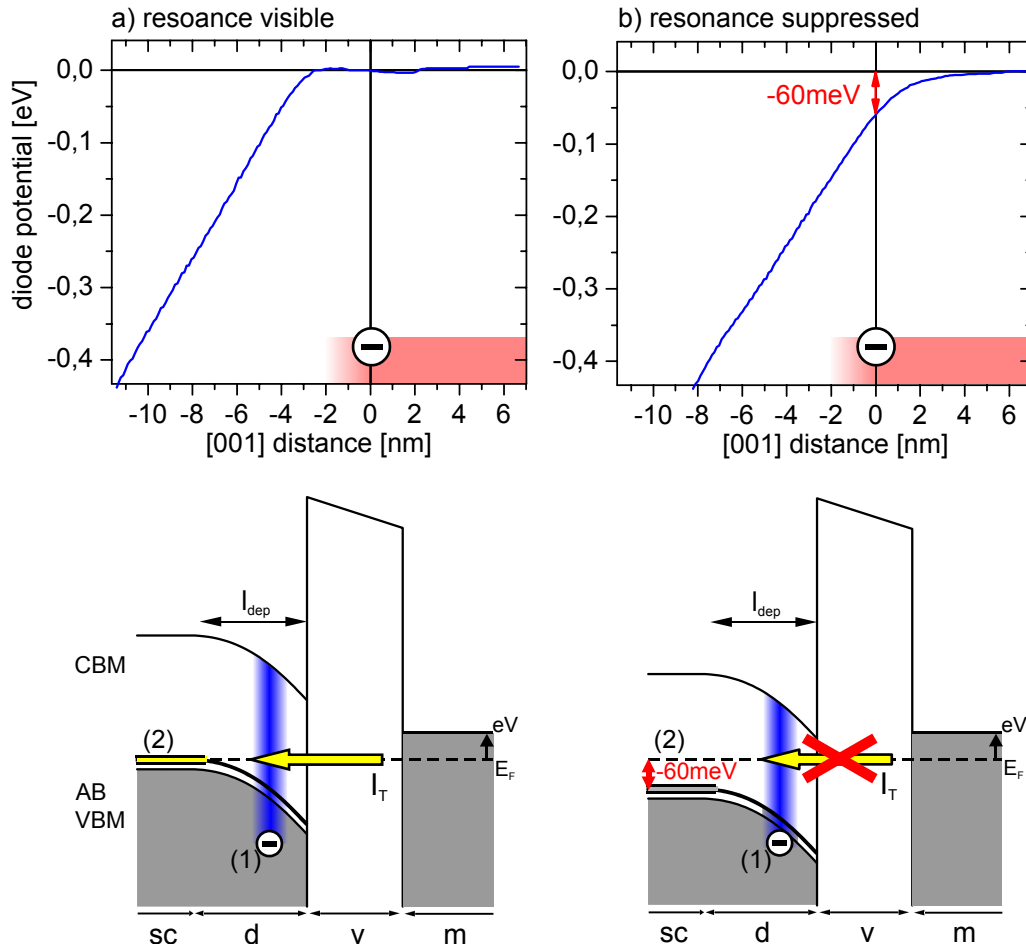


Fig. 8.4 (upper part) Diagrams showing the electrostatic potential of the diode. (a) without diode bias applied and (b) with reverse diode bias -0.78 V applied. The potential is evaluated along a $[001]$ section, i.e. perpendicular to the p-i-n interface planes. Lateral position $=0$ indicates the position of the acceptor core (sketched by the $(-)$ sign). The p-doped region extends to positive distances. The drop of the built-in potential into the intrinsic region (to negative distance) is clearly seen for negative distance. (a) Without diode bias applied, the potential is flat at the acceptor's position. (b) In the reverse diode bias case the potential has a value of -60 meV at the acceptor's position. (lower part) The band alignment schematics are printed for both situations.

The diode potential can be extracted for both situations (no diode bias and reverse diode bias) from the $I(V)$ -spectroscopies in the manner mentioned in chapter 3. Fig. 8.4 plots the diode potential for a line perpendicular to the p-i-n interface planes. The potential drop from the p-doped region (marked red in the diagram) into the intrinsic layer is clearly resolved. Without diode bias applied, the potential is completely screened well before the acceptor's position. It is flat in a window of about 3 nm around the acceptor (Fig. 8.4.a). In the case of reverse diode bias the conduction band edge still rises in energy at this point. The diode potential is not screened at the acceptor's position. In Fig. 8.4b it becomes obvious that the diode potential penetrates further into the p-doped region. The

diode potential has a negative value of -60 meV at the acceptor's position. Thus, an additional (negative) potential component is present at the position of the acceptor core when -0.78 V diode bias is applied. If no diode bias is applied, the band alignment perpendicular to the surface is equal to that on the homogeneously doped samples. Along the tunnel path the negative charge of the acceptor induces a double barrier potential and a tunneling resonance builds up (compare band alignment in Fig. 8.4a with Fig. 7.18). The diode potential perturbs this band alignment throughout the whole depth of the sample. The bands along the tunnel path through the acceptor are shifted downwards by 60 meV (see Fig. 8.4a), when the reverse bias of -0.78 V is applied. The acceptor band which provides the unoccupied final states for the resonant tunneling channel is pulled completely under the Fermi energy. Because no unoccupied states are available along the tunnel path, the acceptor resonance cannot build up and is therefore not measured.

The amount of diode induced downwards shifting of the bands depends on the position relative to the i-p interface. In fact the unoccupied states are repelled only directly behind the acceptor's position. About 4nm into the direction of the p-doped region the diode potential becomes flat (see Fig. 8.4b). There the Fermi energy is still in the acceptor band. Fig. 8.5 shows a schematic of the complete potential configuration from the surface to the bulk sample for the presented sections.

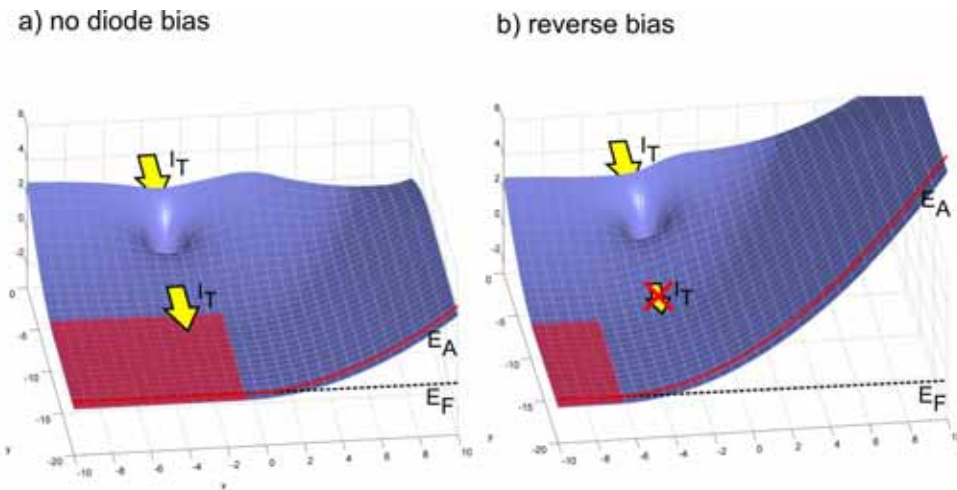


Fig. 8.5 Schematic of the potential distribution for the valence band near an acceptor atom: (a) no diode bias applied (b) reverse diode bias applied. The situation is viewed from the bulk of the sample, i.e., the surface with its depletion layer is in the background. The tunnel current from the tip is marked by yellow arrows. The p-side of the diode is on the left and the intrinsic side on the right. The diode potential is sketched as increasing potential from left to right, that is present from the surface to the bulk. At the surface a tip induced potential is present, as well. The acceptor's Coulomb potential is present in the tunnel path, seen as a hole in the schematic. The unoccupied states in the acceptor band are indicated with red color. Both the tip induced field and the diode potential tend to pull the acceptor band under the Fermi energy and thereby repel the unoccupied states. The red area in (a) is larger than the area in (b).

The position of the band edges is influenced by the tip and by the diode built-in potential. This bending is the consequence of an electrostatic potential rigidly shifting the bands up or down. Near the i-p interface of the p-i-n diode there is the diode depletion layer. Coming from the p-doped region and going into the intrinsic layer, the valence band edge is pulled downwards. For the bias interval of interest (0 V to 1.5 V) the same happens at the sample surface. The tip locally pulls down the valence band edge and creates a depletion layer at the surface. On homogeneously p-doped samples the acceptor resonance is observed, because unoccupied states exist in the bulk at the depth where the surface depletion potential is already screened. The subsurface acceptor induces the tunneling resonances by its Coulomb potential. It is sketched as a hole-like depression in the local potential in Fig. 8.5. In order to build up the resonance, not only the acceptor is needed. Empty states in the sample have to be present that can be resonantly addressed. The additional diode depletion potential may pull these states under the Fermi energy. Without diode bias applied this is not the case. The diode potential is completely screened at the acceptor position and unoccupied states exist behind the acceptor potential as depicted in Fig. 8.5a. Electrons can resonantly tunnel through the acceptor potential and reach the unoccupied states in the bulk (indicated in red in the figure). But when a reverse diode is applied, the diode depletion layer penetrates further into the p-doped region (Fig. 8.4b). The unoccupied states no longer exist behind the acceptor's Coulomb potential. Even with the acceptor potential present (as seen by the distortion of the valence band tunneling in Fig. 8.3), the resonance does no longer evolve, because there are no final states directly behind the acceptor.

It is worth noting that the diode bias needed to switch the resonance depends on the local geometric configuration of the acceptors. The local dopant distribution determines the local strength of the diode field and the way it penetrates into the p-doped region under reverse diode bias. In the case presented here, the resonance is present without applied diode bias and is suppressed, when the diode potential is increased by the external diode bias. If an acceptor is located a bit deeper in the intrinsic region, the diode potential is already present at zero diode bias. The acceptor resonances are suppressed and show up, if the diode potential is decreased by applying a forward diode bias. This is for example the case for the measurements presented in chapter “the p-i-n diode” in Fig. 3.10. At the p-doped interface an acceptor resonance evolves at +0.63 V forward bias.

The ability to switch off the tunneling resonance by depleting the unoccupied final states directly behind the Coulomb potential is strong experimental evidence that a resonant process must be involved. If the acceptor resonance was due to a sequential tunneling process, it would not matter whether the unoccupied final states are located behind the acceptor or to the side of it. In the case of reverse bias the injected electrons could still be drained in unoccupied states that are still present at the right side in the p-doped region. But the resonant tunneling process is extremely dependent on the alignment of source, drain and amplifying double barrier potential.

8.2. Influence of the in-plane electric field on the anisotropy

The previous section demonstrated that the diode potential is capable of depleting the unoccupied states behind the acceptor. Thereby the acceptor resonance is suppressed. Experiments show that the resonance at some acceptors in the intrinsic region is not suppressed, although the electric field distorts the band edges at the position of the dopant. For these cases the surrounding dopant distribution seems to provide enough charge to leave some states unoccupied behind the dopant atom of interest. For these configurations it is possible to study the influence of the electric field on single deeply buried dopants. Fig. 8.6 depicts the corresponding situation.

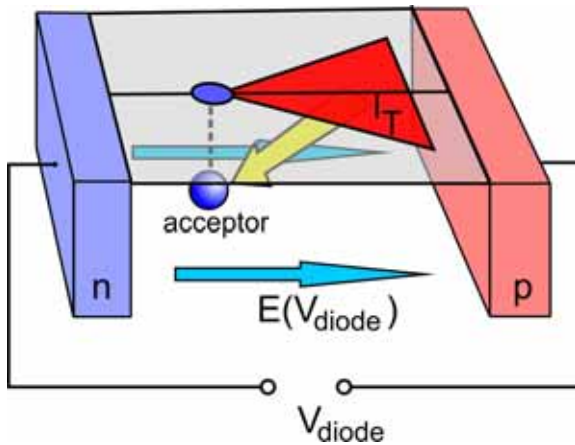


Fig. 8.6 Schematic of an acceptor in the intrinsic region of the p-i-n diode. The acceptor is exposed to the in-plane field. Its influence on the triangular acceptor resonance at the surface is studied.

The electric field in between the n-doped and p-doped layer is nearly constant and has a strength on the order of 10^6 V/m (see chapter 3). The symmetry reducing field at the surface and the diode's electric field are perpendicular to each other. For an acceptor in the sketched configuration both fields add up to an effective field that is tilted out of the surface normal. Additionally the diode's electric field is externally controlled by the diode bias. This results in the possibility to investigate the changes in the acceptor resonance with controlled tilting of the effective electric field in or out of the surface plane.

Fig. 8.7 shows the topographies of a series of spatially resolved $I(V)$ -spectroscopies. The spectroscopy series consists of three measurements. One is recorded with a forward diode bias of +0.8 V, the second with zero diode bias and the third with a reverse diode bias of -0.8 V. At forward and reverse bias a diode current of about 60-70mA is driven through the structure. The experiments on the diode structure show that thermal drift occurs when current load is changed. The lateral drift of the diode structure can exceed 30nm when the current is changed drastically. The thermal drift is inevitable on the p-i-n diode

because the device shows an internal Peltier effect. Depending on the applied bias the active layer of the heterostructure is actively heated or cooled by the diode current [148, 149]. Reference marks on the sample are necessary to register all three spectroscopy sets to each other. In the measurements presented below one dark and one bright defect (denoted with R1 and R2 in Fig. 8.7a) are chosen. The three small images in Fig. 8.7 show the three topographies of the series. Both reference marks are visible in all three images.

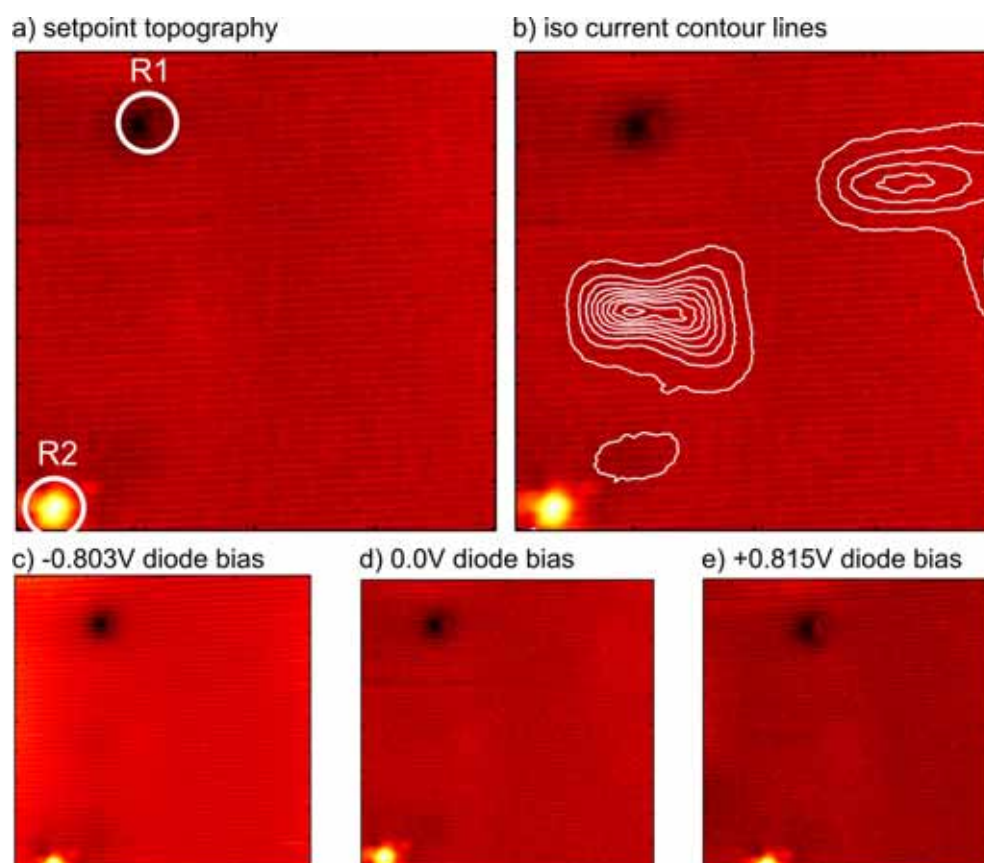


Fig. 8.7 (20 x 20)nm² setpoint topographies of the STS measurements. The setpoint bias is +1.8V. a) the two surface defects serve as reference marks (R1, R2) to follow the thermal drift of the diode structure during diode bias voltage changes. (b) Current contour lines (evaluated at +1.2 V sample bias) show the position of the acceptor resonance relative to the reference marks. c)-e) The three setpoint topographies of the measurement series. c) at reverse diode bias, d) at zero diode bias and e) at forward diode bias. The investigated acceptor has no impact on the topography!

The topography setpoint for all spectroscopies is +1.8 V. At this voltage the acceptor atom of interest has no impact on the topography. This avoids topographic artifacts. Fig. 8.7b plots tunnel current contour lines evaluated at +1.2 V as reference. They show the position of the acceptor resonance in the setpoint topography. All spectroscopies are normalized to a plane of constant height with the simultaneously recorded apparent barrier height.

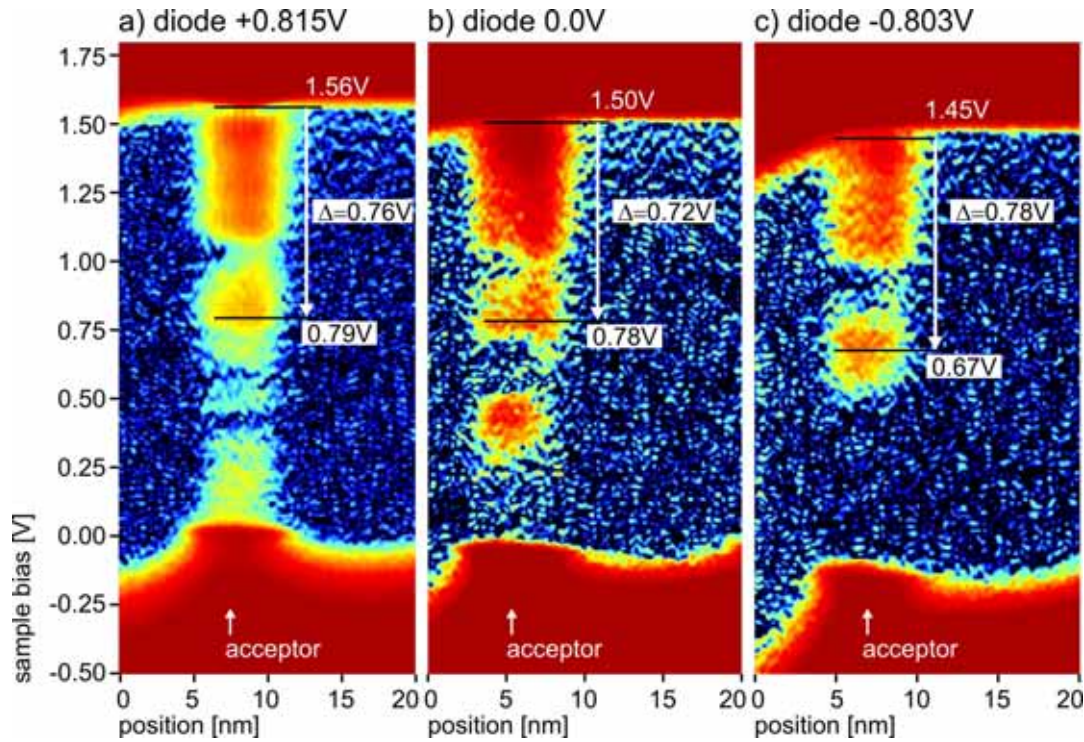


Fig. 8.8 $\log(dI/dV)$ -sections directly through the acceptor at the three different diode biases (a) +0.815 V forward bias, (b) 0.0 V diode bias, (c) -0.803 V reverse bias. The differential conductivity is plotted color coded against lateral position and sample bias voltage. The band related conductivity is red (high conductivity). The band gap region is black to blue (low conductivity). Due to the logarithmic scale the spreading of the acceptor resonance over the band gap window is clearly visible.

The voltage dependent behavior of the area of interest is best observed in dI/dV -sections across the diode active region. A 20 nm wide section through the acceptor atom is presented in Fig. 8.8. All three cross sections are evaluated above the same acceptor atom. The differential conductivity is plotted in logarithmic scale to highlight the acceptor resonances in the band gap. The color scale shows high conductivity in red and low conductivity in blue. Thus, the band related conductivity is seen as red regions. The conduction band tunneling starts at about +1.5 V and the valence band related conductivity is visible at negative sample bias. The acceptor resonance is spread over the band gap region. The diode in-plane potential bends the conduction and valence band. The acceptor investigated here, is close to the p-doped region. The effect of the diode potential only perturbs the left portion of the section. The positions from 0 nm to 10 nm are influenced by the diode. The local strength is best estimated by the conduction band alignment as described in chapter 3. The tip induced band bending is minimal there. From forward bias to reverse bias the field strength at the acceptor increases. In the field free p-doped region of dI/dV -section Fig. 8.8a the conduction band edge is measured at +1.57 V. For zero diode bias (Fig. 8.8b) it is at 1.52 V and for the reverse bias case (Fig. 8.8c) it is at 1.48 V. The diode bias

is applied with reference to the p-doped side. Therefore, the conduction band edge in the field free p-doped regions should be at the same energetic position for all diode bias voltages. However the diode is not ideal. At high forward or reversed bias a fraction of the applied diode bias drops in the thick p-doped and n-doped layers due to series resistance effects. The reference levels of the homogeneously doped regions are shifted by this amount. Energetic positions in the three sections are therefore referenced to the conduction band edge of each dI/dV-section.

For forward bias the externally applied diode bias decreases the built-in potential. The dI/dV-section Fig. 8.8a is recorded for +0.82 V forward bias. The conduction band edge is bent downwards by 50 mV with respect to the edge at the right side of the section. The in-plane electric field at the acceptor is minimal. The second dI/dV-section Fig. 8.8b is recorded without diode bias applied. The conduction band is bent by 90 mV. The section shows that at the position of the acceptor resonances the bands are not flat. An in-plane electric field is present at the position of the acceptor. The third dI/dV-section Fig. 8.8c is acquired at -0.80 V diode bias, corresponding to strong reverse bias. The conduction band edge is bent downwards by 230 mV. The band edge has a high slope at the acceptor position. A strong in-plane electric field acts on the acceptor resonance.

The spectroscopy series from forward diode bias over zero diode bias to reverse diode bias results in a measurement series for increasing in-plane electric field at the acceptor. For minimal in-plane field the acceptor resonance is spread over the whole band gap window. The measured resonances match those observed for acceptors in homogeneously doped environment. The conductivity distribution is comparable with the one shown in Fig. 7.3 (chapter 7.1). Two prominent groups of conductivity are visible one from 0.6 V to 0.9 V and the other from 1.1 V to 1.5 V. At low positive bias from 0 V to 0.6 V a few faint conductivity peaks are resolved. Those peaks vanish when the in-plane field is increased. But it is not possible to judge whether the peaks are suppressed or if they just disappear in the current noise of the measurement. This is due to the changed tip sample distance above the acceptor. Due to the increased built-in potential, more conduction band states are available at the topographic setpoint of +1.8 V. Due to the constant current feedback, the tip is retracted a little bit and the signal-to-noise ratio in the band gap decreases.

The conductivity peaks between +0.6 V and +1.5 V stay above the noise for all three I(V)-spectroscopies. Fig. 8.8 analyses the energetic position of the lower peak. Its contrast maximum is marked with a black line in each section. Its position relative to the local conduction band edge is evaluated for all three diode bias configurations. The resonance position is approximately constant, when the bending of the conduction band edge is taken into account.

$$\Delta = 0.75V \pm 0.03V$$

This acceptor resonance - well inside the band gap window - is a good starting point for the analysis of the resonance shape. At the bias voltage of 0.7 V - 0.8 V no other tunnel channel exists. The background conductivity is zero. The impact

of the in-plane field on the resonance is studied with dI/dV -maps evaluated for this resonance. The three maps in Fig. 8.9 show the same acceptor atom under different diode bias conditions. The images are registered with respect to the reference marks. Positions in the maps are quantitatively comparable. Similar to the dI/dV -sections a logarithmic color scaling is chosen to pronounce the overall shape of the resonance. The projected position of the dopant atom is marked by a white circle in each image.

The shape of the acceptor contrast changes considerably. For the spectroscopy with minimal in-plane field (Fig. 8.9a) the acceptor resonance has a trapezoidal shape with a prominent asymmetry along the $[001]$ direction. The acceptor contrast is similar to the triangular shaped resonance. The dotted line serves as a guide-to-the-eye. The $[00\bar{1}]$ side of the resonance is more pronounced and extends further away from the acceptor atom. Because the images are acquired on the (110) cleavage plane, this orientation matches with the orientation of the triangular acceptor resonances in homogeneously doped samples. At zero diode bias the in-plane field is increased compared to the forward biased device. The shape of the acceptor resonance evolves into a bone like shape (see Fig. 8.9b). The $[00\bar{1}]$ side of the contrast is still more pronounced but the $[001]$ side develops more weight. The contrast elongates into the $[001]$ direction. The third image (Fig. 8.9c) represents the reverse diode bias case. The in-plane electric field is strong. The acceptor exhibits a rectangular shaped resonance. The contrast is approximately symmetric along the $[001]$ direction. For all three situations the contrast stays approximately mirror symmetric along $[\bar{1}10]$.

The evolution of the acceptor contrast with respect to the strength of the in-plane field is well observed in the comparison of the three dI/dV -maps: The acceptor in Fig. 8.9a resembles the triangular acceptor contrasts in homogeneously doped samples. In this case the in-plane electric field is small. With increasing in-plane electric field the acceptor contrasts develops a more symmetric shape. At high reverse diode bias it shows up as a nearly symmetric rectangular contrast.

The mechanisms leading to the highly anisotropic acceptor resonances have been discussed in chapter 7. The contrasts of acceptors near the surface are asymmetric with respect to the (001) mirror axis. Two possible effects are discussed that are capable of producing this asymmetry: uniaxial strain and electric fields. The strain field originates from the surface relaxation after cleavage. The electric field is induced by the presence of the tip. The band structure calculations demonstrate that both effects produce similar distortions in the band structure. The strain field can be treated like an effective electric field perpendicular to the surface. The diode structure adds an additional electric field that is in the plane of the surface.

The additional in-plane electric field is added to the surface induced field. The resulting field vector is tilted out of the surface normal. The dI/dV -maps presented in Fig. 8.9 show that this effective field decreases the (001) -anisotropy.

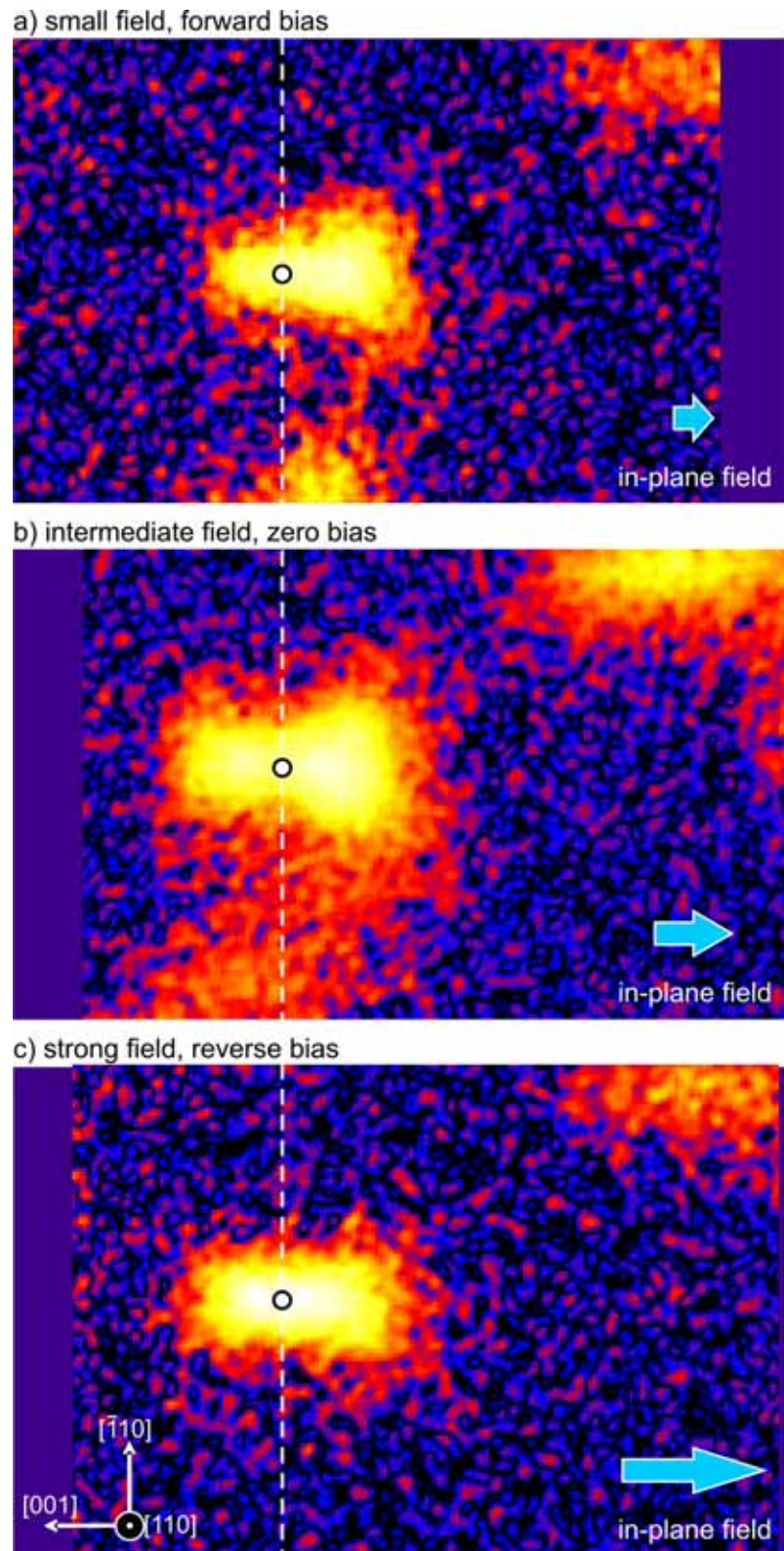


Fig. 8.9 $(18 \times 13) \text{ nm}^2$ $\log(dI/dV)$ maps of the acceptor in between the n- and p-interface. The shape of the acceptor resonance changes with changing diode bias: (a) triangular shaped contrast at minimal in-plane field. (b) bone-like contrast at intermediate in-plane field. (c) rectangular contrast at strong in-plane field. The images are registered to each other by the registration marks. The dotted line is drawn through the dopant atom position.

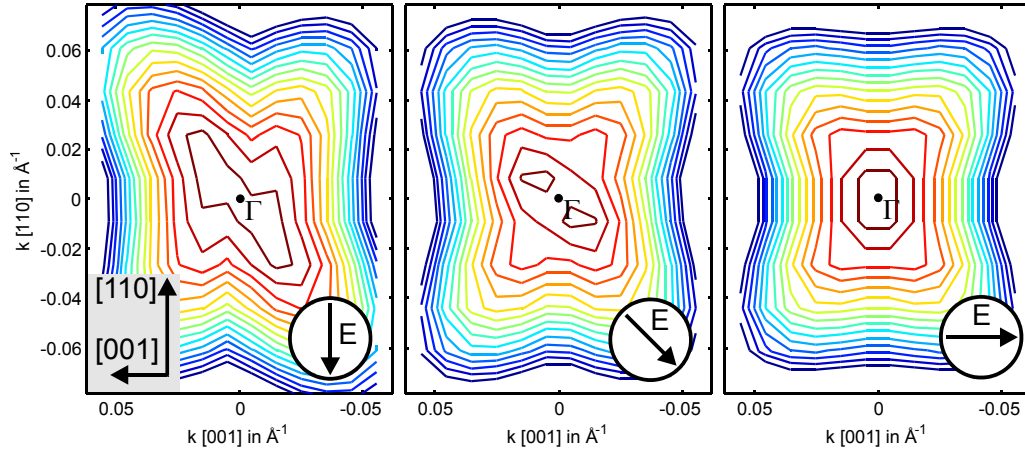


Fig. 8.10 Band structure of GaAs in a plane spanned by $[001]$ and $[110]$. The colored lines are iso-energy lines of the upmost valence band. The plots show the band structure for different orientations of an electric field. The field strength is 1.5 V/nm. (left) field vector parallel to $[110]$. (middle) field vector tilted by 45° out of the $[110]$ axis. (right) electric field parallel to $[001]$.

The electric field at the surface is oriented in $[\overline{1}\overline{1}0]$. The p-i-n diode field is oriented in the $[00\overline{1}]$ direction. The applied diode bias determines the strength of the $[00\overline{1}]$ field. For minimal in-plane field the resulting field vector is nearly parallel to $[\overline{1}\overline{1}0]$. With increasing in-plane field the resulting field vector is successively tilted out of $[\overline{1}\overline{1}0]$ into the $[00\overline{1}]$ direction. Band structure calculations are employed to study the effect of a rotated electric field on the valence band anisotropy. The results are shown in Fig. 8.10 for the highest valence band. When the electric field is oriented perpendicular to the surface (left plot in Fig. 8.10), the asymmetry known from chapter 7.3 is reproduced. The triangular acceptor resonances are observed at the surface. Already for a tilt angle of 45° out of this direction (middle plot), the cubic valence band symmetry is nearly restored. The contour lines illustrate that only the highest states retain an asymmetry with reference to the $[001]$ axis. For about 2% of the Brillouin zone the highest valence band is elongated along $[111]$ (red contour lines in the middle plot of Fig. 8.10). The rest of the band has nearly no asymmetry along the principal $[001]$ axis. The resulting shape of the resonance at the surface will reflect this change. The observed contrast will have some asymmetry left, but the overall shape will be nearly cubic. When the electric field lies in the sample surface and points into $[00\overline{1}]$ the cubic symmetry is restored. The valence band is symmetric again. The resonance at the surface will be completely symmetric, as well. This demonstrates an interesting property of the superposition of bulk inversion asymmetry (BIA) and structure inversion asymmetry (SIA). The effective asymmetry for BIA together with a homogenous electric field in $[110]$ direction leads to an elongation of the highest valence band in $[111]$ direction. When the SIA is induced along $[001]$ the resulting elongation of the bands is along $[110]$ and therefore the symmetry at the surface is not reduced.

The observed change in contrast shape in Fig. 8.9 is explained by this model. The symmetry reducing electric field is tilted out of the surface normal back into the cleavage plane. The band structure becomes less asymmetric with respect to the (001) mirror plane and the contrast develops a more symmetric shape. Already for the forward biased diode a small in-plane field is present. The contrast is more elongated along $[001]$ than acceptor resonances in field-free regions. Instead of a triangle a trapezoidal shape is observed. The change in diode bias by -1.6 V results in an increase of the in-plane electric field. The measurements show that this field is sufficient to nearly restore the symmetry of the contrast. The resulting shape is nearly rectangular.

The p-i-n diode structure is the first experiment that is able to apply a controllable electric field to a single acceptor. For the first time it is possible to deduce the strength of the symmetry breaking field. According to the band structure calculations a tilt angle of 45° nearly restores the (001) mirror symmetry of the bands. Therefore the in-plane electric field needed to change the asymmetric resonance into a symmetric one has to be of the same strength as the symmetry reducing field at the surface. The in-plane field strength of the diode is estimated by the slope of the conduction band edge. The in-plane field is about 60 meV/nm. Although this method gives only a rough approximation, an upper border of the symmetry reducing field can be given. If the effective electric field at the surface was much stronger than the in-plane field, the diode's field would not be capable of changing the contrast shape. Thus the strength of the effective electric field at the surface is pinpointed to be on the order of 100 meV/nm.

It should be mentioned that the electric fields needed in the band structure calculations are of the order of 1 eV/nm, about a factor of 10 higher than the experimentally estimated field strength. The band structure calculations used in this work include the symmetry lowering due to electric fields by spin-orbit interaction (SOI) only (see chapter 6.3). The SOI is a term that originates from a perturbative treatment of the Dirac equation. It is of order

$$\frac{1}{m^2 c^2}$$

Thus it is small unless the electric field is strong. The SOI has impact on the symmetry properties of the band structure [129]. The energetic splitting of the split-off valence band is caused by it and the pronounced cubic shape is enhanced by the SOI. The otherwise spin degenerate bands are split. The additional effect of a homogenous electric field due to SOI is called Rashba coupling. The induced splitting is approximately linear in k and depends on the coupling strength α . The Rashba coupling effect in two dimensional electron and hole gas systems has been studied extensively (a comprehensive report is given by [150]). The symmetry lowering due to the k -linear spin splitting at the Γ_8 valence band maxima is considered to be small. Strong electric fields on the order of 1 eV/nm are needed to produce the pronounced effects observed in the above experiments. Recent reports suggest that additional spin-orbit effects at the surface may be responsible for the enhanced anisotropy. For the interfaces of heterostruc-

tures it was shown that interface induced asymmetry may lead to spin-orbit splitting effects that are one order of magnitude higher than what is expected for the bulk system [151].

Another effect that should be considered for the comparison of the theoretical predictions with the experiments is the resonant tunneling process. The imaged anisotropic contrasts are attributed to the angular anisotropy of the decay constant, rather than directly the valence band asymmetry. Detuning of the resonance by a small change in the local decay constant may lead to a large change in the resonant tunnel current. Smaller asymmetries in the band structure than those calculated here may already lead to considerable asymmetry in the resonance's shape.

Most of the discussions about SOI focus on the real part of the band structure. Last year this issue was addressed by Rougemaille and co-workers [152] who included the spin dependence in III-V semiconductors on the basis of a $k \cdot p$ 14×14 Hamiltonian. Their results indicate that the removed spin degeneracy in the band gap can lead to giant energy splittings and induces forbidden regions in k space where evanescent states are suppressed. These properties of the complex band structure are still under discussion in the theory community [153, 154]. The experiments at acceptors give experimental insight to the interaction of an electric field with those states and may help to finally resolve these questions.

8.3. Summary

The in-plane electric field and built-in potential of the p-i-n diode structure are used to elucidate the anisotropic resonant transport channel at shallow acceptors. The possibility to adjust the strength of the diode field by the externally applied diode bias is exploited to study the field dependent effects at single dopant atoms. Depending on the dopant distribution, the diode locally influences the tunneling transport in two ways:

The built-in potential perturbs the resonant transport channel by changing the alignment of unoccupied final states and acceptor resonance. It is demonstrated that the triangular resonance can be suppressed without suppressing the charge state of the acceptor.

For some configurations the acceptor resonance is not suppressed. Then the influence of the diode's electric field on the spatial distribution of the resonant tunneling is observable. The in-plane electric field adds to the effective electric field at the surface and decreases the resonance anisotropy with reference to the (001) mirror plane. The strength of the symmetry lowering field at the surface is not measurable directly. But the diode's electric field can be estimated by the band edge alignment across the p-i-n interface. The strong impact of the diode field on the acceptor resonance allows inferring that an electric field on the order of 100 mV/nm induces considerable changes in the acceptor resonance.

9. Summary

This thesis focuses on the anisotropic contrasts of acceptors in III-V semiconductors. Shallow and deep acceptors induce pronounced anisotropic conductivity in Scanning Tunneling Microscopy (STM) images of the $\{110\}$ surfaces. The features relate to tunnel channels at the valence band edge which are introduced by the dopant atom. Two different classes of anisotropic contrasts are observed: Bow-tie like shapes that are approximately centered above the buried acceptor and triangular ones that are shifted to one side of the dopant atom. These contrasts have been known for some time, but no comprehensive description was found.

The differentiation of bias voltage windows in which one contrast or the other is observable, constitutes a cornerstone of this thesis. Energy scale diagrams are derived that link the energetic position of the acceptor state at the surface with the bias voltage. The analysis is based on tip induced band bending calculations (TIBB) that are adjusted to experimental parameters of each spatially resolved I(V)-spectroscopy. The individual tip work function turns out to be the most relevant parameter. The energy scale diagrams connect the measured anisotropic contrasts with different charge configurations of the acceptor:

Bow-tie like contrasts are measured when the acceptor state is accessible for tunneling. InAs doped with Mn is chosen for the study of this tunnel process. The acceptor wave function is a hybrid of the valence band states, so it reflects the symmetry properties of the underlying band structure. Images of dopants buried below the 10th subsurface layer are in good agreement with the theoretically derived squared wave function for a bulk acceptor. The acceptor contrasts comply with the cubic symmetry (c_{2v}). They are symmetric over the $\{110\}$ and the (001) mirror planes. However, the contrasts of dopants closer to the surface become asymmetric over (001) . The origin of the observed symmetry reduction effects at the surface is discussed on the basis of band structure calculations. Uniaxial strain due to surface relaxation and also the tip induced electric field are capable of producing the observed asymmetry.

Triangular shaped contrasts are observed when the acceptor is charged and the acceptor state itself does not participate in the tunnel process. For zinc and carbon doped GaAs this tunnel process lies within the GaAs band gap window and is therefore not masked by any other tunnel current. Numerical modeling of the potential along the tunnel path reveals that the acceptor's Coulomb potential

creates a double barrier structure. The triangular shaped conductivity is created by a resonant tunneling channel. The evanescent wave solutions in the semiconductor, i.e., the complex band structure, determine the spatial distribution of the resonance. The symmetry reduction at the surface strongly affects the resonance's shape.

The impact of an electric field on the acceptor resonance is studied in a novel experiment. In a three-terminal geometry single acceptor atoms are exposed to the “in-plane” electric field of a biased p-i-n diode. High-resolution STS measurements show that the resonance's shape depends on the electric field strength, which is now an external control parameter.

In conclusion the anisotropic shapes of acceptors in III-V semiconductors are created by two different tunnel processes. At specific bias voltages, the acceptor state is directly accessible for tunneling at the sample surface. If the acceptor is charged, it gives rise to tunneling resonances over a double barrier potential. Because the host crystal's band structure determines the spatial distribution of both processes, they possess similar symmetry properties. Depth dependent measurements of Mn acceptors demonstrate that symmetry reducing effects at the surface induce an asymmetry along the principal (001) axis. The electric field dependent experiments reveal that the acceptor resonance's shape is changed considerably by electric fields with strengths on the order of 100 meV/nm.

10. Appendix

10.1. Band structure calculation

The evaluation of the band structure induced asymmetries for the different tunnel channels (wave function imaging and resonant tunneling) are based on numerical band structure calculations. This chapter presents the calculation routines used in this thesis. All calculations are performed by empirical pseudopotential methods. This method provides an easy possibility to include strain fields and electric fields. The formalism for standard band structure calculations is given in different textbooks [71, 131]. Here, the calculation is extended to account for the spin-orbit interaction of the electrons with the crystal potential. Additionally, the effect of the Rashba spin-orbit interaction due to the presence of an external electric field is included. The starting point for the calculation is the stationary Schrödinger equation

$$\hat{H}\Psi_{n,\vec{k}}(\vec{r}) = E_n(\vec{k})\Psi_{n,\vec{k}}(\vec{r}) . \quad (10.1)$$

The wave functions are indexed with respect to their electron wave vector \vec{k} and band index n . Because spin dependent interactions are considered, the wave functions are spinors

$$\begin{aligned} \Psi_{n,\vec{k}}(\vec{r}) &= \sum_{\vec{G}} a_{n,\vec{k},\uparrow}(\vec{G}) u_{\vec{G},\vec{k}}^{\uparrow}(\vec{r}) + \sum_{\vec{G}} a_{n,\vec{k},\downarrow}(\vec{G}) u_{\vec{G},\vec{k}}^{\downarrow}(\vec{r}) \\ u_{\vec{G},\vec{k}}^{\uparrow}(\vec{r}) &= \begin{pmatrix} \frac{1}{\Omega} e^{i(\vec{G}+\vec{k})\vec{r}} \\ 0 \end{pmatrix} \\ u_{\vec{G},\vec{k}}^{\downarrow}(\vec{r}) &= \begin{pmatrix} 0 \\ \frac{1}{\Omega} e^{i(\vec{G}+\vec{k})\vec{r}} \end{pmatrix} \end{aligned} \quad (10.2)$$

The wave functions are assumed to be described by a finite set of 65 plane waves $u_{\vec{G},\vec{k}}$. Together with the spin, the complete basis set consists of 130 orthogonal plane waves that are characterized by their spin property, the reciprocal lattice vector \vec{G} and a certain wave vector \vec{k} . Ω is the normalization volume of the crystal and set to 1 for the following discussion.

To facilitate the numerical solution of the eigenvalue problem, a Hamilton matrix is set up for a certain \vec{k} . It consists of the (130 x 130) matrix elements

$$\langle \vec{G}, \vec{k}, \sigma | \hat{H} | \vec{G}', \vec{k}, \sigma' \rangle, \quad \forall \vec{G}, \sigma = \uparrow, \downarrow. \quad (10.3)$$

The complete Hamilton matrix can be decomposed into four blocks according to the ordering of the spin value

$$\begin{aligned} & \Rightarrow \begin{bmatrix} a_{\vec{G}1,\uparrow} \\ \vdots \\ a_{\vec{G}65,\uparrow} \\ a_{\vec{G}1,\downarrow} \\ \vdots \\ a_{\vec{G}65,\downarrow} \end{bmatrix}^* \hat{H} \begin{bmatrix} a_{\vec{G}1,\uparrow} & \cdots & a_{\vec{G}65,\uparrow} & a_{\vec{G}1,\downarrow} & \cdots & a_{\vec{G}65,\downarrow} \end{bmatrix} \\ & \Rightarrow \begin{bmatrix} \langle \vec{G}, \vec{k}, \uparrow | \hat{H} | \vec{G}', \vec{k}, \uparrow \rangle & \langle \vec{G}, \vec{k}, \uparrow | \hat{H} | \vec{G}', \vec{k}, \downarrow \rangle \\ \langle \vec{G}, \vec{k}, \downarrow | \hat{H} | \vec{G}', \vec{k}, \uparrow \rangle & \langle \vec{G}, \vec{k}, \downarrow | \hat{H} | \vec{G}', \vec{k}, \downarrow \rangle \end{bmatrix} \\ & \Rightarrow \begin{bmatrix} a^*a & a^*b \\ b^*a & b^*b \end{bmatrix} \end{aligned} \quad (10.4)$$

The four blocks are denoted with a^*a , a^*b , b^*a and b^*b . The diagonalization of this matrix yields all 130 eigenvalues $E_n(\vec{k})$ and the corresponding expansion coefficients a . The subsequent solution of this Hamilton matrix for different wave vectors produces the band structure, i.e., the dispersion relation $E_n(k)$ with 130 bands.

All material parameters and additional effects are described by the Hamiltonian. For the calculations in this thesis, it consists of four parts

$$\hat{H} = \hat{H}_{kin} + \hat{H}_{pot} + \hat{H}_{SO, crystal} + \hat{H}_{SO, Rashba}, \quad (10.5)$$

- the kinetic energy operator
- the crystal potential
- the spin-orbit interaction of the electron with the crystal potential
- the Rashba spin-orbit interaction of the electron with an external electric field.

The first two parts are treated in the textbooks [71, 131], therefore only a summary will be given here. The spin-orbit Hamiltonians will be discussed in more detail.

Kinetic energy Hamiltonian:

The kinetic energy is given by

$$\hat{H}_{kin} = -\frac{\hbar^2}{2m_0} \Delta \quad (10.6)$$

with the Planck's constant \hbar and the free electron mass m_0 . The matrix elements are produced by applying the operator to a basis function $u_{\vec{G},\vec{k}}^\sigma(\vec{r})$, multiplying from the left with another basis function and integrating over all space

$$\begin{aligned} a^*a &= \langle \vec{G}, \vec{k}, \uparrow | \hat{H}_{kin} | \vec{G}', \vec{k}, \uparrow \rangle \\ &= b^*b = \langle \vec{G}, \vec{k}, \downarrow | \hat{H}_{kin} | \vec{G}', \vec{k}, \downarrow \rangle \\ &= \frac{\hbar^2}{2m_0} \int_{\Omega} (\vec{G} + \vec{k})^2 u_{\vec{G},\vec{k}}^{\uparrow *}(\vec{r}) u_{\vec{G}',\vec{k}}^{\uparrow}(\vec{r}) d^3\vec{r} \\ &= \frac{\hbar^2}{2m_0} (\vec{G} + \vec{k})^2 \delta(\vec{G}, \vec{G}') \\ a^*b &= \langle \vec{G}, \vec{k}, \uparrow | \hat{H}_{kin} | \vec{G}', \vec{k}, \downarrow \rangle = 0 \\ b^*a &= \langle \vec{G}, \vec{k}, \downarrow | \hat{H}_{kin} | \vec{G}', \vec{k}, \uparrow \rangle = 0 \end{aligned} \quad (10.7)$$

The basis functions are orthogonal to each other. The integral over u^*u results in a delta function. The kinetic energy operator is spin independent, so the resulting matrix has two identical blocks. Only the matrix elements with the same spin may contain nonzero entries, i.e., those for a^*a and for b^*b . The two blocks that contain the matrix elements with different spin, i.e., a^*b or b^*a , are zero. Due to the delta function the kinetic energy Hamiltonian decomposes into a diagonal matrix with two identical blocks.

Crystal potential Hamiltonian:

The core of the empirical pseudopotential method is the Fourier expansion of the crystal potential. This method proves to be very useful because already a small number of form factors (Fourier coefficients) suffice to characterize the band structure. The crystal potential for a monoatomic crystal is expanded in the following manner

$$V(\vec{r}) = \sum_{\vec{q}} v_{\vec{q}} e^{i\vec{q}\vec{r}}, \quad v_{\vec{q}} = \int_{\Omega} V(\vec{r}) e^{-i\vec{q}\vec{r}} d^3\vec{r} \quad (10.8)$$

The reciprocal vectors \vec{q} are a priori not further specified. In this work compound semiconductors are considered. The primitive unit cell contains more than one atom. Therefore the Fourier expansion is done for the sublattice of each atom and summed up

$$V(\vec{r}) = \sum_{\vec{q}} \left(\sum_{\vec{t}} v_{\vec{q}}^{\vec{t}} e^{i\vec{q}\vec{t}} \right) e^{i\vec{q}\vec{r}} \quad (10.9)$$

The vectors \vec{t} are the positions of the basis atoms referenced from the lattice points. Similar to the kinetic energy Hamiltonian, the matrix elements of the potential Hamiltonian are independent on the spin. Therefore the a^*a and b^*b blocks of the matrix are equal and the other two blocks for a^*b or b^*a are zero. They are given by

$$\begin{aligned} a^*a &= b^*b \\ &= \langle \vec{G}, \vec{k}, \uparrow | \hat{H}_{pot} | \vec{G}', \vec{k}, \uparrow \rangle \\ &= \int_{\Omega} \sum_{\vec{q}} \left(\sum_{\vec{t}} v_{\vec{q}}^{\vec{t}} e^{i\vec{q}\vec{t}} \right) e^{i(\vec{q} - (\vec{G} - \vec{G}'))\vec{r}} d^3\vec{r} \\ &= \sum_{\vec{q}} \left(\sum_{\vec{t}} v_{\vec{q}}^{\vec{t}} e^{i\vec{q}\vec{t}} \right) \delta(\vec{q}, \vec{G} - \vec{G}') \\ &= \sum_{\vec{t}} v_{(\vec{G} - \vec{G}')}^{\vec{t}} e^{i(\vec{G} - \vec{G}')\vec{t}} \\ a^*b &= \langle \vec{G}, \vec{k}, \uparrow | \hat{H}_{pot} | \vec{G}', \vec{k}, \downarrow \rangle = 0 \\ b^*a &= \langle \vec{G}, \vec{k}, \downarrow | \hat{H}_{pot} | \vec{G}', \vec{k}, \uparrow \rangle = 0 \end{aligned} \quad (10.10)$$

The Fourier expansion reduces to a finite sum over all difference vectors of the reciprocal lattice vectors that are employed for the calculation. Under the assumption, that the atom form factor $v^{\vec{t}}$ is spherical symmetric, it does not depend on the orientation of the difference vector $(\vec{G} - \vec{G}')$, but only on its length $|\vec{G} - \vec{G}'|$. In the following work only form factors for reciprocal lengths up to $\sqrt{11}$ are considered. The form factors for larger lengths are set to zero. This reduces the number of needed form factors per basis atom of the primitive unit cell to four. These are the so-called pseudopotential form factors.

Crystal potential Spin-orbit Hamiltonian:

The spin-orbit interaction is a relativistic correction to the Hamiltonian. In a descriptive model this interaction can be understood by the fact that electrons propagating through the crystal move in the spatially modulated crystal potential. The spatially modulated potential results in electric fields. If the electron moves with relativistic velocities, this electric field transforms into a magnetic field via the Lorentz transformation. This magnetic field acts on the electron spin. The spin-orbit Hamiltonian is given as

$$\hat{H}_{SO, crystal} = -\frac{\hbar}{4m^2c^2} (\vec{\nabla} V_{crystal} \times i\hbar \vec{\nabla}) \hat{\sigma} \quad (10.11)$$

by the cross product of the crystal potential gradient, the momentum operator $-i\hbar\vec{\nabla}$ and the Pauli spin operator $\hat{\sigma}$. Here, basis wave functions with different spin state may interact. This term produces the splitting of the split-off valence band from the heavy and light hole bands. Additionally, it accounts for the splitting of the otherwise spin degenerate bands due to the bulk inversion asymmetry (BIA) in compound semiconductors. With the crystal potential entered, the spin-orbit Hamiltonian is

$$\begin{aligned}
 \hat{H}_{SO, crystal} &= -\frac{\hbar}{4m^2c^2} \left(\vec{\nabla} \sum_{\vec{q}} \left(\sum_{\vec{r}} v_{\vec{q}}^{\vec{r}} e^{i\vec{q}\vec{r}} \right) e^{i\vec{q}\vec{r}} \times i\hbar\vec{\nabla} \right) \hat{\sigma} \\
 &= -\frac{\hbar^2}{4m^2c^2} \sum_{\vec{r}} \sum_{\vec{q}} v_{\vec{q}}^{\vec{r}} e^{i\vec{q}\vec{r}} \cdot \\
 &\quad \cdot \left[\left(q_y \partial_z - q_z \partial_y \right) \begin{bmatrix} 0 & 1 \\ 1 & 0 \end{bmatrix} \right. \\
 &\quad + \left(q_z \partial_x - q_x \partial_z \right) \begin{bmatrix} 0 & -i \\ i & 0 \end{bmatrix} \\
 &\quad \left. + \left(q_x \partial_y - q_y \partial_x \right) \begin{bmatrix} 1 & 0 \\ 0 & -1 \end{bmatrix} \right] \quad (10.12)
 \end{aligned}$$

The matrix elements for each of the four different blocks of the Hamilton matrix can be evaluated by applying the Hamiltonian to a wave function $\Psi_{n,\vec{k}}(\vec{r})$, multiplying from left with a basis function $u_{\vec{G},\vec{k},\sigma}(\vec{r})$ and integrating over all space. The results are

$$\begin{aligned}
 a^*a &= \langle \vec{G}, \vec{k}, \uparrow | \hat{H}_{SO, crystal} | \vec{G}', \vec{k}, \uparrow \rangle \\
 &= -\frac{\hbar^2}{4m^2c^2} \sum_{\vec{r}} v_{\vec{q}}^{\vec{r}} e^{i\vec{q}\vec{r}} \cdot \left[q_x i (G_y + k_y) - q_y i (G_x + k_x) \right] \quad (10.13)
 \end{aligned}$$

$$\begin{aligned}
 a^*b &= \langle \vec{G}, \vec{k}, \uparrow | \hat{H}_{SO, crystal} | \vec{G}', \vec{k}, \downarrow \rangle \\
 &= -\frac{\hbar^2}{4m^2c^2} \sum_{\vec{r}} v_{\vec{q}}^{\vec{r}} e^{i\vec{q}\vec{r}} \cdot \\
 &\quad \cdot \left[\left(q_y i (G_z + k_z) - q_z i (G_y + k_y) \right) + i \left(q_x i (G_z + k_z) - q_z i (G_x + k_x) \right) \right] \quad (10.14)
 \end{aligned}$$

$$\begin{aligned}
b^*a &= \langle \vec{G}, \vec{k}, \downarrow | \hat{H}_{SO, crystal} | \vec{G}', \vec{k}, \uparrow \rangle \\
&= -\frac{\hbar^2}{4m^2c^2} \sum_{\vec{r}} v_{\vec{q}}^{\vec{r}} e^{i\vec{q}\vec{r}} \cdot \\
&\quad \cdot \left[\left(q_y i(G_z + k_z) - q_z i(G_y + k_y) \right) - i \left(q_x i(G_z + k_z) - q_z i(G_x + k_x) \right) \right]
\end{aligned} \tag{10.15}$$

$$\begin{aligned}
b^*b &= \langle \vec{G}, \vec{k}, \downarrow | \hat{H}_{SO, crystal} | \vec{G}', \vec{k}, \downarrow \rangle \\
&= -\frac{\hbar^2}{4m^2c^2} \sum_{\vec{r}} v_{\vec{q}}^{\vec{r}} e^{i\vec{q}\vec{r}} \cdot \left[q_y i(G_x + k_x) - q_x i(G_y + k_y) \right]
\end{aligned} \tag{10.16}$$

The above formulas employ the following vectors

$$\vec{q} = \vec{G} - \vec{G}', \quad \vec{G} = (G_x, G_y, G_z), \quad \vec{k}' = (k_x, k_y, k_z) \tag{10.17}$$

The band structure calculations with this Hamiltonian show that the resulting splitting of the split-off band Δ_{SO} is somewhat smaller than the experimentally obtained values. This is due to the fact that the pseudopotentials are smoother than the real crystal potential. Although the Fourier expansion of the crystal potential reproduces the symmetry properties of the real crystal, it cuts off at spatial frequencies that are too small to describe the full Coulomb potentials. A scaling factor c_{ps} is added to the spin-orbit Hamiltonian, that increases the spin-orbit splitting. The pseudopotential band structure is fitted to the experimentally determined splitting $\Delta_{SO} = 340 \text{ meV}$ [129] for GaAs. This splitting is best met for a scaling factor of $c_{ps} = 4.6625 \cdot 10^3$.

Rashba Hamiltonian:

The Rashba Hamiltonian accounts for the structure inversion asymmetry (SIA) due to a uniform electric field. In the presence of SIA an additional spin splitting is introduced in the band structure of compound semiconductors. The Rashba-Hamilton operator is

$$\hat{H}_{SO, Rashba} = -\frac{\hbar}{4m^2c^2} \alpha (\vec{E}_{ext} \times i\hbar \vec{\nabla}) \hat{\sigma} \tag{10.18}$$

with \vec{E}_{ext} being the externally applied electric field. α is a scaling factor that allows adjusting the band structure calculation to experimentally obtained spin-splittings. The matrix elements of the four blocks of the Hamilton matrix are composed in analogy to the above spin-orbit Hamiltonian.

$$\begin{aligned}
a^*a &= \langle \vec{G}, \vec{k}, \uparrow | \hat{H}_{SO, crystal} | \vec{G}', \vec{k}, \uparrow \rangle \\
&= \frac{\alpha \hbar^2}{4m^2c^2} \left[E_x (G_y + k_y) - E_y (G_x + k_x) \right]
\end{aligned} \tag{10.19}$$

$$\begin{aligned}
a^*b &= \langle \vec{G}, \vec{k}, \uparrow | \hat{H}_{SO, crystal} | \vec{G}', \vec{k}, \downarrow \rangle \\
&= \frac{\alpha \hbar^2}{4m^2 c^2} \left[E_y (G_z + k_z) - E_z (G_y + k_y) \right. \\
&\quad \left. + i (E_x (G_z + k_z) - E_z (G_x + k_x)) \right]
\end{aligned} \tag{10.20}$$

$$\begin{aligned}
b^*a &= \langle \vec{G}, \vec{k}, \downarrow | \hat{H}_{SO, crystal} | \vec{G}', \vec{k}, \uparrow \rangle \\
&= \frac{\alpha \hbar^2}{4m^2 c^2} \left[E_y (G_z + k_z) - E_z (G_y + k_y) \right. \\
&\quad \left. - i (E_x (G_z + k_z) - E_z (G_x + k_x)) \right]
\end{aligned} \tag{10.21}$$

$$\begin{aligned}
b^*b &= \langle \vec{G}, \vec{k}, \downarrow | \hat{H}_{SO, crystal} | \vec{G}', \vec{k}, \downarrow \rangle \\
&= \frac{\alpha \hbar^2}{4m^2 c^2} \left[E_y (G_x + k_x) - E_x (G_y + k_y) \right]
\end{aligned} \tag{10.22}$$

The scaling factor α is adjusted by determination of the conduction band splitting of GaAs in an electric field. The nearly parabolic conduction band is split perpendicular to the applied electric field. The splitting of the two conduction bands is nearly linear in k . On the basis of k p-calculations an analytic expression is obtained for the dispersion relation of wave vectors perpendicular to the electric field. The conduction band of GaAs is

$$E_{\pm}(\vec{k}) = \frac{\hbar^2}{2m^*} k^2 \pm r_{41}^{6c6c} E |\vec{k}| \tag{10.23}$$

with the effective mass $m^* = 0.067m_0$ and the Rashba coefficient $r_{41}^{6c6c} = 0.5206 \text{ eÅ}$ [150]. The pseudopotential band structure is calculated for an electric field of 1 eV/nm and fitted to the analytical expression by adjusting the scaling factor α . The best fit is obtained for $\alpha = 2.1611 \cdot 10^4 r_{41}^{6c6c}$.

10.2. Matlab code for the band structure calculation

The previous sections derived the pseudopotential Hamiltonian for crystals with more than one basis atom. The Schrödinger equation is solved numerically by diagonalization of the Hamilton matrix presented above. The calculation routine is written for Matlab 6.5 and takes advantage of the sophisticated matrix diagonalization routines of the Matlab environment. The program consists of a calling procedure and different subroutines that assemble the Hamilton matrix, pass it to the eigenvalues solver and then handle the diagonalized output.

Fig. 10.1 illustrates the calculation procedure. The main routine 'pssolve.m' starts the band structure evaluation and calls the necessary functions. At first, physical constants and the simulation parameters are defined. The material is selected, the simulation complexity is parameterized and additional effects like strain or electric field are defined. The function 'psglobe.m' serves as an archive for material constants and lattice parameters. The next step is the definition of the k-points that will be calculated. Here, either lines through the Brillouin zone or entire 3D regions can be selected. In the next step the program assembles all matrices that are independent of the wave vector. This saves a lot of time by reducing the commands in the calculation loop. Then, the Hamilton matrix is built for each k-point according to the above formulas. Depending on the chosen simulation complexity the spin-orbit interaction is included and spin expectation values are evaluated. The core of the calculation loop is the diagonalization of the Hamilton matrix by the Matlab function 'eig.m'. After each diagonalization the resulting eigenvalues and expansion coefficients are saved. When the loop terminates, these results are rearranged into a dispersion relation $E_n(k)$ containing all 130 bands. The relevant valence and conduction bands are selected and processed further.

It turns out that by the use of this scheme, nearly all time is spent for the diagonalization procedure. The time for building all matrices and postprocessing of the results is negligible. Since the Hamilton matrix has the size (130 x 130) when the spin-dependent band structure is calculated, the program needs about 0.09sec for every k-point on a standard PC.

The source code may be obtained from the IV. Physikalisches Institut (<http://www.ph4.physik.uni-goettingen.de>)

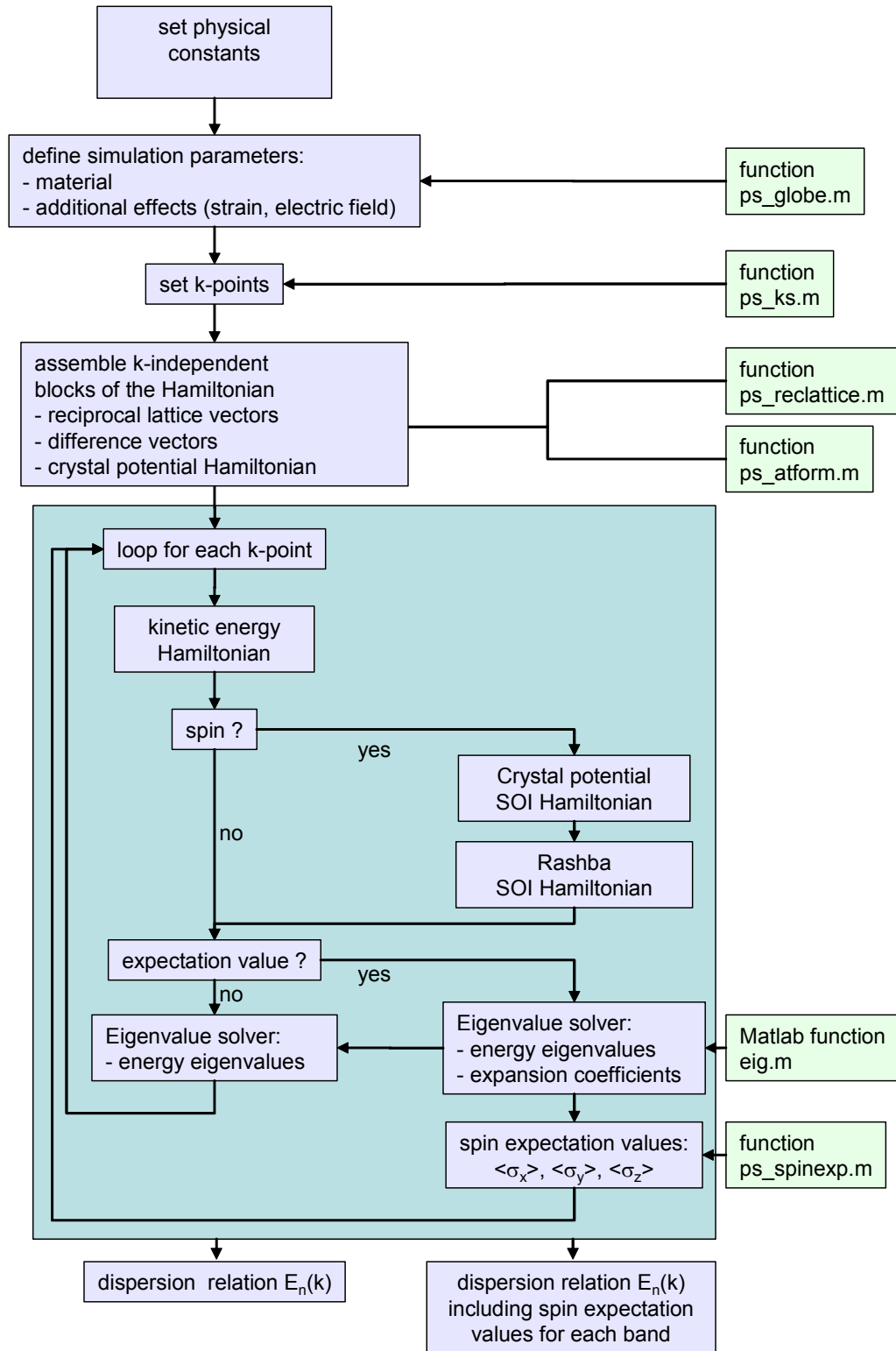
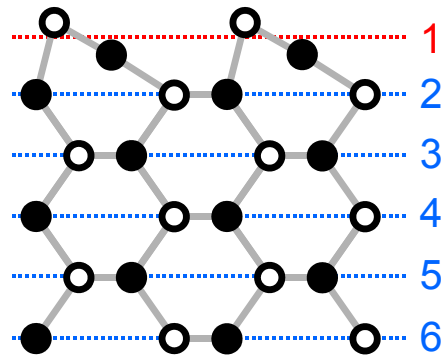


Fig. 10.1 Simulation scheme for the numerical band structure calculation based on the pseudopotential methods as described in the text. The procedure of the main routine 'pssolve.m' is sketched here.

A. Abbreviations and definitions

Dopant depths under the surface are given in units of $\{110\}$ monolayer distances. The highest layer is referred to as layer 1 in this thesis. The numbering is according to the ball-and-stick model.



(hkl)	Miller index notations: specific plane
$[hkl]$	Miller index notations: specific direction
$\{hkl\}$	Miller index notations: group of planes
$\langle hkl \rangle$	Miller index notations: group of directions
3D	three dimensional
Be	beryllium
b_s	sample barrier height at vacuum interface
b_T	tip barrier height at vacuum interface
C	carbon
cb	conduction band
CBM	conduction band minimum
Cd	cadmium
CDO	charge density oscillation
dI/dV	differential conductivity
DOS	density of states
E_C	conduction band energy
E_F	Fermi energy
E_{gap}	sample fundamental band gap
GaAs	gallium arsenide
I, I_T	tunnel current
InAs	indium arsenide
ITRS	international technology roadmap for semiconductors

LDOS	local density of states
MBE	molecular beam epitaxy
Mn	manganese
MOVPE	molecular vapor phase epitaxy
SEM	Scanning Electron Microscope
Si	silicon
Si _{As}	substitutional silicon acceptor on arsenic site
Si _{Ga}	substitutional silicon donor on gallium site
Sn	tin
SOI	spin-orbit interaction
STM	Scanning Tunneling Microscopy
STS	Scanning Tunneling Spectroscopy
TIBB	tip induced band bending
TIBB(V)	functional dependence of TIBB on sample bias
V, eV	sample bias, corresponding energy
vb	valence band
VBM	valence band maximum
WKB	Wentzel-Kramers-Brillouin
X-STM	cross-sectional scanning tunneling microscopy
Zn	zinc
χ_{sample}, χ_S	sample electron affinity
ϕ_{tip}, ϕ_T	tip work function

B. Bibliography

- [1] International Roadmap for Semiconductors, 2005 Edition, <http://www.itrs.net>.
- [2] Luttinger, J. M. and Kohn, W. *Phys. Rev.* **97**(4), 869 February (1955).
- [3] Kohn, W. and Luttinger, J. M. *Phys. Rev.* **98**(4), 915– May (1955).
- [4] Kittel, C. and Mitchell, A. H. *Phys. Rev.* **96**(6), 1488– December (1954).
- [5] Schubert, E. F. *Doping in III-V semiconductors*. Cambridge Univ. Press, Cambridge, (1993).
- [6] Packan, P. A. *Science* **285**, 2079 September (1999).
- [7] Roy, S. and Asenov, A. *Science* **309**, 388 July (2005).
- [8] Binnig, G. and Rohrer, H. *Scanning Tunneling Microscopy – From Birth to Adolescence, in Nobel lectures 1981-1990*. World Scientific Publishing Co., Singapore, (1993).
- [9] Ebert, P. *Surface Science Reports* **33**(4-8), 121 (1999).
- [10] Feenstra, R. M., Meyer, G., Moresco, F., and Rieder, K. H. *Phys. Rev. B* **66**, 165204 (2002).
- [11] Zheng, J. F., Salmeron, M., and Weber, E. R. *Appl. Phys. Lett.* **64**, 1836 (1994).
- [12] Chang, L. L. and Ploog, K. *Molecular Beam Epitaxy and Heterostructures*. NATO ASI Series. Martinus Nijhoff Publ. Dordrecht, Boston, Lancaster, (1985).
- [13] Stringfellow, G. B. *Organometallic Vapor-Phase Epitaxy: Theory and Practice, 2nd Edition*. Academic Press, (1999).
- [14] Johnson, M. B., Albrechtsen, O., Feenstra, R. M., and Salemink, H. W. M. *Appl. Phys. Lett.* **63**(21), 2923 November (1993).
- [15] Ulloa, J. M., Celebi, C., Koenraad, P. M., Simon, A., Gapihan, E., Letoublon, A., Bertru, N., Drouzas, I., Mowbray, D. J., Steer, M. J., and Hopkinson, M. J. *Appl. Phys.* **101**(8), 081707 April (2007).
- [16] Zheng, J. F., Walker, J. D., Salmeron, M. B., and Weber, E. R. *Phys. Rev. Lett.* **72**(15), 2414 April (1994).
- [17] Feenstra, R. M. and Stroscio, J. A. *J. Vac. Sci. Technol. B* **5**, 923 (1987).
- [18] de Raad, G. J., Bruls, D. M., Koenraad, P. M., and Wolter, J. H. *Phys. Rev. B* **66**, 195306 (2002).
- [19] Feenstra, R. M., Dong, Y., Semtsiv, M. P., and Masselink, W. T. *Nanotechnology* **18**(4), 044015– (2007).
- [20] Feenstra, R. M. *J. Vac. Sci. Technol. B* **21**(5), 2080–2088 (2003).

- [21] Sauthoff, K. *Scanning Tunneling Spectroscopy on Single Donors and Donor Complexes near the GaAs(110)-Surface*. PhD thesis, Georg-August University of Göttingen, (2003).
- [22] Zheng, Z. F., Salmeron, M. B., and Weber, E. R. *Appl. Phys. Lett.* **65**, 790 (1994).
- [23] Arseev, P., Maslova, N. S., Panov, V. I., Savinov, S. V., and van Haesendock, C. *JETP Letters* **77**(4), 172–177 February (2003).
- [24] Binnig, G. and Rohrer, H. *Rev. Mod. Phys.* **71**(2), S324 March (1999).
- [25] Binnig, G., Rohrer, H., Gerber, C., and Weibel, E. *Appl. Phys. Lett.* **40**(2), 178 January (1982).
- [26] Binnig, G., Rohrer, H., Gerber, C., and Weibel, E. *Phys. Rev. Lett.* **49**(1), 57 July (1982).
- [27] Besocke, K. *Surf. Sci.* **181**(1-2), 145 March (1987).
- [28] Quast, T. Master's thesis, University of Göttingen, (1995).
- [29] Rosentreter, M. A., Wenderoth, M., Theuerkauf, N. H., Heinrich, A. J., Schneider, M. A., and Ulbrich, R. G. *Phys. Rev. B* **56**(16), 10538 October (1997).
- [30] Heinrich, A. J. *Ordering in Ternary Compound Semiconductors on the atomic scale*. PhD thesis, University of Göttingen, (1998).
- [31] Müller, J. Master's thesis, University of Göttingen, (2003).
- [32] Kemerink, M., Reusch, T. C. G., Bruls, D. M., Koenraad, P. M., Salemink, H. W. M., and Wolter, J. H. *Physica E: Low-dimensional Systems and Nanostructures* **13**(2-4), 1159 March (2002).
- [33] Schleiermacher, H. *Characterization of tips for scanning tunneling microscopy*. Georg-August University of Göttingen, (2006).
- [34] Ibe, J. P., Bey, Jr., P. P., Brandow, S. L., Brizzolara, R. A., Burnham, N. A., DiLella, D. P., Lee, K. P., Marrian, C. R. K., and Colton, R. J. *J. Vac. Sci. Technol. A* **8**(4), 3570 July (1990).
- [35] Sauthoff, K., Wenderoth, M., Heinrich, A. J., Rosentreter, M. A., Engel, K. J., Reusch, T. C. G., and Ulbrich, R. G. *Phys. Rev. B* **60**(7), 4789 (1999).
- [36] Hartnagel, H. and Weiss, B. L. *Journal of Materials Science - Letters* **8**, 1061 (1973).
- [37] Baca, A. G., Ren, F., Zolper, J. C., Briggs, R. D., and Pearton, S. J. *Thin Solid Films* **308-309**, 599 October (1997).
- [38] Kuan, T. S., Batson, P. E., Jackson, T. N., Rupprecht, H., and Wilkie, E. L. *J. Appl. Phys.* **54**(12), 6952 December (1983).
- [39] Garleff, J. K. *Quasi-eindimensionale elektronische Zustände auf der Si(111)-2x1-Oberfläche*. PhD thesis, University of Göttingen, (2005).
- [40] Adachi, S. *GaAs and Related Materials Bulk Semiconducting and Superlattice Properties*. World Scientific, Singapore, (1994).
- [41] Ebert, P., Engels, B., Richard, P., Schroeder, K., Blügel, S., Domke, C., Heinrich, M., and Urban, K. *Phys. Rev. Lett.* **77**(14), 2997 September (1996).
- [42] Engels, B., Richard, P., Schroeder, K., Blügel, S., Ebert, P., and Urban, K. *Phys. Rev. B* **58**(12), 7799 September (1998).

-
- [43] Kitchen, D. S. *Atom-by-Atom Substitution of Transition metals in GaAs and Visualization of Hole-Mediated Interactions*. PhD thesis, University of Illinois at Urbana-Champaign, (2006).
 - [44] Alves, J. L. A., Hebenstreit, J., and Scheffler, M. *Phys. Rev. B* **44**(12), 6188 September (1991).
 - [45] Ruocco, A., Biagini, M., di Bona, A., Gambacorti, N., Valeri, S., Nannarone, S., Santoni, A., and Bonnet, J. *Phys. Rev. B* **51**(4), 2399 January (1995).
 - [46] Chelikowsky, J. R. and Cohen, M. L. *Phys. Rev. B* **20**, 4150 (1979).
 - [47] Messiah, A. *Quantum Mechanics I*. de Gruyter & Co., New York, (1976).
 - [48] Blanco, J. M., Gonzalez, C., Jelinek, P., Ortega, J., Flores, F., and Perez, R. *Phys. Rev. B* **70**(8), 085405 August (2004).
 - [49] Chen, J. *Introduction to Scanning Tunneling Microscopy*. Oxford University Press, (1993).
 - [50] Wiesendanger, R. *Scanning Probe Microscopy and Spectroscopy*. Cambridge University Press, (1994).
 - [51] Bonnell, D. A. *Scanning Tunneling Microscopy and Spectroscopy. Theory, Techniques, and Applications*. VCH, New York, (1993).
 - [52] Bardeen, J. *Phys. Rev. Lett.* **6**(2), 57 January (1961).
 - [53] Tersoff, J. and Hamann, D. R. *Phys. Rev. Lett.* **50**(25), 1998 June (1983).
 - [54] Tersoff, J. and Hamann, D. R. *Phys. Rev. B* **31**, 805 (1985).
 - [55] Hamers, R. J. and Padowitz, D. F. In *Scanning Probe Microscopy and Spectroscopy*, (ed.), D. A. B., editor. Wiley VCH., New York (2001).
 - [56] Hamers, R. J. *Annu. Rev. Phys. Chem.* **40**, 531 (1989).
 - [57] Hasegawa, Y. and Avouris, P. *Phys. Rev. Lett.* **71**(7), 1071– August (1993).
 - [58] Petersen, L., Sprunger, P. T., Hofmann, P., Lægsgaard, E., Briner, B. G., Doering, M., Rust, H.-P., Bradshaw, A. M., Besenbacher, F., and Plummer, E. W. *Phys. Rev. B* **57**(12), R6858 March (1998).
 - [59] Ukraintsev, V. A. *Phys. Rev. B* **53**(16), 11176 April (1996).
 - [60] Mönch, W. *Semiconductor Surfaces and Interfaces*. Springer, Berlin, (1995).
 - [61] Jäger, N. D., Ebert, P., Urban, K., Krause-Rehberg, R., and Weber, E. R. *Phys. Rev. B* **65**(19), 195318 May (2002).
 - [62] Russell, A. M. J. *Appl. Phys.* **33**(3), 970–975 March (1962).
 - [63] Feenstra, R. M. Semitip v.2, <http://www.andrew.cmu.edu/user/feenstra/>.
 - [64] Schroder, D. K. *Semiconductor material and device characterization*. Wiley, New York, (1990).
 - [65] Chelvayohan, M. and Mee, C. H. B. *J. Phys. C* **15**, 2305 (1982).
 - [66] Hahn, P., Clabes, J., and Henzler, M. *Journal of Applied Physics* **51**(4), 2079 (1980).
 - [67] Binnig, G., Garcia, N., Rohrer, H., Soler, J. M., and Flores, F. *Phys. Rev. B* **30**(8), 4816 October (1984).
 - [68] Olesen, L., Brandbyge, M., Sørensen, M. R., Jacobsen, K. W., Lægsgaard, E., Stensgaard, I., and Besenbacher, F. *Phys. Rev. Lett.* **76**(9), 1485 February (1996).

- [69] Teichmann, K. Master's thesis, Georg-August University of Göttingen, (2007).
- [70] Fischer, T. E., Allen, F. G., and Gobeli, G. W. *Phys. Rev.* **163**(3), 703–November (1967).
- [71] Harrison, P. *Quantum Wells, Wires and Dots*. John Wiley & Sons Inc., New York, (2000).
- [72] Loth, S., Wenderoth, M., Winking, L., Ulbrich, R. G., Malzer, S., and Döhler, G. H. *Jpn. J. Appl. Phys* **45**, 2193 (2006).
- [73] Heinrich, A. J., Wenderoth, M., Rosentreter, M. A., Schneider, M. A., and Ulbrich, R. G. *Applied Physics Letters* **70**(4), 449 (1997).
- [74] Depuydt, A., Van Haesendonck, C., Maslova, N. S., Panov, V. I., Savinov, S. V., and Arseev, P. I. *Phys. Rev. B* **60**(4), 2619 (1999).
- [75] Dombrowski, R., Steinebach, C., Wittneven, C., Morgenstern, M., and Wiesendanger, R. *Phys. Rev. B* **59**, 8043 (1999).
- [76] van der Wielen, M. C. M. M., van Roij, A. J. A., and van Kempen, H. *Phys. Rev. Lett.* **76**(7), 1075 (1996).
- [77] Wenderoth, M., Rosentreter, M. A., Engel, K. J., Heinrich, A. J., Schneider, M. A., and Ulbrich, R. G. *Europhys. Lett.* **45**, 579 (1999).
- [78] de Kort, R., van der Wielen, M. C. M. M., van Roij, A. J. A., Kets, W., and van Kempen, H. *Phys. Rev. B* **63**, 125336 (2001).
- [79] Inglesfield, J. E., Boon, M. H., and Crampin, S. *Journal of Physics Condensed Matter* **12**(30), L489 (2000).
- [80] de la Broïse, X., Delerue, C., Lannoo, M., Grandidier, B., and Stiévenard, D. *Phys. Rev. B* **61**, 2138 (2000).
- [81] Hopkins, B. J. and Rivière, J. C. *Proceedings of the Physical Society* **81**(3), 590 (1963).
- [82] Smoluchowski, R. *Phys. Rev.* **60**(9), 661 November (1941).
- [83] Besocke, K. and Wagner, H. *Phys. Rev. B* **8**(10), 4597 November (1973).
- [84] Sze, S. M. *Physics of Semiconductor Devices*, 2nd ed. Willey VCH, New York, (1981).
- [85] Bruls, D. M. *Direct profiling of III/V semiconductor nanostructures at the atomic level* *Direct profiling of III/V semiconductor nanostructures at the atomic level by cross-sectional Scanning Tunneling Microscopy*. PhD thesis, Technical University of Eindhoven, (2003).
- [86] Grandidier, B. *Journal of Physics: Condensed Matter* (2), S161 (2004).
- [87] Koenraad, P. M., Bruls, D. M., Davies, J. H., Gill, S. P. A., Long, F., Hopkinson, M., Skolnick, M., and Wolter, J. H. *Physica E: Low-Dimensional Systems and Nanostructures* **17**(1-4), 526 (2003).
- [88] Mikkelsen, A., Sköld, N., Ouattara, L., Borgström, M., Andersen, J. N., Samuelson, L., Seifert, W., and Lundgren, E. *Nature Materials* **3**, 519–523 August (2004).
- [89] Dong, Y., Feenstra, R. M., Hey, R., and Ploog, K. H. In *J. Vac. Sci. Technol. B*, volume 20, 1677–1681 (AVS, Sante Fe, New Mexico, 2002).
- [90] Ebert, P., Jager, N. D., Urban, K., and Weber, E. R. *J. Vac. Sci. Technol. B* **22**(4), 2018–2025 July (2004).

-
- [91] Landrock, S., Urban, K., and Ebert, P. *Phys. Rev. Lett.* **96**(7), 076101 February (2006).
 - [92] Jäger, N. D., Marso, M., Salmeron, M., Weber, E. R., Urban, K., and Ebert, P. *Phys. Rev. B* **67**(16), 165307 April (2003).
 - [93] Muralt, P., Meier, H., Pohl, D. W., and Salemink, H. W. M. *Appl. Phys. Lett.* **50**(19), 1352 May (1987).
 - [94] Yoshida, S., Kanitani, Y., Oshima, R., Okada, Y., Takeuchi, O., and Shigekawa, H. *Phys. Rev. Lett.* **98**(2), 026802 January (2007).
 - [95] Reusch, T. C. G., Wenderoth, M., Winking, L., Quaas, N., and Ulbrich, R. G. *Phys. Rev. Lett.* **93**(20), 206801 November (2004).
 - [96] Reusch, T. C. G., Wenderoth, M., Winking, L., Quaas, N., and Ulbrich, R. G. *Appl. Phys. Lett.* **87**(9), 093103 August (2005).
 - [97] Jäger, N. D., Urban, K., Weber, E. R., and Ebert, P. *Appl. Phys. Lett.* **82**(16), 2700 April (2003).
 - [98] Koenraad, P. M. In *8th International Conference on Nanometer-Scale Science and Technology, Venice*, (2004).
 - [99] Domke, C., Ebert, P., and Urban, K. *Surface Science* **415**, 285 (1998).
 - [100] Zheng, J. F., Liu, X., Newman, N., Weber, E. R., Ogletree, D. F., and Salmeron, M. *Phys. Rev. Lett.* **72**(10), 1490 (1994).
 - [101] de Kort, R., Kets, W., and van Kempen, H. *Surface Science* **482-485**, 495 (2001).
 - [102] Mahieu, G., Grandidier, B., Deresmes, D., Nys, J. P., Stiévenard, D., and Ebert, P. *Phys. Rev. Lett.* **94**, 26407 (2005).
 - [103] Wiebe, J., Meier, F., Hashimoto, K., Marczinowski, F., Wiesendanger, R., Morgenstern, M., Tang, J.-M., and Flatté, M. E. In *International Conference on Nanoscience and Technology 2006*, (2006).
 - [104] Yakunin, A. M., Silov, A. Y., Koenraad, P. M., Wolter, J. H., Van Roy, W., De Boeck, J., Tang, J.-M., and Flatté, M. E. *Phys. Rev. Lett.* **92**, 216806 (2004).
 - [105] Winking, L., Wenderoth, M., Reusch, T. C. G., Ulbrich, R. G., Wilbrandt, P.-J., Kirchheim, R., Malzer, S., and Döhler, G. H. *J. Vac. Sci. Technol. B* **23**(1), 267 (2005).
 - [106] Loth, S., Wenderoth, M., Winking, L., Ulbrich, R. G., Malzer, S., and Döhler, G. H. *Phys. Rev. Lett.* **96**, 066403 (2006).
 - [107] Depuydt, A., van Haesendonck, C., Savinov, S. V., and Panov, V. I. *Applied Physics A: Materials Science and Processing* **72**(8), S209–S212 (2001).
 - [108] Yakunin, A. M. *Mn in GaAs studied by X-STM: from a single impurity to ferromagnetic layers*. PhD thesis, University of Eindhoven, (2005).
 - [109] Koenraad, P. M. In *International conference on Nanometer-Scale Science and Technology, Venice*, (2004).
 - [110] Koenraad, P. M. and Fiore, A. Technical report, University of Eindhoven department of applied physics Institute for Photonics and Semiconductor Nanophysics, (2006).
 - [111] Winking, L. Master's thesis, Georg-August University of Göttingen, (2003).

- [112] Loth, S., Wenderoth, M., Ulbrich, R. G., Malzer, S., and Döhler, G. H. submitted to *Phys. Rev. B*, available cond-mat/0708.2937, (2007).
- [113] Domke, C., Ebert, P., Heinrich, M., and Urban, K. *Phys. Rev. B* **54**, 10288 (1996).
- [114] Chiu, P. T., Blattner, A. J., May, S. J., and Wessels, B. W. *Physica B: Condensed Matter* **344**(1-4), 379 February (2004).
- [115] Tang, J.-M. and Flatte, M. E. *Phys. Rev. B* **72**(16), 161315(R) October (2005).
- [116] Marczinowski, F.
- [117] Monakov, A. M., Romanov, K. S., Panaiotti, I. E., and Averkiev, N. S. *Solid State Commun.* **140**, 422–425 (2006).
- [118] Schwarz, A., Allers, W., Schwarz, U. D., and Wiesendanger, R. *Phys. Rev. B* **61**(4), 2837– January (2000).
- [119] Koenraad, P. M., Celebi, C., Silov, A., Yakunin, A., Tang, J.-M., Flatte, M., and Kaminska, M. *APS Meeting Abstracts*, 12005 March (2007).
- [120] Stoneham, A. M. *Theory of Defects in Solids: Electronic Structure of Defects in Insulators and Semiconductors*. Oxford: Clarendon Press, (1975).
- [121] Cardona, M., Christensen, N. E., and Fasol, G. *Phys. Rev. Lett.* **56**(26), 2831 (1986).
- [122] Zunger, A. *Phys. Rev. B* **22**, 959 (1980).
- [123] Kahn, A., So, E., Mark, P., Duke, C. B., and Meyer, R. J. *J. Vac. Sci. Technol.* **15**, 1223 (1978).
- [124] Tong, S. Y., Lubinsky, A. R., Mrstik, B. J., and Van Hove, M. A. *Phys. Rev. B* **17**(8), 3303 April (1978).
- [125] Qian, G.-X., Martin, R. M., and Chadi, D. J. *Phys. Rev. B* **37**(3), 1303 January (1988).
- [126] Yakunin, A. M., Silov, A. Y., Koenraad, P. M., Tang, J.-M., Flatté, M. E., Primus, J.-L., Van Roy, W., De Boeck, J., Monakhov, A. M., Romanov, K. S., Panaiotti, I. E., and Averkiev, N. S. *Nature Materials* **6**, 512 (2007).
- [127] Bir, G. L. and Pikus, G. E. *Symmetry and Strain-Induced Effects in Semiconductors*. Wiley VCH, New York, (1974).
- [128] Crooker, S. A. and Smith, D. L. *Phys. Rev. Lett.* **94**(23), 236601 June (2005).
- [129] Cardona, M., Christensen, N. E., and Fasol, G. *Phys. Rev. B* **38**(3), 1806 July (1988).
- [130] Greiner, W. *Relativistic Quantum Mechanics: Wave equations*. Springer Verlag, Berlin, (1997).
- [131] Yu, E. T., Barmak, K., Ronsheim, P., Johnson, M. B., McFarland, P., and Halbout, J.-M. *J. Appl. Phys.* **79**(4), 2115 February (1996).
- [132] Loth, S. Master's thesis, Georg-August University of Göttingen, (2004).
- [133] Einevoll, G. T. and Sham, L. J. *Phys. Rev. B* **49**, 10533 (1996).
- [134] Mavropoulos, P., Papanikolaou, N., and Dederichs, P. H. *Phys. Rev. Lett.* **85**, 1088 (2000).
- [135] Heine, V. *Proc. Phys. Soc. London* **81**(520), 300 (1963).
- [136] Chang, Y. *Phys. Rev. B* **25**(2), 605 January (1982).

-
- [137] Forstmann, F. and Heine, V. *Phys. Rev. Lett.* **24**(25), 1419 June (1970).
 - [138] Jones, R. O. *Proc. Phys. Soc. London* **89**, 443 (1966).
 - [139] Bastard, G. *Wave Mechanics Applied to Semiconductor Heterostructures*. Les Éditions de Physique, Les Ulis, France, (1996).
 - [140] Schuurmans, M. F. H. and 't Hooft, G. W. *Phys. Rev. B* **31**(12), 8041 June (1985).
 - [141] Zhang, X.-G. and Butler, W. H. *Journal of Physics: Condensed Matter* **15**(41), R1603 (2003).
 - [142] Tomfohr, J. K. and Sankey, O. F. *Phys. Rev. B* **65**(24), 245105 May (2002).
 - [143] Wang, H., Lewis, J. P., and Sankey, O. F. *Physical Review Letters* **93**(1), 016401 (2004).
 - [144] Feenstra, R. M., Gaan, S., Meyer, G., and Rieder, K. H. *Phys. Rev. B* **71**(12), 125316 March (2005).
 - [145] Laloyaux, T., Derycke, I., Vigneron, J.-P., Lambin, P., and Lucas, A. A. *Phys. Rev. B* **47**(12), 7508 March (1993).
 - [146] Bracher, C., Riza, M., and Kleber, M. *Phys. Rev. B* **56**(12), 7704 September (1997).
 - [147] Bracher, C., Becker, W., Gurvitz, S. A., Kleber, M., and Marinov, M. S. *Am. J. Phys.* **66**(1), 38 January (1998).
 - [148] Pipe, K. P., Ram, R. J., and Shakouri, A. *Phys. Rev. B* **66**, 125316 (2002).
 - [149] Shi, L., Lyeo, H. K., Shih, C. K., Kim, P., Bachtold, A., Plyosunov, S., McEuen, P. L., and Majumdar, A. *AIP Conference Proceedings* **683**, 462 (2003).
 - [150] Winkler, R. *Spin-Orbit Coupling Effects in Two-Dimensional Electron and Hole Systems*. Springer Verlag, Berlin, (2003).
 - [151] Foreman, B. A. *Phys. Rev. Lett.* **86**(12), 2641 March (2001).
 - [152] Rougemaille, N., Drouhin, H.-J., Richard, S., Fishman, G., and Schmid, A. K. *Phys. Rev. Lett.* **95**, 186406 (2005).
 - [153] Nguyen-Quang, T., Jancu, J.-M., and Voisin, P. *Phys. Rev. Lett.* **97**, 109701 (2006).
 - [154] Rougemaille, N., Drouhin, H.-J., Richard, S., Fishman, G., and Schmid, A. K. *Phys. Rev. Lett.* **97**, 109702 (2006).

Danksagung

Experimentelle Forschung kann man nicht im Alleingang bewerkstelligen. Ergebnisse, wie sie in dieser Arbeit vorgestellt wurden, sind nur möglich durch Teamwork. Das mag wie ein Klischee klingen, trotzdem ist es nicht minder wahr. Darum möchte ich hier die Gelegenheit nutzen, allen Personen, die mir während der vergangenen Jahre mit Rat und Tat zur Seite gestanden haben, herzlich zu danken.

An erster Stelle möchte ich Prof. Dr. Rainer G. Ulbrich danken, den ich gleich zu Beginn meiner Studienzeit in Göttingen kennengelernt habe und seitdem als kompetenten Ratgeber schätze. Er wird mir mit seinem steten Wunsch, die physikalischen Phänomene auf grundlegender Ebene zu verstehen, ein Vorbild bleiben.

Hervorzuheben ist Dr. Martin Wenderoth. Ob im Campingwagen in Venedig oder zu Hause im Institut - die Zusammenarbeit mit Martin ist sowohl fachlich als auch persönlich eine große Bereicherung. Danke für lehrreiche Jahre und die Motivation, nach der Dr.-Zeit das wissenschaftliche Handwerk nicht an den Nagel zu hängen.

Prof. Dr. Kurt Schönhammer möchte ich herzlich für die Übernahme des Korreferats danken.

Auch an den Rest der STM-Arbeitsgruppe werde ich mich gerne erinnern - die ehemaligen und neuen Tunnler: Thomas Druga, Jens Garleff, Jan Homoth, Peter Löptin, Henning Prüser, Thilo Reusch, Katharina Sauthoff, Swante Siewers, Bernhard Spicher, Karen Teichmann, Norbert Quaas, Alexander Weismann, Lars Winking. Wir hatten eine spannende Zeit und haben gemeinsam viel erreicht. Die unzähligen gemeinsamen Kaffeepausen mit Diskussionen über Physik und den Rest der Welt waren immer angenehme Muntermacher.

Dr. Stefan Malzer von der Universität Erlangen-Nürnberg hat mir so manchen Wunsch nach Heterostrukturen sogar zu Weihnachten erfüllt. Seine hervorragenden Proben haben z.B. die feldabhängigen Messungen erst möglich gemacht.

Dank gilt auch Dr. Ulrich Kretzer von der Freiburger Compound Materials GmbH für die freundliche Gabe des hochdotierten GaAs:Si. Es ist sicherlich nicht alltäglich, einen „nicht kaufbaren“ Wafer einfach zur Verfügung gestellt zu bekommen.

Prof. Dr. Paul M. Koenraad von der Universität Eindhoven sowie Felix Marczinowski und Dr. Jens Wiebe von der Universität Hamburg danke ich für die fruchtbaren Diskussionen rund um den eckigen Akzeptor. Ihre Anregungen und Kritiken haben sehr zur Ausarbeitung der in dieser Arbeit vorgestellten Modelle beigetragen.

Vor allem bin ich meiner lieben Familie zutiefst dankbar. Es ist ein gutes Gefühl zu wissen, dass ich mich in allen Lebenslagen auf ihre Unterstützung und unseren engen Zusammenhalt verlassen kann.

Mein ganz besonderer Dank gilt meiner Freundin Katinka für ihre Liebe und die Geduld mit ihrem Physiker.

Curriculum vitae

Sebastian Loth

Diplom-Physiker

geboren am 07.04.1979 in Limburg an der Lahn

- vorauss. 10/2007 Promotion zur Erlangung des Grades eines Doktors der Naturwissenschaften (Dr. rer. nat.) im Fach Physik**
am IV. Physikalischen Institut, Halbleiterphysik
der Georg-August Universität Göttingen
- seit 02/2005 Stipendiat der Studienstiftung des Deutschen Volkes**
im Rahmen der Promotionsförderung
- seit 06/2004 wissenschaftlicher Mitarbeiter**
am IV. Physikalischen Institut, Halbleiterphysik
der Georg-August Universität Göttingen
- 07.06.2004 Dr. Berliner – Dr. Ungewitter – Preis für herausragende Diplomabschlüsse**
- 07.05.2004 Diplom im Fach Physik**
zu Beginn des 10. Fachsemesters
an der Georg-August Universität Göttingen
- 26.11.2001 Vordiplom im Fach Physik**
an der Universität Bielefeld
- 08/1998 - 08/1999 Zivildienst**
in der therapeutischen Abteilung des Klinikums für Rehabilitation „Kliniken am Burggraben“, Bad Salzuflen
- 10.06.1998 Allgemeine Hochschulreife**
am Gymnasium der Stadt Lage

Göttingen, den 04.10.2007

Publikationen

1. S. Loth, M. Wenderoth, R. G. Ulbrich, S. Malzer, und G. H. Döhler
On the Connection of Anisotropic Conductivity to Tip Induced Space Charge Layers in Scanning Tunneling Spectroscopy of p-doped GaAs
arXiv: cond-mat/07082937, submitted to Physical Review B
2. S. Loth, M. Wenderoth, L. Winking, R. G. Ulbrich, S. Malzer, und G. H. Döhler
Probing Semiconductor Gap States with Resonant Tunneling,
Physical Review Letters **96**, 066403 1-4 (2006)
3. S. Loth, M. Wenderoth, L. Winking, R. G. Ulbrich, S. Malzer, und G. H. Döhler
Depth Resolved Scanning Tunneling Spectroscopy of Shallow Acceptors in Gallium Arsenide
Japanese Journal of Applied Physics **45**, 2193-2196 (2006)

Präsentationen

4. S. Loth, M. Wenderoth, K. Teichmann, R. G. Ulbrich, S. Malzer und G. H. Döhler
Tunneling spectroscopy of an operating p-i-n diode interface
International Conference on Nano Science and Technology, Stockholm, Schweden (2007) LOW01-Or3
5. K. Teichmann, M. Wenderoth, S. Loth, und R. G. Ulbrich
Scanning tunneling spectroscopy of Si donors on GaAs {110}
International Conference on Nano Science and Technology, Stockholm, Schweden (2007) SS01-Or1
6. (eingeladener Vortrag) S. Loth, M. Wenderoth, R. G. Ulbrich, S. Malzer und G. H. Döhler
Resonant tunneling through single dopant atoms and the impact of controlled electric fields
Séminaire - Institut de Physique des Nanostructures, Ecole Polytechnique Federale de Lausanne, Schweiz (2007)
7. S. Loth, M. Wenderoth, K. Teichmann, R. G. Ulbrich, S. Malzer, und G. H. Döhler
Tunneling Spectroscopy on the interface of an operating pin-Diode
Workshop des Virtuellen Instituts für Spinelektronik, Aachen (2007)
8. S. Loth, M. Wenderoth, S. Siewers, K. Teichmann, R. G. Ulbrich, S. Malzer, and G. H. Döhler
Tunneling Transport Involving Evanescent States in III-V semiconductors
Frühjahrstagung der Deutschen Physikalischen Gesellschaft (DPG), Regensburg, (2007) HL 46.30

9. K. Teichmann, M. Wenderoth, S. Loth, and R. G. Ulbrich
Scanning Tunneling Spectroscopy of Si donors in GaAs {110}
 Frühjahrstagung der DPG, Regensburg, (2007) HL21.7
10. S. Loth, M. Wenderoth, K. Teichmann, R. G. Ulbrich, S. Malzer, and G. H. Döhler
Tunneling Spectroscopy on the Interface of an Operating pin-Diode
 Frühjahrstagung der DPG, Regensburg, (2007) HL 36.9
11. S. Loth, M. Wenderoth, L. Winking, R. G. Ulbrich, S. Malzer, and G. H. Döhler
Resonant Tunneling as a Probe for Semiconductor Gap States,
 International Conference on Nanoscience and Technology, Basel, Schweiz,
 (2006) Nr. 459
12. S. Loth, M. Wenderoth, L. Winking, R. G. Ulbrich, S. Malzer, and G. H. Döhler
Anisotropy of Semiconductor Gap States Probed by Resonant Tunneling
 28th International Conference on the Physics of Semiconductors, Wien,
 Österreich, (2006) Nr. FrM2f.45
13. S. Loth, M. Wenderoth, L. Winking, R. G. Ulbrich, S. Malzer, and G. H. Döhler
Anisotropy of Semiconductor Gap States Probed with Resonant Tunneling
 Workshop des Virtuellen Instituts für Spinelektronik, Jülich (2006)
14. S. Loth, M. Wenderoth, L. Winking, R. G. Ulbrich, S. Malzer, and G. H. Döhler
Resonant Tunneling through space-charge layers at GaAs surfaces,
 Frühjahrstagung der DPG, Dresden, (2006) Nr. HL3.6
15. K. Teichmann, S. Loth, M. Wenderoth, R. G. Ulbrich, and U. Kretzer
Spatial fluctuations of the local potential in Silicon doped GaAs
 Frühjahrstagung der DPG, Dresden, (2006) Nr. HL9.6
16. (eingeladener Vortrag) S. Loth, M. Wenderoth, T. C. G. Reusch, L. Winking,
 R. G. Ulbrich, S. Malzer, and G. H. Döhler
Electronic properties of shallow acceptors in GaAs - Scanning Tunneling Spectroscopy Studies.
 Seminar des Instituts für Angewandte und Experimentelle Physik, Lehrstuhl
 Prof. Dr. W. Wegscheider, Universität Regensburg (2005)
17. S. Loth, M. Wenderoth, T. C. G. Reusch, L. Winking, R. G. Ulbrich, S. Malzer, and G. H. Döhler
Scanning Tunneling Spectroscopy of Carbon and Zinc Acceptors in GaAs
 Frühjahrstagung der DPG, Berlin, (2005) Nr. HL17.61
18. S. Loth, M. Wenderoth, T. C. G. Reusch, L. Winking, R. G. Ulbrich, S. Malzer, and G. H. Döhler
Electronic properties of Carbon and Zinc acceptors in GaAs studied with Low Temperature Scanning Tunneling Microscopy
 8th International Conference on Nanometer-Scale Science and Technology,
 Venedig, Italien, (2004) Nr. SS2-FrM9

19. S. Loth, M. Wenderoth, T. C. G. Reusch, L. Winking, R. G. Ulbrich, S. Malzer, and G. H. Döhler
Electronic properties of Carbon and Zinc acceptors in GaAs studied with Low Temperature Scanning Tunneling Microscopy
Frühjahrstagung der DPG, Regensburg, (2004) Nr. HL33.2